Quantum diffusion and tunneling in the solid hydrogens (a short review)

Horst Meyer

*Department of Physics, Duke University, Durham, North Carolina 27708-0305, U.S.A.**

(Submitted December 15, 1997)
Fiz. Nizk. Temp. **24**, 507–521 (June 1998)

The first observations 30 years ago of molecular clustering via quantum diffusion in solid H_2 in nuclear magnetic resonance (NMR) and pressure experiments are described. A previous review on quantum diffusion and tunneling up to 1986 is updated to reflect progress in the last ten years. In particular I review the effect of clustering on heat capacity in solid D_2 and on the thermal conductivity in solid H_2. The configurational relaxation time observed in D_2 at 1.75 K is found to scale with that in H_2 at the same temperature in terms of the predictions of ortho–para resonant conversion-induced hopping. The relaxation times measured simultaneously on the same sample in NMR and conductivity experiments reflect different configurational processes. The theory of molecular hopping and pairing in solid H_2 is outlined and compared with experiments. The tunneling frequency of HD in solid H_2 deduced from transverse and longitudinal NMR relaxation experiments between 0.03 and 14 K is discussed. The hopping of ortho-H_2, invoked as a mechanism in the enhanced ortho–para conversion in presence of O_2 impurities, is mentioned. Finally, recent tunneling results for H, D and H_2^- anions in solid H_2 during the studies of low temperature reaction dynamics are also briefly described. In the Appendix, the hopping frequency determination in HD from NMR transverse relaxation time measurements is reviewed.
[S1063-777X(98)00106-6]

1. INTRODUCTION

It is an honor for me to have been invited by Professor V. G. Manzhelii to write an article for the 30th anniversary of the first observation of ortho-H_2 impurity quantum diffusion in a solid para-H_2 matrix. I would like to start this article with a few reminiscences on how this phenomenon was observed. A previous review[1] has given an account of work done until fall 1986 that, besides quantum diffusion in solid hydrogen, includes tunneling of HD impurities in hcp H_2 and recombination of H in H_2 via tunneling. Since that time further progress—both theoretical and experimental—has been made in this field and there has been increased awareness of the interesting tunneling reactions as a new type of low temperature chemical reaction.

The publication of the earlier review article permits restricting the description of experiments and theory since 1986, and one of the purposes of this review is to draw attention to some of the open questions that need to be addressed. I may be forgiven for including some details and figures of yet unpublished experiments at Duke University, and also for comparing the '81 HD tunneling results with more recent ones obtained by the group of N. Sullivan.

This article is organized as follows. Sections 2 A and 2 B contain an account of the initial observation of quantum diffusion in solid H_2, followed by experiments since 1986,—both in H_2 and in D_2—and by the theoretical treatment of the hopping process in solid H_2. Section 2 C deals with HD tunneling in solid H_2 including mechanisms ranging from quantum to classical diffusion. In Section 2 D, atom tunneling in both H_2, D_2 and in their mixtures is briefly reviewed. In the Appendix, the analysis of NMR T_2 measurements to obtain the HD hopping frequency is reviewed.

2. QUANTUM DIFFUSION AND TUNNELING IN SOLID H_2 AND D_2

A. The initial observation of *o*-H_2 clustering in solid H_2

The observation of molecular motion in solid H_2 below 4 K was not the result of a systematic search, but was a fortunate accident brought about by a puzzling problem during NMR experiments. L. I. Amstutz, J. R. Thompson, and I were engaged in studying the NMR spectrum of ortho-H_2 impurities in a hcp matrix of para-H_2. Ortho-H_2 has a nuclear spin $I=1$ and a rotational angular momentum $J=1$ and gives a proton NMR signal, while para-H_2 has $I=0$ and $J=0$, with no NMR signal. [Henceforth, in order to avoid confusion farther in this review, I use $(J=1)$ and $(J=0)$ to denote respectively ortho- and para-H_2.] We were trying to improve recent experiments[2] where the NMR ''pair spectrum'' of nearest $(J=1)H_2$ neighbors had been studied as a function of temperature, which led to the first determination of the electric quadrupole-quadrupole interaction energy parameter in solid H_2, $\Gamma/k_B=0.82$ K, a value that has stood the test of time.

We were studying the NMR spectrum of a sample with ortho molefraction $X(J=1)=0.01$, which shows two signal components: a) a sharp intense line at the Larmor frequency ν_L that represents the signal of the ''isolated'' $(J=1)H_2$ molecules surrounded by 12 $(J=1)H_2$ nearest neighbors and b) a structure with three peaks, placed symmetrically on each side of the sharp line. The center of gravity of this structure is located at a frequency $\nu(T)=\nu_L\pm\delta\nu(T)$ where

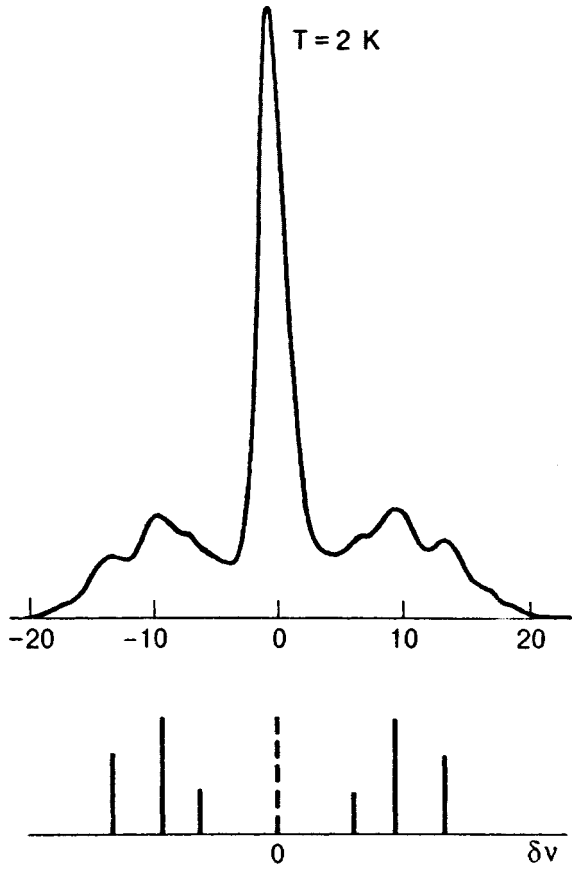

FIG. 1. Representative NMR absorption spectrum of H_2 at $X(J=1)=0.06$ and $T=2$ K. The spectrum under the curve represents the three pairs of satellites with their predicted respective intensities.[2] At $X(J=1)=0.005$, the satellite intensities are ten times smaller than in this Figure.

$\delta\nu(T)$ increases from ≈ 0 to 20 kHz as T decreases from 4 to 0.4 K. A representative spectrum for $X=0.06$ is shown in Fig. 1. The structure represents the ''pair spectrum'' of nearest $(J=1)H_2$ neighbors and the temperature dependence of $\delta\nu$ reflects the orientational ordering of these pairs as T decreases. For such a low value of $X=0.01$, the signal of the pairs was weak at the initial temperature of our measurement $T_i \approx 2$ K and our attention was focused on the NMR center line. We fully expected that when we decreased T, the integrated amplitude of this line would increase, because it is proportional to the nuclear susceptibility χ, which in turn is expected to obey Curie's law $\chi \propto T^{-1}$. We found indeed that, after rapidly cooling the sample by about $\Delta T \approx 0.5$ K, the signal amplitude rapidly increased, as expected. But then, to our surprise, it passed over a maximum and decreased to an equilibrium value over the course of several hours. When we warned the sample back to T_i, the amplitude rapidly decreased at first, then increased slowly back to the original value we had at the beginning of the experiment. We first suspected that these observations resulted from a drift in the amplifier of our NMR detection equipment, and we spent much time checking and calibrating carefully our electronics. However both our Robinson spectrometer[3] and the phase-detection amplifier system were found to perform without any drift in time. We then started to investigate this anomalous NMR signal behavior systematically and concluded that for unknown reasons over the range from 3 to 0.4 K the number of isolated o-H_2 decreased with temperature and equilibrated with a characteristic time $\tau(T)$. That time τ increased with decreasing T. Conversely, as T was increased, these isolated $(J=1)H_2$ reappeared, as evidenced by the recovery of the signal amplitude. We wondered how this process could take place, as we knew that classical activated diffusion rate was negligible at these temperatures, because the energy barrier for vacancy hopping is ≈ 200 K in solid H_2. We concluded that there had to be some other tunneling mechanism or molecular interchange with a rate that was not strongly temperature dependent. From previous work,[2] we realized that the internal energy of isolated $(J=1)H_2$ pairs was lower than that of the isolated $(J=1)H_2$ ''singles'', and it suddenly occurred to us that what we had witnessed was the clustering of $(J=1)H_2$ into pairs as the temperature decreased, and their unclustering as the sample was warmed up. The next step in our analysis was then to form the free energy F of the total system of $(J=1)H_2$ in the solid matrix, including both ''singles,'' N_s, and those molecules forming nearest neighbor $(J=1)$ ''pairs'', N_p, with respective fractions N_s/N and N_p/N, where N is the total number of $(J=1)H_2$ particles. By minimizing this free energy, it was possible to calculate the equilibrium fraction of these two types at a given $X(J=1)$ and T. The transient of the signal increase (or decrease) with time was found to be represented by an exponential $\exp(-t/\tau)$. The experimental results for the relaxation time as a function of temperature, but without a numerical calculation of the equilibrium fractions N_s/N as a function of T, were presented in our original publication.[4]

But we believed that a quantitative measurement of N_s/N from NMR experiments would be affected by systematic uncertainties from electronics, geometry etc. Therefore another approach was explored: while the NMR experiments were still in progress, pressure measurements at constant volume with a sensitive strain gauge were carried out in another cryostat by Ramm and myself on samples of H_2 with similar low $(J=1)$ concentration. We expected that after cooling the sample to a final temperature, $T_{\rm fin}$, the pressure $P=(\partial F/\partial V)_T$ was going to change with time at $T_{\rm fin}$ while the free energy F tended to its minimum value. The change $\Delta P(T)=[P(4.2\ \text{K})-P(T_{\rm fin})]$ to be observed between the initial temperature (4.2 K) and $T_{\rm fin}$, could then be compared with calculations from simple statistical mechanics. This expectation was indeed fulfilled and the relaxation time for the equilibration process at each temperature could be obtained by automatically recording the pressure versus time. The transient $[P(t)-P(t=\infty)]$ at the temperature $T_{\rm fin}$ was found to follow again an exponential with the relaxation time τ. As the molecules cluster, the pressure is predicted to decrease, reflecting a more ordered orientational state in the system, and this was verified by the experiment. Just as in NMR experiments, the characteristic time to cluster upon cooling increased as $T_{\rm fin}$ was decreased. These experiments and their analysis were first presented in preliminary form in the thesis of Ramm[5] and a statistical analysis was also published[6] where the equilibrium concentration of ''singles,'' ''pairs,'' and ''triangles'' of $(J=1)H_2$ and the pressure changes were calculated. The energy levels of the triangular configurations

used here had been calculated by Miyagi, and independently by Harris.[7]

Within a few years, optical experiments in other laboratories confirmed and measured the effects from clustering in H_2.[8–10] The insight stimulating these experiments was provided by the important paper by Oyarzun and van Kranendonk[11] who identified the mechanism of molecular motion as the ''resonant ortho–para conversion,'' a mechanism distinct from tunneling, and by which a $(J=1)$ particle excitation can propagate through a lattice of $(J=0)H_2$ molecules, leading to ''quantum diffusion.'' The authors calculated that this mechanism was faster than that of quantum mechanical tunneling.

The final publication of Ramm's experiments was delayed by more than ten years by other seemingly higher priorities, but in hindsight for no good reasons at all. The pressure results were finally published[12] together with more recent clustering experiments[13] showing quite novel results at temperatures as low as 0.02 K. These revived greatly the interest in this topic.

B. Research on H_2 and D_2 since 1986

1. Calorimetry

Detailed investigations of molecular clustering in the hydrogens were carried out at the B. Verkin Institute for Low Temperature Physics and Engineering in Kharkov by calorimetric methods that follow the earlier detailed studies.[14] A very interesting result was the unambiguous demonstration of $(J=1)D_2$ clustering in a matrix of $(J=0)D_2$, called, respectively, ''para'' and ''ortho''. As van Kranendonk[15] has pointed out, the molecular hopping frequency ν via resonant ortho-para conversion is $\nu \propto \gamma^2/R_0^5$, where γ is the nuclear gyromagnetic factor and R_0 is the intermolecular spacing with $R_0(H_2)/R_0(D_2)=1.05$. The ratio for the deuteron and proton factors is $\gamma(D)/\gamma(H)=0.154$, and hence the hopping frequency in D_2 is much smaller than in H_2. A calculation on p. 266 of Ref. 15, and which included other factors than γ gives

$$\nu(D_2)=0.48\times 10^{-2}\nu(H_2). \tag{1}$$

To detect the effect of clustering in D_2, Bagatskii *et al.*[16] measured the specific heat C_p of a sample with $X(J=1)=0.028$ as a function of time. Two processes contribute to a slow variation of C_p with time: a) the irreversible $(J=1)\rightarrow(J=0)$ conversion rate that causes C_p to decrease and b) the clustering with a characteristic time τ of the isolated $J=1$ particles into pairs via resonant $(J=1)\leftrightarrow(J=0)$ conversion, leading to an increase of C_p. Hence these two processes tend to compensate each other, but the good measuring accuracy enabled the authors to isolate the two contributions in the following way: the experiment started with the sample having random distribution of the p-D_2, which is reached after cooling the crystallized sample from the melting point at 18.7 K. As shown in Fig. 2, C_p slowly decreases with time during which the measurements are repeated at the same temperature over a period of 250 h. The sample was then heated to the melting point and cooled back to 1.65 K over a time of about 2 h. During this time, the distribution of $(J=1)D_2$ became randomized again, just as it was initially at the beginning of the experiment. However the mole fraction $X(J=1)$ had decreased by conversion, and the C_p, measured again at 1.65 K, was considerably lower than before this thermal cycling operation. This decrease of C_p from the value at $t=0$ was then due solely to conversion. From the combined analysis of the two experiments, the authors deduced a clustering characteristic time $\tau(D_2)=630\pm 50$ h at $T=1.65$ K.

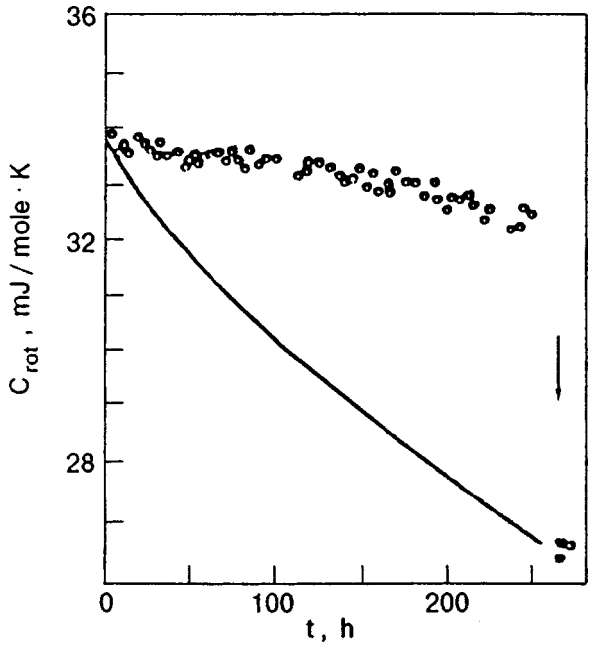

FIG. 2. Time dependence of the heat capacity C of $D_2[X(J=1)=0.028,\ T=1.73$ K]. Open circles: experimental values. Open squares: experimental data obtained after melting and recrystallizing the sample. The solid line represents the theoretical curve calculated on the assumption that no diffusion occurs $(\tau=\infty)$.[16]

Comparing this result with predictions is difficult: although theory provides an estimate of the resonant conversion frequency, the predictions of the average number of hops per particle to achieve clustering is uncertain, and will be discussed in a later section. However a more immediate check of the predictions can be made by comparing the clustering time in D_2 and in H_2 under similar conditions of $X(J=1)$ and T. Because the anisotropic electrostatic interactions, characterized by the parameter Γ, are comparable for H_2 and D_2 $[\Gamma(H_2)/\Gamma(D_2)\sim 0.8]$, we can expect that the number of hops to achieve clustering is also comparable, while the ratio of the hopping rates if given by Eq. (1). From pressure measurements in H_2 at $T=1.7$ K and with $X=0.025$, $\tau(H_2)=3.0$ h.[12] The ratio $\tau(H_2)/\tau(D_2)=0.46\times 10^{-2}$ is then in surprisingly good agreement with the predictions given by Eq. (1). (This scaling of the hopping times is only valid at ''high'' temperatures, i.e., above ≈ 0.5 K, but should not work at low temperatures where the hopping probability is more sensitive to the electric potential distortion in the surroundings and to its gradient. There the directions for a most probably jump for D_2 and for H_2 under similar conditions could be quite different, resulting in clus-

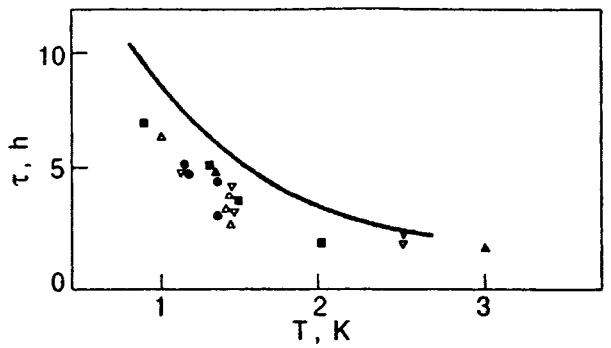

FIG. 3. Experimental values of the configurational relaxation time τ versus T in solid H_2 with added Ne impurities having a concentration $n(\mathrm{Ne})$. Open triangles: $n(\mathrm{Ne})=0.02\%$, $X(J=1)=0.5\%$. Inverse open triangles: $n(\mathrm{Ne})=0.04\%$ $X(J=1)=0.5\%$. Solid circles: $n(\mathrm{Ne})=0.06\%$, $X(J=1)=0.5\%$. Solid triangles: $n(\mathrm{Ne})=0.06\%$, $X(J=1)=1\%$. Solid squares: H_2 with $X(J=1)=0.5\%$ and added impurity of 2% D_2. The solid curve represents averaged values of τ for pure H_2.[19]

tering trajectories of different lengths.[17] See also Section 2 B3.)

Another interesting aspect in the calorimetric studies is the effect of heavier impurities on the clustering time constant τ in solid H_2. Minchina *et al.*[18] reported that at two temperatures, 0.5 and 1.3 K, where the experiments were carried out, the introduction of D_2 impurities first decreases τ from the value of pure H_2. Beyond a concentration $X(D_2)=0.02$, τ increases monotonically for doping up to $X(D_2)=0.3$, but by less than a factor of 2 (Ref. 18). Experiments were subsequently carried out on H_2 doped with the heavier impurity neon.[19] Mixtures with $X(\mathrm{Ne})<6\times10^{-4}$ showed a decrease of τ by the order of 30%, consistent with the result for D_2 impurity doping. These results are shown in Fig. 3. The reasons for this intriguing phenomenon have been discussed in Ref. 19 in terms of lattice distortions by the heavy impurity, but this needs to be further clarified. According to Fig. 3, τ is independent of $X(\mathrm{Ne})$ in the 0.02–0.06% range. It has been assumed in Ref. 19 that the upper limit of solubility of Ne in H_2 is not higher than 0.02%.

A further calorimetric experiment by the same group probed whether quantum diffusion of $(J=1)D_2$ in $(J=0)H_2$ could be observed.[20] A sample with 3% D_2, corresponding to $X(J=1)=9.4\times10^{-4}$ of $(J=1)D_2$ in $(J=0)H_2$ was investigated. No evidence of a clustering on the specific heat after a period of 290 h at 1.7 K could be found, indicating the characterizing clustering time to be in excess of 10^4 h.

2. Thermal conductivity

Simultaneous thermal conductivity and NMR experiments at Duke University were carried out on a sample of solid H_2 grown at constant density, corresponding to a pressure of $\approx$ 90 bar, and from which information of the clustering could be obtained.[21] More recently, further conductivity experiments[22] at a similar pressure were carried out in another cell where the sample was grown at constant pressure[23] instead of constant volume. Such a check with a different crystal growth arrangement was made necessary in view of

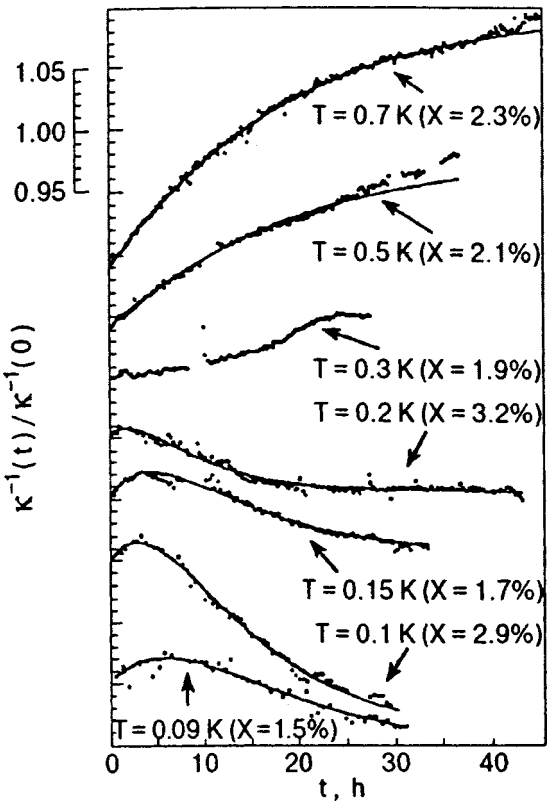

FIG. 4. Normalized thermal resistivity $\kappa^{-1}(t)/\kappa^{-1}(0)$ versus time at several temperatures for samples grown at constant density. To avoid overcrowding, the origin of the vertical scale for the various isotherms has been shifted from 1.00. The solid lines are fits of exponential transients to the data, as described in the text (after Ref. 21).

the unusual results reported in Ref. 21. To analyze the results, the additivity of the thermal resistivities from phonon scattering is assumed, namely

$$\kappa^{-1}(X,T)=\kappa^{-1}_{(J=0)H_2}(T)+\kappa^{-1}_{(J=1)H_2}(X,T). \tag{2}$$

Here $\kappa^{-1}_{(J=0)H_2}(X,T)$ is the resistivity of a pure $(J=0)H_2$ crystal and represents the phonon scattering by the lattice as determined by grain boundaries, lattice imperfections, etc. The second term, $\kappa^{-1}_{(J=1)H_2}(X,T)$ is the contribution from the inelastic phonon scattering by the excitation of the rotational energy states in the $(J=1)H_2$ molecules. During the clustering process, we expect $\kappa^{-1}_{(J=1)H_2}(X,T)$ to change as a function of time.

The experiments were carried out in a special thermal conductivity cell made of a proton-free commercial plastic, ''Kel-F'', that enabled the NMR spectrum to be scanned continuously while conductivity measurements were performed automatically as a function of time. The cell was cooled rapidly from a standard temperature, usually 2.2 K, where clustering is small, to a final temperature T_{fin} which was then stabilized for periods up to 45 h. During this time data on the conductivity and on the central NMR line amplitude, the latter being the signal of the ''isolated'' $(J=1)H_2$, were recorded. A sample of the results, suitably normalized to the initial observed resistivity $\kappa^{-1}(0)$ is shown in Fig. 4 for the earlier experiments[21] with the

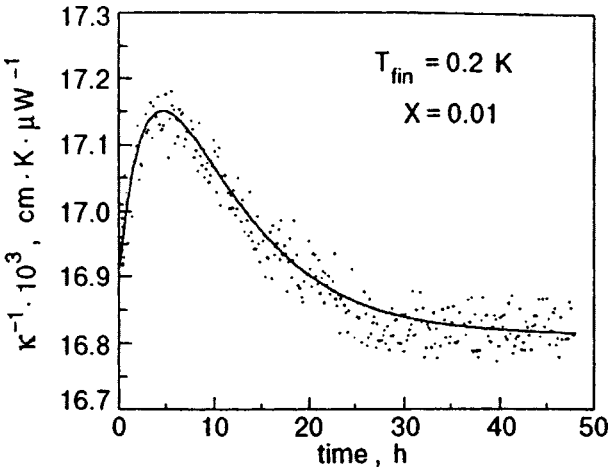

FIG. 5. A representative time evolution of the resistivity κ^{-1} at $T=0.2$ K and $X(J=1)=0.01$ obtained with a sample grown at constant pressure. This should be compared with the curve for the same temperature in Fig. 4. The solid line is again a fit of exponential transients to the data (from Ref. 22).

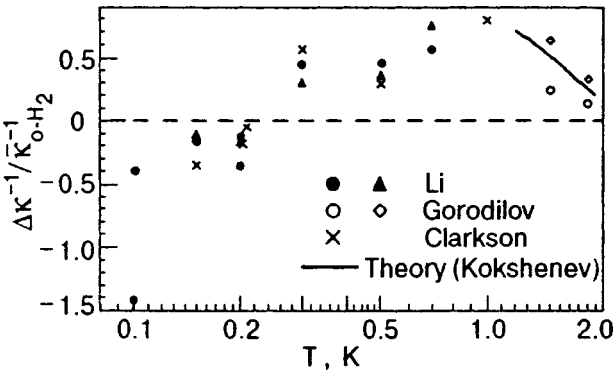

FIG. 6. The normalized change $\Delta\kappa^{-1}/\bar{\kappa}^{-1}_{(J=1)H_2}$ versus T for two series of experiments where $\bar{\kappa}^{-1}_{(J=1)H_2}$ is the average resistivity of the $(J=1)H_2$. Solid circles: $1.5\%<X<3.4\%$, solid triangles: $0.9\%<X<1.1\%$ from Ref. 21. Open circles and diamonds: for $X=1$ and 2% from Ref. 24. Crosses: $1.0\%<X<2.5\%$ from Ref. 22. The solid line is the prediction by Kokshenev[25] for $X=1\%$.

samples grown at constant density. Figure 5 shows a representative, vertically expanded time profile for $\kappa^{-1}(t)$ for $X=0.01$ and $T_{fin}=0.20$ K, obtained with the sample grown at constant pressure.[22] The curve is similar to that in Fig. 4 for the same T_{fin}. In both figures, the solid lines are fits to a sum of two exponential terms,

$$\kappa^{-1}(t)=A+B\ \exp(-t/\tau_1)+C\ \exp(-t/\tau_2). \tag{3}$$

The thermal transport and NMR data show remarkable features, the two principal ones being as follows:

a) Thermal resistivity change. Above $T\approx 0.3$ K, the resistivity increases as clustering proceeds. The equilibration can then be represented approximately by a single exponential term with a time constant τ_1. The change $\Delta\kappa^{-1}=[\kappa^{-1}(t=\infty)-\kappa^{-1}(0)]$ is positive. However as T decreases, $\Delta\kappa^{-1}$ decreases and changes sign near 0.3 K. The time profile of $\kappa^{-1}(t)$ becomes more complex with decreasing temperature, first rising and then decreasing to its equilibrium value. As a result, $\Delta\kappa^{-1}$ becomes negative. This is shown in Fig. 6 where the results at Kharkov obtained by Gorodilov *et al.*,[24] the predictions by Kokshenev at high temperatures[25] and the published[21] and unpublished[22] data in this laboratory are shown. (The single data point obtained in Ref. 26 has been omitted.) Given the various uncertainties, there is good consistency between the various measurements. The unexpected behavior change in sign of $\Delta\kappa^{-1}$ near 0.3 K is therefore confirmed.

b) Relaxation times. The transients shown by the exponential decay of the ''isolated'' $(J=1)H_2$ (from NMR) and by the change of conductivity, and measured simultaneously on the same sample, show different relaxation times. This is illustrated in Fig. 7 for a representative temperature above $T=0.3$ K. While both observations reflect clustering, they represent different aspects: the NMR shows the signal of ''singles'' decaying with time, while measurements of thermodynamic averages such as heat capacities and thermal conductivity reflect the complicated dynamics of $(J=1)H_2$ cluster formation (pairs and larger groups). In Fig. 8 the relaxation times from NMR measurements are presented together with those from C_p and from κ. For simplicity, I do not show the data from conductivity experiments below 0.3 K, where the situation becomes rather complex, with the formation of ''pair'' clusters that subsequently hop and congregate to form larger clusters (see Fig. 7b in Ref. 21). Based on the evidence from NMR data[13] that describe the decay rate of $(J=1)H_2$ pairs into larger $(J=1)H_2$ clusters, and which accelerates with decreasing temperature, it is reasonable to expect that the clustering relaxation times observed in calorimetric and thermal conductivity experiments will pass

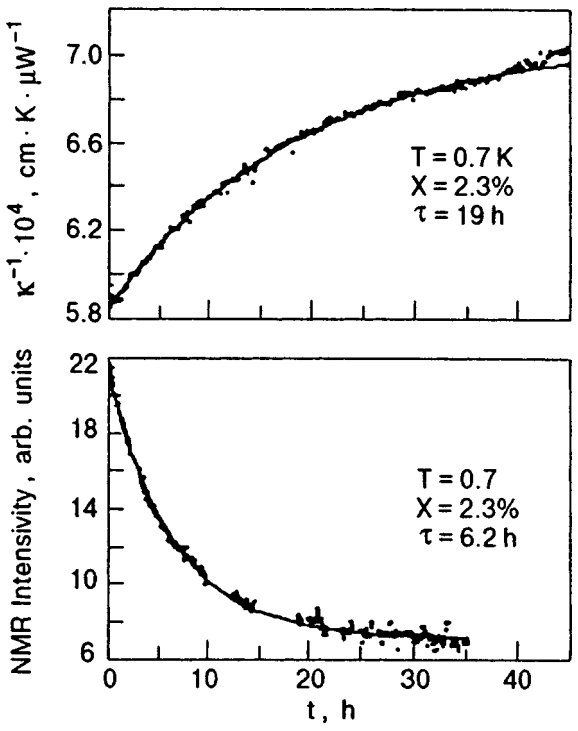

FIG. 7. Simultaneously recorded thermal resistivity and NMR signal intensity versus time at 0.7 K (from Ref. 21).

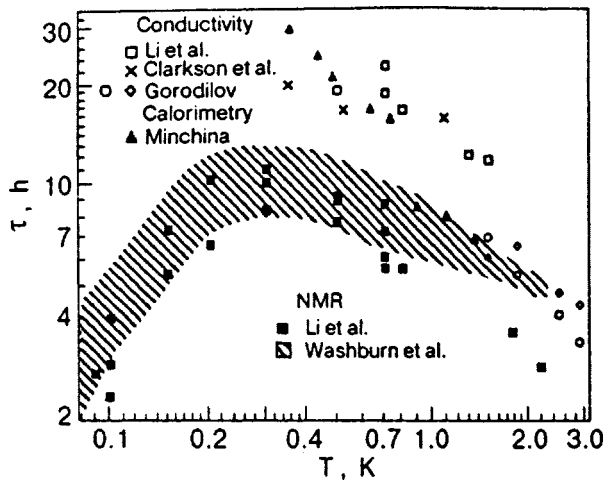

FIG. 8. Observed configurational relaxation times τ from various experiments in pure solid H_2. Solid squares NMR, isolated $(J=1)H_2$; open squares: conductivity, obtained during simultaneous experiments.[21] Open circles and diamonds: conductivity from Ref. 24. Crosses: conductivity with sample grown under constant pressure (from Ref. 22). Solid triangles: calorimetry from Ref. 14. The shaded area includes the NMR results on isolated $(J=1)H_2$ impurities (Ref. 13).

over a maximum and decrease with decreasing temperature below 0.3 K.

As can be seen from Fig. 8, the characteristic clustering times τ obtained from NMR in both experiments performed at zero pressure[13] and at a pressure of approximately 90 bar[21] agree within the considerable experimental scatter. The *resonant* $(J=1)\leftrightarrow(J=0)$ *conversion* mechanism[11] leads to the prediction of a roughly 10% increase in the hopping frequency for a density increase of 5%, which corresponds to a pressure change from 0 to 100 bars. This pressure effect might be too small to detect, given the scatter in the measurements of τ. By contrast, *mass quantum diffusion* of $(J=1)$ impurities, as produced by the motion of three-body cyclic permutation in the $(J=0)$ lattice[27] is predicted to decrease by a factor of 60 for this 5% density increase. Therefore the observations mentioned above favor resonant conversion over tunneling as the dominant mechanism of quantum diffusion, at least below 4 K.

The thermal transport measurements can be summarized as follows: at temperatures above ≈ 0.5 K, the time dependence and the sign of the resistivity κ^{-1} after a temperature quench to $T_{\rm fin}$ indicate that clustering of isolated ''single'' $(J=1)H_2$ particles takes place, but as $T_{\rm fin}$ is decreased, there appears to be competition between several clustering variations, and the time dependence of κ^{-1} becomes more complex. It is probable that clustering into larger configurations causes the trend of $\kappa^{-1}(t)$ to change direction. The initial increase of $\kappa^{-1}(t)$—which reflects the simple clustering of single particles—is compensated within a few hours after the temperature quench and is exceeded in magnitude by the effect from the clustering of larger groups. The quantitative understanding of this phenomenon remains to be clarified.

3. Theory on the pairing of $(J=1)H_2$ impurities

Significant progress has been made in recent years in the understanding and the simulation of the pairing procedure of $(J=1)H_2$ particles in a solid $(J=0)H_2$ matrix.[28–30] As already calculated by Oyarzun and van Kranendonk[11] and discussed by van Kranendonk,[15] the order of magnitude of resonant $(J=1)\leftrightarrow(J=0)$ conversion ''hopping'' frequency ν_0 for an ''isolated'' $(J=1)H_2$ surrounded only by $(J=0)H_2$, is of the order of 1×10^3 s$^{-1.}$ Electrostatic quadrupole-quadrupole interactions with $(J=1)H_2$ neighbors produces randomly fluctuating orientations, corresponding to an energy band width that increases rapidly as $X(J=1)$ increases. This reduces the probability of an energy-conserving jump. For $X=10^{-2}$, the reduction factor is calculated to be 10^{-7}, hence the hopping frequency is only $\nu(X=0.01)=5\times10^{-5}$ s^{-1}. Meyerovich and collaborators note that this small frequency ν_0 is very sensitive to inhomogeneities of the potential relief $U(\tau)\approx U_0(a/\tau)^5$, where $U_0/k_B\approx0.8$ K, and depends on the orientation. They explore the existence of a strong directional bias, which will influence the time where one $(J=1)H_2$ impurity approaches another one to form a pair. Stimulated partly by the observation of the maximum in the characteristic time of pair formation near 0.3 K,[13,31] Meyerovich advanced the idea that a directional bias might lead to such a maximum even if the individual hopping rates should show a monotonic behavior with T, i.e., an increase as T decreases. The two energy-conserving mechanisms for enabling hopping in the presence of an energy mismatch $\varepsilon_{i,j}=U(r_i)-U(r_j)$ from site i to site j are a) spontaneous emission of photons with an energy $h\omega/2\pi=\varepsilon_{i,j}>0$, and b) inelastic scattering of thermal phonons. The former process is only possible for $\varepsilon_{i,j}>0$ and is highly anisotropic, while the latter operates for any sign of $\varepsilon_{i,j}$. When $\varepsilon\ll h\omega_0/2\pi$, the hopping time is much larger than that calculated for phonon-assisted hopping and is given by ω^{-1}. The authors calculate the average pairing time with the help of a computational model for $X=10^{-2}$ and 10^{-3}. One $(J=1)$ impurity is moving while all the others, randomly distributed, stay fixed. The single particle diffuses in the cell and can pair with any one of the immobile impurities. The motion of the particle is tracked and the times of hopping are adjusted as the energy mismatch $\varepsilon_{i,j}$ and particle distribution change. In the calculation, hcp lattices with 100 to more than 10^3 lattice sites per cell were generated when the concentration decreased from about $X=10^{-2}$ to 10^{-3}.

The calculation gave the number of paired impurities as a function of time, assuming a random initial distribution of impurities over all sites, except at the origin, from where the diffusing particle starts, and its nearest neighbors. However, instead of a smooth curve indicating the pairing process to be exponential with time and characterized by a time τ, the plot gave a staircase (Fig. 9) which the authors interpreted to indicate that the pairing process is characterized by a set of times rather than by a single τ. They speculated that the staircase should become smoother when account is taken of an averaging effect by the motion of other particles. For their choice of a characteristic time τ, the authors used the time profile $t(n)$ describing the initial stage of pairing (the first step of the staircase). Here $n=N/N_T$, where N is the number of impurities that have been paired and N_T is the total number of impurities considered in the calculation. In a plot versus temperature, they show that this time τ passes over a

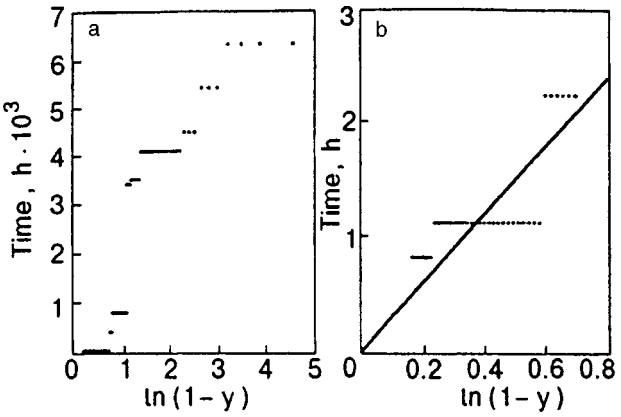

FIG. 9. The fraction y of pairs versus time (in hours) for a cell size with 100 lattice sites, corresponding to $X(J=1)=1\times10^{-2}$, pictures the pairing of 88 impurities, each marked by a symbol (*). a) overall picture; b) the initial stage of pairing of 38 impurities (after Fig. 2 of Ref. 30). It is from the initial stage that the pairing time is derived by the slope of the straight line.

maximum near $T=0.4$ K. By contrast, the characteristic time of the final stage of pairing is much longer and steadily increases with decreasing T. The authors then discuss in detail the numerical value of the two independent parameters in their calculations that produce a reasonable fit with experiment. They find, for instance, that the temperature position of the maximum in τ is rather insensitive to the value of (ξ_1/ξ), where ξ_1 and ξ are constants appearing in the expression for the time of the phonon-assisted impurity hopping. The lower bound of the estimate for ν_0 coincided with the value[15] 10^3 s^{-1} while the upper bound was about two orders of magnitude higher.

In Fig. 10 we present experimental data and theoretical curves from Ref. 30. Two unknown computation parameters (bare tunneling frequency ν_0 and a coefficient in its temperature renormalization) were chosen so as to fit the position and height of the maximum $\tau(T)$ to experimental data. The main difference between experimental data and computational results is in the position of the maximum. In principle,

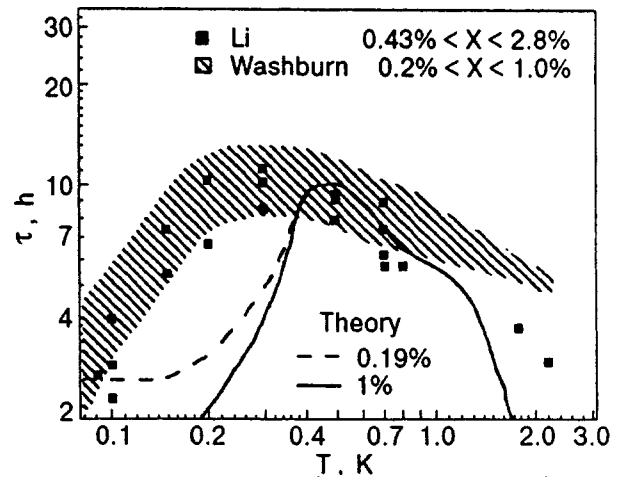

FIG. 10. Characteristic pairing time of isolated $(J=1)$ impurities. The shaded area represents the NMR data monitoring the signal decay of the ''isolated'' $(J=1)$ impurities.[13,21] The solid line represents an average of the predictions for $X=10^{-2}$ and 1.9×10^{-3} (after Ref. 29).

the theoretical curve should be shifted to the left by 0.2 K, from 0.5 to 0.3 K, and stretched vertically to make experimental and theoretical maxima coincide. This procedure should improve agreement between experimental and theoretical data. However, the position of the maximum and the shape of the curve were not very sensitive to the fitting parameters, and such a shift would require changing the unknown renormalization coefficient by an order of magnitude away from its expected range.[17] On the other hand, this insensitivity is a good sign demonstrating that the existence of the maximum is a stable general phenomenon. Better agreement with experimental data requires improvement of an over-simplified computational model.[30]

The numerical calculation leads to the following conclusion, as stated by the authors:[29] the low temperature peak in the characteristic pairing time is caused by a directional bias in the diffusion, which is conditioned by the interaction mechanism of the pairing particles with the surroundings. One of the diffusion mechanisms—the hopping with inelastic phonon scattering—is biased against mutual approach of the particles and opposes pairing. When this mechanism dominates at temperatures above the maximum in τ, a decrease in the temperature results in a slow-down in motion, including the pairing. As T further decreases, a temperature-independent motion with emission of phonons becomes increasingly important, and this neutralizes the first mechanism and increases the pairing rates.

So far, theory has considered the clustering dynamics from an isolated $(J=1)$ impurity to the final paired state. The statistical mechanics aspects (equilibrium concentration of pairs at a given temperature, as based on the Free Energy minimum) were ignored within the considered model with single-particle motion. The theory assumes all single impurities will cluster, which should be nearly realized only below ≈ 0.5 K.

Furthermore I note that the calculation of the characteristic clustering time τ has been made from the initial pairing stage, as computation of τ from the later stages gave a substantially larger value. The experimentally observed transient of the ''single'' $(J=1)$ signal $[n(t)-n(t=\infty)]$ followed an exponential decay all the way, and not just in the initial stages, as shown by all the NMR experiments.[4,13,21] It is hoped that these problems in the theory can be addressed in the near future.

C. Tunneling of HD and of $(J=1)H_2$ in solid H_2

There has been considerable activity in the study of low-temperature tunneling motions, both of molecules (HD) and of atoms in a matrix of solid H_2. (This process of motion is, of course, different from quantum diffusion resulting from ortho-para resonant conversion in H_2 and in D_2.) Furthermore experiments have been reported on H_2^- anion tunneling (see Section 2D). First the detailed NMR studies by the group of Sullivan, showing evidence of HD tunneling, will be described. This will be followed by the account of an experiment that indicates tunneling motion of $(J=1)H_2$.

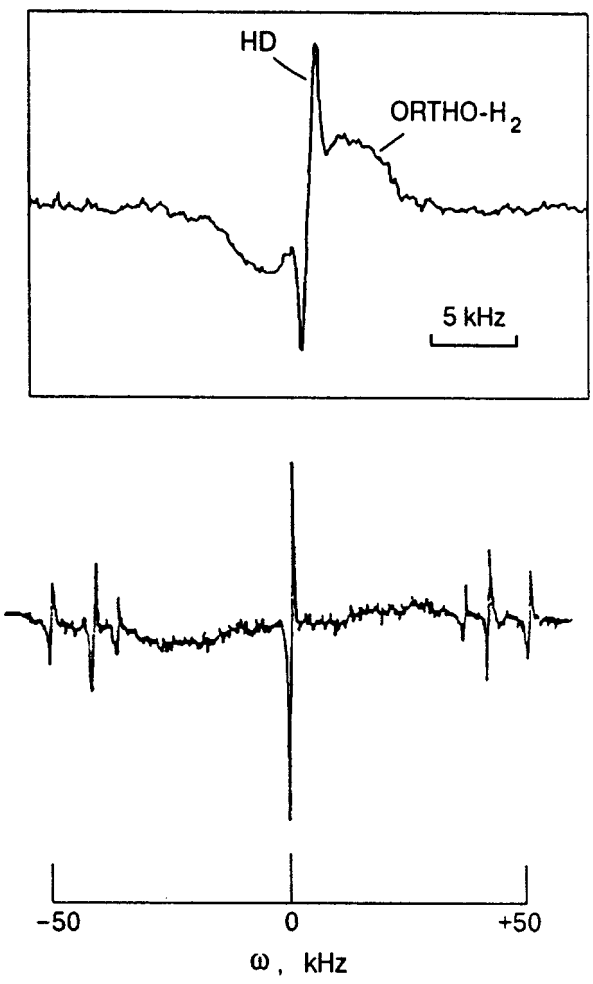

FIG. 11. The NMR derivative line shapes of the proton spectrum of HD (1.1%) and $(J=1)H_2$ ($X=0.018$) in solid $(J=0)H_2$ at temperatures below 4 K, where they can be separated (from Ref. 34).

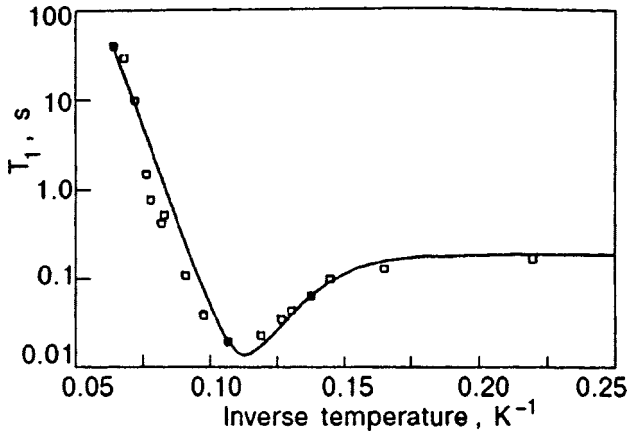

FIG. 12. The observed and calculated temperature dependence of the spin-lattice relaxation time T_1 of the HD impurities (1.1%) in H_2 with $X(J=1)=1.8\%$. Symbols: data of Rall *et al.*[34] Solid curve: theory.[35]

1. HD tunneling from NMR experiments

Pulse measurements[32–35] were carried out at 268 MHz and both the longitudinal and the transverse relaxation times, T_1 and T_2, of the proton nuclei were measured. The samples consisted of HD and of $(J=1)H_2$ impurities in a matrix of solid $(J=0)H_2$. The most extensively studied sample contained 1.1% of HD and 1.6% of $(J=1)H_2$. Although the proton line shapes of HD and H_2 can only be resolved below ≈ 4 K (see Fig. 11), they have very different relaxation times. Therefore the respective signal contributions can be separated and this is most striking for T_1. It is known that the spin-lattice relaxation time in pure H_2 for such low $(J=1)H_2$ concentrations is of the order of ms and has only a weak temperature dependence. (See, for instance, Ref. 36 and references therein). The characteristic molecular orientation fluctuation frequency spectrum ω_Q from the intermolecular electric quadrupole-quadrupole interactions modulate the dipolar interaction between the two protons. For $(J=1)H_2$ concentrations of a few percent, $\omega_Q/2\pi$ is comparable to the Larmor frequency of the order of 10 to 10^2 MHz, and this favors rapid energy transfer from the spin ''bath'' to the rotational energy bath, and from there to the lattice. The protons of HD do not have this mechanism of energy transfer, and their intrinsic relaxation rate to the lattice is very slow. However, as shown in Ref. 35, the cross-relaxation from the HD spin system to that of $(J=1)H_2$ permits a faster relaxation. Furthermore, this mode of energy transfer is sensitive to the motion of the HD molecule. In the high temperature regime (for $T>11$ K), the mechanism of cross-relaxation is attributed to the motion of vacancies, while in the low temperature regime ($T<8$ K), quantum tunneling of HD impurities is the responsible mechanism.

The longitudinal relaxation time measurements showed a pronounced minimum (Fig. 12) which was analyzed in Ref. 35. Starting from the low temperature end, where the cross-relaxation time is nearly constant and is determined by the quantum tunneling frequency J of the HD particles, impurity scattering with an activation energy E_F becomes important and leads to a decrease of T_1. The progressive excitation of vacancy motion with an activation energy E_B then pulls up T_1 as the temperature increases. The theory is thus able to account for the observed minimum. The quantum tunneling frequency so derived is $J=1.3\times10^3$ Hz, which is of the same order as the hopping frequency of $(J=1)H_2$ impurities from resonant conversion.[15] The energies obtained by fit to the data are $E_F/k_B=91$ K and $E_B/k_B=100$ K. It is the sum $(E_F+E_B)/k_B$ that determines the limiting high temperature slope seen in Fig. 12, and which agrees with previous determination of the activation energies in $(J=1)H_2$. It should be noted that, in pure solid H_2 with such low values of $X(J=1)$ as used here, this temperature dependence of T_1 is not observed, but the addition of HD impurities leads to a temperature profile of both T_1 and T_2—a pronounced minimum and a sharp rise with T— and permits the separate determination of these activation energies.

The transverse relaxation times show a similar behavior to the longitudinal ones, but with a less pronounced minimum. Figure 13 shows a representative curve for T_2 with 1.1% HD and 2.1% $(J=1)H_2$ between 15 and 4 K.[34] There is a weak linear temperature dependence below 4 K where T_2 rises to ≈ 3 ms near 0.1 K (Fig. 4 in Ref. 34). Again the results could be interpreted by quantum diffusion of the HD impurities at temperatures below ≈ 6 K. This value of T_2 is higher than calculated for HD in a rigid H_2 lattice, and this

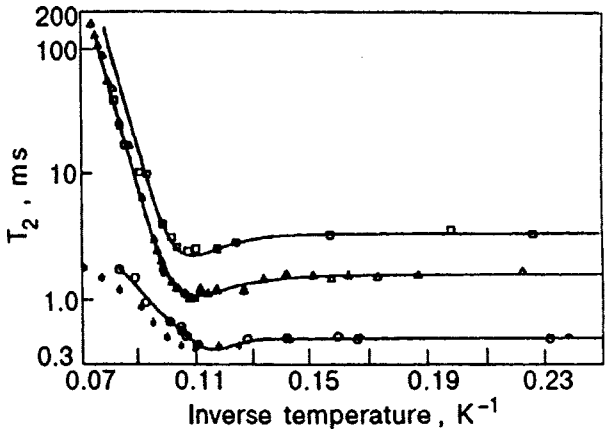

FIG. 13. Observed temperature dependence of the transverse nuclear relaxation time T_2 from the proton signal of HD and $(J=1)H_2$ impurities in solid $(J=0)H_2$ for three different samples. Squares: 1.1% HD, 1.8% $(J=1)H_2$; triangles: 1.1% HD, 2.1% $(J=1)H_2$; circles: 0.05% HD, 2.5% $(J=1)H_2$ (after Ref. 34). (The data represented by the asterisks are from Ref. 36).

leads to the conclusion that diffusion narrows the linewidth (or raises T_2). As the temperature increases, first vacancy-impurity scattering with an activation energy $E_B/k_B = 91$ K, and then vacancy motion with an activation energy $(E_B+E_F)/k_B = 196$ K explain the data very well. Neglecting the small temperature dependence that is attributed to formation of $(J=1)H_2$ clusters at temperatures below 4 K, the diffusion coefficient can be represented by

$$D_V=[D_0^{\text{quantum}}+D_0^{\text{classic}}e^{-E_B/k_BT}]e^{-E_F/k_BT}, \tag{4}$$

where $D_0^{\text{quantum}}=1.6\times10^{-8}$ cm^2/s and $D_0^{\text{classic}}=5.9\times10^{-3}$ cm^2/s. From the value of D_0^{quantum}, the authors calculate a tunneling frequency of $J_{\text{eff}}=1.5$ kHz. (See, however, the revised analysis below.)

Rall *et al.*[34] pointed out that it would be valuable if both results obtained at Duke University and at the University of Florida could be compared at the same temperature. In fact such a comparison can be made readily for the temperature range below 0.1 K, where the temperature dependence of T_2 is only weak, and is based on the experiments carried out at Duke[37,38] as presented in Ref. 38. The details of this comparison and their analysis to obtain the tunneling frequency J are deferred to the Appendix. Briefly, the result is that the T_2 data obtained in both laboratories under comparable conditions of $X(J=1)$ of temperature and of r.f. pulse length are of the same order. The uncertainty lies in the analysis of T_2 to obtain the tunneling frequency. This frequency, when derived with the use of the relations reviewed in the Appendix, is lower than the $J_{\text{eff}}=1.34$ kHz claimed by Rall *et al.*[34] While tunneling of HD in the matrix of $(J=0)H_2$ no doubt exists, its frequency, as obtained from the Duke data, is of the order of 3×10^2 Hz, and independent of $X(J=1)$ and of T within the experimental uncertainty. The reanalyzed UF data[39] give $J_{\text{eff}}\approx800$ Hz. The results are shown in Fig. 14b where the DU and the UF data are compared.

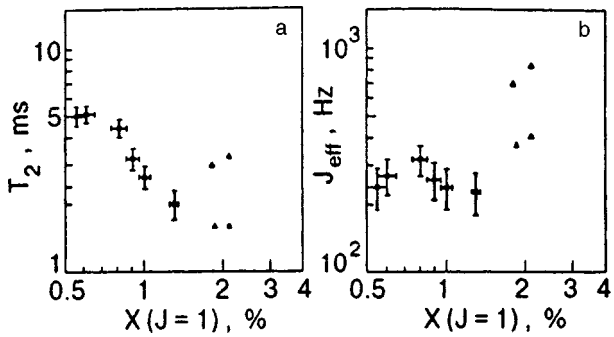

FIG. 14. a) The T_2 data in the temperature range of 50–100 mK as a function of $X(J=1)$. Solid circles: from Ref. 38, open triangles: from Figs. 3 and 4 in Refs. 34 and 39. b) The derived tunneling frequency J_{eff} versus $[X(J=1)]$, as obtained from the T_2 data via equations (9)–(11) (in Ref. 34).

2. Enhanced ortho–para conversion in solid H_2 with O_2 impurities

Tunneling appears also to be important in the $(J=1)\rightarrow(J=0)$ conversion in solid H_2 catalyzed by O_2 impurities, as shown by Shevtsov *et al.*[40] Here the conversion rate for small concentrations of O_2 was studied between 4.2 and 7 K. The authors report a very different conversion rate (magnitude, as well as temperature dependence) from that for pure solid H_2. Diffusion of $(J=1)H_2$ is invoked, and a fit of the proposed model to the data gives a diffusion coefficient $D(T)=D_0\exp(-96/T)$. The activation energy is comparable to that obtained by the group of Sullivan for the HD tunneling in this temperature region, where the potential energy of (91 ± 6) K was attributed to impurity-vacancy scattering.[35] The prefactor $D_0=3\times10^{-11}$ cm^2/s corresponds to a tunneling frequency $\sim10^3$ times smaller than that for HD and smaller than ν_0 for the resonant $(J=1)\leftrightarrow(J=0)$ conversion of an isolated pair in $(J=0)H_2$,[15] where ν_0 is of the order 10^3 s^{-1}.

D. Tunneling of D or H atoms and H_2^- anions in solid H_2

A very interesting development over the last fifteen years is the systematic study of low temperature chemical reactions. Here electron spin resonance techniques are used to observe the H or D signal intensity in a matrix of solid H_2, HD or H_2–D_2 mixtures. The atoms are produced by the irradiation of the solid sample by γ rays from a Co^{60} source or with x-rays, and their ESR signal shows an exponential decay with time that is interpreted as recombination through tunneling. This research elucidates chemical kinetics near 4 K and below, where all the thermally activated reactions are suppressed, and only those driven by quantum tunneling take place.

A major portion of this research has been carried out at Nagoya University by the group of Miyazaki, and a review of papers before 1990 has been presented by him in Ref. 41. Among the many reactions studied experimentally and also theoretically, a very interesting one has been the irradiation of a solid D_2–HD mixture by γ rays at 4.2 K.[42] Simultaneous ESR measurements of H and D atoms, made after the irradiation, showed clearly the D signal to decrease while that of

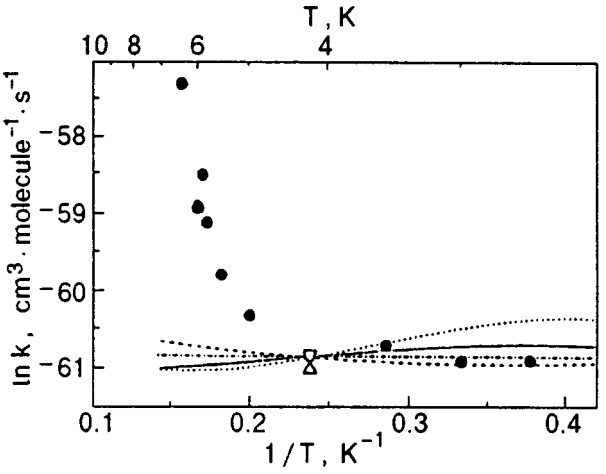

FIG. 15. The rate constant k for the tunneling reaction $HD+D\rightarrow H+D_2$, solid circles: experimental data; curves: calculations based upon different potential surfaces (after Ref. 43).

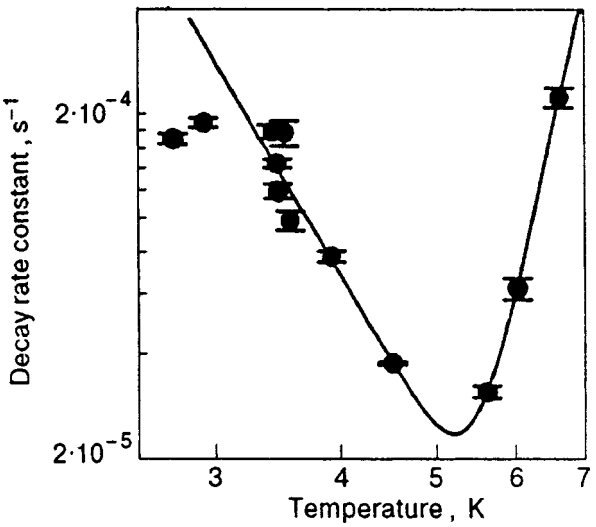

FIG. 16. The decay rate constant of H_2^- anions in x-ray irradiated solid ($J=1$)H_2 over the temperature range 2.7–6.6 K. The solid curve shows a two term fit to the data, as explained in the text (after Ref. 45.)

H increased with time. The results indicated convincingly the occurrence of the reaction

$$HD+D\rightarrow H+D_2. \tag{5}$$

The signal transient curve obtained for $T=4.2$ K was found to be the same at 1.9 K, indicating that the reaction rate was temperature independent. Because the potential barrier for this reaction is $\Delta E/k_B\approx 5\times 10^3$ K, the reaction cannot occur by thermal activation, but must take place by quantum tunneling. Several types of calculations of the rate constants in this tunneling regime have been carried out and were listed in Miyazaki's review. In a review of more recent papers,[43] the temperature dependence of the above reaction has been investigated in detailed fashion and shows a dramatic temperature dependence of the reaction constant k defined by the relation

$$\frac{d[D]}{dt}=-k[D][HD], \tag{6}$$

where the components in brackets signify the fraction of the reactants.

This behavior of k is shown in Fig. 15 where k sharply decreases with falling temperature as thermal activation becomes frozen out. Below 4 K, k remains constant. From the temperature dependence between 6.5 and 5 K, the authors[44] derive an activation energy $\Delta E/k_B=95$ K, which is similar to values between 85 and 105 K obtained for vacancy diffusion in solid HD from NMR transverse relaxation time measurements.[34] This result is discussed in terms of the distortion of the solid hydrogen lattice structure by the H and the D atoms, which is caused by the large zero-point vibration of these atoms. The authors argue that in the tunneling process, the deformation accompanies the atoms. When a vacancy moves to another site by thermal activation, the atom tunneling is accelerated by the vacancy motion. This is vacancy-assisted tunneling reaction, which becomes temperature-independent below about 4 K. Investigation of the ESR fine-structure and the linewidth for H atoms in solid HD furthermore gave information on the distance between the tunneling atom and the nearest neighbor host molecules. It was found that the average distance H–HD was ≈3 Å.

Another interesting investigation is that of the decay rate of H_2^- anions.[45] In the reaction accompanying the decay, the anions change into electron bubbles, as represented by the equation

$$H_2^-+HD\rightarrow H_2+HD+e^-_{\text{bubble}}. \tag{7}$$

The ESR spectrum of electron bubbles has been observed to become more intense while that of the H_2^- decreases. The decay rate constant has a rather striking temperature dependence, as shown in Fig. 16. Here solid $(J=0)H_2$ has been irradiated with x-rays. The measured decay rate constant can be represented by a sum of two terms. The first is a thermally-activated process above 5 K with an activation energy of $\Delta E/k_B=93$ K, the same as in the reaction given by Eq. (4). The second term is a phonon scattering process in quantum diffusion. The tendency of the decay rate constant towards temperature independence below 3.2 K might indicate quantum diffusion in the absence of phonon scattering. The possibility has been raised[45] that the origin of anion motion might be through reaction with a tunneling impurity HD molecule. However another mechanism of anion hopping is given by the conversion

$$(J=0)H_2^-+(J=0)H_2\rightarrow(J=0)H_2+(J=0)H_2^-. \tag{8}$$

Because of the light mass of the excess electron, and the symmetry between the initial and final compound, this conversion might occur by quantum tunneling of the electron. However information on the anion H_2^- in solid H_2 is insufficient so far to permit more discussion.

3. CONCLUSION

Much progress has been made in the past ten years in the understanding of quantum diffusion and tunneling phenomena in the solid hydrogens. It is hoped that this review will stimulate further investigations in several areas. Since the

tunneling study of HD, H and D atoms in solid hydrogen is a very active subject of research at present, I restrict myself to the topic of $(J=1)H_2$ quantum diffusion through the resonant conversion process.

i) More and better NMR experiments are certainly needed with dilute mixtures below 0.1 K to explore whether the clustering time τ tends to a constant value, as suggested by theory.

ii) Although the theory of single-particle clustering is already quite complex, it is hoped that still further improvements can be made to bring theory into better agreement with experiments and to clarify the problem of the transient decay, which is observed to be exponential during the whole process and not only in the initial stages of clustering.

iii) The complicated time dependence of the thermal resistivity after the quench to a final temperature $T_{\rm fin}$ needs to be quantitatively explained as a function of T. It would be interesting to find out whether calorimetric experiments also show a complex time dependence at temperatures below 0.5 K after a temperature quench.

iv) There is also the intriguing question of what happens to clustering at larger $(J=1)$ concentrations than a few %. Pressure experiments[12] at constant volume, $P_V(t)$, suggest that as $X(J=1)$ increases, the clustering time decreases. Could quantum diffusion play a role in the martensitic transformation (from $Pa3$ cubic to hexagonal close packed) that accompanies the orientational order–disorder transition? The transformation, which is observed for $X(J=1)>0.55$, has been known for about thirty years and is very different for solid H_2 and D_2. The dynamics of the thermal cycling and phase stability for this transition have been recently reviewed.[46] While the effect of quantum diffusion on the irreversible $(J=1)\rightarrow(J=0)$ conversion rate can be observed in various types of experiments at low concentrations when clustering has occurred, it also appears that diffusion at intermediate concentrations is still efficient in bringing about a random distribution of the $(J=1)H_2$ in the matrix as the conversion proceeds. It is difficult to observe directly this diffusion from $P_V(t)$ measurements, because the time dependence of P_V from the $(J=1)\rightarrow(J=0)$ conversion masks any molecular rearrangement effect due to diffusion.

This short review has been restricted to the solid hydrogens in three dimensions. The very interesting subject of molecular motions in thin films of H_2, HD and D_2 has received much attention, especially over the past ten years, and a review on this topic is certainly due. For the reader's convenience I list some of the recent works[48–51] where references to previous research in this field are given.

4. DEDICATION AND ACKNOWLEDGMENTS

This review is dedicated to the memory of Neville Robinson (1925–1996), whose gift of several ''Robinson'' spectrometers was crucial both in the NMR research that led to the first observation of clustering in solid H_2 and to its further study over the next 20 years, and also in my Undergraduate Advanced Physics Laboratory at Duke University.

My thanks go to my former associates L. I. Amstutz, J. R. Thompson, D. Ramm, S. Washburn, R. Schweizer, I. Yu, X. Li, and D. Clarkson who contributed significantly to the study of quantum diffusion at Duke University.

I have profited greatly from stimulating interaction with A. M. Meyerovich, N. S. Sullivan, and S. Washburn who gave detailed advice on a draft of this paper. In particular I am grateful to the first two for clarifications and discussions of several aspects of their papers.

Also my sincere thanks go to D. Murphy for recasting several of the figures into a presentable form.

5. APPENDIX: THE HD HOPPING FREQUENCY AS DERIVED FROM T_2 MEASUREMENTS

First I review the data for the transverse relaxation time T_2 obtained at the University of Florida (UF) and at Duke University (DU) under comparable experimental conditions. This is followed by a data analysis to obtain the HD tunneling frequency.

It might be noted that the statistical rigid-lattice NMR full width at half maximum (FWHM) for the HD spins is given by $\Delta_{\rm FWHM}=63.4\ X(J=1)$ (kHz) in Ref. 34. The numerical coefficient is larger by a factor of about 3 than that presented in Ref. 37, Eq. (7a), and was based on a model by Delrieu and Sullivan.[27] (This width was denoted by δ/π in Refs. 27 and 37.) The new value of $\Delta_{\rm FWHM}$, which is larger than the experimental one deduced from T_2 data, indicates ''motional narrowing'' of the (Lorentzian) line, and signifies that HD tunneling is taking place.

The data at UF were obtained with r.f. pulse amplitudes giving a field of 15 G in the rotating frame.[34] For a $\pi/2$ pulse, this corresponds to a pulse length of $\approx 4\ \mu$s. In the DU experiments,[37,38] pulse lengths for a $\pi/2$ pulse were between 11 and 100 μs and the T_2 results were extrapolated to zero pulse length. The UF sample concentrations were $C(\mathrm{HD})=1.1\%$, $X(J=1)=2.1\%$ and $C(\mathrm{HD})=1.1\%$, $X(J=1)1.8\%$. Those of the DU sample IV were $C(\mathrm{HD})=0.04\%$ and $0.55\%<X<1.3\%$, where $X(J=1)$ decreased through conversion over the period of the experiment. The data taken near $T=50$ mK are shown in Fig. 14a. Because of the significant dependence of T_2 on pulse length,[37,38] the DU T_2 data near $X=1.3\%$, converted to 4 μs pulse length, would have been respectively ≈ 0.7 ms larger than for zero pulse length, namely ≈ 3.1 ms, which is comparable with the data obtained at UF, namely 3.4 ms for $X(J=1)=2.1\%$ and 4.6 ms for $X(J=1)=1.8\%$.

The next step, the calculation of the HD jump frequency, has uncertainties which were discussed previously.[37] The difficulty lies in the correct choice of the rigid lattice second moment of the HD line for low values of $X(J=1)$ and in the presence of clustering. It is therefore interesting that for short $\pi/2$ pulses of 11 μs or less, T_2 does not seem to change significantly as clustering proceeds in time (Fig. 4a in Ref. 38 and Fig. 4 in Ref. 34).

For comparison of the data of UF and DU in a consistent way, I use Eqs. (18), (28), and (30) in the paper by Rall *et al.*[34] (Note: the ''X'' in the denominator of Eq. (18) should be suppressed.)[39] The tunneling frequency $J_{\rm eff}$ is then given by

$$J_{\rm eff}=\frac{4T_2M_2^{\rm HD}}{6\pi} \tag{9}$$

where the second moment $M_2^{\rm HD}$ of the HD rigid lattice NMR line is given by

$$M_2^{\rm HD}=\left[\frac{3}{8}\frac{C({\rm HD})}{X(J=1)}+\frac{4}{9}\right]M_2^{\rm H_2}(X). \tag{10}$$

Here $M_2^{\rm H_2}$ is the second moment of the H_2 line. For this quantity the high temperature limit value under the assumption of random $(J=1)H_2$ distribution[47] was taken,

$$M_2^{\rm H_2}(X)=90\ X\ \ ({\rm kHz})^2. \tag{11}$$

Inserting the respective values of $X(J=1)$ and $C({\rm HD})$ into the equations, the values of $J_{\rm eff}$ are obtained as shown in Fig. 14b. There appears to be no significant variation of $J_{\rm eff}$ with $X(J=1)$ in the DU experiment, but a discrepancy exists with the results from the UF group which is diminished if one takes into account the pulse length-dependence of T_2, as discussed above. The UF values for $J_{\rm eff}$, quoted here after clarifications by Sullivan,[39] are lower than 1.34 kHz, reported in the paper of Kisvarsanyi and Sullivan.[35]

*E-mail: hm@phy.duke.edu

[1] H. Meyer, Can. J. Phys. **65**, 1453 (1987).
[2] A. B. Harris, L. I. Amstutz, H. Meyer, and S. M. Myers, Phys. Rev. **175**, 603 (1968).
[3] F. N. H. Robinson, J. Sci. Instrum. **36**, 481 (1959).
[4] L. I. Amstutz, J. R. Thompson, and H. Meyer, Phys. Rev. Lett. **21**, 1175 (1968).
[5] D. Ramm, *Pressure Studies in Solid* H_2 and D_2, PhD thesis, Duke University (1969) (unpublished).
[6] H. Meyer, Phys. Rev. **187**, 1173 (1969).
[7] H. Miyagi, Prog. Theor. Phys. **40**, 1448 (1968); A. B. Harris, Unpublished Calculations (1968).
[8] S. A. Boggs and H. L. Welsh, Can. J. Phys. **51**, 1910 (1973).
[9] B. J. Roffey, S. A. Boggs, and H. L. Welsh, Can. J. Phys. **52**, 2451 (1974).
[10] W. N. Hardy, A. J. Berlinsky, and A. B. Harris, Can. J. Phys. **55**, 1150 (1977).
[11] R. Oyarzun and J. van Kranendonk, Can. J. Phys. **50**, 1494 (1972).
[12] D. Ramm and H. Meyer, J. Low Temp. Phys. **40**, 173 (1980).
[13] S. Washburn, R. Schweizer, and H. Meyer, J. Low Temp. Phys. **40**, 187 (1980).
[14] I. Ya. Minchina, M. I. Bagatskii, V. G. Manzhelii, and A. I. Krivchikov, Fiz. Nizk. Temp. **10**, 1051 (1984) [Sov. J. Low Temp. Phys. **10**, 549 (1984)].
[15] J. van Kranendonk, *Solid Hydrogen*, Plenum Press, New York, (1983).
[16] M. I. Bagatskii, A. I. Krivchikov, V. G. Manzhelii, I. Ya. Minchina, and P. I. Muromtsev, Fiz. Nizk. Temp. **13**, 1001 (1987) [Sov. J. Low Temp. Phys. **13**, 571 (1987)].
[17] A. M. Meyerovich, private communication (1997).
[18] M. I. Bagatskii, I. Ya. Minchina, V. G. Manzhelii, and A. I. Krivchikov, Fiz. Nizk. Temp. **12**, 343 (1986) [Sov. J. Low Temp. Phys. **12**, 194 (1986)].
[19] I. Ya. Minchina, M. I. Bagatskii, V. G. Manzhelii, and P. I. Muromtsev, Fiz. Nizk. Temp. **21**, 678 (1995) [Low Temp. Phys. **21**, 530 (1995)]; Czech. J. Phys. **46**, 533 (1996).
[20] A. I. Krivchikov, M. I. Bagatskii, V. G. Manzhelii, I. Ya. Minchina, and P. I. Muromtsev, Fiz. Nizk. Temp. **15**, 3 (1989) [Sov. J. Low Temp. Phys. **15**, 1 (1989)].
[21] X. Li, D. Clarkson, and H. Meyer, J. Low Temp. Phys. **78**, 335 (1990).
[22] D. Clarkson and H. Meyer, unpublished results (1993).
[23] D. Clarkson and H. Meyer, Fiz. Nizk. Temp. **19**, 487 (1993) [Low Temp. Phys. **19**, 343 (1993)].
[24] B. Ya. Gorodilov, I. N. Krupski, V. G. Manzhelii, and O. A. Korolyuk, Fiz. Nizk. Temp. **12**, 326 (1986) [Sov. J. Low Temp. Phys. **12**, 186 (1986)].
[25] V. B. Kokshenev, J. Low Temp. Phys. **20**, 373 (1975).
[26] M. Calkins and H. Meyer, J. Low Temp. Phys. **57**, 265 (1984).
[27] J. M. Delrieu and N. S. Sullivan, Phys. Rev. **B23**, 3197 (1981).
[28] A. E. Meyerovich, Phys. Rev. B **42**, 6068 (1990).
[29] A. E. Meyerovich, M. P. Nightingale, and M. Tammaro, Physica **B194–196**, 925 (1994).
[30] M. Tammaro, M. P. Nightingale, and A. E. Meyerovich, Phys. Rev. **B47**, 2573 (1993).
[31] R. Schweizer, S. Washburn, and H. Meyer, Phys. Rev. Lett. **40**, 1035 (1978).
[32] D. Zhou, M. Rall, J. P. Brison, and N. S. Sullivan, Phys. Rev. **B42**, 1929 (1990).
[33] E. G. Kisvarsanyi, K. Runge, and N. S. Sullivan, Phys. Lett. **155A**, 337 (1991).
[34] M. Rall, D. Zhou, E. G. Kisvarsanyi, and N. S. Sullivan, Phys. Rev. **B45**, 2800 (1992).
[35] E. G. Kisvarsanyi and N. S. Sullivan, Phys. Rev. **B46**, 2814 (1992).
[36] R. F. Buzerak, M. Chan, and H. Meyer, J. Low Temp. Phys. **28**, 415 (1977).
[37] S. Washburn, R. Schweizer, and H. Meyer, J. Low Temp. Phys. **45**, 167 (1981).
[38] I. Yu, J. Low Temp. Phys. **60**, 425 (1985).
[39] N. S. Sullivan and E. Kisvarsanyi, private communication (1997).
[40] V. Shevtsov, A. Scherbakov, P. Malmi, E. Ylinen, and M. Punkkinen, J. Low Temp. Phys. **104**, 211 (1996).
[41] T. Miyazaki, Radiat. Phys. Chem. **37**, 635 (1991).
[42] K. Lee, T. Miyazaki, K. Fueki, and K. Gotoh, J. Chem. Phys. **10**, 341 (1987).
[43] T. Miyazaki, T. Kumada, N. Kitagawa, K. Komaguchi, and Y. Aratono, *Proceedings 2nd Conference, Cryocrystals 1997*, Polanica, Poland; J. Low Temp. Phys. (in press).
[44] T. Kumada, K. Komaguchi, Y. Aratono, and T. Miyazaki, Chem. Phys. Lett. **261**, 463 (1996).
[45] T. Kumada, N. Kitasgawa, T. Takayanagi, Y. Aratono, and T. Miyazaki, *Proceedings Meeting on Tunneling Reaction and Low Temperature Chemistry*, Oct. 1997, JAERI, Tokai, Japan.
[46] H. Meyer, Physica B **197**, 13 (1994).
[47] L. I. Amstutz, H. Meyer, S. M. Myers, and D. C. Rorer, Phys. Rev. **181**, 589 (1969).
[48] K. Eschenroeder, H. Kiefhaber, G. Weiss, and J. Classen, J. Low Temp. Phys. **109**, 163 (1997).
[49] K. G. Sukhatme, J. E. Rutledge, and P. Taborek, J. Low Temp. Phys. **103**, 301 (1996).
[50] M. Wagner and D. M. Ceperley, J. Low Temp. Phys. **102**, 301 (1996).
[51] R. N. Conradt, U. Albrecht, S. Hermingshaus, and P. Leiderer, Physica B **194–196**, 679 (1994).

This article was published in English in the original Russian journal.

* * *

Thirty years ago L. I. Amstutz, J. R. Thompson, and H. Meyer detected quantum diffusion in solid hydrogen. This discovery has considerably influenced the evolution of the concept of tunnel processes in solids and stimulated numerous experimental and theoretical studies. Many aspects of this interesting phenomenon are not yet clear and its further investigation will undoubtedly reward researchers' efforts with results of fundamental importance. Professor H. Meyer, F. London Prize winner, agreed to contribute to the celebration of the anniversary and to write a paper for our Journal describing the progress achieved in quantum diffusion in solid hydrogens during the recent decade. Professor H. Meyer is not only one of the authors of the discovery; it is to his further studies that we owe the first experimental detection and investigation of the most interesting features of quantum diffusion in hydrogen.

Editorial Board

QUANTUM LIQUIDS AND QUANTUM CRYSTALS

Long-wave fluctuation kinetics and quasi-linear relaxation for zero-point sound in a normal Fermi liquid

Yu. V. Slyusarenko

*National Science Center ''Kharkov Institute of Physics and Technology,'' 310108 Kharkov, Ukraine**
(Submitted January 12, 1998; revised February 10, 1998)
Fiz. Nizk. Temp. **24**, 522–532 (June 1998)

A universal phenomenological approach to studying macroscopic fluctuations is proposed and general kinetic equations for long-wave fluctuations in a normal Fermi liquid are derived. These kinetic equations form the basis of the theory of quasi-linear relaxation for zero-point sound in a normal Fermi liquid in the paired fluctuation approximation. The conditions for the existence of the quasi-linear approximation are considered. © *1998 American Institute of Physics.* [S1063-777X(98)00206-0]

INTRODUCTION

Macroscopic (long-wave) fluctuations play a noticeable role in a wide range of physical phenomena in classical as well as quantum systems.[1)] It is well known that fluctuations are very important in the theories of turbulence[3,4] and ''long hydrodynamic tails,'' [5–8] as well as in the theory of interacting modes.[9,10] A microscopic approach (based on a generalization of the Bogoliubov method of brief description) to the construction of the kinetic and hydrodynamic theory of long-wave fluctuations was developed in Ref. 2 (see in this connection Refs. 11 and 12 also). It was established that the equations of quasi-linear relaxation in plasma can easily be obtained from general fluctuation-kinetics equations in the approximation of paired fluctuations for a weak Coulomb interaction between particles. In this case, a decisive role is played by the terms in kinetic equations describing the effect of a self-consistent field on the system dynamics. In view of specific properties associated with the dependence of the Hamiltonian of a quasiparticle on the distribution function (see, for example, Refs. 13–17), effects similar to collisionless relaxation in plasma must be observed for normal Fermi liquids (both charged and neutral). Naturally, this is only one (although peculiar) phenomenon that stimulates the construction of a kinetic theory of macroscopic fluctuations in a normal Fermi liquid developed in this article. The derivation of equations for quasi-linear relaxation in the case of ''zero-point sound'' is considered here as an application of the general equations of long-wave fluctuation kinetics obtained by us for a normal Fermi liquid.

1. KINETIC EQUATIONS FOR LONG-WAVE FLUCTUATIONS IN A NORMAL FERMI LIQUID

While constructing the kinetic theory of macroscopic fluctuations in a normal Fermi liquid, it is most convenient to use, for better visualization, not the microscopic approach[2,11,12] which often involves considerable mathematical difficulties (which in principle can be overcome) when applied to complex systems, but an equivalent universal and simple phenomenological approach developed in Refs. 18 and 19 and verified for concordance to the microscopic approach for gaseous media. This approach is based on the application of the procedure of averaging kinetic equations (without taking into account fluctuations) over random initial conditions[18] or over a random external force[19] generating fluctuations.

Before going over to direct derivation of equations in the kinetic theory of long-wave fluctuations in a normal Fermi liquid, we shall make a few remarks concerning the approximations that will be used here.

A ''normal Fermi liquid'' is the term applied traditionally to a degenerate Fermi liquid preserving basic properties of systems of noninteracting fermions. We shall mainly be interested in neutral Fermi liquids. It is quite possible, however, that the results obtained by us here are valid in principle for charged Fermi liquids also since the latter also exhibit weakly attenuating zero-point sound vibrations.[30] For this reason, we shall emphasize typical properties that are common for charged and neutral Fermi liquids, the main property being the dependence of the Hamiltonian of excitations ε on the quasiparticle distribution function $n(\mathbf{x},\mathbf{p},t);\varepsilon(\mathbf{x},\mathbf{p},t)=\varepsilon(\mathbf{x},\mathbf{p};n)$.[13–17,20–28] We shall also disregard the existence of particle spin, which is admissible in the solution of a wide range of problems. In other words, we assume that the state of the system can be described by the one-particle distribution function $n(x,t)(x\equiv(\mathbf{x},\mathbf{p}))$ which depends on the coordinate $\mathbf{x}$ and momentum $\mathbf{p}$ at instant t and does not depend on spin variables. It will be seen from subsequent analysis that many simplifying assumptions could be omitted in the approach proposed here, but this would lead to unjustifiable complication of calculations without changing basically the main results.

Naturally, we assume that the main condition of the applicability of the theory of a normal Fermi liquid, i.e.,

$$\varepsilon_F \gg T, \tag{1}$$

is satisfied, where T is the temperature in energy units.

Under the above assumptions, the kinetic equation describing the nonequilibrium state of a normal Fermi liquid in the absence of fluctuations can be written in the form

$$\frac{\partial}{\partial t}\, n(x,t)+\frac{\partial \varepsilon(x;n)}{\partial \mathbf{p}}\,\frac{\partial n(x,t)}{\partial \mathbf{x}} - \frac{\partial \varepsilon(x;n)}{\partial \mathbf{x}}\,\frac{\partial n(x,t)}{\partial \mathbf{p}}=L(x,n), \tag{2}$$

where $L(x,n)=L(\mathbf{x},\mathbf{p};n(\mathbf{x}',\mathbf{p}'))$ is the collision integral whose explicit form will not be required (see, for example, Refs. 13–17, 20–24). The form of quasiparticle energy $\varepsilon(\mathbf{x},\mathbf{p};n)$ as a functional of the distribution function $n(x,t)$ will be specified in Sec. 2 while considering collisionless relaxation at zero-point sound in a normal Fermi liquid (it should be recalled that the explicit form of the energy of interaction of quasiparticles in the phenomenological theory is unknown, and its parameters should be determined from experiments).

In the approximations stipulated above, Eq. (2) describes kinetic phenomena in a normal Fermi liquid generally only for definite initial values of the distribution function $n(x,t)$. Such a situation, however, is quite special (see Ref. 2). The case when the initial conditions for the kinetic equation (2) are random is more general, and hence this equation should be averaged over such a distribution of initial conditions.[2] In such an approach, the one-particle distribution function satisfying Eq. (2) is random in view of the specified initial conditions $\hat{n}(x,t)=n(x,t;n(x',0))$. The symbol ''$\hat{}$'' above n emphasizes the random nature of this quantity. An attempt to average the kinetic equation (2) over initial conditions necessitates the introduction of the quantities

$$n_s(x_1,\ldots x_s;t)\equiv\langle \hat{n}(x_1,t)\ldots\hat{n}(x_s,t)\rangle, \tag{3}$$

where

$$\langle\ldots\rangle=\int D\hat{n}(x,0)W[\hat{n}(x,0)]\ldots \tag{4}$$

indicates averaging in the space of functions $\hat{n}(x,0)$ $\times(W[\hat{n}(x,0)]$ is the corresponding probability density). The quantities $n_s(x_1,\ldots,x_s;t)$ which are analogous to many-particle distribution functions can be obtained by s-fold differentiation with respect to the functional argument $u(x)$ $\equiv u(\mathbf{x},\mathbf{p})$ of the generating functional

$$F(u;n_a(t))=\left\langle \exp\left(\sum_{\mathbf{p}}\int d\mathbf{x}u(x)\hat{n}(x,t)\right)\right\rangle, \tag{5}$$

where $n_a(t)$ stands for the entire set of the quantities n_s. Further, we introduce the generating functional $\mathcal{G}(u;g)$ of the correlation functions $g_s(x_1,\ldots,x_s;t)(s\geqslant 2)$

$$\mathcal{G}(u;g_a(t))=\sum_{s=2}^{\infty}\frac{1}{s!}\sum_{\mathbf{p}_1}\int d\mathbf{x}_1\ldots \times\sum_{\mathbf{p}_s}\int d\mathbf{x}_s u(x_1)\ldots u(x_s)g_s(x_1,\ldots x_s;t), \tag{6}$$

connected with the generating functional $F[u;n_a(t)]$ through the relation

$$F(u;n_a(t))=\exp(G_0(u;n)+\mathcal{G}(u;g_a(t))), \tag{7}$$

where

$$G_0(u;n)=\sum_{\mathbf{p}}\int d\mathbf{x}u(x)n(x,t), \tag{8}$$

$g_1(x,t)\equiv n_1(x,t)=n(x,t)$, while $g_a(t)$ denotes the entire set of correlation functions g_s. It can easily be seen that the correlation functions g_s introduced through formulas (6)–(8) are fluctuations of a one-particle distribution function determined by the distribution of initial conditions [see Eq. (4)]. Thus, macroscopic fluctuations in a normal Fermi liquid can be described either in terms of momenta defined by (3) and (4), or in terms of correlation functions $g_a(t)$ (it should be recalled that the term ''macroscopic'' or ''long-wave'' fluctuations in the given case can be used in view of the validity of the Wigner approximation in the description of the system only on temporal and spatial scales much larger than the corresponding atomic characteristic scales). The equations of motion for these parameters are just the kinetic equations for macroscopic fluctuations in a normal Fermi liquid. Before we go over to the derivation of these equations, let us prove that any quantity $A[n;g_a(t)]$ which is an arbitrary functional of a random distribution function $\hat{n}(x,t)$ averaged over random initial conditions in accordance with formula (4), i.e.,

$$A(n;g_a(t))\equiv\langle A(\hat{n})\rangle,\quad n=\langle\hat{n}\rangle, \tag{9}$$

satisfies the formula

$$A(n;g_a(t))=\exp\left\{\mathcal{G}\left(\frac{\delta}{\delta \underline{n}};\, g_a(t)\right)\right\}A(n), \tag{10}$$

where the functional operator $\mathcal{G}(\delta/\delta n;g_a(t))$ is the generating functional $\mathcal{G}(u;g_a(t))$ in which the functional argument $u(x)$ is replaced by the operation of functional differentiation with respect to $n(x,t)$. In order to prove relation (10), we note that, according to (5), the quantity $\langle A(\hat{n})\rangle$ can be written in the form

$$\langle A(\hat{n})\rangle=\left\langle \exp\left\{\sum_{\mathbf{p}'}\int d\mathbf{x}'\hat{n}(x')\,\frac{\delta}{\delta \underline{n}(x')}\right\}A(\underline{n})\right\rangle\Bigg|_{\underline{n}=0} =F\left(\frac{\delta}{\delta \underline{n}};\, n_a(t)\right)A(\underline{n})\Bigg|_{n=0}. \tag{11}$$

Considering that

$$\exp\left\{G_0\left(\frac{g d}{\delta \underline{n}};\, n\right)\right\}A(\underline{n})=A(\underline{n}+n), \tag{12}$$

in accordance with (8) and taking into account formula (7), we arrive at the expressions (10).

The evolution equations for the quantities $n_s(x_1,\ldots,x_s;t)$ or, which is the same, for the generating functional $F[u;n_a(t))]$ are derived from Eq. (2) by writing it in the form convenient for the subsequent analysis:

$$\frac{\partial}{\partial t}\,\hat{n}(x,t)=\mathcal{L}(x;\hat{n}), \tag{13}$$

where we have introduced the notation

$$\mathscr{L}(x;\hat{n}) \equiv L(x;\hat{n}) + \frac{\partial \varepsilon(x,\hat{n})}{\partial \mathbf{x}} \frac{\partial \hat{n}(x,t)}{\partial \mathbf{p}} - \frac{\partial \varepsilon(x,\hat{n})}{\partial \mathbf{p}} \frac{\partial \hat{n}(x,t)}{\partial \mathbf{x}}. \tag{14}$$

Differentiating definition (5) with respect to time and using relations (12) and (13), we obtain

$$\frac{\partial}{\partial t} F(u;n_a(l)) = \exp\{G_0(u,n)\} \exp\left\{ \mathscr{G}\left(u + \frac{\delta}{\delta n};\ g_a(l) \right) \right\} \times \sum_{\mathbf{p}} \int d\mathbf{x} u(x) \mathscr{L}(x;n). \tag{15}$$

Taking into account (7) and (8), we can write Eq. (14) in the form of the equation of motion for a one-particle distribution function averaged over random initial conditions $n(x,t) = \langle \hat{n}(x,t) \rangle$, i.e.,

$$\frac{\partial n(x,t)}{\partial t} = \exp\left[\mathscr{G}\left(\frac{\delta}{\delta n};\ g_a(t) \right) \right] \mathscr{L}(x;n), \tag{16}$$

and the equation of motion for the generating functional $\mathscr{G}(u;g_a(t))$ of the correlation functions $g_s(x_1,\ldots,x_s;t)(s \geqslant 2)$:

$$\frac{\partial \mathscr{G}(u;g_a(t))}{\partial t} = \left\{ \exp\left[\mathscr{G}\left(u + \frac{\delta}{\delta n};\ g_a(t) \right) - \mathscr{G}(u;g_a(t)) \right] - \exp\left[\mathscr{G}\left(\frac{\delta}{\delta n};\ g_a(t) \right) \right] \right\} \times \sum_{\mathbf{p}} \int d\mathbf{x}\ u(x) \mathscr{L}(x;n). \tag{17}$$

Equations (16) and (17) completely describe the dynamics of macroscopic fluctuations in the system under investigation. It should be noted that the functional $\mathscr{L}(x;\hat{n})$ in these equations (see (14)) is the only quantity determining the evolution of macroscopic fluctuations at its kinetic stage as in the case of ordinary (fluctuationless) kinetics. This corresponds to the Onsager principle,[31] according to which macroscopic fluctuations evolve according to the laws of macroscopic physics (in the case under investigation, the kinetic equation (13) is such a law). It should also be noted that the explicit form of the functional $\mathscr{L}(x;\hat{n})$ was not required for deriving Eqs. (16) and (17).

It is also worthwhile to note that Eq. (17) has the solution $\mathscr{G}=0$. In this case, Eq. (16) is transformed into (13). However, the solution $\mathscr{G}=0$ corresponds to very special initial conditions $g_s(t=0)=0$, $s \geqslant 2$, which necessitates the clarification of the role of large-scale fluctuations in the kinetics of a normal Fermi liquid. The possibility of a considerable influence of macroscopic fluctuations on the system evolution can be demonstrated by constructing the theory of quasi-linear relaxation at zero-point sound in a normal Fermi liquid, bearing in mind the certain above-mentioned similar properties of a normal Fermi liquid and a plasma for which such a quasi-linear relaxation at weakly attenuating oscillations with characteristic plasma frequencies is known long ago (see, for example, Refs. 31 and 32)

2. QUASI-LINEAR RELAXATION AT ZERO-POINT SOUND IN A NORMAL FERMI LIQUID

One of the conditions for the existence of quasi-linear relaxation is associated with the possibility of propagation of long-lived oscillations in the system with a collisionless mechanism of damping. Such oscillations with characteristic plasma frequencies (e.g., Langmuir frequencies) must exist in a charged Fermi liquid. As a result, quasi-linear relaxation based on the exchange of fermions by plasmons, cannot differ basically from a similar phenomenon in a nondegenerate plasma. For this reason, we shall not consider the possibility of typical plasma oscillations existing in a charged Fermi liquid and try to construct a quasi-linear theory based on the existence of zero-point sound, viz., a specific phenomenon inherent only in normal Fermi liquids irrespective of whether the fermions are charged or neutral.

We shall consider a simple model of a normal Fermi liquid assuming that the dependence of the excitation energy functional on the distribution function is given by (see, for example, Refs. 23 and 24)

$$\varepsilon(x;n) = \varepsilon(p) + \sum_{\mathbf{p}'} \int d\mathbf{x}' f(\mathbf{x}-\mathbf{x}') n(x',t), \tag{18}$$

In other words, we shall actually confine our analysis to spatially homogeneous and isotropic energy–momentum relation $\varepsilon(p)$ for quasiparticles and the dependence $\varepsilon(x;n)$ on the distribution function $n(x,t)=n(\mathbf{x},\mathbf{p},t)$ only through the density $\rho(\mathbf{x},t)=\Sigma_{\mathbf{p}} n(x,t)$. The function $f(\mathbf{x}-\mathbf{x}')$ in formula (18) describes the interaction of quasiparticles.

We shall also be interested in kinetic effects in the system under investigation in the collisionless approximation, which immediately imposes certain limitations on the time interval of the approximation under investigation:

$$\tau_0 \ll t \ll \tau_r, \tag{19}$$

where τ_r is the relaxation time determined by the collision integral. The time τ_0 bounding this interval from below can be determined from the requirement of applicability of Eqs. (16) and (17) to the description of the fluctuation–kinetic stage of evolution in a collisionless normal Fermi liquid. Indeed, the slow rate of time variation of ''many-particle distribution functions'' $n_s(x_1,\ldots,x_s;t)$ [see (3)] satisfying Eqs. (16) and (17) as applied to fluctuating Fermi liquids must indicate the smallness of characteristic periods of vibrations as compared to the characteristic time t of variation of the functions $n_s(x_1,\ldots,x_s;t)$; $\omega_{\mathrm{ch}} t \gg 1$, where ω_{ch} is the characteristic frequency of vibrations. Since we are going to single out only the vibrational frequency $\omega_0(k)$ of zero-point sound from the entire possible spectrum of characteristic frequencies (see below), the time interval in which this approximation is valid is determined in accordance with (19) by the relation

$$1 \ll \omega_0(k) t \ll \omega_0(k) \tau_r. \tag{20}$$

It should be noted that the conditions under which the quasi-linear approximation in a nondegenerate plasma can be valid are described most comprehensively in Ref. 34.

Let us now derive the equations of quasi-linear approximation. We shall confine our analysis only to the effect of paired fluctuations on the system dynamics, which is in accord with the approximations of the quasi-linear theory in conventional plasmas.

In the approximations stipulated above, the equations of kinetics of long-wave fluctuations taking into account only paired correlation functions $g(x_1,x_2,t)$ based on (16)–(18) can be reduced to the form

$$\frac{\partial n(x)}{\partial t}=\left\{-\frac{\partial\varepsilon(p)}{\partial\mathbf{p}}\frac{\partial}{\partial\mathbf{x}}+\frac{\partial U(\mathbf{x})}{\partial\mathbf{x}}\frac{\partial}{\partial\mathbf{p}}\right\}n(x)$$
$$+\frac{\partial}{\partial\mathbf{p}}\sum_{\mathbf{p}'}\int d\mathbf{x}'\,\frac{\partial f(\mathbf{x}-\mathbf{x}')}{\partial\mathbf{x}}\,g(x,x'),\qquad(21)$$

$$\frac{\partial}{\partial t}\,g(x_1,x_2)=\left\{-\frac{\partial\varepsilon(p_1)}{\partial\mathbf{p}_1}\frac{\partial}{\partial\mathbf{x}_1}+\frac{\partial U(\mathbf{x}_1)}{\partial\mathbf{x}_1}\frac{\partial}{\partial\mathbf{p}_1}\right\}g(x_1,x_2)$$
$$+\left\{-\frac{\partial\varepsilon(p_2)}{\partial\mathbf{p}_2}\frac{\partial}{\partial\mathbf{x}_2}+\frac{\partial U(\mathbf{x}_2)}{\partial\mathbf{x}_2}\frac{\partial}{\partial\mathbf{p}_2}\right\}g(x_1,x_2)$$
$$+\frac{\partial n(x_1)}{\partial\mathbf{p}_1}\frac{\partial}{\partial\mathbf{x}_1}\sum_{\mathbf{p}'}\int d\mathbf{x}'f(\mathbf{x}_1-\mathbf{x}')g(x',x_2)$$
$$+\frac{\partial n(x_2)}{\partial\mathbf{p}_2}\frac{\partial}{\partial\mathbf{x}_2}\sum_{\mathbf{p}'}\int d\mathbf{x}'f(\mathbf{x}_2-\mathbf{x}')g(x_1,x'),$$

where the quantity $U(\mathbf{x})$ is defined by

$$U(\mathbf{x})\equiv\sum_{\mathbf{p}'}\int d\mathbf{x}'f(\mathbf{x}-\mathbf{x}')n(x').\qquad(22)$$

Equations (21) together with (22) form a closed system of equations describing the evolution of a normal Fermi liquid for time periods specified by relation (20). These equations are simplified considerably in the spatially homogeneous case. The first equation in (21) can be written in the form

$$\frac{\partial n(\mathbf{p})}{\partial t}=-\frac{\partial}{\partial p_i}J_i(\mathbf{p}),\qquad(23)$$

where the quasiparticle flux density $J_i(\mathbf{p})$ in the momentum space is given by

$$J_i(\mathbf{p})=\frac{1}{(2\pi)^3}\int d\mathbf{k}k_i f_{-\mathbf{k}}\sum_{\mathbf{p}'}g_{\mathbf{k}}(\mathbf{p},\mathbf{p}';t),\qquad(24)$$

in which the quantities $f_{\mathbf{k}},g_{\mathbf{k}}(\mathbf{p},\mathbf{p}';t)$ are the Fourier transforms of the interaction function $f(\mathbf{x}-\mathbf{x}')$ and the paired correlation function $g(\mathbf{x}-\mathbf{x}',\mathbf{p},\mathbf{p}',t)$ respectively:

$$f_{\mathbf{k}}=\int d\mathbf{x}\,\exp(-i\mathbf{k}\cdot\mathbf{x})f(\mathbf{x}),$$
$$g_{\mathbf{k}}(\mathbf{p},\mathbf{p}';t)=\int d\mathbf{x}\,\exp(-i\mathbf{k}\cdot\mathbf{x})g(\mathbf{x},\mathbf{p},\mathbf{p}',t).\qquad(25)$$

Since $g(x,x')=g(x',x)$, the quantity $g_{\mathbf{k}}$ satisfies the relation

$$g^*_{\mathbf{k}}(\mathbf{p},\mathbf{p}';t)=g_{-\mathbf{k}}(\mathbf{p},\mathbf{p}';t)\qquad(26)$$

(in formulas (24) and (25), we take into account the fact that the paired correlation function $g(x,x';t)$ in the spatially homogeneous case depends only on the difference between the coordinates $\mathbf{x}$ and $\mathbf{x}'$: $g(x,x';t)\equiv g(\mathbf{x}-\mathbf{x}';\mathbf{p},\mathbf{p}';t)$.

According to (21), the Fourier component $g_{\mathbf{k}}(\mathbf{p},\mathbf{p}';t)$ satisfies the equation

$$\dot g_{\mathbf{k}}(\mathbf{p}_1,\mathbf{p}_2)=i\mathbf{k}(\mathbf{v}_1-\mathbf{v}_2)g_{\mathbf{k}}(\mathbf{p}_1,\mathbf{p}_2)$$
$$+i\mathbf{k}\,\frac{\partial n(\mathbf{p}_1)}{\partial\mathbf{p}_1}\,f_{\mathbf{k}}\sum_{\mathbf{p}'}\,g_{\mathbf{k}}(\mathbf{p}',\mathbf{p}_2)$$
$$-i\mathbf{k}\,\frac{\partial n(\mathbf{p}_2)}{\partial\mathbf{p}_2}\,f_{-\mathbf{k}}\sum_{\mathbf{p}'}\,g_{-\mathbf{k}}(\mathbf{p}',\mathbf{p}_1),\qquad(27)$$

where

$$\mathbf{v}\equiv\frac{\partial\varepsilon(\mathbf{p})}{\partial\mathbf{p}}.\qquad(28)$$

Equations (23) and (27) combined with (24) and (27) are initial equations in the derivation of the basic equations of the quasi-linear theory of a normal Fermi liquid. The next step is the solution of Eq. (27). According to the method of separation of variables, we shall seek the solution of this equation in the form

$$g_{\mathbf{k}}(\mathbf{p}_1,\mathbf{p}_2;t)=g_{\mathbf{k}}(\mathbf{p}_1,t)g_{-\mathbf{k}}(\mathbf{p}_2,t).\qquad(29)$$

In accordance with (26), the functions $g_{\mathbf{k}}(\mathbf{p},t)$ and $g_{-\mathbf{k}}(\mathbf{p},t)$ are connected through the relation

$$g^*_{\mathbf{k}}(\mathbf{p},t)=g_{-\mathbf{k}}(\mathbf{p},t).\qquad(30)$$

Equation (27) leads to the equation of motion for the quantity $g_{\mathbf{k}}(\mathbf{p},t)$:

$$g_{\mathbf{k}}(\mathbf{p},t)=-i\mathbf{k}\cdot\mathbf{v}g_{\mathbf{k}}(\mathbf{p},t)+i\mathbf{k}\,\frac{\partial n(\mathbf{p})}{\partial\mathbf{p}}\,\varphi_{\mathbf{k}}(t),\qquad(31)$$

where the following notation has been introduced:

$$\varphi_{\mathbf{k}}(t)\equiv f_{\mathbf{k}}\sum_{\mathbf{p}}\,g_{\mathbf{k}}(\mathbf{p},t).\qquad(32)$$

Since we assume that the distribution function $n(\mathbf{p},t)$ in the state of the system under investigation varies slowly with time in the interval (20), we shall seek the solution of Eq. (31) in the form of the expansion of the function $g_{\mathbf{k}}(\mathbf{p},t)$ into a Fourier integral with respect to time:

$$g_{\mathbf{k}}(\mathbf{p},t)=\int_{-\infty}^{\infty}d\omega\,\exp(-i\omega t)g_{\mathbf{k}}(\mathbf{p},\omega),$$
$$\varphi_{\mathbf{k}}(t)=\int_{-\infty}^{\infty}d\omega\,\exp(-i\omega t)\varphi_{\mathbf{k}}(\omega),\qquad(33)$$

assuming that $n(\mathbf{p}$ in (31) does not depend on time at all in the main approximation. According to (31), in this approximation we obtain the following equation for the Fourier transform $g_{\mathbf{k}}(\mathbf{p},\omega)$:

$$-i(\omega-\mathbf{k}\cdot\mathbf{v})g_{\mathbf{k}}(\mathbf{p},\omega)=i\mathbf{k}\,\frac{\partial f(\mathbf{p})}{\partial\mathbf{p}}\,\varphi_{\mathbf{k}}(\omega).\qquad(34)$$

Taking into account (32) and (33), we can write the solution of this equation in the form

$$g_{\nu,\mathbf{k}}(\mathbf{p},\omega)=A_\nu(\mathbf{k},\mathbf{p})\,\delta(\omega-\mathbf{v}\cdot\mathbf{k}) - \frac{\tilde{A}_\nu(\mathbf{k},\omega)}{\varepsilon(\mathbf{k},\omega)(\omega-\mathbf{k}\cdot\mathbf{v}+i0)}\,\mathbf{k}\,\frac{\partial n(\mathbf{p})}{\partial\mathbf{p}}, \tag{35}$$

$$\tilde{A}_\nu(\mathbf{k},\omega)=\tilde{A}^*_\nu(\mathbf{k},\omega)\equiv f_{\mathbf{k}}\sum_{\mathbf{p}} A_\nu(\mathbf{k},\mathbf{p})\,\delta(\omega-\mathbf{v}\cdot\mathbf{k}),$$

where the quantities $A_\nu(\mathbf{k},\mathbf{p})$ are arbitrary functions subjected to the natural limitation associated with the fact that the functions $g(\mathbf{x}_1-\mathbf{x}_2,\mathbf{p}_1,\mathbf{p}_2;t)$ determined from (25), (29), (33), and (35) must satisfy all the properties of correlation functions. The symbolic discrete or continuous parameter ν ''labels'' or orders the entire admissible set of such functions. The quantity $\varepsilon(\mathbf{k},\omega)=\varepsilon^*(-\mathbf{k},-\omega)$ in (35), defined as

$$\varepsilon(\mathbf{k},\omega)\equiv 1+f_{\mathbf{k}}\mathbf{k}\sum_{\mathbf{p}}\ \frac{\partial n(\mathbf{p})}{\partial\mathbf{p}}\,(\omega-\mathbf{k}\cdot\mathbf{v}+i0)^{-1} \tag{36}$$

and being an analog of the complex permittivity of the plasma (it should be recalled that here we are not necessarily speaking of a charged Fermi liquid), after the replacement of summation over $\mathbf{p}$ by integration in accordance with (33), can be written in the form

$$\varepsilon(\mathbf{k},\omega)=\varepsilon_1(\mathbf{k},\omega)+i\varepsilon_2(\mathbf{k},\omega), \tag{37}$$

$$\varepsilon_1(\mathbf{k},\omega)=1+(2\pi)^{-3}f_{\mathbf{k}}\mathbf{k}P\int d\mathbf{p}\cdot\mathbf{k}\,\frac{\partial n(\mathbf{p})}{\partial\mathbf{p}}\,(\omega-\mathbf{k}\cdot\mathbf{v})^{-1},$$

$$\varepsilon_2(\mathbf{k},\omega)=-f_{\mathbf{k}}(8\pi^2\hbar^3)^{-1}\int d\mathbf{p}\cdot\mathbf{k}\,\frac{\partial n(\mathbf{p})}{\partial\mathbf{p}}\,\delta(\omega-\mathbf{v}\cdot\mathbf{k}),$$

while deriving expressions (37), we have used the formula

$$(z+i0)^{-1}=P\,\frac{1}{z}-i\pi\delta(z),$$

where the symbol P indicates that we take the principal value in subsequent integration.

The functions $g_{\nu,\mathbf{k}}(\mathbf{p},t)$ can be found from (35) taking into account (33) with the help of the residue theory, which necessitates the determining of zeros of the function $\varepsilon(\mathbf{k},\omega)$. As usual, we shall determine the zeros of the function $\varepsilon(\mathbf{k},\omega)$ from the equation

$$\varepsilon(\mathbf{k},\omega_0-i\gamma_{\mathbf{k}})=0,\ \ \omega_0|\gg|\gamma_{\mathbf{k}}|. \tag{38}$$

Under the assumption of the smallness of the imaginary component $\varepsilon_2(\mathbf{k},\omega)$ as compared to the real component $\varepsilon_1(\mathbf{k},\omega)$ of the permittivity $\varepsilon(\mathbf{k},\omega)$, the frequency ω_0 and the decrement (increment) $\gamma_{\mathbf{k}}$ must be defined as

$$\varepsilon_1(\mathbf{k},\omega_0)=0\quad\text{and}\quad\gamma_{\mathbf{k}}=\varepsilon_2(\mathbf{k},\omega_0)\left(\frac{\partial\varepsilon_1(\mathbf{k},\omega)}{\partial\omega}\right)^{-1}_{\omega=\omega_0}. \tag{39}$$

In concordance with the requirements imposed by the conditions of applicability of the theory of a normal Fermi liquid, the derivative $\partial n(\mathbf{p})/\partial\mathbf{p}$ must have a sharp peak for $p=p_F$. Consequently, the integral with respect to momentum in formula (37) for $\varepsilon_1(\mathbf{k},\omega)$ in the main approximation can be calculated under the assumption that $\partial n(\mathbf{p})/\partial\mathbf{p}\approx-(\mathbf{p}/p)\,\delta(p-p_F)$. This leads to the following energy–momentum relation:

$$\omega_0^{\pm}=\pm s_k k v_F,\ \ s_k>1, \tag{40}$$

where the quantity s_k must be determined from the equation

$$1+F_k\left\{1-\frac{s_k}{2}\ln\frac{s_k+1}{s_k-1}\right\}=0 \tag{41}$$

and the following notation has been introduced [see (22), (25), and (28)]:

$$v_F=v(p)|_{p=p_F},\ \ F_K\equiv\frac{f_k p_F^2}{2\pi^2\hbar^3 v_F}. \tag{42}$$

Formulas (40) and (41) define the energy–momentum relation for zero-point sound in a normal Fermi liquid with a quasiparticle Hamiltonian defined by (18). It should be noted that the problem concerning the necessity of taking into account the effect of deviations of the distribution function $n(\mathbf{p})$ from the ''step'' distribution $n(p)=\theta(p_F-p)$ on the frequency of zero-point sound can be solved in principle; at any rate, this can be verified by solving the equations in the quasi-linear theory which will be derived below (we shall not do it here).

Considering further that the derivative $\{\partial\varepsilon_1(k,\omega)/\partial\omega\}|_{\omega=\omega_0(k)}$ satisfies the formula

$$\left.\frac{\partial\varepsilon_1(\mathbf{k},\omega)}{\partial\omega}\right|_{\omega=\omega_0(k)}=\frac{F+1-s_k^2}{s_k^2-1}\,\frac{1}{\omega_0(k)}, \tag{43}$$

and using (39), we obtain the following expression for $\gamma_{\mathbf{k}}$:

$$\gamma_{\mathbf{k}}=\omega_0(k)\,\frac{s_k^2-1}{(s_k^2-1)-F_k}\,\frac{f_k}{8\pi^2\hbar^3} \times\int d\mathbf{p}\cdot\mathbf{k}\,\frac{\partial n(\mathbf{p})}{\partial\mathbf{p}}\,\delta(\omega_0(k)-\mathbf{k}\cdot\mathbf{v}). \tag{44}$$

This expression shows that in contrast to the energy–momentum relation for oscillations determined by the behavior of the one-particle distribution function for $p\approx p_F$, the quantity $\gamma_{\mathbf{k}}$ is determined by the behavior of the distribution function at the ''tail'' for $\varepsilon>\varepsilon_F$, and hence fluctuations of the one-particle distribution function may play a significant role. The validity of this assumption can easily be verified if we assume that the distribution function is isotropic in the momentum space, i.e., $n(\mathbf{p})=n(p)$. Integrating in (44) over angles and going over from the integration with respect to momentum to integration with respect to $\varepsilon=\varepsilon(p)$ in the remaining integral, we can write the expression for $\gamma_{\mathbf{k}}$ in the form

$$\gamma_k=\omega_0(k)\,\frac{\pi}{2}\,\frac{F_k s_k(s_k^2-1)}{(s_k^2-1)-F_k} \times\int_{\varepsilon_k}^{\infty}d\varepsilon\left(\frac{p(\varepsilon)}{p_F}\right)^2\left(\frac{v_F}{v(\varepsilon)}\right)^2\frac{\partial n(\varepsilon)}{\partial\varepsilon}, \tag{45}$$

where the boundary energy $\overline{\varepsilon}_k \gtrsim \varepsilon_F$ can be determined from the relation

$$\overline{\varepsilon}_k = \varepsilon(\overline{p}_k), \quad \left.\frac{\partial\varepsilon(p)}{\partial p}\right|_{p=\overline{p}_k} = s_k \left.\frac{\partial\varepsilon(p)}{\partial p}\right|_{p=p_F}. \tag{46}$$

For this reason, we can refer to the quantity $\gamma_{\mathbf{k}}$ as an increment or as a decrement on equivalent basis depending on the sign of the derivative $\partial n(\varepsilon)/\partial\varepsilon$ (note that in the case of equilibrium distribution, the derivative $\partial n(\varepsilon)/\partial\varepsilon$ is always negative).

Taking into account formulas (32), (35), (40), and (45), we can present the results of evaluation of integrals in (33) in the form

$$\varphi_{\nu,\mathbf{k}}(t) \approx \frac{1}{2}\{\varphi^{+}_{\nu,\mathbf{k}}(t) + \varphi^{-}_{\nu,\mathbf{k}}(t)\}, \tag{47}$$

$$\begin{aligned} g_{\nu,\mathbf{k}}(\mathbf{p},l) \approx{}& \exp(-i\mathbf{k}\boldsymbol{\nu}l) A_\nu(\mathbf{p},\mathbf{k}) \\ &+ 2\pi i \frac{A_\nu(\mathbf{k},\mathbf{k}\cdot\mathbf{v})}{\varepsilon(\mathbf{k},\mathbf{k}\cdot\mathbf{v})} \mathbf{k}\frac{\partial n(p)}{\partial\mathbf{p}} + \frac{1}{2}\varphi^{-}_{\nu,\mathbf{k}}(t) \\ &\times(\omega_0(k) + \mathbf{k}\mathbf{v} - i0)^{-1} - \varphi^{+}_{\nu,\mathbf{k}}(t)(\omega_0(k) - \mathbf{k}\mathbf{v} \\ &+ i0)^{-1}\mathbf{k}\frac{\partial n(p)}{\partial\mathbf{p}}, \end{aligned}$$

where the functions $\varphi^{\pm}_{\nu,\mathbf{k}}(t)$ are defined as

$$\begin{aligned} \varphi^{\pm}_{\nu,\mathbf{k}}(t) = {}& \mp 2\pi i\omega_0(k)\tilde{A}_\nu[\mathbf{k}, \pm\omega_0(k)]\exp(-\gamma_{\mathbf{k}}t \\ &\mp i\omega_0(k)t). \end{aligned} \tag{48}$$

In view of (30) and (35), these functions are connected through the relation

$$(\varphi^{+}_{\nu,\mathbf{k}}(t))^* = \varphi^{-}_{\nu,-\mathbf{k}}(t). \tag{49}$$

While deriving formulas (47), we have taken into account the fact that the value of $\gamma_{\mathbf{k}}$ is smaller than the frequency $\omega_0(k)$; for this reason, we used the approximate equality in (47).

It should be noted that, apart from convenience, the introduction of quantities $\varphi^{\pm}_{\nu\mathbf{k}}(t)$ is dictated by the fact that the operators of creation and annihilation of zero-point sound quanta in the quasiparticle approach to an analysis of oscillations in a normal Fermi liquid can be introduced by formulas similar to (47). For this reason, the quantity

$$I_{\mathbf{k}(t)} = \sum_\nu \varphi^{+}_{\nu,\mathbf{k}}(t)\varphi^{-}_{\nu,-\mathbf{k}}(t) = \sum_\nu |\varphi^{+}_{\nu,\mathbf{k}}(t)|^2 \tag{50}$$

coincides with the distribution of intensity of zero-point vibrations in a normal Fermi liquid over wave numbers $\mathbf{k}$. By virtue of (29), the most general form of the solution of Eqs. (27) is given by

$$g_{\mathbf{k}}(\mathbf{p}_1,\mathbf{p}_2;t) = \sum_\nu g_{\nu,\mathbf{k}}(\mathbf{p}_1,t) g_{\nu,-\mathbf{k}}(\mathbf{p}_2,t). \tag{51}$$

This formula explains the index ν introduced in the functions $A_\nu(\mathbf{p},\mathbf{k})$: at $t=0$, the number of functions $A_\nu(\mathbf{p},\mathbf{k})$ must be large enough to construct with their help an arbitrary initial correlation function $g_{\mathbf{k}}(\mathbf{p}_1,\mathbf{p}_2;0) = \Sigma_\nu g_{\nu,\mathbf{k}}(\mathbf{p}_1,0) g_{\nu,-\mathbf{k}}(\mathbf{p}_2,0)$

Using (51) as well as formulas (24) and (32), we can present the flux density $J_i(\mathbf{p})$ in Eq. (23) in the momentum space in the form

$$J_i(\mathbf{p}) = (2\pi)^{-3}\int d\mathbf{k}\ k_i \sum_\nu g_{\nu,\mathbf{k}}(\mathbf{p},t)\varphi_{\nu,-\mathbf{k}}(t), \tag{52}$$

where the quantities $g_{\nu\mathbf{k}}(\mathbf{p},t)$ and $\varphi_{\nu,-\mathbf{k}}(t)$ are defined by formulas (47).

It is appropriate to make the following important remark. According to (20), expression (47) contains rapidly oscillating terms leading to the emergence of the same terms in formulas (51) and (52). On the other hand, it was noted above that Eqs. (16), (17), and (21) can be used only when the parameters of abbreviated description vary slowly with time [see (20)] (by the way, this allows us to seek the solution of Eq. (27) in the form (33) and (47)). Obviously, the emergence of rapidly oscillating terms is associated with the choice of the method of solution of Eq. (27). For this reason, while determining the explicit form of the quantities $g_{\mathbf{k}}(\mathbf{p}_1,\mathbf{p}_2;t)$ and $J_i(\mathbf{p})$ in subsequent analysis taking into account (47) and (48), we must retain only the terms that do not contain rapidly oscillating factors of the type $\exp(\pm i\omega_0 t)$ or $\exp(\pm i\mathbf{k}\cdot\mathbf{v}t)$.

Such an slightly artificial approach is equivalent to averaging of expressions (51) and (52) over characteristic periods of zero-point vibrations, which are smaller than the characteristic times of variation of a one-particle distribution function. The disregard of rapid oscillations allows us to reject the assumption concerning the independence of the one-particle distribution function $n(\mathbf{p})$ of time (it should be recalled that such an approximation was used in our analysis starting from Eq. (34). This means that all the physical quantities describing the state of the system under investigation vary slowly with time, the characteristic scales of this dependence being of the order of characteristic times of temporal variation of the one-particle distribution function $n(\mathbf{p},t)$.

Taking into account the above remarks, we can write the basic evolution equations of the state of the system under investigation in a simple form. The structure of the equation for the one-particle distribution function remains the same as (23) (for convenience, we write this equation once again):

$$\frac{\partial n(\mathbf{p})}{\partial t} = -\frac{\partial}{\partial p_i} J_i(\mathbf{p}), \tag{53}$$

where the fermion flux density $J_i(\mathbf{p})$ in the momentum space can be written, in accordance with (47), (48), (52), in the form

$$J_i(\mathbf{p}) = -D_{ij}(\mathbf{p})\frac{\partial n(\mathbf{p})}{\partial p_j}. \tag{54}$$

The diffusion coefficient $D_{ij}(\mathbf{p})$ in the momentum space is defined as

$$D_{ij}(\mathbf{p}) = \frac{1}{16\pi^2}\int d\mathbf{k} k_i k_j \delta(\omega_0(k) - \mathbf{k}\mathbf{v}) I_{\mathbf{k}}(t), \tag{55}$$

where the quantity $I_{\mathbf{k}}(t)$ proportional to the distribution of the intensity of oscillations over the wave number $\mathbf{k}$ is given, in accordance with (48) and (50), by the formula

$$I_{\mathbf{k}}(t)=4\pi^2\omega_0^2(k)\exp(-2\gamma_{\mathbf{k}}t)\sum_{\nu}|A_{\nu}(\mathbf{k},\omega_0(k))|^2. \quad (56)$$

It can easily be seen that in view of the smallness of the increment (decrement) $\gamma_{\mathbf{k}}$ in (45) and the slow rate of its variation with time, the quantity $I_{\mathbf{k}}(t)$ satisfies the equation

$$\frac{\partial}{\partial t}I_{\mathbf{k}}(t)=-2\gamma_{\mathbf{k}}(t)I_{\mathbf{k}}(t). \quad (57)$$

The system of equations (53) and (57), which is closed by formulas (45), (54), and (55) and describes the relaxation of zero-point sound vibrations and fermion relaxation, can be regarded as equations of the quasi-linear theory of the normal Fermi liquid, or equations of quasi-linear approximation. The analytical structure of these equations is identical to the structure of equations of the quasi-linear theory of Langmuir plasma, in which the possibility of quasi-linear relaxation of plasma at the frequencies of characteristic plasma oscillations was noted for the first time (see Refs. 32–34 in this connection).

CONCLUSION

Let us consider the condition for the existence of quasi-linear approximation at zero-point sound in a normal Fermi liquid. According to (53) and (54), the characteristic time τ_q of stabilization of a quasi-linear mode can be estimated as follows:

$$\tau_q\sim p_F^2/D(p_F). \quad (58)$$

We assume that at the initial instant, the paired correlation function has the form

$$g(\mathbf{x}_1-\mathbf{x}_2;\mathbf{p}_1,\mathbf{p}_2;0)=g_0\xi(|\mathbf{p}_1|,|\mathbf{p}_2|)\exp\left(-\frac{(\mathbf{x}_1-\mathbf{x}_2)^2}{R^2}\right), \quad (59)$$

where g_0 is the amplitude of initial pulsations, $\xi(p_1,p_2)$ a certain function defining the momentum dependence of the paired correlation function, and R the characteristic size of spatial localization of initial pulsations. Using simple but cumbersome calculations, we can estimate the value of the quantity $I_{\mathbf{k}}(0)$ appearing in the expression for $D(p)$ [see (55) and (56)]:

$$I_k(0)\sim g_0\xi(sv_F)^2F^2p_F^2R^3\exp\left(\frac{-R^2k^2}{4}\right), \quad (60)$$

where s and F, as before, are defined by formulas (41) and (42), and the quantity ξ is given by the formula

$$\xi=\int_{\overline{p}/p_F}^{\infty}dz_1z_1^2\int_{\overline{p}/p_F}^{\infty}dz_2z_2^2\xi(z_1,z_2),$$

in which the boundary momentum $\overline{p}$ can be determined from conditions (46). Using (55) and taking into account (60), we obtain the following estimate for $D(p_F)$:

$$D(p_F)\sim g_0\xi F^2p_F^2\omega_0,\quad \omega_0\sim sv_F/R,$$

which leads, in accordance with (58), to the expression for the characteristic time τ_q of stabilization of quasi-linear conditions:

$$\tau_q\sim\frac{1}{g_0\xi F^2}\,\omega_0^{-1},\quad \omega_0\sim sv_F/R. \quad (61)$$

Since the inequality $\omega_0\tau_q\gg 1$ must be satisfied in accordance with (19) and (20), we arrive at the following relation connecting the initial conditions and the function of interaction between quasiparticles [see (18), (24), (41), (42), and (59)]:

$$(g_0\xi F^2)^{-1}\gg 1. \quad (62)$$

Obviously, this relation is satisfied the better, the smaller the amplitude of pulsations and the dimensionless Landau amplitude.

The inequality

$$\tau_q\ll\tau_d \quad (63)$$

holds due to the fact that the characteristic time τ_q of stabilization of quasi-linear conditions must be shorter than the characteristic time $\tau_d\sim 1/\gamma_k$ of Landau damping for zero-point sound [see (45)]. In order to clarify relation (63), we shall write the expression from Ref. 35 for the damping coefficient γ_k for zero-point sound in two limiting cases of large and small dimensionless Landau amplitudes F_k in statistical equilibrium which is described by a one-particle distribution function at a nonzero temperature.[35] The value of damping coefficient for zero-point sound in this case is most significant for $s\gtrsim 1$, which is observed, according to (41), for $0<F_k\lesssim 2$. We can prove that if the condition

$$\frac{\pi T}{\varepsilon_F(s-1)}\lesssim 1 \quad (64)$$

is satisfied (T is the temperature), i.e., we can disregard thermal corrections to the frequency of zero-point sound, and the relation (41) remains valid, the following expression for the quantity s holds:

$$s\approx 1+2\exp\{-2(1+1/F)\}.$$

Taking into account this relation and proceeding from (45), we can arrive at the following expression for the nondissipative damping coefficient for zero-point sound:

$$\gamma_k\approx\pi(s-1)\left\{\exp\left[2\pi\frac{(s-1)\varepsilon_F}{\pi T}\right]+1\right\}^{-1}\omega_0(k),$$

$$\omega_0(k)\sim kv_F,\quad k\sim 1/R. \quad (65)$$

According to this formula, relation (63) is equivalent to the condition

$$\pi(s-1)\left\{\exp\left[2\pi\frac{(s-1)\varepsilon_F}{\pi T}\right]+1\right\}^{-1}\gg\frac{1}{g_0\xi F^2},$$

$$0<F_k\lesssim 2. \quad (66)$$

We can also verify that in the opposite case of large dimensionless Landau amplitudes $F\gg 1$, condition (63) assumes the form

$$\exp\left(\frac{F}{3}\frac{\varepsilon_F}{T}\right) \gg \frac{1}{g_0\xi}. \tag{67}$$

The following circumstance is worth noting. Generally speaking, the coefficient γ_k of collisionless damping of zero-point sound is much smaller than the coefficient $1/\tau_r$ of damping due to collisions (τ_r is the relaxation time), and hence relations (62) and (64)–(67) do not ensure the stabilization of quasi-linear conditions during the time interval (20) in all cases. However, for $0<F_k\lesssim 2$, when γ_k satisfies expression (65), the coefficient of collisionless damping of zero-point sound can be of the order of the coefficient of absorption due to collisions.[35] Indeed, the time τ_r of relaxation due to collisions of quasiparticles in ^{3}He is in good agreement with experimental results[26–29] and can be estimated by the formula

$$\tau_r \sim 10^2 \frac{\hbar}{\varepsilon_F}\left(\frac{\varepsilon_F}{T}\right)^2.$$

According to (64) and (65), the maximum value of the damping coefficient $\gamma_k^{\max}$ for zero-point sound is defined as

$$\gamma_k^{\max} \approx \pi(s-1)\exp(-2\pi)\omega_0,$$

$$\omega_0 \sim v_F/R, \quad k\sim 1/R.$$

It can easily be verified that for frequencies ω_0 satisfying the relations

$$\frac{\hbar\omega_0}{\varepsilon_F} \sim 10^{-2}\frac{(s-1)}{\pi^3}\exp(2\pi),$$

$$\frac{\hbar\omega_0}{\varepsilon_F} \ll 1, \quad \omega_0 \sim v_F/R,$$

the coefficient of collisionless attenuation of zero-point sound can be of the order of the coefficient of absorption due to collisions. In this case, relations (62) and (64)–(67) characterize the conditions for the existence of quasi-linear relaxation in a normal Fermi liquid depending on temperature and parameters associated with the initial state of the system in the model representation (59) as well as with the fermion interaction function in this model representation (18).

In all the remaining cases, the inequality (63) determining the smallness of the characteristic time of stabilization of quasi-linear mode in a normal Fermi liquid as compared to the characteristic times of zero-point sound attenuation should be replaced by the relation

$$\tau_q \ll \tau_r.$$

It should be emphasized once again that the considerations and formulas given in Conclusion are approximate. Naturally, the limits of applicability of the quasi-linear approximation can be established only in the special case by solving the equations (53)–(57) of quasi-linear relaxation and specifying the initial conditions for the paired correlation function $g(\mathbf{x}_1-\mathbf{x}_2;\mathbf{p}_1,\mathbf{p}_2;0)$.

This research was carried out under the financial support from the Ukrainian State Foundation of Fundamental Studies (Grant No. 24/378).

The author is grateful to the Academician S. V. Peletminsky, National Academy of Sciences of the Ukraine, for valuable discussions of the obtained results.

*E-mail: slusarenko@kipt.kharkov.ua

[1)] By macroscopic (longwave, large-scale) fluctuations, we mean in the traditional sense the smoothing of parameters describing the system in terms of pulsations whose partial localization scales are comparable with characteristic spatial scales for forces of interaction between particles or quasiparticles.[1,2]

[1] Yu. L. Klimontovich, *Turbulent Flow and Structure of Chaos* [in Russian], Nauka, Moscow (1990).
[2] S. V. Peletminsky and Yu. V. Slyusarenko, Physica A **210**, 165 (1994).
[3] L. D. Landau and E. M. Lifshitz, *Fluid Dynamics* [in Russian], Nauka, Moscow (1986).
[4] A. S. Monin and F. M. Yaglom, *Statistical Fluid Mechanics* [in Russian], (Parts 1 and 2), Nauka, Moscow (1965, 1967).
[5] J. R. Dorfman and E. G. D. Cohen, Phys. Rev. Lett. **23**, 1257 (1970).
[6] N. G. Inozemtseva and B. I. Sadovnikov, Teor. Mat. Fiz. **31**, 260 (1977).
[7] S. V. Peletminsky, S. S. Plokhov, and V. I. Prikhot'ko, Teor. Mat. Fiz. **46**, 263 (1981).
[8] Yu. V. Slyusarenko, Ukr. Fiz. Zh. **35**, 441 (1990).
[9] A. F. Andreev, Zh. Éksp. Teor. Fiz. **78**, 2064 (1980) [Sov. Phys. JETP **51**, 1038 (1980)].
[10] S. V. Peletminsky and A. I. Sokolovskii, Ukr. Fiz. Zh. **37**, 1527 (1992).
[11] S. V. Peletminsky and Yu. V. Slyusarenko, in *Problems in Solid State Physics* [in Russian], Naukova Dumka, Kiev (1991).
[12] S. V. Peletminsky and Yu. V. Slyusarenko, Teor. Mat. Fiz. **106**, 469 (1996).
[13] L. D. Landau, Zh. Éksp. Teor. Fiz. **30**, 1058 (1957) [Sov. Phys. JETP **3**, 920 (1957)].
[14] V. P. Silin, Zh. Éksp. Teor. Fiz. **33**, 495 (1957) [Sov. Phys. JETP **6**, 387 (1957)].
[15] L. D. Landau, Zh. Éksp. Teor. Fiz. **32**, 59 (1957) [Sov. Phys. JETP **5**, 101 (1957)].
[16] V. P. Silin, Zh. Éksp. Teor. Fiz. **35**, 1243 (1958) [Sov. Phys. JETP **8**, 870 (1958)].
[17] E. M. Lifshitz and L. P. Pitaevskii, *Statistical Physics* [in Russian], Part 2, Nauka, Moscow (1978).
[18] S. V. Peletminsky and Yu. V. Slyusarenko, Ukr. Fiz. Zh. **39**, 112 (1994).
[19] Yu. V. Slyusarenko, Preprint of National Science Center ''Kharkov Inst. Phys. Technol.'' No. 96-1, Kharkov (1996).
[20] E. M. Lifshitz and L. P. Pitaevskii, *Physical Kinetics*, Pergamon Press, Oxford (1981).
[21] D. Pines and Ph. Noziere, *The Theory of Quantum Liquids*, New York (1966).
[22] P. Platzman and P. Wolff, *Waves and Interactions in Solid State Plasmas*, Academic Press, New York (1973).
[23] A. I. Akhiezer, V. V. Krasil'nikov, S. V. Peletminsky, and A. A. Yatsenko, Usp. Fiz. Nauk **163**, 1 (1993) [Phys. Usp. **36**, 35 (1993)].
[24] M. Luft and S. V. Peletminsky, Physica A **162**, 542 (1990).
[25] A. I. Akhiezer and S. V. Peletminsky, *Methods of Statistical Physics*, Pergamon, Oxford (1981).
[26] J. Gavoret, Phys. Rev. A **137**, 731 (1965).
[27] A. C. Anderson, J. I. Connoly, and J. C. Wheatley, Phys. Rev. A **135**, 910 (1964).
[28] B. E. Keen, P. W. Matthews, and J. Wilks, Phys. Lett. **5**, 5 (1963).
[29] W. P. Halperin and L. P. Pitaevskii (Eds.), *Helium Three*, North-Holland, Amsterdam, Oxford, New York, Tokyo (1990).
[30] E. V. Bezuglyi *et al.*, J. Phys. Condens. Matter **3**, 7867 (1991); E. V. Bezuglyi, N. G. Burma, A. Yu. Deineka, and V. D. Fil, Fiz. Nizk. Temp. **19**, 667 (1993) [Low Temp. Phys. **19**, 477 (1993)].
[31] L. Onsager, Phys. Rev. **37**, 405 (1931); Phys. Rev. **38**, 2265 (1931).
[32] Yu. A. Romanov and G. F. Filippov, Zh. Éksp. Teor. Fiz. **40**, 123 (1961) [Sov. Phys. JETP **13**, 87 (1961)].
[33] A. A. Vedenov, E. P. Velikhov, and R. Z. Sagdeev, Yad. Sintez **1**, 82 (1961).
[34] G. Ecker, *Theory of Fully Ionized Plasmas*, McGraw-Hill, New York (1972).
[35] Yu. V. Slyusarenko, Fiz. Nizk. Temp. **24**, 291 (1998) [Low Temp. Phys. **24**, 219 (1998).

Translated by R. S. Wadhwa

SUPERCONDUCTIVITY, HIGH-TEMPERATURE SUPERCONDUCTIVITY

Influence of pulsed electric current on the structure and superconducting properties of high-temperature superconductors

A. I. Raitchenko, A. A. Flis, L. I. Chernenko, and N. I. Kryuchkova

*Institute of Material Science Problems, National Academy of Sciences of the Ukraine, 252142 Kiev, Ukraine**

(Submitted January 4, 1998)
Fiz. Nizk. Temp. **24**, 533–537 (June 1998)

The influence of high-density current pulses on the structure and superconducting properties of HTSC ceramics $YBa_2Cu_3O_x$ is studied at room temperature. A gradual increase in the pulsed current density causes appreciable structural changes: when a certain threshold value is reached, the melting of large grains occurs and is accompanied by partial breaking of intergranular contacts resulting in degradation of superconductivity. A further increase in the current density leads to the recovery of superconducting properties, which is probably due to the formation of superconducting bridges between grains aligned along the current flow. The superconducting transition temperature remains unchanged in such samples, but subsequent thermal treatment leads to an increase in the superconducting transition temperature.
 [S1063-777X(98)00306-5]

The discovery of the La–Ba–Cu–O superconducting system by Bednorz and Müller[1] stimulated a competition in obtaining materials with superconducting parameters better than for this system. During intense studies of HTSC materials, most publications were devoted to the superconducting compound $YBa_2Cu_3O_x$ with the superconducting transition temperature $T_c = 90$ K.

The superconductor $YBa_2Cu_3O_x$ attracts attention of researchers due to the possibility of its employment in electronic instruments and strong-current devices applied in many branches of technology. High-temperature superconductors were initially synthesized in the form of granular structures. In such structures, current flows mainly through broad contacting surfaces of granules extended along *ab* planes.[2] If the length L of granules is larger than their thickness h, the effective density of transport current in the ceramics considerably exceeds the Josephson current density in the direction of the *c*-axis ($L/h \gg 1$).

Intergranular contacts are not always perfect on the microscopic level in view of the presence of amorphous interlayers, a large number of weak links at the grain boundaries, disorientation of these boundaries, and a small number of pinning centers. The currents flows in such structures along paths piercing chaotically the sample volume, which leads to suppression of the critical current.[3–5] The current-carrying characteristics of the sample can be affected by the method of directed texturization, e.g., in a gradient temperature field in which a structure of the ''masonry'' type is formed.[6] For this reason, the development of new technological conditions which produce a positive effect on the superconducting properties of HTSC systems and the creation of grain-oriented structure is an interesting and promising trend in the modern technology of manufacturing three-dimensional articles from HTSC material.

The treatment by passing the direct current is one of such methods, which was used for other technological processes, but was new in processing HTSC materials (Fig. 1).

Voltage pulses from a source (a setup with a capacitive accumulator) were applied to copper electrodes *5* pressed to the end faces of sample *4* (which was in the form of a cylinder as a rule) by press slabs *3* (which were electrically insulated from its casing by insulating layers *2*). The output of the discharger of the source was connected with the press slabs through flexible copper busbars *6*.

Our aim was to determine the possibility of formation of a grain-oriented structure in order to improve current-carrying parameters of Y-based HTSC materials by treating the samples by high-density current pulses at room temperature.

In order to understand the nature of phenomena arising upon the passage of current through HTSC materials, it is worth noting that the structure of HTSC ceramics is similar to a certain extent to the structure of metal powders in the state of free packing or a pressed sample with a porosity 20–25% without annealing. Both types of samples are characterized by porosity, the presence of imperfect contacts between structural units (crystallites, granules, grains, and powder particles) as well as a nonuniform density distribution over the volume. What are the changes induced by the current passed through an HTSC sample containing such defects in the structure and properties of the material? To answer this question, we use the approach developed for understanding processes occurring during processing of powders by electric current.[8]

Under the action of an electric pulse on a metallic pow-

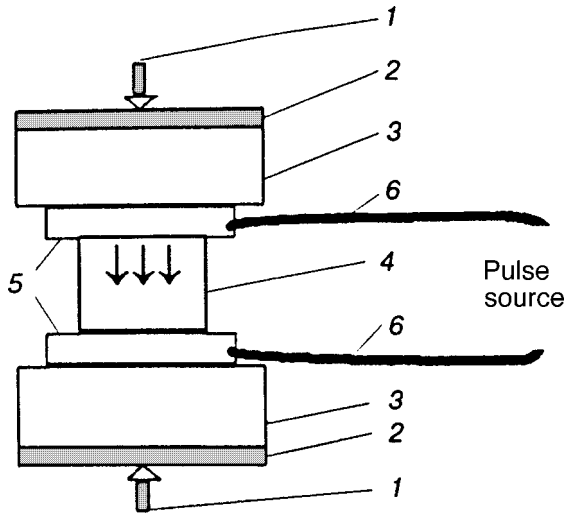

FIG. 1. Schematic diagram of treatment by electric current pulses: mechanical load (*1*), insulating layer (*2*), press slab (*3*), sample (*4*), copper electrode (*5*), and flexible busbar (*6*).

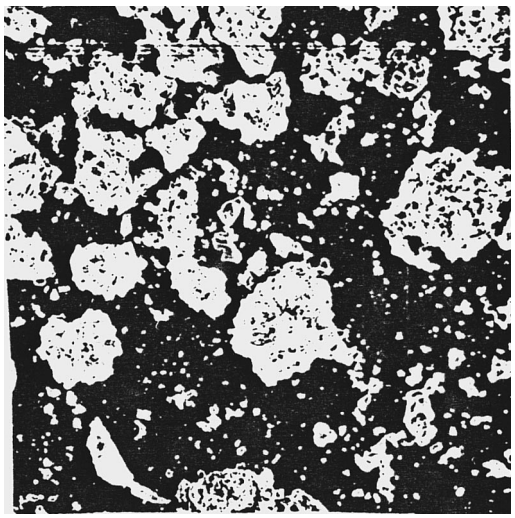

FIG. 2. Microstructure of particles in $YBa_2Cu_3O_x$ ceramics after annealing at 1173 K, ×150.

der, the sample is heated rapidly and its particles are fritted.[9–12] When the current passes through a defective HTSC ceramic in the normal (nonsuperconducting) state, we should expect (in analogy with processes occurring in the collective of metal powder particles) (1) the destruction of weakly conducting layers between adjacent crystallites (granules) in directions close to the general direction of electrical current; (2) the formation of liquid bridges (menisci) between crystallites, and (3) the strengthening of links between granules with the formation of ''filaments'' parallel to the direction of current (we assume that the direction of current is parallel to the axial direction of the imaginary cylindrical system of coordinates). As a result of the pinch effect, the ''filaments'' must be compressed according to the pressure law $P \sim (r_0^2 - r^2)$, where r_0 is the radius of the cylindrical sample and r the radial coordinate.[12] This can lead to breaking of intercrystallite barriers in the radial and azimuthal directions, and hence to a denser packing and improvement of the quality of intercrystallite contacts in both these directions. In view of the difference in local electrical resistance in different regions of the HTSC sample (especially at the boundaries between particles), the values of locally liberated electric power can exceed the values above which the thermal effect of current leads to local melting with the formation of a conducting liquid bridge converted after cooling into an interlayer with the previous or changed composition. However, a conducting liquid bridge can become unstable under certain conditions, and its breaking[8] leads to the violation of an electric contact between particles. Local electrical explosions on a microscopic level are also possible. Thus, the passage of an electric current can lead to phenomena affecting the conductivity of the HTSC sample in opposite directions, and the extent of improvement or deterioration of conductivity is determined by their competition.

The effect of high-density current pulses was analyzed for Y–Ba–Cu–O ceramic samples. Since the technology of sample preparation is known in principle,[13] it will be described here only briefly.

High-purity powders of $BaCO_3$, Y_2O_3, and CuO were used as initial materials for preparing samples. These powders taken in the molar ratio 2:0.5:3 were mixed and annealed for 28 hours at 1173 K. The obtained cake was crushed, sieved and mixed. The cake particles were in the form of a mixture of crystalline polyhedrons with clearly manifested angles and rounded vortices (with different radii of rounding) (Fig. 2). The obtained powder was pressed into pellets of diameter 5–10 mm and height 5–7 mm. The pellets were annealed for 24 hours at 1123–1233 K, and then the temperature was lowered to 623–673 K, and the sample was held at this temperature for 4 hours.

The results of x-ray diffraction analysis and x-ray spectral microanalysis of the composition of particles of $YBa_2Cu_3O_x$ powder (for $x < 6.5$) before the thermal treatment indicate phase homogeneity. The results of x-ray analysis of the samples after the last stage of thermal treatment proved that the prepared samples have the phase composition described by the formula $YBa_2Cu_3O_{6.8}$ and have an orthorhombic structure with the lattice parameters $a = 3.818$ Å, $b = 3.895$ Å and $c = 11.665$ Å. The analysis was carried out on a diffractometer DRON-3M with the CuK_α radiation. The grains of fritted material are separated by boundary layers. The ac permeability measurements revealed that the superconducting transition temperature T_c of the material of the boundary layer is lower than T_c of the bulk material, and Josephson junctions are formed between a boundary and a grain. The composition of the boundary layer material has not been determined. According to the authors, this composition is nonuniform (especially as regards the oxygen concentration). In all probability, the chemical composition of the material of the boundary layers is affected by the reactions of barium with water and CO_2 from air. An electron-microscopic analysis of microscopic structure revealed the absence of impurities in the boundary layers.

Compact samples were subjected to processing by current pulses from the discharge of a capacitor charged to

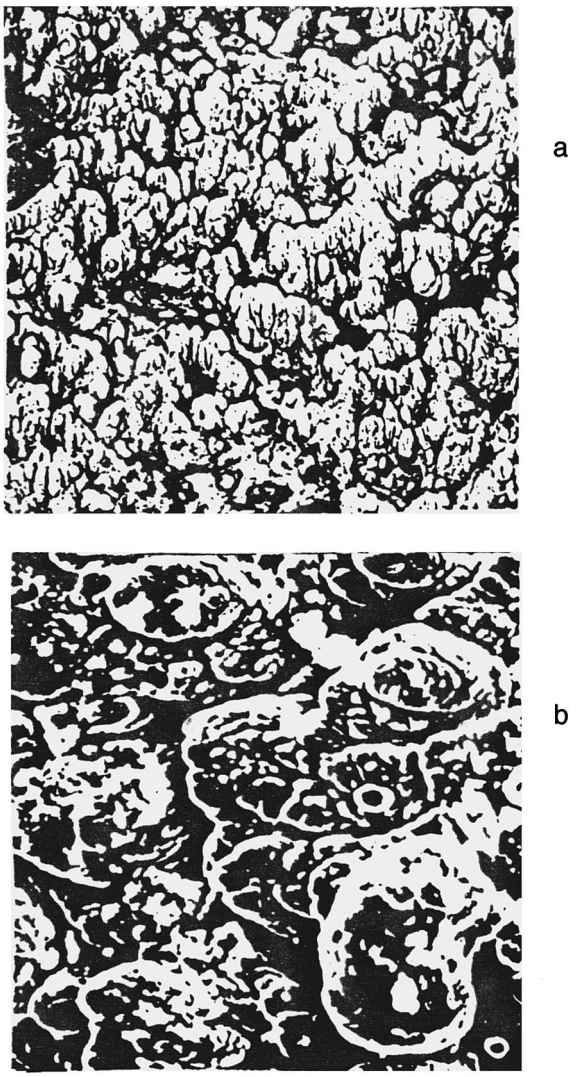

FIG. 3. Microstructure of HTSC material after treatment by electric pulses: $\times 150$ (a) and $\times 1000$ (b).

0.2–0.5 kV under a mechanical load of 0.1–1.0 kN, corresponding to a pressure of $(4–12)\times 10^6$ Pa. At the upper limits of electrical and mechanical loading, current pulse signals have the form of rapidly attenuating sinusoid with a period of 80 μs, which is characteristic of the pulse source used by us. Under a load smaller than 0.1 kN, current signals were converted into a series of irregular pulses having a duration from a few microseconds to two tens of microseconds. The filling structure of these signals has not been studied in detail.

The passage of current pulses for the initial voltage exceeding 0.45 kV caused significant changes in the sample structure (Fig. 3), which was manifested as a local orientation of crystallites along the direction of the current.

Since the resistance to electron flow has elevated values at certain points of a fritted ceramic sample (e.g., at the points of junction between the bulk material and the boundary layer in each grain or granule or at the points of contact between granules of grains), liquid ''bridges'' can be formed on the path of the electron flow. After solidification, these bridges are transformed, as a rule, into interlayers having

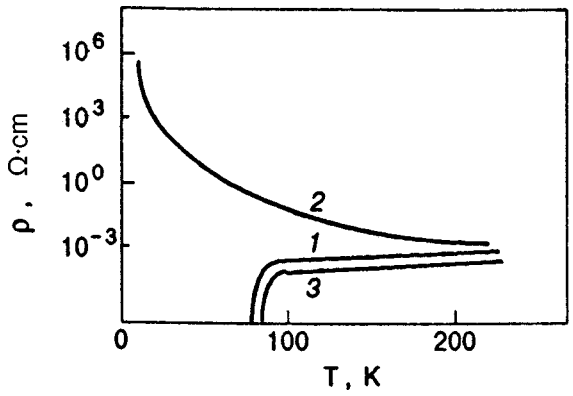

FIG. 4. Effect of electric pulses on the temperature dependence of resistivity of $YBa_2Cu_3O_x$: initial sample (*1*), after the passage of current through the sample (*2*), and after annealing (*3*).

the previous composition of $YBa_2Cu_3O_x$. As an exception, some samples exhibited a change in the composition of the interlayer between granules with the formation of $YBa_2Cu_3O_x$ (80%) and $Y_{1-x}Ba_xCuO_\delta$ (where $x=0.33–0.44$, $\delta=0.5$) with $T_c=55$ K (20%).

Figure 4 (curve *1*) shows the temperature dependence $\rho(T)$ of the resistivity of the initial sample ($T_c=90$ K, $\rho=6.0\times 10^{-2}\Omega\cdot$cm at 20 °C). Curve *2* in Fig. 4 shows that after the passage of a current pulse corresponding to an applied voltage below 0.45 kV under a mechanical pressure not exceeding 5.0 MPa, the resistivity increases monotonically to 10^6 $\Omega\cdot$cm as the temperature is lowered to 4.2 K. Such samples do not exhibit Meissner's effect. We can propose that such a treatment does not lead to the formation of liquid bridges, or weak links between granules are broken as a result of electrical microexplosions. Since electrons possess a high energy, they might cause local phase transformations. All this leads to a change in local properties, which deteriorates the superconducting characteristics of the sample.

An increase in voltage or mechanical pressure leads to a change in the microscopic structure of the sample, which creates premises for the formation of grain-oriented structure, but the superconducting transition remains the same as in a sample not subjected to treatment (curve *1* in Fig. 4). However, subsequent annealing of such a sample in air for 10–15 hours at 1233 K leads to an increase in the superconducting transition temperature to 93 K (curve *3* in Fig. 4).

CONCLUSIONS

(1) The passage of pulsed electric current through a bulk sample of Y-based HTSC ceramic leads to the formation of a grain-oriented structure.
(2) The treatment of samples by pulses of discharge current from a capacitor charged to a voltage below 0.45 kV under a mechanical pressure not lower than 5.0 MPa leads to a deterioration of the superconducting properties of the material.
(3) The superconducting properties remain unchanged if the sample is treated by pulses of discharge current from a capacitor charged to a voltage 0.45–0.5 kV under a me-

chanical pressure of 5.0–12.0 MPa, but additional annealing of these samples for 10–15 hours at 1233 K leads to an increase in T_c to 93 K.

The obtained results lead to the conclusion that the local texturing observed by us can be extended to the entire volume of the material by electric-pulse treatment of Y-based HTSC ceramics of the 123 type, which might improve their critical parameters.

*E-mail: raitch@ipms.kiev.ua

[1] I. G. Bednorz and K. A. Müller, Z. Phys. B **64**, 189 (1987).
[2] G. Deutscher, O. Entin-Wohlman, S. Fishmen, and Y. Shapira, Phys. Rev. B **21**, 5041 (1980).
[3] D. Dimos, P. Chaudhari, and J. Mannhart, Phys. Rev. B **41**, 4038 (1990).
[4] V. M. Svistunov and A. I. D'yachenko, Supercond. Sci. Technol. **5**, 4346 (1992).
[5] E. A. Eremina, A. M. Gas'kov, R. R. Oleinikov, and Yu. V. Tret'yakov, in *Proceedings of the 1st Int. Conf. on Material Science of High-Temperature Superconductors*, Vol. 1, Kharkov (1993).
[6] V. P. Seminizhenko, in *Proceedings of Seminar on New Materials and Their Application in Machine Building*, United Nations, Economic Commission for Europe, Kiev (1992).
[7] Yu. V. Gomeniuk, V. Z. Lozovski, V. S. Lysenko *et al.*, Phys. Status Solidi A **132**, 155 (1992).
[8] A. I. Raitchenko, *Fundamentals of Powder Fritting by Passing Electric Current* [in Russian], Metallurgiya, Moscow (1987).
[9] S. T. S. Al-Hassani, Wire Industry **46**, 809 (1979).
[10] D. Y. Williams and W. Johnson, Powder Metalurgy **25**, 85 (1982).
[11] A. I. Raitchenko, Poroshkovaya Metallurgiya No. 1, 29 (1985).
[12] S. Clyens, S. T. S. Al-Hassani, and W. Johnson, Int. J. Mech. Sci. **18**, 37 (1976).
[13] E. K. Kotlyarchuk, D. M. Popovich, A. A. Flis, and V. S. Flis, Poroshkovaya Metallurgiya No. 11, 76 (1990).

Translated by R. S. Wadhwa

HTSC critical state investigation by energy balance technique

V. K. Ignat'ev and A. E. Konshin

*Volgograd State University, 400062 Volgograd, Russia**

(Submitted October 13, 1997; revised January 19, 1998)
Fiz. Nizk. Temp. **24**, 538–543 (June 1998)

The energy balance technique is used for contactless measuring of integral electrical characteristics of annular samples of Y–Ba–Cu–O ceramics. Dependences of the loss resistance and internal inductance of HTSC samples on transport current are obtained. The critical and resistive states of samples are studied at various frequencies of transport current as functions of the applied constant magnetic field. © *1998 American Institute of Physics.* [S1063-777X(98)00406-X]

INTRODUCTION

Investigation of the electric and magnetic properties of high-temperature superconductors (HTSC) is one of the most important problems in modern low-temperature physics. In several models of HTSC (e.g., Bean's model,[1] spin-glass model,[2] Josephson medium model,[3] and percolation model[4]), the superconducting ceramic is treated as a nonlinear medium with a considerable dispersion in space and time. In the present work, we describe a contactless technique for measuring the dependence of loss power and inductance on the transport current as well as delay time in annular YBaCuO superconducting ceramic samples for various values of the constant applied magnetic field and the frequency of the transport current passing through the sample. These integral electrical characteristics carry vital information about the critical and resistive states of HTSC and can be used not only to confirm the validity of the theoretical model used for its description, but also to evaluate various parameters of the superconducting ceramic like the critical current, penetration depth and the velocity of propagation of magnetic field perturbations. For example, a sharp variation in the sample inductance during a transition from the critical to resistive state and a considerable delay in the propagation of electromagnetic perturbations can only be associated with a comparatively slow movement of the magnetic vortex structures characteristic of Bean's model. In the percolation model, the inductance depends weakly on transport current and the delay is negligibly small. The widely used steady-state IVC do not provide sufficient information about the electromagnetic processes occurring in a superconductor and cannot be used, for example, for determining the magnetic field propagation in space and time since the IVC obtained from almost all models of the critical state are qualitatively similar under appropriate choice of parameters.

ENERGY BALANCE FOR SUPERCONDUCTORS

From the point of view of the circuit theory, an HTSC sample is a nonlinear inertial two-terminal network.[5] Investigation of inertial nonlinear elements is a complicated problem that does not have a general solution. In order to determine the response of an element with nonlinear conductivity to an external agency, we must consider it from the energy point of view. Let us write the first law of thermodynamics for the sample in the form of an energy balance equation.[5] If divided charges do not appear in a nonlinear medium upon the passage of a current through it, this equation can be represented in the form

$$u(t)i(t)=dW(t)/dt+P(t), \tag{1}$$

where $u(t)$ is the voltage across the terminals of the nonlinear sample, $i(t)$ the current passing through it, $W(t)$ the magnetic field energy for the sample, and $P(t)$ the power loss in the sample.

Thus, knowing the variation of the magnetic energy and dissipative power in the sample from the intrinsic properties of the nonlinear medium, we can use Eq. (1) to determine the voltage $u(t)$ across the sample for a given law of variation of the current $i(t)$ through it. In order to solve this equation, we must first get rid of the explicit time dependence of W and P, and present them as functions of the current passing through the sample. It must be noted, however, that for an inertial medium with a nonlinear conductivity the energy and loss power are generally functions of not only the instantaneous value of the current $i(t)$, but also the past history of the agency, i.e., the values of current at the previous instants of time. This dependence may be in the form of quite complicated nonlinear delayed potentials. For a quite slow variation of the current $i(t)$, we can write to a high degree of accuracy $P(t)=P[i(t-\tau)]$ and $W(t)=W[i(t-\tau)]$, where τ is a small delay ($\tau \ll T$), T being the period of the current which can be assumed to be identical for W and P if we assume that both the dissipative power and the magnetic energy in an HTSC are determined by the dynamics of distribution of hypervortices.[6] Let us expand these functions into Taylor series in the vicinity of the time instant t:

$$i(t-\tau)=i(t)-\tau\frac{di}{dt}+\frac{\tau^2}{2}\frac{d^2i}{dt^2}-\ldots,$$

$$P(t)=P[i(t)]-\tau\frac{di}{dt}\frac{dP}{di}+\frac{\tau^2}{2}\left(\frac{d^2i}{dt^2}\frac{dP}{di}+\left(\frac{di}{dt}\right)^2\frac{d^2P}{di^2}\right)-\ldots, \tag{2}$$

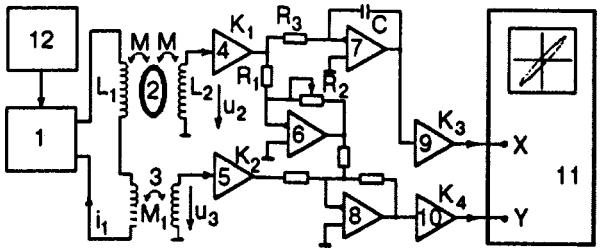

FIG. 1. Measuring circuit diagram.

$$W(t)=W[i(t)]-\tau\frac{di}{dt}\frac{dW}{di}+\frac{\tau^2}{2}\left(\frac{d^2i}{dt^2}\frac{dW}{di}+\left(\frac{di}{dt}\right)^2\frac{d^2W}{di^2}\right)-\ldots,$$

$$\frac{dW(t)}{dt}=\frac{dW(t)}{di}\frac{di}{dt}=\left(\frac{dW}{di}-\tau\frac{di}{dt}\frac{d^2W}{di^2}-\ldots\right)\frac{di}{dt}.$$

We now introduce the active resistance of a nonlinear element $R(i)=P(i)/i^2$ and its differential inductance $L(i)=2dW(i)/d(i^2)=(1/i)(dW/di)$. Confining ourselves to terms having the first order of smallness in τ and to the first derivatives of W and P with respect to the current i, we can substitute the expansion (2) into the energy balance equation (1):

$$u(t)=L(i)\frac{di}{dt}+R(i)i-\tau\left(2R(i)+i\frac{dR}{di}\right)\frac{di}{dt}. \tag{3}$$

Thus the response $u(t)$ to an arbitrary action $i(t)$ can be calculated in the first approximation from the known characteristics of the nonlinear element $R(i),L(i)$ and the delay τ. Let us consider the inverse problem of determining the characteristics $R(i),L(i)$ and τ of the nonlinear element from the measured values of $u(t)$ and $i(t)$. This problem can be split into two parts, viz., measurement of the voltage $u(t)$ and the solution of Eq. (3) containing all these unknown quantities.

MEASURING TECHNIQUE AND PROCESSING OF RESULTS

For characteristic values of the sample resistance $10^{-5}-10^{-6}\Omega$, contact methods are inapplicable for voltage measurements due to a rather large value of the contact resistance and different potentials of contact surfaces due to different positions of the Fermi level in the sample and at the contact.[7] Inductive methods using one or two solenoids[8,9] do not allow measurements under the conditions of developed skin effect since they do not take into account the current distribution over the sample cross-section. The most informative technique involves contactless measurement of resistance and inductance of an annular sample with the help of Rogovskii hoops since the mutual inductance of such hoops with the sample is independent of current distribution over its cross-section. Figure 1 shows the circuit diagram for measurements.[10] The circuit consists of a current source 1 controlled by the voltage supplied by an external generator 12, a pickup containing two identical Rogovskii hoops ($L_1=L_2$) embracing the annular sample 2 and the transformer 3, as well as a signal processing block containing preamplifiers 4 and 5, an adjustable amplifier 6, an integrator 7, a summator 8, and input amplifiers 9 and 10 supplying signals to the horizontal and vertical sweeps respectively of a two-channel oscillograph 11.

The current source 1 generates an alternating current i_1 in the Rogovskii hoop L_1 and the primary winding of the transformer 3. Let us assume that M is the mutual inductance of the Rogovskii hoops with the annular sample, the mutual inductance between the hoops is zero, and the mutual inductance of the windings of the transformer 3 is M_1. Denoting by u_1 the emf induced in the first Rogovskii hoop L_1, we can write the energy balance equation of the type (1) for the pickup:

$$u_1i_1=\frac{d}{dt}\left(W(t)+\frac{L_1i_1^2}{2}+Mii_1\right)+P(t), \tag{4}$$

where i is the current in the sample itself. From the law of electromagnetic induction, we obtain

$$u_1=\frac{Mdi}{dt}+\frac{L_1di_1}{dt};\quad u_2=\frac{Mdi}{dt};\quad u_3=-\frac{M_1di_1}{dt}, \tag{5}$$

where $u_2(t)$ and $u_3(t)$ are the voltages across the hoop L_2 and the secondary winding of the transformer 3, respectively. Solving the system of equations (4) and (5) jointly, we obtain

$$\frac{M}{M_1}u_3i=\frac{d}{dt}W(t)+P(t), \tag{6}$$

$$i(t)=\frac{1}{M}\int_{-\infty}^{t}u_2(t')dt'. \tag{7}$$

It can be seen easily that Eq. (6) is the energy balance equation for the sample itself, and with the exception of a constant multiplier, u_3 can be treated as the voltage across the annular sample cut along the generator perpendicular to the current lines if the surfaces of the cuts are clamps.

Substituting expansion (2) for $P(t)$ and dW/dt into (6) and confining to terms having the first order of smallness in τ and to the first derivatives of W and P with respect to the current i, we arrive at the following equation:

$$\frac{M}{M_1}u_3(t)=\left[L(i)-\tau\left(2R(i)+i\frac{dR}{di}\right)\right]\frac{di}{dt}+R(i)i. \tag{8}$$

Taking into consideration the measuring circuit diagram shown in Fig. 1, we obtain the voltage supplied to the horizontal and vertical sweep of the oscillograph:

$$u_X(t)=\frac{K_1K_3}{R_3C}\int_{-\infty}^{t}u_2(t')dt'=\frac{K_1K_3M}{R_3C}i(t), \tag{9}$$

$$u_Y(t)=K_4\left(K_2u_3(t)-\frac{K_1R_2}{R_1}u_2(t)\right)=\frac{K_4K_2M_1}{M}\left\{\left[L(i)-\tau\left(2R(i)+i\frac{dR}{di}\right)-\frac{K_1M^2R_2}{K_2M_1R_1}\right]\frac{di}{dt}+R(i)i\right\}, \tag{10}$$

where K_1,K_2,K_3 and K_4 are the amplification factors of the amplifiers 4, 5, 9 and 10 respectively.

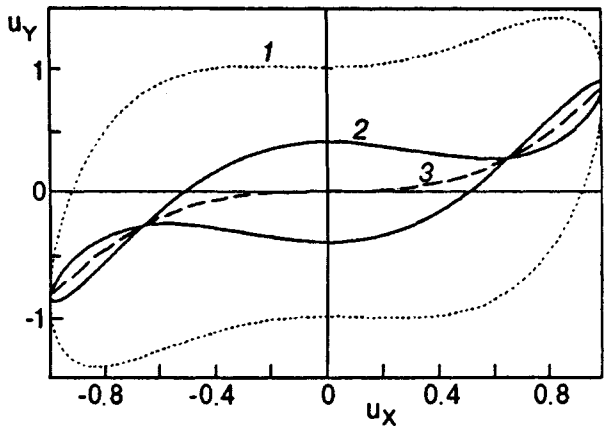

FIG. 2. Hysteresis loop on the oscillograph screen for various values of R_2: $R_2=0$ (curve *1*), $R_2>0$ (curve *2*). Curve *3* is formed by points of intersection of the hysteresis loop upon variation of R_2.

Equations (9) and (10) describe a closed parametric curve (hysteresis loop) seen on the oscillograph screen (Fig. 2). It can be seen from Eq. (10) that the shape of the loop depends on the properties of the sample as well as the resistance of the variable resistor R_2. If the quantities $L(i)$ and $R(i)$ do not depend on the direction of the current i through the sample, the loop will be symmetric relative to the origin of coordinates $u_X=0$, $u_Y=0$. In a certain range of values of resistance R_2, the loop may have points of intersection where the following conditions are satisfied: $i(t_1)=i(t_2)$, $u_Y(t_1)=u_Y(t_2)$ t_1 and t_2 being, respectively, the instants of time corresponding to the build-up (front) and fall-off (decay) intervals of the half-period of the current $i(t)$. Equating the right-hand sides of Eq. (10) obtained for the instants of time t_1 and t_2, we arrive at the expression

$$\frac{K_1M^2R_2}{K_2M_1R_1}\left(\frac{di}{dt}(t_1)-\frac{di}{dt}(t_2)\right)=\left[L(i)-\tau\left(2R(i)+i\frac{dR}{di}\right)\right]\left(\frac{di}{dt}(t_1)-\frac{di}{dt}(t_2)\right)$$

or

$$\frac{K_1M^2}{K_2M_1R_1}R_2=L(i)-\tau\left(2R(i)+i\frac{dR}{di}\right). \tag{11}$$

Substituting this relation into (10), we obtain

$$u_Y(t_1)=u_Y(t_2)=\frac{K_2K_4M_1}{M}R(i)i. \tag{12}$$

As the resistance of the variable resistor R_2 changes, the points of intersection of the loop defined by Eqs. (9) and (10) are displaced over the oscillograph screen and assume all possible values of the current i from zero to its maximum value, thus constituting the smooth curve $U(i)$. Equations (11) and (12) can be written in the form

$$L(i)-\tau\left(2R(i)+i\frac{dR}{di}\right)=\frac{K_1M^2}{K_2M_1}\frac{R_2}{R_1},$$

$$R(i)i=\frac{M}{K_2K_4M_1}U(i). \tag{13}$$

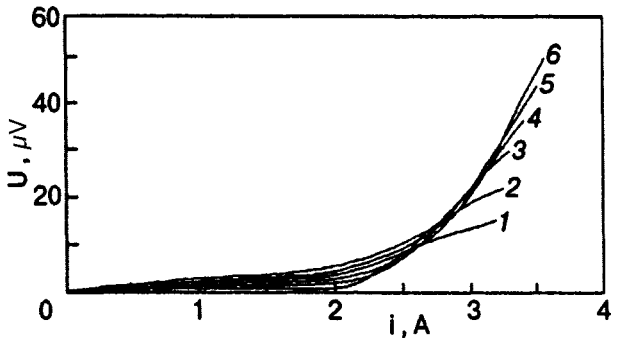

FIG. 3. Dependence of the loss voltage of a superconducting sample on current at various frequencies f (in Hz): 100 (curve *1*), 150 (curve *2*), 200 (curve *3*), 250 (curve *4*), 300 (curve *5*), and 350 (curve *6*).

The system of equations (13) connects $L(i)$,$R(i)$ with directly measurable quantities R_2 and $U(i)$. The delay τ appears in these equations as a parameter and can be determined from physical considerations by imposing constraints on the form of the function $L(i)$.

RESULTS OF MEASUREMENTS

The circuit described above was used for investigating annular superconducting samples prepared from yttrium ceramics according to the standard technique. Figures 3 and 4 show the dependence of loss voltage $U(i)=R(i)i$ (current–voltage characteristic) and integral inductance, respectively

$$L_i(i)=\frac{2W(i)}{i^2}=\frac{1}{i^2}\int_0^i L(i_1)di_1^2$$

for a cylindrical sample of length 40 mm, outer diameter 30 mm and inner diameter 11 mm for different frequencies of the current. Figures 3 and 4 shows clearly the subcritical region of $U(i)$ with a low loss resistance that is transformed abruptly into the resistive region. With increasing frequency of the current $i(t)$, the loss resistance of an HTSC sample increases both in subcritical and resistive states. Since the inductance of a loop is directly proportional to the area of the

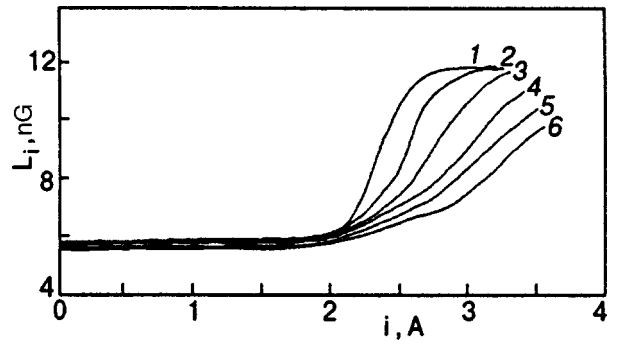

FIG. 4. Dependence of the inductance of a superconducting sample on current at various frequencies f (in Hz): 100 (curve *1*), 150 (curve *2*), 200 (curve *3*), 250 (curve *4*), 300 (curve *5*), and 350 (curve *6*).

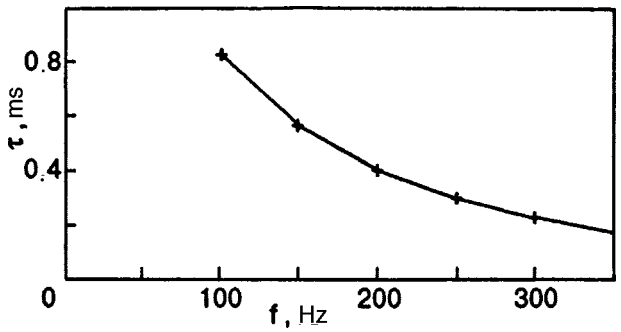

FIG. 5. Dependence of the delay τ on the transport current frequency.

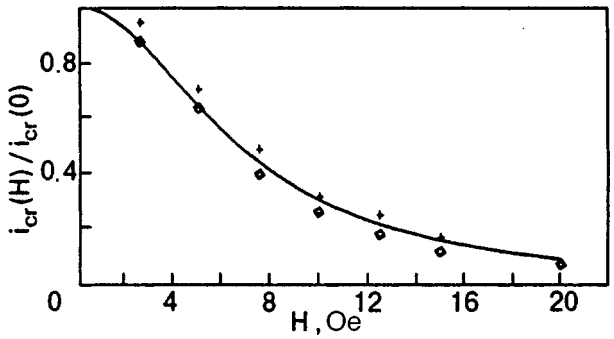

FIG. 6. Dependence of the critical current of a superconducting sample on constant magnetic field at various frequencies f (in Hz): 120 ($\diamond$) and 200 ($+$).

surface stretching over it, $L_i(i)$ should apparently depend on the current distribution over the sample cross-section. The range of variation of $L_i(i)$ can be determined as follows: the minimum inductance corresponds to the state when the magnetic field is expelled into the inner cavity of the annular sample (3.5 nH), and the entire current flows over a thin surface layer. The maximum inductance corresponds to a uniform current distribution over the entire sample cross-section. Hence while processing the results of measurements, we chose the delay τ in such a way that the inductance $L_i(i)$ does not decrease but tends to its maximum constant value for $i > i_{cr}$. Such a value of the delay could be selected only for frequencies 100–200 Hz. The plots shown in Fig. 4 reveal that $L_i(i)$ increases sharply at these frequencies upon a transition from critical to resistive state. The corresponding delay times shown in Fig. 5 are hundreds of microseconds, but the condition $\tau \ll T$ is still satisfied. A sharp increase in inductance and considerably long delay times amounting to about 10% of the transport current period indicate that the HTSC state is determined by the viscous flow of magnetic vortex structures (hypervortices). With increasing frequency, the inductance decreases due to skin effect and for a certain amplitude of the transport current, the hypervortices apparently have no time to occupy the entire superconductors during the time for which $i(t) > i_{cr}$. Hence the conductance does not attain its highest constant value at frequencies exceeding 200 Hz. In this case, the delay τ is determined in accordance with the model of critical and resistive state of HTSC developed in Ref. 6. According to this model, τ must decrease in proportion to $1/f^{3/2}$ for a delay time of the order of l/v (l is the skin-depth and v the average velocity of hypervortices) if we consider that the velocity of hypervortices increases in proportion to the frequency of the alternating transport current under conditions of developed skin effect while the skin-layer thickness decreases as the square root of the frequency.

Figure 6 shows the dependence of the critical current of an HTSC sample on the applied constant magnetic field for two frequencies of the alternating transport current i. It can be seen that the dependence of the critical current on constant magnetic field is described quite well by the function

$$\frac{i_{cr}(H)}{i_{cr}(0)} = \frac{1}{1+(H/H_0)^2},$$

where $H_0 = 6.7$ Oe. This function is shown by a solid curve in the figure.

CONCLUSIONS

The experimental results presented in Figs. 3–6 and processed by the energy balance method are in good accord with the model of critical and resistive states of a granular superconductor based on pinning and viscous flow of hypervortices.[6] Figure 7 shows in arbitrary units two current–voltage characteristics of a plate made of a granular superconductor, calculated by using this model for an alternating transport current, curve *2* corresponding to a frequency ten times higher than curve *1*. Note that this curve is in qualitative agreement with the experimental curves *1* and *6* in Fig. 3. In both cases, a sharp kink is observed in the region of the critical current i_{cr} at low frequencies, which vanishes as the frequency increases.

The fact that the a.c. loss resistance in a ceramic superconductor is nonzero in the subcritical current region and depends weakly on current in this region but increases with frequency is explained by an enhancement of the vortex lattice vibrations, and hence an increase in losses, upon an increase in frequency.

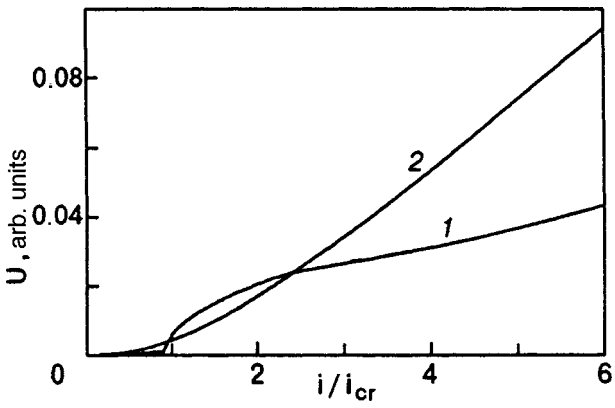

FIG. 7. Theoretical current–voltage characteristics of a superconducting sample. $f_2/f_1 = 10$.

The method of investigating the electrical properties of nonlinear and, in particular, superconducting samples can be used for measuring their loss resistance and differential inductance the more accurately, the smaller the delay τ characterizing the intrinsic inertia of the nonlinear medium. Within the framework of the method described here, this inertia is taken into account only in the first approximation, i.e., as a small delay. The error in this method is the sum of the measuring error due to instrumental distortion and noises, and the error due to terms omitted in the expansion (2). The relative value of this unavoidable error is proportional to τ/T.

This research was carried out under Project No. 96015 of the State Program on Current Problems in the Physics of Condensed State.

*E-mail: ivanov@physic.vgu.tsaritsyn.su

[1] S. Takacs, Czech. J. Phys. **40**, 1040 (1990).
[2] I. Morgenstern, K. A. Muller, and J. G. Bednorz, Physica B **152**, 85 (1988).
[3] T. C. Choy and A. M. Stoneham, J. Phys. Condens. Matter **2**, 939 (1990).
[4] V. F. Gantmakher, A. M. Neminskii, and D. V. Shovkun, Pis'ma Zh. Éksp. Teor. Fiz. **52**, 1214 (1990) [JETP Lett. **52**, 630 (1990)].
[5] V. P. Popov, *Fundametals of the Circuit Theory. A Textbook for Universities* [in Russian], Vysshaya Shkola, Moscow (1985).
[6] V. K. Ignat'ev, Fiz. Nizk. Temp. **23**, 686 (1997) [Low Temp. Phys. **23**, (1997)].
[7] O. N. Alifertsev, Sverkhprovodimost', Fiz., Khim., Tekh. **6**, 1881 (1993).
[8] A. A. Zhukov, D. A. Komarkov, and A. V. Mirkovich, Sverkhprovodimost', Fiz., Khim., Tekh. **6**, 743 (1993).
[9] V. I. Batakin and O. Ya. Savchenko, Sverkhprovodimost', Fiz., Khim., Tekh. **6**, 1842 (1993).
[10] V. K. Ignat'ev and A. E. Konshin, Prib. Tekh. Éksp. No. **3**, 94 (1997).

Translated by R. S. Wadhwa

Dependence of the superconducting transition temperature on the thickness of superconducting films with different coherence lengths

V. G. Prokhorov

*Institute of Metal Physics, National Academy of Sciences, 252680, Kiev, Ukraine**
(Submitted August 12, 1997; revised December 8, 1997)
Fiz. Nizk. Temp. **24**, 544–548 (June 1998)

The dependence of the superconducting transition temperature on the thickness of films of niobium, VN, TaN, and $YBa_2Cu_3O_{7-x}$ are determined experimentally. It is shown that, in addition to the proximity effect, the fluctuations of the electromagnetic field and order parameter of the superconducting phase may also play a significant role in superconductors with a small coherence length. © *1998 American Institute of Physics.* [S1063-777X(98)00506-4]

The study of the effect of geometrical size (e.g., film thickness) of superconductors on the transition temperature T_c is interesting in view of the fact that the physical nature of this effect continues to be a matter of controversy (both from experimental and theoretical points of view). In many cases, a decrease in the film thickness d leads to a decrease in the value of T_c as a rule. However, the functional form of the dependence $T_c(d)$ differs considerably for different superconductors (see, for example, Ref. 1). The size effect in thin films may be due to two reasons. The first reason is the proximity effect, which causes the normal component of electrons to diffuse into the superconducting layer and thus reduces the volume occupied by Cooper pairs in the phase space.[2,3] (Naturally, one has to assume that a thin layer of normal metal is formed on the surface of the superconducting film in this case.) The second reason is the emergence of strong fluctuations of the electromagnetic field and superconducting order parameter, which are especially significant for high-resistivity films and increase with decreasing film thickness.[4,5]

In this work, we describe the results of an analysis of the $T_c(d)$ dependences obtained for films with different values of the coherence length ξ. It is shown that, for traditional low-T_c superconductors with a high value of ξ, the proximity effect plays the main role in the decrease in the transition temperature with thickness. The experimental $T_c(d)$ dependences are described quite well by the theoretical model developed by Kresin and de Gennes.[2,3] However, according to the predictions of the models developed by Kulik[4] and Ovchinnikov,[5] the fluctuations of the electromagnetic field and order parameter in the superconducting phase of YBCO films with anomalously small values of ξ may also play a significant role in the lowering of the superconducting transition temperature in addition to the proximity effect.

1. EXPERIMENTAL RESULTS

Investigations were made on films of pure niobium, vanadium and tantalum nitrides, as well as YBCO (1-2-3). Niobium films were prepared by using the standard technique of electron-beam evaporation in vacuum.[6] Nitrides of transition metals (TaN, VN) were prepared by reactive cathode sputtering in a dc getter-diode discharge system using a mixture of argon and nitrogen.[7] The YBCO (1-2-3) films were obtained by pulse laser deposition.[8]

For thick films in which the superconducting transition temperature corresponds to the values for the bulk material, we measured the temperature dependence of the upper critical magnetic field near T_c. Using the model proposed by Werthamer, Helfand, and Hohenberg,[9] we can estimate the upper critical field at zero temperature from the experimental values of $dH_{c2}/dT|_{T_c}$: $H_{c2}(0) \cong 0.69(dH_{c2}/dT|_{T_c})T_c$. Using the familiar relation $H_{c2}(0)=\varphi_0/2\pi\xi^2(0)$, where φ_0 is the magnetic flux quantum ($\varphi_0 = 2.07 \cdot 10^{-15}\ \mathrm{T \cdot m^2}$), we can estimate the coherence length for each sample.

The following values of physical parameters were obtained from the experimental data: Nb $dH_{c2}/dT|_{T_c} \approx -1.5$ kOe/K, $T_c = 9.0$ K, $H_{c2}(0) \approx 9.3$ kOe, $\xi(0) \approx 20$ nm for Nb, $dH_{c2}/dT|_{T_c} \approx -20$ kOe/K; $T_c = 10$ K; $H_{c2}(0) \approx 138$ kOe, $\xi(0) \approx 5$ nm for VN; $dH_{c2}/dT|_{T_c} \approx -11.5$ kOe/K; $T_c = 9.6$ K; $H_{c2}(0) \approx 76.2$ kOe, $\xi(0) \approx 6.5$ nm for TaN; and $dH_{c2}/dT|_{T_c} \approx -11.3$ kOe/K; $T_c = 92$ K; $H_{c2}(0) \approx 717$ kOe, $\xi(0) \approx 2$ nm for YBCO (1-2-3).[10,11,13]

For all samples, the value of T_c was determined at the middle of the resistive transition $R(T)$. However, while an increase in the external magnetic field in traditional low-temperature superconducting films of Nb, VN or TaN leads, as a rule, to a parallel displacement of the resistive transition curve (especially for thick films[1)]) and $dH_{c2}/dT|_{T_c}$ is practically the same irrespective of whether T_c is evaluated at the beginning, middle, or end of the superconducting transition, the situation is quite different for YBCO films. An increase in the external magnetic field in this case results in a considerable broadening of the superconducting transition. Hence the slope of the temperature dependence of the upper critical field is found to be different for different values of resistance corresponding to the superconducting transition.

For example, $dH_{c2}/dT|_{T_c} = -33.5$ kOe/K for $R(T)/R_0 = 0.9$, i.e., at the very beginning of the transition from normal to the superconducting state, and $dH_{c2}/dT|_{T_c} = -6.4$ kOe/K for $R(T)/R_0 = 0.1$, i.e., at the end of the transi-

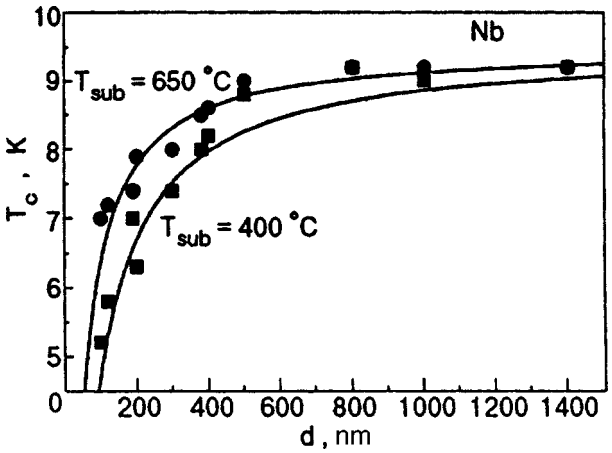

FIG. 1. Dependence of the superconducting transition temperature on thickness for niobium films obtained at different substrate temperatures. Solid curves were obtained theoretically taking the proximity effect into account.

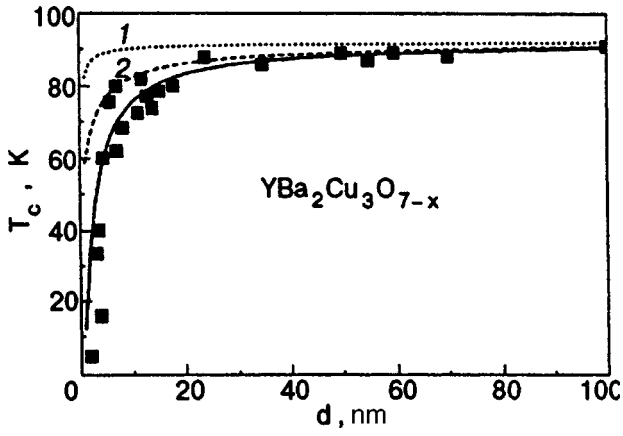

FIG. 3. Dependence of the superconducting transition temperature on thickness for $YBa_2Cu_3O_{7-x}$ films. The solid curve was obtained theoretically taking the proximity effect into account, while the dotted and dashed curves were obtained by using the fluctuational model for $\rho_0 = 100\ \mu\Omega\cdot$cm (curve *1*) and $\rho_0 = 1.0\ \mu\Omega\cdot$cm (curve *2*).

tion (R_0 is the resistance of the normal phase). The obtained results are in good agreement with the results of measurement of $dH_{c2}/dT|_{T_c}$ in monocrystalline samples for different orientations of the basal (**ab**) plane relative to the magnetic field vector: $dH_{c2}/dT|_{T_c} = -(4.6-7.1)$ kOe/K for $\mathbf{H}\perp(\mathbf{ab})$ and -23 kOe/K for $\mathbf{H}\parallel(\mathbf{ab})$.[14]

It can be assumed that the observed temperature broadening of the superconducting transition in a magnetic field is probably linked with strong anisotropy of $H_{c2}(T)$ in various crystallographic directions. Such a statement is valid for polycrystalline films which represent most of the samples investigated by us. Thus, by choosing the value of T_c at the middle of the superconducting transition curve, we eventually obtain a certain averaged coherence length characteristic of the given sample.[2)]

Figures 1, 2, and 3 show the experimental results of the dependence of the transition temperature on the thickness of films of niobium, vanadium and tantalum nitrides, and YBCO. The observed spread of the experimental points for small values of the YBCO film thickness is apparently associated with the fact that we have presented not only our results, but also the results of other authors[15–19] who obtained their samples on substrates of different materials by using different techniques. It can be seen from the curves that the $T_c(d)$ dependence becomes steeper with decreasing coherence length, and a noticeable decrease in the superconducting transition temperature is observed in films of smaller thickness.

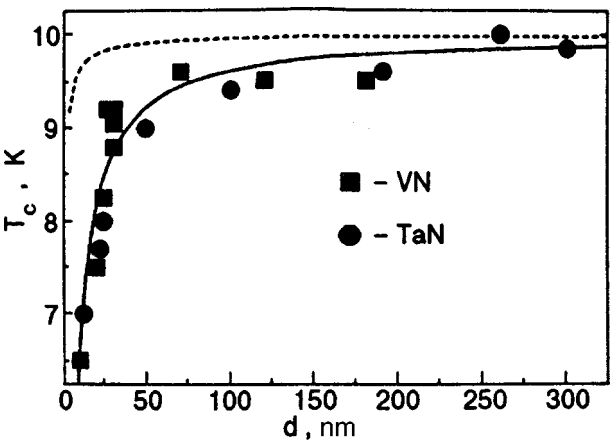

FIG. 2. Dependence of the superconducting transition temperature on thickness for VN and TaN films. The solid curve was obtained theoretically taking the proximity effect into account, and the dashed curve was obtained by using the fluctuational model.

Two theories have been developed to explain the observed effect in thin films. The first is based on the assumption that all superconducting films are sandwiches formed by superconducting and nonsuperconducting materials. As a rule, this is associated with processes of chemical interaction of the sample surface with the atmosphere, and with the formation of an oxide layer, which is typical especially of transition metals. The second approach assumes an enhancement of the role of fluctuations of the superconducting order parameter and of electromagnetic field upon a change in the geometrical parameters of the superconductors. The probability of observing this effect is the highest in samples with a high resistivity and small mean-free paths of electrons, i.e., with small values of the coherence length (since $\xi(0) = 0.85(\xi_0 l_{tr})^{1/2}$), where ξ_0 is the microscopic coherence length, and l_{tr} is the electron mean free path.

2. DISCUSSION OF RESULTS

De Gennes[2] offered a theoretical description of the proximity effect by considering the example of two-layered sandwiches for superconductors with a weak electron-phonon interaction. Kresin[3] developed this approach for superconductors with a strong coupling, like certain transition metals and alloys based on them. Hence we can use the expressions presented in Ref. 3 for an analysis of the obtained experimental results.

The expressions defining the dependence of the superconducting transition temperature on film thickness can be presented in the form

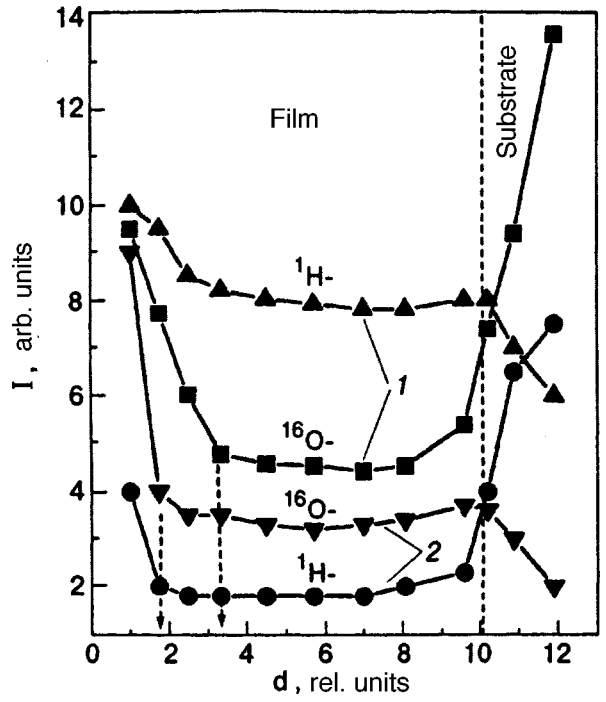

FIG. 4. Concentration profiles for oxygen and hydrogen ions in niobium films obtained at different substrate temperatures: $T_{sub}=300\,^\circ$C (curves *1*) and $T_{sub}=800\,^\circ$C (curves *2*).

$$\ln\left(\frac{T_c}{T_{cs}}\right)=-\frac{\delta}{d_s};\quad \delta=\frac{N_n}{N_s}\,d_n\,\ln\left(\frac{\omega_s}{T_{cs}}\right). \tag{1}$$

Here, d_s is the thickness of the superconducting film layer, d_n the normal film layer thickness, T_{cs} the transition temperature for the superconducting layer without proximity effect, N_n and N_s are the electron density of states in the normal and superconducting layers, and ω_s is the characteristic phonon frequency. It can be assumed naturally that $d_s \gg d_n$ in thick films if the normal layer thickness is taken equal to the thickness of the surface film which reacts with the atmosphere. Hence the superconducting transition temperature tends to attain saturation in films of large thickness ($T_c \approx T_{cs}$).

Assuming that $T_{cs}=9.2$ K for Nb and that d_s corresponds to the real sample thickness, we used the method of variation of the model parameter δ for calculating the theoretical dependences $T_c(d)$ describing the experimental dependences most accurately (see Fig. 1). It was found that, for niobium films obtained at a substrate temperature $T_{sub}=650\,^\circ$C, the experimental and theoretical curves have closest resemblance for $\delta=40$, while the corresponding situation for films formed at $T_{sub}=400\,^\circ$C is observed for $\delta=70$.

Putting $\omega_s \approx 110$ K and $N_n/N_s \approx 0.8$ for Nb films,[20] we can estimate the normal layer thickness for the investigated samples. For a niobium film obtained at $T_{sub}=650\,^\circ$C, the value of d_n is found to be close to 20 nm, while the corresponding value for films formed at $T_{sub}=400\,^\circ$C is $d_n \approx 28$ nm. These results are in very good agreement with those obtained from an analysis of concentration profiles of oxygen ions by using secondary-ion mass-spectrometry (Fig. 4). It can be seen from the figure that the higher the temperature at which the film was deposited on the substrate, the smaller the depth to which the diffusion of oxygen atoms into the film occurs. Arrows indicate the relative thickness of the film surface layer with an enhanced oxygen concentration: the thickness of this film is $\approx 0.32d$ (≈ 35 nm) for $T_{sub}=300\,^\circ$C and $\approx 0.18d$ (≈ 20 nm) for $T_{sub}=800\,^\circ$C, d being the total film thickness (≈ 110 nm).

It can be seen from Fig. 2 that an analysis of the experimental dependences $T_c(d)$ for vanadium and tantalum nitrides using formulas (1) leads to the value $\delta=4$. Assuming that the ratio of electron density of states in normal and superconducting layers as well as the characteristic phonon frequencies for them do not differ significantly from the corresponding values for niobium films, we can determine the normal surface layer thickness $d_n \approx 2$ nm. For the sake of comparison, Fig. 2 also shows the theoretical $T_c(d)$ dependence obtained in the Kulik's fluctuational model[4] by using the expression

$$\frac{T_{co}-T_c}{T_{co}}=\frac{e^2R^*}{8\hbar}\,\ln\left(\frac{8\hbar}{e^2R^*}\right); \tag{2}$$

where T_{co} is the transition temperature obtained without taking fluctuations into consideration, $R^*=(\sigma_0 d)^{-1}$ is the resistance of an area element of the film, σ_0 is the residual conductivity, and $e^2/16\hbar=1.5\times10^{-5}\ \Omega^{-1}$. The residual resistivity ρ_0 of the nitride films was found to be 57.9 $\mu\Omega\cdot$cm for TaN and 55.7 $\mu\Omega\cdot$cm for VN. It can be seen from Fig. 2 that the obtained curve differs significantly from the experimental results. Apparently, fluctuations of the order parameter of the superconducting phase and of the electromagnetic field in transition metal nitride films do not play a significant role, and the observed decrease in the superconducting transition temperature is mainly associated with the emergence of the proximity effect.

This conclusion is confirmed by the high corrosion resistance of the nitrides of transition metals. Hence thin films based on such materials are practically not oxidized upon exposure to atmosphere.

An analysis of the experimental dependences $T_c(d)$ for YBCO films using the de Gennes–Kresin model shows that the best agreement with the theoretical curve is obtained for the value $\delta=2$ of the fitting parameter. This theoretical dependence is shown by a solid curve in Fig. 3. Assuming that a non-superconducting surface layer can be formed as a result of departure from oxygen stoichiometry in YBCO (1-2-3), it can be concluded that the mean density of electron states in the vicinity of the Fermi surface will not change significantly, i.e., $N_n/N_s \approx 1$. Taking the characteristic phonon frequency appearing in the model equal to half the Debye frequency $\omega_s \approx 200$ K,[21] we can estimate the thickness of the normal layer as $d_n \approx 2.5$ nm. The existence of such a ''defective'' layer is confirmed by surface resistance studies in the microwave frequency range[22] as well as by the data corresponding to the concentration profiles of secondary ions.[23]

On the other hand, it can be seen from Fig. 3 that in contrast to films of nitrides of transition metals, the $T_c(d)$ dependence for YBCO films may be described quite adequately by the fluctuation model. For example, curve *1* is

calculated from formula (2) for residual resistivity $\rho_0 = 100\ \mu\Omega\cdot$cm, while curve *2* is obtained for $\rho_0 = 1.0\ \mu\Omega\cdot$cm. Such values of residual resistivity were actually observed for most of the YBCO films investigated by us.

CONCLUSION

Experimental dependences of the superconducting transition temperature on film thickness show that a decrease in the coherence length leads to a sharper decrease in the value of T_c for smaller thicknesses. Such a situation can be observed in superconductors with a suppressed proximity effect. Indeed, the $T_c(d)$ dependence for low-resistance superconductors must be in the form of steps in the absence of proximity effect, and the transition temperature attains a value characteristic of bulk samples during the formation of the first monolayer of the growing film. In high-resistance superconductors, including HTSC, the $T_c(d)$ dependence may differ significantly from the ideal curve even in the absence of the proximity effect due to the emergence of strong fluctuations of the electromagnetic field and order parameter. However, it is hard to draw an unambiguous conclusion in favor of any of the above mechanisms responsible for a decrease in the value of T_c for HTSC films because of a strong effect of the peculiarities associated with the microstructure, crystal structure and defect concentration on the superconducting and physical properties. On the other hand, a solution of this problem is extremely important for the application of such materials in band-pass resonators, delay lines, or other elements in microwave technology requiring low resistance-associated energy losses and a high value of the Q-factor.

The author is indebted to S. P. Chenakin for an analysis of niobium films with the help of the VIMS technique. This research was carried out under contract No. 2/573 with the Ukrainian Ministry of Science and Technology.

*E-mail: pvg@imp.kiev.ua

[1)] An increase in the applied magnetic field may change the dimensions of fluctuations and a considerable broadening of resistive transition curves for their films.[12]

[2)] It should be remarked, however, that the shape of the resistive transition curve in a magnetic field may also depend on thermoactivational magnetic flux creep, especially at the end of superconducting transition when $R(T)/R_0 \to 0$.

[1] Yu. F. Komnik, *Physics of Metal Films* [in Russian], Atomizdat, Moscow (1979).
[2] P. de Gennes, Rev. Mod. Phys. **36**, 225 (1964).
[3] V. Z. Kresin, IEEE Trans. Magn. **21**, 524 (1985).
[4] I. O. Kulik, Pis'ma Zh. Éksp. Teor. Fiz. **14**, 341 (1971) [JETP Lett. **14**, 228 (1971)].
[5] Yu. N. Ovchinnikov, Zh. Éksp. Teor. Fiz. **64**, 719 (1973) [Sov. Phys. JETP **37**, 336 (1973)].
[6] M. A. Vasil'ev, G. G. Kaminskii, V. G. Prokhorv *et al.*, Ukr. Fiz. Zh. **22**, 1028 (1977).
[7] V. A. Komashko, V. A. Noskov, and V. N. Statkevich, Sov. Phys. Crystallogr. **27**, 1204 (1982).
[8] V. G. Prokhorv, V. I. Matsui, and V. A. Vas'ko, Supercond., Phys. Chem. Technol. **6**, 505 (1992).
[9] N. R. Werthamer, F. Helfand, and P. C. Hohenberg, Phys. Rev. **147**, 295 (1966).
[10] V. M. Pan, V. G. Prokhorov, and G. G. Kaminsky, Fiz. Nizk. Temp. **6**, 968 (1980) [Sov. J. Low Temp. Phys. **6**, 470 (1980)].
[11] V. M. Pan, V. G. Prokhorov, V. A. Komashko *et al.*, IEEE Trans. Magn. **25**, 2000 (1989).
[12] I. M. Dmitrenko, A. S. Sidorenko, and N. Ya. Fogel', Fiz. Nizk. Temp. **8**, 1153 (1982) [Sov. J. Low Temp. Phys. **8**, 583 (1982)].
[13] V. M. Pan, V. G. Prokhorov, S. V. Gaponov *et al.*, Cryogenics **29**, 392 (1989).
[14] T. K. Worthington, W. J. Gallagher, and T. R. Dinger, Phys. Rev. Lett. **59**, 1160 (1987).
[15] S. C. Fan and R. E. Somekh, in *Applied Superconductivity* (ed. by D. Dew-Hughes), Int. Conf. Ser. No. 148, Vol. 2, 923 (1995).
[16] M. Yeadon, M. Aindow, and J. S. Abell, in *Applied Superconductivity* (ed. by D. Dew-Hughes), Int. Conf. Ser. No. 148, Vol. 2, 991 (1995).
[17] K. Kamigaki, H. Terauchi, and T. Terashima, J. Appl. Phys. **69**, 3653 (1991).
[18] I. Raistrick, M. Hawley, and J. Beery, Appl. Phys. Lett. **59**, 3177 (1991).
[19] J. Burger, M. Lippert, and W. Dorsch, Appl. Phys. **A58**, 49 (1994).
[20] M. E. Gershenzon and V. P. Koshelets, Zh. Éksp. Teor. Fiz. **77**, 1134 (1979) [Sov. Phys. JETP **50**, 572 (1979)].
[21] S. E. Stupp, T. A. Friedmann, J. P. Rice *et al.*, Phys. Rev. B **43**, 13073 (1991).
[22] V. F. Tarasov, V. F. Taborov, V. G. Prokhorov, and V. M. Pan, Czech. J. Phys. **46**, 1067 (1996).
[23] M. A. Vasiliev and V. V. Martynyuk, J. Electron Spectrosc. Relat. Phenom. **68**, 485 (1994).

Translated by R. S. Wadhwa

ELECTRONIC PROPERTIES OF METALS AND ALLOYS

Evolution of oscillations of semiconfined electron plasma

V. L. Falko, S. I. Khankina, and V. M. Yakovenko

*Institute of Radiophysics and Electronics, National Academy of Sciences of the Ukraine, 310085 Kharkov, Ukraine**

(Submitted February 5, 1998)
Fiz. Nizk. Temp. **24**, 549–558 (June 1998)

The evolution of an arbitrary initial nonequilibrium distribution of electrons and electric fields is investigated in a structure consisting of semiconfined media, viz., plasma and insulator (vacuum). The comprehensive spectrum of potential oscillations of electric fields is obtained. It is shown that the set of frequency eigenvalues is determined by the properties of the electron distribution function in equilibrium and perturbed states. In a cold plasma, volume and surface oscillations with the Langmuir frequency can propagate along with surface plasmons, while only a surface plasmon field exists in the insulator. In the presence of spatial dispersion, all types of volume and surface oscillations emerging in the plasma are emitted to the insulator. In addition to the field of intrinsic oscillations, an electric field of anomalous penetration associated with the effects of ballistic transport of conduction electrons at low temperatures also exists in the plasma. For a cold plasma, delay effects are taken into account, and the spatial and time distributions of the fields in the insulator are found. [S1063-777X(98)00606-9]

INTRODUCTION

In order to analyze comprehensively the electromagnetic oscillations in confined plasma-like media, we must solve the general problem on the evolution of an initial perturbation in such media. Such a problem for unconfined plasmas was formulated and solved by Landau.[1] A nonequilibrium electron distribution at the initial instant was defined in the entire volume of the plasma, and the electron distribution function and electric field were determined for all subsequent instants as well as dependence of frequency and decrement of oscillations on the wave vector. Oscillations of a semiconfined plasma were considered in Refs. 2–6, but the initial conditions were not taken into account. Consequently, the obtained vibrational spectrum cannot be regarded as comprehensive.

In this research, we study the evolution of an arbitrary initial perturbation of the field and electron distribution in the structure consisting of semiconfined plasma and insulator; the nature of penetration of the field in both media is determined; the interaction of surface and volume oscillations at the interface is studied, and eigenfrequencies and decrements of oscillations are obtained. We analyze the ballistic mode existing in a solid-state plasma at low temperatures.

FORMULATION OF THE PROBLEM. SYSTEM OF EQUATIONS. INITIAL AND BOUNDARY CONDITIONS

Let us consider a heterogeneous structure consisting of two semiconfined media, i.e., a (solid-state or gaseous) plasma and a nonabsorbing nondispersive medium (insulator or vacuum). At the initial instant $t=0$, the nonequilibrium electron distribution function $f^{(0)}(\mathbf{r},\mathbf{p})$ and the electromagnetic fields $\mathbf{H}^{(0)}(\mathbf{r})$ and $\mathbf{E}^{(0)}(\mathbf{r})$ are defined. We study the evolution of the distribution function $f(t,\mathbf{r},\mathbf{p})$ and fields $\mathbf{E}(t,\mathbf{r})$ at all subsequent instant of time in such a structure.

The complete system of Maxwell's equations in the plasma (medium 1, $y>0$) has the form

$$\begin{aligned} &\text{curl } \mathbf{H}=\frac{4\pi}{c}j+\frac{1}{c}\frac{\partial \mathbf{D}}{\partial t};\quad \mathbf{D}=\varepsilon_0\mathbf{E};\\ &\text{curl } \mathbf{E}-\frac{1}{c}\frac{\partial \mathbf{H}}{\partial t};\quad \text{div } \mathbf{D}=4\pi\rho;\quad \text{div } \mathbf{H}=0, \end{aligned} \tag{1}$$

where ε_0 is the dielectric constant of the lattice; the charge and current densities ρ and $\mathbf{j}$ are defined as

$$\rho=e\int f(t,\mathbf{r},p)d\mathbf{p},\quad \mathbf{j}(t,\mathbf{r})=e\int \mathbf{v}f(t,\mathbf{r},\mathbf{p})\cdot d\mathbf{p}. \tag{2}$$

The nonequilibrium distribution function $f(t,\mathbf{r},\mathbf{p})$ for conduction electrons satisfies the linearized kinetic equation

$$\frac{\partial f}{\partial t}+\mathbf{v}\cdot\nabla f+e\mathbf{E}\cdot\frac{\partial f_0(\mathbf{p})}{\partial \mathbf{p}}=-\upsilon f. \tag{3}$$

Here $e,\mathbf{v},\mathbf{p},f_0(\mathbf{p})$ and ν are the charge, velocity, momentum, equilibrium distribution function, and reciprocal relaxation time for conduction electrons.

The field in the insulator (medium 2, $y<0$) is described by the equations

$$\text{curl } \mathbf{H}=\frac{1}{c}\frac{\partial \mathbf{D}}{\partial t};\quad \mathbf{D}=\varepsilon_2\mathbf{E}; \tag{4}$$

$$\text{curl } \mathbf{E} = -\frac{1}{c}\frac{\partial \mathbf{H}}{\partial t}; \quad \text{div } \mathbf{D} = 0; \quad \text{div } \mathbf{H} = 0.$$

The boundary conditions to Eqs. (1)–(4) are the continuity conditions for the tangential components of the electric and magnetic fields at the interface $y=0$ and radiation conditions: all the quantities appearing in the equations vanish for $y \to \pm\infty$ at any instant of time. We assume that the surface $y=0$ is a perfectly reflecting wall at which electrons experience specular reflection, i.e., the relation

$$f(v_y>0,t) = f(v_y<0,t)|_{y=0}, \tag{5}$$

is satisfied for the distribution function at any instant of time. The coordinate system is chosen so that the x-axis coincides with the direction of propagation of the wave on the surface $y=0$; accordingly, the dependence of all these quantities on the x coordinate is proportional to $\exp(iq_x x)$ in Eqs. (1)–(4). In order to solve the problem with the initial conditions, we must expand all functions of time t in Eqs. (1)–(4) into Fourier integrals for $t>0$:

$$P(t,y) = \frac{1}{2\pi}\int_{-\infty+i\sigma}^{\infty+i\sigma} d\omega P_\omega(y) e^{-i\omega t};$$
$$P_\omega(y) = \int_0^\infty dt P(t,y) e^{i\omega t}. \tag{6}$$

Integration is carried out on the entire complex plane ω along the straight line parallel to the real axis and passing above all singularities of the integrand. As a result, the system of equations in the Fourier representation contains the values of electric and magnetic fields and the nonequilibrium distribution function at the initial instant.

The condition (5) for specular reflection of electrons at the interface makes it possible to continue the fields $\mathbf{E}_\omega(\mathbf{r})$ and currents $\mathbf{j}_\omega(\mathbf{r})$ from the region $y>0$ to the region $y<0$ so that their x-components are even functions of y, while y-components are odd functions.[2] Then the expression for the current $\mathbf{j}_\omega$ can be written for the entire space $-\infty<y<\infty$:

$$j_{\omega_i}(y) = \int_{-\infty}^{\infty} dy' \sigma_{ik}(|y-y'|) E_{\omega_k}(y') + j_i^{(0)}(y), \tag{7}$$

where $\mathbf{j}^{(0)}(y)$ is determined by the initial distribution function $f^{(0)}(\mathbf{r},\mathbf{p})$. The tensor $\sigma_{ik}(|y|)$ in the Fourier representation is known[2] to coincide with the conductivity tensor of an unconfined isotropic plasma:

$$\sigma_{ik}(\omega,\mathbf{q}) = -ie^2 \int \frac{d\mathbf{p} v_i (\partial f_0/\partial p_k)}{\omega - \mathbf{q}\cdot\mathbf{v} + i\nu}$$
$$(i=x,y), \quad (\mathbf{q}=(q_x,q_y)), \tag{8}$$

while the Fourier transform of the current $\mathbf{j}^{(0)}(\mathbf{r})$ has the form

$$j^{(0)}(\mathbf{q}) = iem^3 \int_{-\infty}^{\infty} d\mathbf{v} \frac{\mathbf{v} f^{(0)}(\mathbf{q},\mathbf{v})}{\omega - \mathbf{q}\cdot\mathbf{v} + i\nu} \tag{9}$$

(m is the effective mass of the electron). Here we have used the assumption on the possibility of expansion of the initial function $f^{(0)}(\mathbf{r},\mathbf{p})$ into a Fourier integral in coordinates.

Owing to the symmetry of tensor (8), the system of equations (1)–(4) splits into two independent subsystems: E_x, E_y, H_z (E-wave) and E_z, H_x, H_y (H-wave). We shall consider an E-wave below since it permits a solution in the form of surface plasma waves in a heterogeneous structure.

Using the boundary conditions, we obtain the expressions for the fields in the two media (we shall write formulas only for the x-components of the electric field):

$$E_{x1}(t,y) = \frac{1}{(2\pi)^2}\int_{-\infty+i\sigma}^{\infty+i\sigma} \frac{d\omega e^{-i\omega t}}{\omega} \times \int_{-\infty}^{\infty} dq_y e^{iq_y y}\left[\frac{L_l^{(0)}(\mathbf{q})}{q^2\varepsilon^l(\omega,\mathbf{q})} + \frac{L_t^{(0)}(q)}{q^2-(\omega^2/c^2)\varepsilon^t(\omega,\mathbf{q})}\right] + \frac{1}{\pi\Delta(\omega)}\left[\frac{L_l^{(0)}(\mathbf{q})}{q^2\varepsilon^l(\omega,\mathbf{q})} + \frac{L_t^{(0)}(\mathbf{q})}{q^2-(\omega^2/c^2)\varepsilon^t(\omega,\mathbf{q})} - \frac{M^{(0)}(\mathbf{q})}{q^2-(\omega^2/c^2)\varepsilon_2}\right]\int_{-\infty}^{\infty}\frac{dq_y' e^{iq_y' y}}{q'^2}\left[\frac{q_x^2}{\varepsilon^l(\omega,\mathbf{q})} - \frac{\omega^2}{c^2}\frac{q_y^2}{q'^2-(\omega^2/c^2)\varepsilon^t(\omega,\mathbf{q}')}\right], \quad y>0; \tag{10}$$

$$E_{x2}(t,y) = \frac{i}{(2\pi)^2}\int_{-\infty+i\sigma}^{\infty+i\sigma} \frac{d\omega e^{-i\omega t}}{\omega} \times \int_{-\infty}^{\infty} dq_y e^{iq_y y}\frac{M^{(0)}(\mathbf{q})}{q^2-(\omega^2/c^2)\varepsilon_2} - \frac{\sqrt{q_x^2-(\omega^2/c^2)\varepsilon_2}}{\pi\varepsilon_2\Delta(\omega)} e^{-|y|\sqrt{q_x^2-(\omega^2/c^2)\varepsilon_2}} \times\left[\frac{L_l^{(0)}(\mathbf{q})}{q^2\varepsilon^l(\omega,\mathbf{q})} + \frac{L_t^{(0)}(\mathbf{q})}{q^2-(\omega^2/c^2)\varepsilon^t(\omega,\mathbf{q})} - \frac{M^{(0)}(\mathbf{q})}{q^2-(\omega^2/c^2)\varepsilon_2}\right]. \tag{11}$$

Here the subscripts ''1'' and ''2'' mark the two media, and ε^l and ε^t are the longitudinal and transverse permittivities

$$\varepsilon^l(\omega,\mathbf{q}) = \varepsilon_0 + \frac{4\pi i}{\omega}\frac{q_i q_k}{q^2}\sigma_{ik}(\omega,\mathbf{q}); \tag{12}$$

$$\varepsilon^t(\omega,\mathbf{q}) = \varepsilon_0 + \frac{2\pi i}{\omega}\left(\delta_{ik} - \frac{q_i q_k}{q^2}\right)\sigma_{ik}(\omega,\mathbf{q});$$

$$\Delta(\omega,q_x) = \frac{1}{\varepsilon_2}\sqrt{q_x^2-(\omega^2/c^2)\varepsilon_2} + \frac{1}{\pi}\int_{-\infty}^{\infty}\frac{dq_y}{q^2} \times\left[\frac{q_x^2}{\varepsilon^l(\omega,\mathbf{q})} - \frac{\omega^2}{c^2}\frac{q_y^2}{q^2-(\omega^2/c^2)\varepsilon^t(\omega,\mathbf{q})}\right]. \tag{13}$$

The functions $L_{l,t}^{(0)}(\mathbf{q})$ and $M^{(0)}(\mathbf{q})$ are determined by the Fourier transforms of the electric and magnetic fields at the instant $t=0$:

$$L_l^{(0)}(\mathbf{q})=q_x[\mathbf{q}\cdot\mathbf{D}^{(0)}(\mathbf{q})]; \tag{14}$$

$$L_t^{(0)}(\mathbf{q})=\frac{\omega}{c}\,q_y\left[H_{z1}^{(0)}(\mathbf{q})+\frac{\omega}{c}\,\frac{q_xD_y^{(0)}(\mathbf{q})-q_yD_x^{(0)}(\mathbf{q})}{q^2}\right];$$

$$\mathbf{D}^{(0)}(\mathbf{q})=\varepsilon_0\mathbf{E}_1^{(0)}(\mathbf{q})-4\pi\mathbf{J}^{(0)}(\mathbf{q});$$

$$M^{(0)}(\mathbf{q})=q_x(\mathbf{q}\mathbf{E}_2^{(0)}(\mathbf{q}))+\frac{\omega}{c}\left[q_yH_{z2}^{(0)}(\mathbf{q})-\frac{\omega^2}{c^2}\,\varepsilon_2E_{x2}^{(0)}(\mathbf{q})\right]. \tag{15}$$

The initial fields in the two media and the initial distribution function $f^{(0)}(\mathbf{q},\mathbf{p})$ are connected through the Maxwell equations and the boundary conditions at the surface $y=0$ for $t=0$.

In formulas (10) and (11), the first terms in the brackets [proportional to $\exp(iq_yy)$] correspond to the space–time harmonics of the field in an unbounded homogeneous medium (in the plasma (10) and in the insulator (11)) created by the initial perturbation. The second terms in (10) and (11) describe the time harmonics of the field, which emerge as a result of reflection and refraction of spatial harmonics at the interface $y=0$. It can be seen that the evolution of the field is determined by singularities of the functions $\Delta(\omega),\varepsilon^l(\omega,\mathbf{q})$, and $\varepsilon^t(\omega,\mathbf{q})$ in the plane of the complex variable ω. (Following Landau,[1] we assume that the initial function of complex variables $\mathbf{p}$ is an integral function of $\mathbf{p}$, while the integral

$$\int_{-\infty}^{\infty}d\mathbf{p}\,\frac{f^{(0)}(\mathbf{q},\mathbf{p})}{\omega-\mathbf{q}\cdot\mathbf{v}+i\nu}, \tag{16}$$

continued analytically to the lower half-plane is an integral function of ω.)

In the general form, taking into account delay effects and thermal motion of electrons in the plasma, an analysis of formulas (10)–(16) is very complicated and cumbersome. For this reason, we consider the following special cases:

(1) potential oscillations ($c\to\infty, v_T\neq 0$);
(2) cold plasma ($v_T=0, c$ is a finite quantity).

SPACE–TIME DISTRIBUTION OF POTENTIAL OSCILLATIONS FIELDS FOR WEAK SPATIAL DISPERSION

In the limiting case $c\to\infty$, all the functions (14), and (15) can be expressed in terms of the initial distribution function $f^{(0)}(\mathbf{q},\mathbf{p})$ for conduction electrons. In this case, the fields (10) and (11) have the form

$$E_{1i}(t,y)=\frac{1}{2\pi}\int_{-\infty+i\sigma}^{\infty+i\sigma}d\omega e^{-i\omega t}\left[2e\int_{-\infty}^{\infty}\frac{dq_yq_ie^{iq_yy}}{q^2\varepsilon^l(\omega,\mathbf{q})}\right.$$
$$\times\int_{-\infty}^{\infty}d\mathbf{p}\,\frac{f^{(0)}(\mathbf{q},\mathbf{p})}{\omega-\mathbf{q}\cdot\mathbf{v}+i\nu}+\varepsilon_dE_x(\omega,q_x,0)\,\frac{1}{\pi}$$
$$\left.\times\int_{-\infty}^{\infty}dq_y\,\frac{q_ie^{iq_yy}}{q^2\varepsilon^l(\omega,\mathbf{q})}\right]\quad(i=x,y) \tag{17}$$

in the plasma ($y>0$) and

$$E_{2x}(t,y)=\frac{e^{q_xy}}{2\pi}\int_{-\infty+i\sigma}^{\infty+i\sigma}d\omega e^{-i\omega t}E_x(\omega,q_x,0);$$
$$E_{2y}(t,y)=-iE_{2x}(t,y) \tag{18}$$

in the insulator ($y<0$). Here and below, we assume that $q_x>0$. The electric field at the surface $E_x(\omega,q_x,0)$ is given by

$$E_x(\omega,q_x,0)=\frac{2eq_x}{\Delta(\omega)}\int_{-\infty}^{\infty}\int_{-\infty}^{\infty}\frac{dq_ydp f^{(0)}(\mathbf{q},\mathbf{p})}{q^2\varepsilon^l(\omega,\mathbf{q})(\omega-\mathbf{q}\cdot\mathbf{v}+i\nu)}, \tag{19}$$

$$\Delta(\omega)=1+\frac{q_x\varepsilon_d}{\pi}\int_{-\infty}^{\infty}\frac{dq_y}{q^2\varepsilon^l(\omega,\mathbf{q})}. \tag{20}$$

It can easily be seen that all singularities of the integrands in (17)–(20) are connected with the longitudinal permittivity $\varepsilon^l(\omega,\mathbf{q})$ which strongly depends on the form of the equilibrium function $f_0(\mathbf{p})$ and conditions of spatial dispersion.

Cold Plasma

Let us first consider the simplest case of cold plasma on the absence of spatial dispersion and for

$$f_0(\mathbf{p})=n_0\delta(\mathbf{p});\quad f^{(0)}(y,\mathbf{p})=n^{(0)}(y)\,\delta(\mathbf{p}), \tag{21}$$

where n_0 and $n^{(0)}(y)$ are the equilibrium and perturbed (at the instant $t=0$) electron concentrations, respectively. In this case,

$$\varepsilon^l(\omega,\mathbf{q})\equiv\varepsilon(\omega)=\varepsilon_0-\frac{\omega_0^2}{\omega(\omega+i\nu)},\quad \omega_0^2=\frac{4\pi e^2n_0}{m}$$

and the fields have the form

$$E_{1x}(t,q_x,y)=\frac{eq_x}{\pi}\int_{-\infty+i\sigma}^{\infty+i\sigma}\frac{d\omega e^{-i\omega t}}{\omega\varepsilon(\omega)}\int_{-\infty}^{\infty}dq_y\,\frac{n^{(0)}(q_y)}{q^2}$$
$$\times\left[e^{iq_yy}-\frac{\varepsilon_d}{\varepsilon_d+\varepsilon(\omega)}\,e^{-q_xy}\right](y>0); \tag{22}$$

$$E_{2x}(t,q_x,y)=\frac{eq_x}{\pi}\int_{-\infty+i\sigma}^{\infty+i\sigma}\frac{d\omega e^{-i\omega t}}{\omega[\varepsilon_d+\varepsilon(\omega)]}$$
$$\times\int_{-\infty}^{\infty}dq_y\,\frac{n^{(0)}(q_y)}{q^2}\,e^{q_xy}\quad(y<0). \tag{23}$$

In the plane of the complex variable ω, the singularities of the integrands in (22) and (23) are determined by the roots of equations $\varepsilon(\omega)=0$ and $\varepsilon_d+\varepsilon(\omega)=0$, which describe the volume (Langmuir) and surface oscillations in the structure under consideration. After integration with respect of ω, we obtain

$$E_{1x}(t,q_x,y)=-\frac{2ieq_x}{\varepsilon_0}\cos\,\omega_pt e^{-(\nu/2)t}$$
$$\times\int_{-\infty}^{\infty}dq_y\,\frac{n^{(0)}(\mathbf{q})}{q^2}\,(e^{iq_yy}-e^{-q_xy})$$

$$-\frac{2ieq_x}{\varepsilon_0+\varepsilon_d}\cos\,\omega_s t e^{-(\nu/2)t-q_x y}\times\int_{-\infty}^{\infty}\frac{n^{(0)}(\mathbf{q})}{q^2}\,dq_y\quad(y>0);\tag{24}$$

$$E_{2x}(t,q_x,y)=-\frac{2ieq_x}{\varepsilon_0+\varepsilon_d}\cos\,\omega_s t e^{-(\nu/2)t+q_x y}\times\int_{-\infty}^{\infty}\frac{n^{(0)}(\mathbf{q})}{q^2}\,dq_y\quad(y<0).\tag{25}$$

It follows from formula (24) that, along with the Langmuir volume oscillations of frequency $\omega_p=\omega_0/\sqrt{\varepsilon_0}$, the plasma exhibits two types of surface oscillations with different frequencies, viz., ω_p and

$$\omega_s=\frac{\omega_0}{\sqrt{\varepsilon_0+\varepsilon_d}},\tag{26}$$

ω_s being the frequency of a surface plasmon. Near the interface $y=0$, the electric fields of volume and surface oscillations at frequency $\omega=\omega_p$ are compensated. As a result, only the field of a surface plasmon at frequency ω_s (26) is formed in the insulator. Attenuation of the fields (24) and (25) is determined by the collision frequency ν.

Maxwellian Plasma

The inclusion of spatial dispersion of permittivity leads to the emergence of additional waves (as compared with cold plasma).

For a nondegenerate electron gas with the Maxwell distribution of the equilibrium function $f_0(\mathbf{p})$, analytic formulas (8) and (12) for the functions $\varepsilon^l(\omega,\mathbf{q})$ (see, for example, Ref. 2) and (20) for $\Delta(\omega,q_x)$ can be obtained only in the form of asymptotic expansions. In the collisionless limit ($\nu\to 0$)

$$\mathrm{Re}\;\varepsilon^l(\omega,\mathbf{q})=\varepsilon_0\left[1-\frac{\omega_p^2}{\omega^2}\left(1+\frac{3q^2v_T^2}{\omega^2}\right)\right],\quad \omega\gg qv_T;\tag{27}$$

$$\mathrm{Re}\;\varepsilon^l(\omega,\mathbf{q})=\varepsilon_0\left[1+\frac{1}{q^2r_d^2}\right],\quad \omega\ll qv_T\tag{28}$$

($v_T=\sqrt{T/m}$ is the thermal velocity of electrons, T the electron gas temperature, $r_d=v_T/\omega_p$ the Debye radius, and $q^2=q_x^2+q_y^2$), we have

$$\mathrm{Im}\;\varepsilon^l=\sqrt{\pi/2}\,\frac{\varepsilon_0\omega_p^2\omega}{q^3v_T^3}\exp\left(-\frac{\omega^2}{2q^2v_T^2}\right),\qquad |\mathrm{Im}\;\varepsilon^l|\ll|\mathrm{Re}\;\varepsilon^l|.\tag{29}$$

Henceforth, we shall assume that the conditions of weak spatial dispersion

$$\omega_p\gg q_xv_T\gg\nu.$$

In this case, the function $\Delta\omega$ (20) has the form[7]

$$\Delta(\omega,q_x)=\frac{\varepsilon_0+\varepsilon_d}{\varepsilon_0(\omega^2-\omega_p^2)}(\omega^2-\omega_s^2)+\frac{\varepsilon_d}{\varepsilon_0}q_xr_d-2i\sqrt{2/\pi}\,\frac{\varepsilon_d}{\varepsilon_0}\,\frac{\omega_p^3}{\omega^3}\,q_xr_d,\quad q_xr_d\ll 1.\tag{30}$$

It can easily be seen that, as a result of integration with respect to ω in formulas (17)–(19), the field becomes a superposition of oscillations with different frequencies: $\omega_n(\mathbf{q})$ (the roots of the equation $\varepsilon^l(\omega_n,\mathbf{q})=0$) and Ω_s [the root of the equation (30) $\Delta(\Omega_s,q_x)=0$]:

$$\mathrm{Re}\;\omega_n=\omega_p\left(1+\frac{3}{2}\,q^2r_d^2\right);\qquad \mathrm{Im}\;\omega_n=-\omega_p\sqrt{\pi/8}\,\frac{e^{-1/(2q^2r_d^2)}}{q^2r_d^2};\tag{31}$$

$$\mathrm{Re}\;\Omega_s=\omega_s\left[1+\frac{\varepsilon_d^2}{2\varepsilon_0(\varepsilon_0+\varepsilon_d)}\,q_xr_d\right];\qquad \mathrm{Im}\;Q_s=-\gamma_s=-\sqrt{2/\pi}\,\frac{\varepsilon_d^2}{\varepsilon_0^2}\,q_xv_T.\tag{32}$$

It should be noted that the plasma exhibits both volume [the first term in (17)] and surface oscillations with frequency $\omega_n(\mathbf{q})$ (31). An analytic expression for volume oscillations can be obtained knowing the specific form of the initial function $f^{(0)}(\mathbf{q},\mathbf{p})$. The field of surface oscillations with frequency ω_n is given by

$$E_{1x}^{(n)}(t,q_x,y)=\frac{2ieq_xr_d}{\varepsilon_0}\,e^{-q_xy}\int_{-1}^{1}d\xi\times\frac{\cos[\omega_pt+3/2\omega_pt\xi^2]e^{-\mathrm{Im}\;\omega_n(\xi)t}}{\xi^2+q_x^2r_d^2}\times\int\!\!\!\!\!\!-\,d\mathbf{p}\,\frac{f^{(0)}(\xi,\mathbf{p})}{1-\xi(v_y/v_T)}\tag{33}$$

(the symbol $\int\!\!\!\!\!\!-$ indicates the principal value of the integral, and $\xi=q_yr_d$). Let us consider surface oscillations with the frequency Ω_s (32). The corresponding field in the plasma can be written as

$$E_{1x}^{(s)}(t,q_x,y)=E^{(s)}(t,q_x)G(\Omega_s,q_x,y);\tag{34}$$

$$E^{(s)}(t,q_x)=2ieq_x\cos\,\Omega_s t e^{-\gamma_s t}\,\frac{\varepsilon_d\Omega_s}{\varepsilon_0+\varepsilon_d}\times\int_{-\infty}^{\infty}\frac{dq_y}{q^2\varepsilon^l(\Omega_s,\mathbf{q})}\int\!\!\!\!\!\!-\,d\mathbf{p}\,\frac{f^{(0)}(\mathbf{q},\mathbf{p})}{\Omega_s-\mathbf{qv}}.\tag{35}$$

The Green's function $G(\omega,q_x,y)$ describes the spatial field distribution

$$G(\omega,q_x,y)=\frac{q_x}{\pi}\int_{-\infty}^{\infty}\frac{dq_y e^{iq_yy}}{q^2\varepsilon^l(\omega,\mathbf{q})}.\tag{36}$$

Considering that for $\nu\to 0$ the contribution to $\varepsilon^l(\omega,\mathbf{q})$ [see (8) and (12)] from resonant particles for which $\mathbf{q}\cdot\mathbf{v}=\omega$ (Landau damping) is smaller than the contribution from nonresonant particles, we can represent $G(\omega,q_x,y)$ in the form of an expansion in the small parameter $|\mathrm{Im}\;\varepsilon^l(\omega,\mathbf{q})/\mathrm{Re}\;\varepsilon^l(\omega,\mathbf{q})|$. As a result, we obtain for the case of weak spatial dispersion

$$G(\Omega_s,q_x,y)=\frac{1}{\varepsilon(\Omega_s)}\,\mathrm{e}^{-q_xy}+\frac{q_xr_d}{\varepsilon_0}\,\mathrm{e}^{-y/r_d}$$
$$-\frac{i\omega_0q_x}{\sqrt{2\pi}\varepsilon^2(\Omega_s)v_T^3\Omega_s^3}$$
$$\times\int_{-\infty}^{\infty}dv_y|v_y|^3\mathrm{e}^{-v_y^2/2v_T^2+i(\Omega_s/v_y)y}. \quad (37)$$

The first term in this equation is the contribution from the pole $q^2=0$ to integral (36) and describes, as in cold plasma, the penetration of the longitudinal–transverse field associated with the collective behavior of electrons. The second term is the result of inclusion of the pole $\varepsilon^l(\omega,\mathbf{q})=0$ for large values of $q_y\gg 1/r_d$ [see the asymptotic expansion (28)]. The third term G_3 characterizes the ballistic transport of the field by charged particles along the y-axis (Van Kampen waves).[8] It can be estimated for large values of y

$$y\gg 1/q_x\gg r_d, \quad (38)$$

by using the steepest descent method

$$G_3(\Omega_s,q_x,y)=i\,\frac{\omega_0^2q_xy}{\sqrt{3}\Omega_s^2\varepsilon^2(\Omega_s)}\,\mathrm{e}^{-(3/4)(\Omega_sy/v_T)^{2/3}}$$
$$\times\cos\left[\frac{3\sqrt{3}}{4}\left(\frac{\Omega_sy}{v_T}\right)^{2/3}-\frac{2\pi}{3}\right]. \quad (39)$$

This expression shows that electrons form a field which decreases at large distances (38) according to an exponential law with $y^{2/3}$ in the exponent and contains, along with attenuating term, an oscillating term. At distance $y>(3/4)^3\Omega_s^2/(q_x^3v_T^2)$ this field is stronger than the field described by the first term in (37) and will be referred to as the field of anomalous penetration at the frequency Ω_s of surface plasmons. The smallness of its amplitude is determined by the following two factors. First, it is due to the smallness of the dissipative component of permittivity Im ε^l. Second, the ballistic transport involves all electrons with velocities $0<v_y<\infty$, which resonantly interact with various spatial harmonics of surface plasmons and create fields with various phases in the bulk of the plasma. Expression (39) is the result of interference of these fields.

A comparison of the expressions for fields and damping decrements of surface oscillations with different frequencies ω_n (33) and Ω_s (34)–(37) (with the same penetration depth equal to $1/q_x$) shows that the amplitude $E_{1x}^{(n)}$ is smaller than the amplitude $E_{1x}^{(s)}$, but the lifetime of oscillations with frequency ω_n is longer.

The field of surface oscillations in the insulator $y<0$ is described by the formula

$$E_{2x}(t,q_x,y)=\frac{6ieq_xr_d}{\varepsilon_d}\,\mathrm{e}^{q_xy}\int_{-1}^{1}d\xi\,\cos\left(\omega_p^t+\frac{3}{2}\,\omega_pt\xi^2\right)$$
$$\times\mathrm{e}^{-\mathrm{Im}\,\omega_n(\xi)t}\oint\frac{d\mathbf{p}f^{(0)}(\xi,\mathbf{p})}{1-(v_y/v_T)\xi}+E^{(s)}(t,q_x)\mathrm{e}^{q_xy}. \quad (40)$$

The field is a superposition of oscillations with different frequencies ω_n and Ω_s attenuating at the depth $1/q_x$ along the y-axis.

Degenerate Plasma

In the case of a degenerate plasma with the Fermi distribution function, the permittivity is given by[5]

$$\mathrm{Re}\;\varepsilon^l=\varepsilon_0\left\{1+\frac{3\omega_p^2}{q^2v_F^2}\left[1-\frac{1}{2}\,\frac{\omega}{qv_F}\ln\frac{\omega+qv_F}{\omega-qv_F}\right]\right\}; \quad (41)$$

$$\mathrm{Im}\;\varepsilon^l=\begin{cases}\varepsilon_0\,\dfrac{3\pi}{2}\,\dfrac{\omega_p^2\omega}{q^3v_F^3}, & -qv_F<\omega<qv_F;\\ 0, & |\omega|>qv_F\end{cases} \quad (42)$$

(v_F is the Fermi velocity of electrons). The function $\Delta(\omega)$ differs from expression (30) only in the imaginary component and the definition of r_d

$$\mathrm{Im}\;\Delta(\omega)=-\frac{3}{4}\,\frac{\omega_p^2}{\varepsilon_0\omega^3}\,q_xv_F; \quad r_d=\frac{v_F}{\sqrt{3}\omega_p}. \quad (43)$$

In formula (17) for the field in the plasma, we must take into account in the integration with respect to ω the contribution from the branching points of the function $\varepsilon^l(\omega,\mathbf{q})$ (41) in addition to the contributions from poles (31) and (32). As a result, the field in the plasma is the superposition of the fields

$$E_{1x}(t,q_x,y)=E_{1x}^{(n)}(t,q_x,y)+E_{1x}^{(s)}(t,q_x,y)$$
$$+E_{1x}^{(p)}(t,q_x,y),$$

where $E_{1x}^{(n)}$ and $E_{1x}^{(s)}$ are described by formulas (33) and (35). The imaginary part of $G(\omega,q_x,y)$ (36) in the component $E_{1x}^{(s)}$, which is determined by Im $\varepsilon^l(\omega,\mathbf{q})$, has a form differing from that in (37) and is negligibly small for large values of $y\gg r_d$. Thus, for a degenerate gas we have

$$G(\Omega_s,q_x,y)=\frac{1}{\varepsilon(\Omega_s)}\,\mathrm{e}^{-q_xy}+\frac{q_xr_d}{\varepsilon_d}\,\mathrm{e}^{-y/r_d}.$$

In order to calculate the field $E_{1x}^{(p)}(t,q_x.y)$, we must include the integration over the banks of the cut along the real axis (qv_F,∞) and $(-qv_F,-\infty)$. The contribution from the branching points of permittivity (41) was considered for the first time by Silian[9] who solved the initial problem for the longitudinal field in an unconfined degenerate electron gas. However, the integration over the banks of the cut in the confined structure under investigation differs considerably from the one-dimensional case[9] in the possibility to calculate the field distribution in space. The two-dimensional nature of the wave vector leads to the emergence of two terms with oscillating factors in the integrands of integrals with respect to q_y in (17):

$$\exp\pm i[q_yy-v_Ft\sqrt{q_x^2+q_y^2}]; \quad (44)$$

$$\exp\pm i[q_y+v_Ft\sqrt{q_x^2+q_y^2}]. \quad (45)$$

The main contribution to field $E_{1x}^{(p)}$ we comes from the terms proportional to exponents (44) since the method of stationary phases for large values of the parameters

$$tv_F q_x \gg 1 \tag{46}$$

(the remaining terms are smaller by a factor of $\sqrt{tv_F q_x}$). The stationary phase point is defined as

$$q_{y1} = q_x \frac{y}{\sqrt{t^2 v_F^2 - y^2}}. \tag{47}$$

At distances y smaller than the electron path traversed over the time t, i.e.,

$$tv_F > y \gg \frac{1}{q_x}, \tag{48}$$

the field $E_{1x}^{(p)}$ is oscillating:

$$E_{1x}^{(p)}(t,q_x,y) = i \frac{4\sqrt{2}}{3^{3/4}\pi\sqrt{\pi}} \sqrt{q_0 r_d} \frac{\omega^{(0)} E_x(\omega_0, q_x, 0)}{(\omega_p t)^{3/2}} \times \cos\left[q_x \sqrt{t^2 v_F^2 - y^2} + \frac{\pi}{4} \right],$$

$$\omega^{(0)} = q_0(t,y) v_F \ll \omega_p, \tag{49}$$

$$q_0(t,y) = q_x \frac{tv_F}{\sqrt{t^2 v_F^2 - y^2}}.$$

In the case when the inequality opposite to the left inequality in (48) is satisfied, the field $E_{1x}^{(p)}(t,q_x,y)$ attenuates exponentially ($E_{1x}^{(p)} \sim \exp[-q_x \sqrt{y^x - t^2 v_F^2}]$).

It should be noted that the anomalous penetration field (49) is of a different physical origin as compared to the oscillating field in a Maxwellian plasma (39) since it is associated with the nondissipative component of permittivity $\mathrm{Re}\,\varepsilon^l(\omega,\mathbf{q})$. Ballistic transport of the field energy involves all electrons drifting from the surface to the bulk of the plasma and interacting with a large set of space–time harmonics of the field. In view of the sharp boundary in the Fermi velocity distribution for electrons, a group of particles in the vicinity of the maximum values of $v_y \simeq v_F$ plays the major role in this process (the contributions of the remaining particles are mutually compensated). The smallness of the amplitude of the field $E_{1x}^{(p)}$ is of a power nature and is determined by the small number of electrons in this group.

Until now, we assumed that integral (16) in formulas (17)–(19) describes an integral function of the complex variable ω in the lower half-plane. Generally speaking, the function (16) can have a number of singularities for $\omega = \omega_r$, whose position in the plane ω depends only on the form of the initial perturbation and is not associated with the properties of equilibrium plasmas. The field determined by the singularities of the function (16) contains terms of the type $E_r(y,q_x) \mathrm{e}^{-\mathrm{Im}\,\omega_r t - i\,\mathrm{Re}\,\omega_r t}$, and can be regarded as the field of perturbed oscillations.

SPACE–TIME STRUCTURE OF FIELDS IN THE INSULATOR TAKING INTO ACCOUNT DELAY EFFECTS

Let us trace the evolution and analyze the distribution of electromagnetic fields in the insulator taking into account delay effect and field penetration from the cold plasma. In the case of a cold plasma, $\varepsilon^t(\omega,\mathbf{q}) = \varepsilon^l(\omega,\mathbf{q}) = \varepsilon(\omega)$. in the expression (11) for the field. It is convenient to analyze the function $E_{2x}(t,y)$ (11) as the sum of three terms $E_{2x} = \sum_{i=1,2,3} E_x^{(i)}(t,q_x,y)$. The first term $E_x^{(1)}$ is the field of a volume wave with the frequency

$$\omega_k(q) = \frac{cq}{\sqrt{\varepsilon_2}}, \tag{50}$$

which is created by the initial perturbation in the insulator (the first term in formula (11)). The expression $E_x^{(2)} \times (t,q_x,y)$ is described by the last term in the brackets in (11) and determines the field of the wave associated with the initial perturbation (15) in the insulator. The third term $E_x^{(3)} \times (t,q_x,y)$ associated with the penetration of the wave from the plasma to the insulator and having the form

$$E_x^{(3)}(t,q_x,y) = \frac{i}{(2\pi)^2 \varepsilon_2} \int_{-\infty+i\sigma}^{\infty+i\sigma} d\omega \frac{\sqrt{q_x^2 - (\omega^2/c^2)\varepsilon_2}}{\omega\varepsilon(\omega)\Delta(\omega)} \times \mathrm{e}^{-i\omega t - |y|\sqrt{q_x^2 - (\omega^2/c^2)\varepsilon_2}} \times \int_{-\infty}^{\infty} dq_y \frac{P^{(0)}(\mathbf{q})}{q^2 - (\omega^2/c^2)\varepsilon(\omega)},$$

$$P^{(0)}(\mathbf{q}) = \frac{\omega}{c} \varepsilon(\omega) \left[q_y H_{z1}(0)(\mathbf{q}) - \frac{\omega}{c} \varepsilon_0 E_{x1}^{(0)}(\mathbf{q}) \right] + q_x \varepsilon_0 [\mathbf{q} \cdot \mathbf{E}_1^{(0)}(\mathbf{q})], \tag{51}$$

is the combination of the functions (14) in which $\mathbf{J}^{(0)}(\mathbf{q}) = 0$. The integral representation of the field $E_x^{(1)}$ has only one singularity in the space of the complex variable ω, viz., the pole (50). The integrand for the field $E_x^{(2)}$ contains in the ω plane the poles and branching points of the function $\Delta(\omega)$ apart from the pole (50). For a cold plasma, we have

$$\Delta(\omega) = \sqrt{q_x^2 - (\omega^2/c^2)\varepsilon_2} + \frac{\varepsilon_2}{\varepsilon(\omega)} \sqrt{q_x^2 - (\omega^2/c^2)\varepsilon(\omega)}. \tag{52}$$

The poles

$$\Delta(\omega_{ni}) = 0 \tag{53}$$

appear under the condition $\varepsilon(\omega_{ni}) < 0$, while ω_{ni} describes the frequency and attenuation of a surface polariton. Expression (52) has two types of branching points: the points on the real axis

$$\omega_{1,2} = \pm \frac{cq_x}{\sqrt{\varepsilon_2}} \tag{54}$$

and the complex branching points $\omega = \omega_{3,4}$

$$\text{Re } \omega_{3,4} = \pm \sqrt{\omega_p^2 + c^2 q_x^2/\varepsilon_0};$$

$$\text{Im } \omega_{3,4} = -\frac{\nu \omega_p^2}{2(\text{Re } \omega_3)^2}. \tag{55}$$

In the expression for $E_x^{(2)}$, we go over in the plane ω from integration in the limits $(-\infty + i\sigma, \infty + i\sigma)$ to a closed contour including the segment $(-R + i\sigma, R + i\sigma)$, a semicircle of radius $R \to \infty$ in the lower half-plane, and rectilinear segments along the line of the cut $(-cq_x/\sqrt{\varepsilon_2}, cq_x/\sqrt{\varepsilon_2})$, $(\omega_3, \infty + \text{Im } \omega_3)$ and $(-\infty + i \text{ Im } \omega_4, \omega_4.)$ The singularities of the integrand in the third field term $E_x^{(3)}$ are the poles, viz., the roots of the equation

$$\omega_l^2 \varepsilon(\omega_l) = c^2 q^2, \tag{56}$$

the poles $\omega = \omega_{ni}$, and the branching points (54) and (55). In this case, it is more convenient to choose the integration contour so that it includes the lines of the cut $(\infty, cq_x/\sqrt{\varepsilon_2})$, $(\infty, cq_x/\sqrt{\varepsilon_2})$, and (ω_3, ω_4). The integrals with respect to ω along the lines of the cut in the terms $E_x^{(2)}$ and $E_x^{(3)}$ can be evaluated asymptotically by using the stationary phase method for large values of the parameter $q_x ct/\sqrt{\varepsilon_2}$. As a result, we find that the insulator exhibits oscillations of a different origin along with the known modes, viz., the volume wave of frequency $\omega_k(q)$ (50) and the surface polariton of frequency ω_{ni} (53). One of these is the contribution from poles (56) to the integrals with respect to ω and is associated with the penetration of the field of volume wave ω_l from a semiconductor to an insulator. It can be written in the form of the integral with respect to q_y:

$$\begin{aligned} E_{xv} &= E_x^{(+)} + E_x^{(-)}, \\ E_{xv}^{(\pm)} &= -\frac{1}{4\pi\varepsilon_0\varepsilon_2} \int_{-\infty}^{\infty} dq_y \frac{\sqrt{q_x^2 - (\omega^2/c^2)\varepsilon_2}}{q^2 \Delta(\pm\omega_l)} P^{(0)} \\ &\quad \times \exp\left(\pm i\omega_l(q_y)t - i \frac{|y|}{c} \sqrt{\omega_l^2 \varepsilon_2 - q_x^2 c^2} \right). \end{aligned} \tag{57}$$

The field of the second type is the result of evaluation of integrals with respect to ω and q_y along the banks of the cut in the plane of the complex variable ω. This field is formed by oscillations emerging in the insulator as well as those penetrating into it from the plasma. For large values of the parameter $ct/\sqrt{\varepsilon_2} > y > 1/q_r$, this field has the form

$$\begin{aligned} E_{xr}(t,y) &= \frac{\Theta(ct/\sqrt{\varepsilon_2} - y)}{\sqrt{q_x ct/\varepsilon_2}} [A(P^{(0)}, t, y) + B(M^{(0)}, t, y)] \\ &\quad \times \cos\left[q_x \sqrt{c^2 t^2/\varepsilon_2 - y^2} + \frac{3\pi}{4} \right] \end{aligned} \tag{58}$$

($\Theta(x)$ is the Heaviside function, $\Theta(x>0) = 1$; $\Theta(x<0) = 0$).

CONCLUSIONS

Thus, we have obtained a comprehensive spectrum of eigenfrequencies of the electric field in a plasma and a nondissipative nondispersive medium (vacuum or insulator) bordering it. The set of eigenfrequencies of such a system is determined by the singularities of the electron distribution function in the equilibrium and perturbed states. In a cold plasma with a perturbed initial electron concentration, which is distributed in the entire half-space, surface and volume oscillations at the Langmuir frequency ω_p exist along with the surface oscillations at the frequency ω_s (26). The amplitudes and phases of partial fields with frequency ω_p are mutually compensated near the interface between the media, and the field with such a frequency does not penetrates the insulator. In the vacuum, field oscillations occur only at the frequency ω_s. If the perturbed electron concentration is localized at the interface at the initial instant, the oscillations in the insulator as well as in the plasma exist only at the frequency ω_s of a surface plasmon.

In a Maxwellian plasma with an electron distribution function perturbed at the initial instant of time in the entire half-space, partial fields do not compensate one another at the interface in view of dispersion of Langmuir oscillations. For this reason, surface oscillations emerge in the insulator and in the plasma not only at the frequency ω_s, but also at the frequency ω_n (31). The damping decrement of these oscillations has the same form as the Landau damping in a nonconfined plasma. This is not surprising since the entire set of plasma oscillations of frequencies $\omega_n(q)$ is emitted to the insulator at the boundary.

In the presence of thermal motion of electrons, the plasma becomes transparent at frequency $\omega_s (\omega_s < \omega_p)$ owing to ballistic transport of the energy of surface plasmons by charges to the bulk of the plasma. In other words, volume waves (Van Kampen waves) are excited as a result of the Cherenkov resonance between electrons and spatial harmonics of surface plasmons. The phase velocities of these waves coincide with the velocity of particles along the normal to the surface. The field of the surface plasmon is transformed at the boundary into the field of volume waves. The interference of these waves with different q_y leads to an anomalous penetration effect, in which the resultant field penetrates the plasma to distances much larger than the penetration depth of surface plasmons in a cold plasma. The field amplitude in this case is an oscillating function of the coordinate y.

Anomalous penetration of the electric field is also observed in a degenerate plasma. However, the physical origin of this effect differs completely from the case of a Maxwellian plasma. First, the effect is associated with the nondissipative component of permittivity $\text{Re } \varepsilon_l$ rather than with the dissipative component for which the condition $|\text{Im } \varepsilon_l| \ll |\text{Re } \varepsilon_l|$ in the collisionless limit. For this reason, the amplitude of the field in the degenerate plasma is larger than in a Maxwellian plasma. Second, electrons interact with a large set of space– time harmonics of the field, and there is no mechanism of frequency selection. As a result, the period of oscillations is a function of two parameters: the coordinate y and the time t. In a nondegenerate plasma, the dependences on the parameters y and t are separated.

If we take into account the delay effects in the cold plasma–insulator structure, the field in the insulator is a superposition of the fields of the surface polariton (53), volume oscillations of frequencies ω_k (50) and ω_l (56), and the oscillating field (58).

*E-mail: beletski@ire.kharkov.ua

[1] L. D. Landau, Sov. Phys. JETP **16**, 574 (1946).
[2] V. P. Silin and A. A. Rukhadze, *Electromagnetic Properties of Plasma and Plasma-like Media* [in Russian], Gosatomizdat, Moscow (1961).
[3] A. I. Akhiezer, I. A. Akhiezer, R. V. Polovin *et al.*, *Electrodynamics of Plasma*, Pergamon, Oxford (1975).
[4] Yu. A. Romanov, Izv. Vuzov, Radiofizika **7**, 242 (1964).
[5] A. F. Aleksandrov, L. S. Bogdankevich and A. A. Rukhadze, *Oscillations and Waves in Plasma Media* [in Russian], MGU, Moscow (1990).
[6] B. B. Kadomtsev, *Collective Phenomena in Plasma* [in Russian], Nauka, Moscow (1976).
[7] V. L. Falko, S. I. Khankina, and V. M. Yakovenko, Fiz. Nizk. Temp. **22**, 1147 (1996) [Low Temp. Phys. **22**, 877 (1996)].
[8] N. G. Van Kampen, Physica (Amsterdam) **21**, 949 (1955).
[9] V. P. Silin, Fiz. Met. Metalloved. **10**, 942 (1960).

Translated by R. S. Wadhwa

LOW-DIMENSIONAL AND DISORDERED SYSTEMS

Magnetostructural topological defects in two-dimensional antiferromagnets

O. K. Dudko*

Kharkov State University, 310077 Kharkov, Ukraine; B. Verkin Institute for Low Temperature Physics and Engineering, National Academy of Sciences of the Ukraine, 310164 Kharkov, Ukraine

A. S. Kovalev

B. Verkin Institute for Low Temperature Physics and Engineering, National Academy of Sciences of the Ukraine, 310164 Kharkov, Ukraine

(Submitted December 22, 1997)
Fiz. Nizk. Temp. **24**, 559–570 (June 1998)

A two-dimensional model generalizing the Peierls model to the case of coupled fields of magnetization and elastic displacement distribution is proposed for describing the structure of a complex magnetoelastic topological defect which has the form of the bound state of a dislocation and a magnetic disclination in an antiferromagnet. The obtained system of nonlinear one-dimensional integro-differential equations has solutions for magnetic vortices and for magnetic disclinations connected with dislocations and having regular asymptotic forms at large distances and no singularities at the core of the topological defect. © *1998 American Institute of Physics.* [S1063-777X(98)00706-3]

INTRODUCTION

Various types of nonlinear excitations in magnetically ordered media have been investigated recently both theoretically and experimentally.[1] The variety of existing magnetic structures is responsible for a wide range of such excitations: nonlinear spin waves, domain walls, dynamic magnetic solitons, magnetization rotation waves, etc. ''Topological magnetic solitons'' form a special class of localized states of magnets.[2] Thoroughly investigated domain walls (DW) can be regarded as the simplest one-dimensional form of such objects. Multidimensional magnetic topological excitations such as two-dimensional magnetic vortices (MV), magnetic disclinations (MD) and frustrations, Bloch lines in domain walls, Bloch points and three-dimensional topological solitons have a more complex structure.[1] An analysis of magnetic vortices and disclinations has become especially important in view of the development of new layered, quasi-two-dimensional, and two-dimensional magnets in which the magnetic order is broken due to the formation of a large number of two-dimensional topological defects (Kosterlitz–Thouless mechanism). Since the number of structural topological defects (two-dimensional analogs of dislocations) in two-dimensional systems must also be anomalously large, the question concerning the interaction of these two types of defects naturally arises. This interaction in ferromagnets (FM) is determined by weak magnetoelastic coupling which can be taken into account in perturbation theory. However, most existing two-dimensional magnets are antiferromagnets (AFM) in which the ordinary weak magnetoelastic interaction is accompanied by an additional strong interaction between the elastic and magnetic subsystems, which is of topological type and is determined by the multisublattice structure of the AFM (different sizes of magnetic and crystal cells). Such a ''topological interaction'' leads to coupling between dislocations and magnetic disclinations or domain walls. This fact was indicated qualitatively for the first time in Refs. 3 and 4 on the basis of simple geometrical considerations. Later,[5] a simple one-dimensional model was proposed, which generalized the well-known Frenkel–Kontorova model for coupled fields of elastic displacements around a dislocation and the field magnetization distribution around the MD core. This model made it possible to describe qualitatively a complex magnetostructural topological defect (MSTD), but lead to wrong asymptotic forms of the fields at large distances from the defect core in view of its one-dimensional nature.

It has been established that the topological coupling between dislocations and domain walls in an antiferromagnet can lead to important physical consequences, i.e., a change in the dislocation density, and hence in plastic properties of crystals, and the emergence of specific intrinsic modes in the crystals during the magnetic phase transition to the antiferromagnetic state. For this reason, it is necessary to study in greater detail the magnetostructural defects theoretically on the basis of more adequate two-dimensional models. An example of such an approach using numerical calculations was presented by Ivanov *et al.*[6]

Here, we propose a simple two-dimensional model generalizing the well-known two-dimensional Peierls model[7] to the case of coupled fields of atomic displacements and magnetization and generalizing the one-dimensional model proposed earlier[5] to the two-dimensional case. Using this model, we obtained a system of two coupled one-dimensional integro-differential equations permitting analytical investiga-

tion. We obtained approximate solutions of these equations, describing the distribution of displacements and magnetization around a magnetostructural topological defect (MSTD), having no singularities at the defect core, and possessing correct asymptotic forms at large distances from the center. We also obtained exact solutions for MV, which describe their structure adequately at large as well as at small distances from the vortex core.

1. CONTINUAL MODELS OF TOPOLOGICAL DEFECTS IN TWO-DIMENSIONAL ELASTIC AND MAGNETICALLY ORDERED SYSTEMS

1.1. Dislocation in the continual theory of elasticity

In the description of the elastic subsystem, we confine ourselves to the scalar model of the crystal, assuming that only one component of the displacement vector differs from zero. Let us consider the two-dimensional elastic plane (xz) in which lattice atoms are labeled by two indices: n (x-coordinate) and m (z-coordinate). We denote by u_{nm} the displacement of the nmth atom from the equilibrium position. Then the potential energy of elastic interaction of atoms can be reduced to

$$U_1=\sum_{nm}\left[\frac{\alpha}{2}(u_{nm}-u_{n-1,m})^2+\frac{\beta}{2}(u_{nm}-u_{n,m-1})^2\right], \quad (1)$$

where α and β are the constant of elastic interaction along the directions x and z, respectively. In the long-wave limit, the dynamic equations for $u(x,z,t)$ have the form

$$mu_{tt}-\alpha a^2u_{xx}-\beta b^2u_{zz}=0, \quad (2)$$

where a and b are lattice constants in the directions x and z, and m is the mass of an atom.

A static dislocation corresponds to the following solution of this equation[7]:

$$u(x,z)=\frac{a}{2\pi}\arctan\left(\frac{z}{x}\,\zeta\right), \quad (3)$$

where $\zeta=(a/b)\sqrt{\alpha/\beta}$ (for definiteness, we assume that the x-component of the displacement vector differs from zero, and the Burgers vector coincides with the lattice constant a along the x-axis).

Solution (3) correctly describes the distribution of the displacement field at large distances from the defect center $(x=z=0)$, where deformations are small:

$$\frac{\partial u}{\partial z}=\frac{a}{2\pi}\frac{x\zeta}{x^2+z^2\zeta^2}, \quad (4)$$

$$\frac{\partial u}{\partial x}=-\frac{a}{2\pi}\frac{z\zeta}{x^2+z^2\zeta^2}. \quad (5)$$

However, this solution has a singularity at the dislocation center and does not describe the structure of the dislocation core.

1.2. Magnetic vortex in the continual model

Let us consider a perfect AFM without dislocations. Since most quasi-two-dimensional and layered AFM possess one-ion anisotropy of the type of the easy magnetization plane, we consider an easy-plane, strongly anisotropic AFM. Such a medium can contain topological solitons of the MV type.[1] According to the results of numerical calculations, all spins in such nonuniform states lie in the easy plane when the easy-plane anisotropy exceeds a certain critical value.[8] The local state of magnetization in this case is characterized by only one quantity, viz., the azimuthal angle of spin rotation at a given point. In other words, such a system can be described by a scalar model. Moreover, we shall assume for simplicity that magnetic anisotropy in the easy plane is equal to zero.

We denote the deviation of the spin of the nmth atom in the xz plane from the direction of the z-axis by φ_{nm}. Then the potential energy of magnetic interaction in the classical Heisenberg model can be written in the form

$$W=M_0^2\sum_{nm}\left[J_1\cos(\varphi_{nm}-\varphi_{n-1,m})+J_2\cos(\varphi_{nm}-\varphi_{n,m-1})\right], \quad (6)$$

where M_0 is the magnetic moment and J_1 and J_2 are exchange interaction constants in the directions of the x- and z-axes, respectively ($J_i>0$ in the case of AFM).

In order to take into account antiferromagnetic ordering (which is ''staggered' in the xz plane), it is convenient to introduce (instead of the variables φ_{nm}) the new variables ψ_{nm}:

$$\varphi_{nm}=\begin{cases}\psi_{nm}, & n+m=2s\\ \pi+\psi_{nm}, & n+m=2s+1\end{cases}, \quad (7)$$

where s is an integer. Then expression (6) in the long-wave approximation leads to the following form of the dynamic equation for the quantity $\psi(x,z,t)$:

$$\mu\psi_{tt}-M_0^2J_1a^2\psi_{xx}-M_0^2J_2b^2\psi_{zz}=0, \quad (8)$$

where $\mu=\hbar^2/4\mu_0^2\gamma$ is the effective mass of magnetic moment[5] (γ is the easy-plane anisotropy constant and μ_0 Bohr's magneton).

A static MV corresponds to the following solution of this equation:

$$\psi(x,z)=\arctan\left(\frac{z}{x}\,\xi\right), \quad (9)$$

where $\xi=(a/b)\sqrt{J_1/J_2}$. This solution describes a MV for which a circumvention around its center $(x=z=0)$ along a closed loop leads to rotation of spins through 2π (by analogy with the physics of liquid crystals, such a defect can be referred to as a magnetic disclination with the Frank index $k=2$).

Solution (9) correctly describes the magnetization distribution away from the center of the vortex:

$$\frac{\partial\psi}{\partial z}=\frac{x\xi}{x^2+z^2\xi^2}, \quad (10)$$

$$\frac{\partial\psi}{\partial x}=-\frac{z\xi}{x^2+z^2\xi^2}. \quad (11)$$

However, the long-wave approximation becomes inapplicable at the center of the vortex, where the discreteness effects are significant.

2. PEIERLS MODELS FOR DISLOCATION AND MAGNETIC VORTEX

2.1. Dislocation in Peierls model

The one-dimensional Frenkel–Kontorova model is the simplest model that provides a correct description for the dislocation core and takes into account the discreteness of the lattice at the core. In this model, elastic subspaces ''above'' the dislocation slip plane ($z>0$) and ''below'' it ($z<0$) are replaced by two elastic chains whose interaction takes into account the discreteness of the lattice and the periodic nature of the potential of interactions between particles. This potential is usually chosen in the form of a trigonometric function

$$U=\beta\,\frac{a^2}{4\pi^2}\left\{1-\cos\left[\frac{2\pi(u_+-u_-)}{a}\right]\right\}, \tag{12}$$

where $u_+(x)$ and $u_-(x)$ are the displacements of atoms in the upper ($z>0$) and lower ($z<0$) chains (in the long-wave approximation). The amplitude of the potential is chosen so that it matches with formula (1) in the linear limit. The equation for the difference $w=u_+(x)-u_-(x)$ of displacements in the upper and lower chains emerging in this model has the form of a static sinusoidal Klein–Gordon equation. The solution of this equation corresponding to a dislocation[7] has no singularity at the center of the dislocation and correctly describes the structure of its core. However, at large distances the fields decrease according to an exponential rather than a power law (see Eqs. (3)–(6)) in view of the one-dimensional nature of the model.

Peierls proposed a two-dimensional generalization of the Frenkel–Kontorova model, in which the solution for a dislocation has no singularity at the center of the dislocation and correctly describes the field distribution away from the core.[7]

We shall consider below an analog of the Peierls model for a vortex in an easy-plane magnet (in Sec. 2.2) and the generalization of this model for coupled fields of elastic displacements and magnetization (in Sec. 3). Here, we shall briefly describe the derivation of Peierls results for a simple scalar model, which differs slightly from that usually presented in monographs and in the original work by Peierls.

Let us consider an elastic plane containing a dislocation at the point $x=z=0$. The dislocation slip line (the line $z=0$) divides the plane into two half-spaces in which relative displacements of atoms are small in the case of strong anisotropy ($\alpha\gg\beta$), and the long-wave description of solutions on the basis of the differential equations (2) is possible. However, the displacement along the dislocation slip line at the boundary between the upper half-space [$u_+=u(z=+0)$] and the lower half-space [$u_-=u(z=-0)$] can differ by a value of the order of interatomic distance a. Consequently, we can describe the interaction between the boundaries of the half-spaces by using expression (12) employed in the Frenkel–Kontorova model.

In the static case, Eq. (2) can be reduced to the Laplace equation, and the solution of the Neuman problem for the scalar field $u(x,z)$ in the half-spaces $z>0$ and $z<0$ can be reduced to the following relation between the field $u(x,z)$ in the bulk and the strain $\partial u/\partial z|_{z=\pm 0}$ at the surface[9]:

$$u(x,z\gtrless 0)=\pm\frac{b}{2\pi a}\left(\frac{\beta}{\alpha}\right)^{1/2}\int_{-\infty}^{+\infty}dx'\left(\frac{\partial u}{\partial z}\right)\Bigg|_{z=\pm 0}\times\ln\left[\frac{(x-x')^2}{\alpha a^2}+\frac{z^2}{\beta b^2}\right], \tag{13}$$

while the relation between strain components at these surfaces is defined by the simple relation

$$\left.\frac{\partial u}{\partial x}\right|_{z=\pm 0}=\mp\left(\frac{\beta}{\alpha}\right)^{1/2}\frac{b}{a}\,\hat{H}\left(\frac{\partial u}{\partial z}\right)\Bigg|_{z=\pm 0}, \tag{14}$$

where the notation

$$\hat{H}F=\frac{1}{\pi}\int dx'\,\frac{F(x')}{(x'-x)} \tag{15}$$

typical of the Hilbert transformation of the function $F(x)$ has been introduced.

Using the property of skew symmetry of the $\hat{H}$-transformation and relation (14), we can easily connect the stresses at interfaces with longitudinal strains on them:

$$\sigma|_{z=\pm 0}=\beta b\left(\frac{\partial u}{\partial z}\right)\Bigg|_{z=\pm 0}=\pm(\alpha\beta)^{1/2}a\hat{H}\left(\frac{\partial u}{\partial x}\right)\Bigg|_{z=\pm 0}. \tag{16}$$

Equating these expressions to the forces at the interface determined from formula (12), i.e.,

$$f_\pm=\mp\frac{\beta\alpha}{2\pi}\sin\frac{2\pi w}{a}, \tag{17}$$

and subtracting the obtained relations from one another, we arrive at the final integro-differential equation for the relative displacements $w=u_+-u_-$ on the dislocation slip line:

$$\sin\frac{2\pi w}{a}=\pi\left(\frac{\alpha}{\beta}\right)^{1/2}\hat{H}\left(\frac{\partial w}{\partial x}\right). \tag{18}$$

For convenience, we go over to the dimensionless coordinate and dimensionless relative displacement:

$$\frac{2\pi x}{a}\to x,\ \frac{\pi w}{a}\to w. \tag{19}$$

Taking these renormalizations into account, we can write Eq. (18) in the form

$$\frac{d}{dx}(\hat{H}w)=\frac{1}{2l}\sin 2w, \tag{20}$$

where we have introduced the notation $l=\pi(\alpha/\beta)^{1/2}$ for the ''elastic length,'' i.e., the size of the dislocation core in the direction of the x-axis.

Equation (20) has the structure similar to that of the Klein–Gordon equation emerging in the one-dimensional

model, but one spatial derivative is now replaced by the Hilbert transformation. This equation has a simple solution describing a dislocation[7]:

$$w=\frac{\pi}{2}+\arctan\frac{x}{l}=-\arctan\frac{l}{x}. \tag{21}$$

Solution (21), as well as the solution of the Frenkel–Kontorova equation, has no singularities at the dislocation center. On the other hand, it has regular asymptotic forms at large distances matching with the description of a dislocation in the continual linear theory of elasticity. In the initial variables, solution (21) coincides with solution (3) if we put $z=b$ in the latter solution.

2.2. Peierls model for a magnetic vortex

At the first stage, we can propose a magnetic analog of the one-dimensional Frenkel– Kontorova model for a correct description of the vortex core. Following this model, we replace the magnetically ordered half-plane above the MV center ($z>0$) by a chain of antiferromagnetically ordered spins with rotational angles $\psi_+(x)$, while the half-plane below the vortex center ($z<0$) will be replaced by a spin chain with rotational angles $\psi_-(x)$. For $J_1 \gg J_2$, the long-wave description is valid along the chains (along the x-axis), but relative rotations of spins in the neighboring chains can be of the order of π. Consequently, the magnetic interaction between the chains should be taken into account completely. The choice of interchain potential in the form of the trigonometric function (12) was of model nature in the conventional Frenkel–Kontorova ''elastic'' model, while in the case of a magnet it is more justified since it follows from the Heisenberg nature of the magnetic exchange interaction:

$$W=-M_0^2 J_2\cos(\psi_+-\psi_-). \tag{22}$$

The solution of the Klein–Gordon equation emerging in this model for relative angles of magnetization rotation, which corresponds to a MV, has no singularity at the vortex center and correctly describes the vortex core. However, at large distances the fields decrease exponentially and not according to a power law following from a consistent analysis based on a continual description [see (10) and (11)].

In order to describe correctly the vortex structure at large distances and at its core, we propose a model which is similar to the Peierls model for the magnetic system.

We consider a magnetically ordered plane containing a magnetic vortex at the point $x=z=0$ and possessing strong anisotropy of exchange integrals in the direction of the axes x and z ($J_1 \gg J_2$). The characteristic size of the magnetic vortex in the x-direction is considerably larger than its size in the z-axis. The rotation of magnetization vector at the core through π occurs over a distance of the order of atomic spacing in the z-direction and over the ''magnetic length'' $a\sqrt{J_1/J_2}/2 \gg a$ in the direction of the x-axis (the ''magnetic length'' is the term usually applied to the quantity $\sqrt{J/A}$, where A is the anisotropy constant in the easy plane; in our case, $A=0$). Consequently, the discrete nature of the magnetic lattice should be taken into account only on the line passing through the vortex core in the direction of the x-axis. According to the Peierls model, we introduce the magnetization rotation angle $\psi_+=\psi(z=+0)$ in the row of atoms above the vortex center and the angle $\psi_-=\psi(z=-0)$ in the row below the vortex center. The magnetic interaction between these rows of spins must be taken into account fully and described by formula (22). The remaining volume of the two half-spaces will be described by the differential equation (8).

The magnetization field distribution $\psi(x,t)$ for the MV in the two half-spaces can be expressed in terms of the distribution of density of effective forces (in fact, moments) $\tilde{f}_\pm(x)$ acting on the line $z=0$ as follows[9]:

$$\psi(x,z\gtrless 0)=\pm\frac{1}{2\pi a M_0^2\sqrt{J_1J_2}}\int dx'\,\ln\left[\frac{(x-x')^2}{J_1a^2M_0^2}+\frac{z^2}{J_2b^2M_0^2}\right]\tilde{f}_\pm(x'), \tag{23}$$

where

$$\tilde{f}_\pm(x)=M_0^2J_2b\left(\frac{\partial\psi}{\partial z}\right)_{z=\pm 0}=\pm M_0^2a\sqrt{J_1J_2}\hat{H}\left(\frac{\partial\psi}{\partial x}\right)_{z=\pm 0}. \tag{24}$$

On the other hand, the forces $\tilde{f}_\pm(x)$ can be determined from the magnetic interaction energy (22):

$$\tilde{f}_\pm(x)=\mp M_0^2J_2\sin\chi, \tag{25}$$

where we have introduced the relative rotation $\chi=\psi_+-\psi_-$ of spins in two chains near the vortex core.

Differentiating relation (23) with respect to x, taking the obtained relations for $z=0$, subtracting one from the other, and (25), taking into account, we obtain a closed equation for the difference in the rotational angles for magnetization in spin chains near the vortex center. In the dimensionless variables (19), it has the form

$$\frac{d}{dx}(\hat{H}\chi)=\frac{1}{\tilde{l}}\sin\chi \tag{26}$$

and in fact coincides with the Peierls equation (20) for the function $\chi=2w$ if we replace the ''elastic length'' l by the ''magnetic length'' $\tilde{l}=\pi\sqrt{J_1/J_2}$. The solution of Eq. (26) describing a magnetic vortex has the following simple form:

$$\chi=\pi+2\arctan\frac{x}{\tilde{l}}. \tag{27}$$

As in the Frenkel–Kontorova model, the change in the function χ upon a change in x from $-\infty$ to $+\infty$ is equal to 2π, and solution (27) has no singularities at the center of the magnetic vortex, but the asymptotic forms of the solution at large distances in the present case have a regular power form and coincide with the results (9) of the continual analysis for $z=b$. The resultant distribution of the magnetization field, e.g., in the upper half-plane, can be obtained from formula (23) by substituting into it the expression for the ''force'' $\tilde{f}_+=M_0^2J_2 2x\tilde{l}/(\tilde{l}^2+x^2)$ following from solution (27) and formula (25).

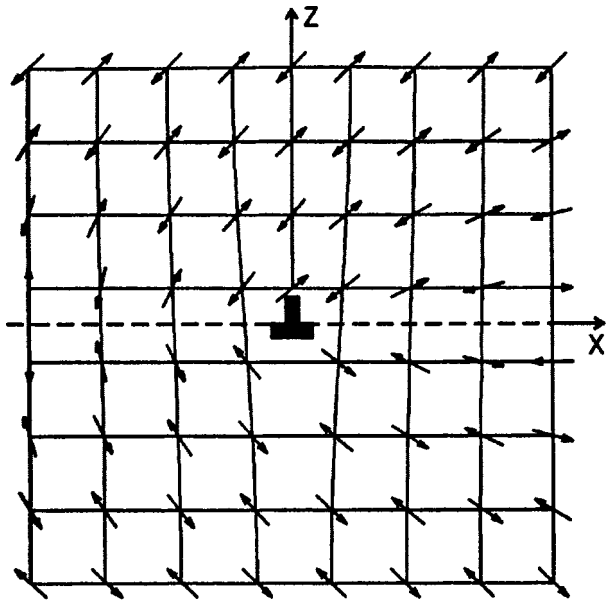

FIG. 1. Magnetization distribution in a two-sublattice AFM with a ''staggered'' spin ordering and with an edge dislocation.

3. MAGNETOSTRUCTURAL TOPOLOGICAL DEFECTS IN TWO-DIMENSIONAL ANTIFERROMAGNETS

3.1. Formulation of the model

Let us consider the magnetization distribution in the magnetically ordered state of an AFM containing a dislocation. Figure 1 shows this distribution for a two-sublattice AFM with a ''staggered'' spin ordering in the presence of an edge dislocation. It can be seen that, when the dislocation center is circumvented along the closed contour, we arrive at a site belonging to another magnetic sublattice with the opposite direction of spin. Consequently, a magnetic disclination with the Frank index $k=1$ (which does not exist in the absence of the dislocation) must be connected with the edge dislocation in order to compensate the spin rotation through π. In the case of a layered AFM with alternating ferromagnetically ordered layers, a similar situation arises in the presence of a screw dislocation: while circumventing the dislocation center, we arrive at the neighboring layer in which the direction of magnetic moments must be opposite. This can be attained in the presence of magnetic disclination with the Frank index $k=1$ (such a disclination can be regarded as ''half the magnetic vortex''). Although the above considerations are very simple and visual, an analytic description of complex magnetostructural topological solitons involves considerable difficulties. A simple one-dimensional model proposed in Ref. 5 generalized the Frenkel–Kontorova model to the case of two topologically coupled fields: the field of elastic displacements and the field of magnetization distribution. The main idea underlying this model can be formulated as follows. If we consider a tetragonal two-dimensional lattice of atoms with a staggered orientation of spins at lattice sites, and confine the analysis to the scalar model of the elastic subsystem, assuming that atoms can be displaced only in the direction of the x-axis, the spins of neighboring atoms from neighboring chains become oriented ferromagnetically (disadvantageously) for fixed orientations of spins and relative displacement of atoms in neighboring atomic chains by an atomic spacing. In order to take into account this circumstance, we can assume that the integral of exchange interaction of a spin from a given chain with all the spins of the neighboring chain (along the z-axis) is a periodic function of the displacement of a given atom with the period $2a$ (for the sake of simplicity, we assume that this dependence is trigonometric, which is naturally a model assumption). In other words, instead of formula (6) for the exchange magnetic interaction we shall use the modernized formula

$$W=M_0^2\sum_{nm}\{J_1\cos(\varphi_{nm}-\varphi_{n-1,m})+J_2\cos(\varphi_{nm}-\varphi_{n,m-1})\cos[\pi(u_{nm}-u_{n,m-1})/a]\}, \tag{28}$$

which is transformed into (6) for $u_{nm}=u_{n,m-1}$.

It should be noted that in order to take into account the magnetoelastic interaction, the exchange integral is expanded into a series in small relative displacements of neighboring atoms. This gives rise to ''crossed'' nonlinear terms which are linear in relative displacements (strain) and contain new material constants, viz., the constants of magnetoelastic interaction. In the given case, the magnetoelastic interaction is of the topological type and is characterized by the previous constant J_2 (the expansion of $\cos[\pi(u_{nm}-u_{n,m-1})/a]$ in formula (28) in small relative displacements leads to terms quadratic in strain). The inclusion of such a ''topological'' interaction leads to coupling of equations of magnetization dynamics and of the elastic subsystem. In the simple model considered in Ref. 5, the index n runs through only two values, and two coupled chains are described. In an analysis of a two-dimensional subsystem, we must take an infinite sequence of coupled magnetic chains.

The expression for the total potential energy of the system has the form

$$E=U+W, \tag{29}$$

where W is defined by formula (28), and

$$U=\sum_{nm}\left\{\frac{\alpha}{2}(u_{nm}-u_{n-1,m})^2+U_0\times\left[1-\cos\left(2\pi\frac{u_{nm}-u_{n,m-1}}{a}\right)\right]\right\}. \tag{30}$$

For AFM in the variables ψ_{nm}, we use (28)–(30) to obtain the dynamic equations for the quantities u_{nm} and ψ_{nm} in the form

$$m(u_{nm})_{tt}+\alpha(2u_{nm}-u_{n-1,m}-u_{n+1,m})+\beta(2u_{nm}-u_{n,m+1}-u_{n,m-1})+\frac{\pi}{a}M_0^2J_2\{\cos(\psi_{nm}-\psi_{n,m-1})\times\sin[\pi(u_{nm}-u_{n,m-1})/a]-\cos(\psi_{n,m+1}-\psi_{nm})\times\sin[\pi(u_{n,m+1}-u_{nm})/a]\}=0, \tag{31}$$

$$\mu(\psi_{nm})_{tt}+M_0^2J_1\{\sin(\psi_{nm}-\psi_{n-1,m})+\sin(\psi_{nm}-\psi_{n+1,m})\}+M_0^2J_2\{\sin(\psi_{nm}-\psi_{n,m-1})\cos[\pi(u_{nm}-u_{n,m-1})/a]$$

$$+\sin(\psi_{nm}-\psi_{n,m+1})\cos[\pi(u_{n,m+1}-u_{nm})/a]\}=0. \quad (32)$$

In accordance with the conventional Peierls model, in the volume outside the line $z=0$ containing the center of a complex magnetostructural defect we replace the differences in displacements and deviations of spins by spatial derivatives, going over to the long-wave description in linear differential equations:

$$mu_{tt}-\alpha a^2 u_{xx}-\beta^* b^2 u_{zz}=0, \quad (33)$$

$$\mu\psi_{tt}-M_0^2 J_1 a^2 \psi_{xx}-M_0^2 J_2 b^2 \psi_{zz}=0. \quad (34)$$

These equations coincide with Eqs. (2) and (8), but Eq. (33) contains the renormalized constant of elastic interaction along the z-axis: $\beta^*=\beta+(\pi/a)^2 M_0^2 J_2$. However, this renormalization is insignificant since magnetic interactions are much weaker than elastic interactions in actual practice, and $\beta^*\cong\beta$.

We shall consider below possible static topological elastic and magnetic defects in the proposed two-dimensional model (note that $u_+=-u_-$ and $\psi_+=-\psi_-$ in the configuration of the defect shown in Fig. 1). We can express the fields of elastic displacements $u(x,z)$ and spin rotations $\psi(x,z)$ about a magnetoelastic defect in terms of the distribution of forces f and $\tilde{f}$ at the interface between the half-planes (See Secs. 2.1 and 2.2). However, expressions (17) and (25) change since we take into account the energy of interaction of elastic displacements and rotations of spins near the line passing through the defect. This energy now has the form

$$U=\beta\left(\frac{a}{2\pi}\right)^2\left[1-\cos\frac{2\pi w}{a}\right]-M_0^2 J_2\cos\chi\cos\frac{\pi w}{a}. \quad (35)$$

It follows from this expression that

$$f_\pm=\mp\frac{\beta a}{2\pi}\sin\frac{2\pi w}{a}-\frac{\pi}{a}M_0^2 J_2\cos\chi\sin\frac{\pi w}{a}, \quad (36)$$

$$\tilde{f}_\pm=\mp M_0^2 J_2\cos\frac{\pi w}{a}\sin\chi. \quad (37)$$

Substituting these expressions (36), (37) for effective forces into relations (13) and (23), carrying out the Hilbert transformation, and going over to the dimensionless coordinate x and relative displacement w, we obtain the final form of the system of nonlinear integro-differential equations for fields of relative displacements (and relative spin deviations) at the banks of the cut:

$$-\pi\frac{d}{dx}(\hat{H}w)+\frac{\beta}{2(\alpha\beta^*)^{1/2}}\sin 2w + \frac{\pi^2 M_0^2 J_2}{a^2(\alpha\beta^*)^{1/2}}\cos\chi\sin w=0, \quad (38)$$

$$-\pi\frac{d}{dx}(\hat{H}\chi)+\left(\frac{J_2}{J_1}\right)^{1/2}\cos w\sin\chi=0. \quad (39)$$

Let us consider possible solutions of this system, which describe static topological structural, magnetic, and magnetostructural solitons of the type of dislocations, disclinations, magnetic vortices, and coupled states of dislocations and magnetic disclinations.

3.2. Structure of solution. Integrable case

First of all, we consider the simplest static elastic and magnetic topological defects which can exist in the two-dimensional model described by Eqs. (38) and (39).

The average magnetic moment M_0 vanishes above the Néel temperature in a magnetically disordered state, and Eq. (38) is transformed into Eq. (20) with solution (21) describing a solitary dislocation.

In the absence of dislocations and weak magnetoelastic interaction, we must put $w=0$ in Eqs. (38) and (39). In this case, Eq. (39) is transformed into Eq. (26) in the initial variables and has an exact solution (27) for a magnetic vortex.

The structure of the system of equations (38) and (39) resembles the Peierls equation, but it is much more complicated for analysis in view of the presence of ''crossed'' terms. The solutions of these equations can be found only in some particular cases. It should be noted that the magnitudes of terms not containing spatial derivatives have different values. In Eq. (38), the coefficient of the purely elastic term $\beta/[2\sqrt{\alpha\beta^*}]\cong\sqrt{\beta/\alpha}/2$ is small under our assumption concerning the anisotropy of elastic properties. The coefficient $\sqrt{J_2/J_1}$ in Eq. (39) is also small under the assumption of spatial anisotropy of the exchange interaction. Finally, the coefficient $\pi^2 M_0^2 J_2/a^2\sqrt{\alpha\beta^*}$ of the magnetoelastic term in Eq. (38) is of the order of $\sqrt{\beta/\alpha}(M_0^2 J_2/\beta)$, i.e., in contrast to the coefficient of the elastic term, it contains the factor $M_0^2 J_2/\beta$ describing the ratio of magnetic and elastic interactions in the direction of the z-axis. In the actual physical situation, this ratio is always very small, and hence the last term in Eq. (38) can be neglected. In this case, the basic system of equations is simplified considerably:

$$\frac{d}{dx}(\hat{H}w)=\frac{1}{l}\cos w\sin w, \quad (40)$$

$$\frac{d}{dx}(\hat{H}\chi)=\frac{1}{\tilde{l}}\cos w\sin\chi, \quad (41)$$

since Eq. (40) describing the elastic subsystem ''splits.'' In fact, this system (with an appropriate renormalization of the coordinate) depends on only one parameter $l/\tilde{l}=\sqrt{J_2/J_1}\sqrt{\beta/\alpha}$. For an arbitrary value of this parameter, the system of equations (40) and (41) has no explicit analytic solutions. However, it is important that from the methodological point of view it has a simple analytic solution in the particular case when $l/\tilde{l}=1$, which clarifies the topological nature of a complex MSTD and its topological distinction from a magnetic vortex. It should be noted that this assumption is not connected with the smallness of magnetic interactions as compared with the elastic interaction and can be realized in principle. In an isotropic crystal with $J_1=J_2$ and $\alpha=\beta$, the characteristic length l and $\tilde{l}$ are of the same order of magnitude, but the cores of dislocation and disclination are of atomic size, and hence the system can be described in

terms of differential equations at a considerable stretch. In the case of an anisotropic crystal and large values of l and $\tilde{l}$, we can use integro-differential equations (40) and (41), assuming that the values of l and $\tilde{l}$ are approximately equal for close degrees of anisotropy of elastic and magnetic interactions. In this case, the system of equations (40) and (41) has the obvious solution

$$w=\chi, \tag{42}$$

for which Eq. (41) for the magnetic subsystem acquires the form

$$\frac{d}{dx}(\hat{H}\chi)=\frac{1}{\tilde{l}}\cos\chi\sin\chi. \tag{43}$$

It can be seen that this equation differs significantly from Eq. (26) for a magnetic vortex. In solution (27) for a MV, the function χ varies by 2π upon a change in x from $-\infty$ to $+\infty$. Equation (43) has the basically different solution

$$\chi=\frac{\pi}{2}+\arctan\frac{x}{l}, \tag{44}$$

in which the function χ changes by π upon a change in x from $-\infty$ to $+\infty$, and which describes a magnetic disclination with the Frank index $k=1$.

Thus, Eqs. (40) and (43) have an exact solution for $l=\tilde{l}$, which describes a complex magnetostructural topological defect, viz., a coupled state of a dislocation and a magnetic disclination with the Frank index $k=1$. The existence of such a solution is very important since it indicates the existence of the above-mentioned topological defect for an arbitrary ratio of the parameters l and $\tilde{l}$. Variations in the structure of the solution can only be of quantitative and not qualitative nature.

Let us return to the general case of the system (40) and (41) for $l\neq\tilde{l}$. Linearizing these equations at large distances over small amplitudes of the fields w and χ and replacing the derivatives $dw(p)/dp$ and $d\chi(p)/dp$ in the integral terms by δ-functions, we can easily find the asymptotic forms of solutions at large distances:

$$w\propto l/x, \quad \chi\propto\tilde{l}/x \quad \text{for } x\to\pm\infty. \tag{45}$$

Since $w=u_+-u_-\approx b(\partial u/\partial z)_{z=0}$ and $\chi=\psi_+-\psi_-\approx b(\partial\psi/\partial z)_{z=0}$ in this limit, results (45) are in accord with formulas (4) and (10).

In the system of equations (40) and (41), Eq. (40) for elastic displacements splits, and we can use its exact solution (21) for a dislocation. Substituting this solution into Eq. (41), we arrive at a closed equation for the function χ, in which it is convenient to express the coordinate in terms of magnetic length, i.e.,

$$x/\tilde{l}=\kappa, \tag{46}$$

and introduce the single dimensionless parameter

$$\lambda=l/\tilde{l}, \tag{47}$$

characterizing the ratio of scales of variation of the fields of displacements and magnetization rotation. Finally, we can write the basic equation (41) in the new variables in the form

$$\frac{d}{d\kappa}(\hat{H}\chi)+\frac{\kappa}{(\kappa^2+\lambda^2)^{1/2}}\sin\chi=0. \tag{48}$$

An analysis of this nonlinear integro-differential equation with varying coefficients is quire complicated. Hence we shall analyze its solution for small values of the parameter λ. This limit is physically sensible since the dislocation size is normally of the order of atomic spacing, and the width of domain walls can be considerably larger. (It should be borne in mind, however, that domain walls are absent altogether in the model without anisotropy in the easy plane under consideration, and we are speaking of the size of a dislocation core rather than of the domain wall while analyzing the magnetic length.)

3.3. Magnetization distribution around a point dislocation

First of all, we shall analyze Eq. (48) in the limit $\lambda=0$, in which it assumes the form

$$\frac{d}{d\kappa}(\hat{H}\chi)+\operatorname{sgn}\kappa\sin\chi=0. \tag{49}$$

We can easily find the asymptotic forms of the solution for a magnetostructural defect under investigation at large distances and at the center of the defect. At large distances ($\kappa\to-\infty$) and for small values of χ, Eq. (49) gives $\chi\approx\hat{H}(d\chi/d\kappa)$. In view of rapid decrease of the derivative $d\chi/d\kappa$, the asymptotic form of χ is determined by the kernel of the Hilbert transformation, i.e., $\chi\propto1/\kappa$ for $\kappa\to-\infty$ (in this case, $d\chi/d\kappa\propto1/\kappa^2$, and actually ensures the convergence of the integral). In order to find the asymptotic form of the solution at the center of a disclination, we shall use the skew-reciprocity of the Hilbert transformation and the symmetry of the function $\sin\chi(\kappa)$ about κ to transform Eq. (49) to

$$\frac{d\chi}{d\kappa}=\frac{1}{\pi}\int_0^\infty dp\,\frac{\sin\chi(\sqrt{p})}{p-\kappa^2}. \tag{50}$$

The decrease of the function $\sin\chi$ at large distances ($\sin\chi\propto1/\kappa=1/\sqrt{p}$) ensures the convergence of the integral for $p\to\infty$. For small values of κ, the main contribution to its value comes from small p for which $\sin\chi\approx1$. Truncating the integral at distances of the order of unity, we obtain the asymptotic forms of the solution at the center of the defect:

$$\frac{d\chi}{d\kappa}\approx-\frac{2}{\pi}\ln\kappa. \tag{51}$$

This asymptotic form has a logarithmic singularity, although the function $\chi(\kappa)$ remains finite at the disclination center:

$$\chi\approx\frac{\pi}{2}-\frac{2}{\pi}\kappa\ln\kappa. \tag{52}$$

Since the function $G=\sin\chi(\kappa)$ in Eq. (50) appears in the integrand, the solution of this equation depends on the form of this functions only slightly. It is only important that the

function decreases at large distances, ensuring the convergence of the integral. Since Eq. (50) contains no parameters, the amplitude and the region of localization of the function G are of the order of unity.

Considering a number of trial expressions for G [e.g., $G=1$ for $\kappa<1$ and $G=0$ for $\kappa>1$; $G=1/(1+\kappa)$, $G=1/(1+\kappa^2)^2$], we can easily see that the profile of the function $d\chi/d\kappa$ following from (50) weakly depends on the form of $G(\kappa)$, has a logarithmic singularity (51) at zero, and decreases according to a power law $\propto 1/\kappa^2$ at infinity.

We can find an explicit analytic solution for the magnetization profile in a complex defect by using a model piecewise linear system in which the Heisenberg exchange interaction of spins through the dislocation slip line (22) is replaced by an interaction of the form

$$W=M_0^2 J_2 \times \begin{cases} -(\pi/2)^2+\chi^2, & 0<\chi<\pi/2, \\ (\pi/2)^2-(\chi-\pi)^2, & \pi/2<\chi<\pi. \end{cases} \tag{53}$$

In this case, Eq. (49) becomes piece-wise linear:

$$\frac{d}{d\kappa}(\hat{H}\chi)=\chi-\frac{\pi}{2}(1-\operatorname{sgn}\kappa). \tag{54}$$

Differentiating this equation with respect to κ and applying the Fourier transformation for the function $d\chi/d\kappa$, we can easily obtain the final expression for the dependence $\chi(\kappa)$. For $\kappa>0$, this dependence has the form

$$\chi(\kappa)=\pi-\mathrm{Ci}\ \kappa\ \sin\kappa+\mathrm{si}\ \kappa\ \cos\kappa, \tag{55}$$

where $\mathrm{Ci}(\kappa)$ and $\mathrm{si}(\kappa)$ are integral cosine and sine. An analysis of solution (55) shows that the magnetization field at large distances has the asymptotic form $\chi\approx\pi-1/\kappa$, which is in accord with the above results. For small values of κ, the derivative of the magnetization field at the center of the defect has a logarithmic singularity $d\chi/d\kappa\propto\ln\gamma\kappa$, where γ is the Euler–Mascheroni constant, which is also in agreement with the asymptotic form obtained earlier. It should be noted that solution (55) oscillates near the values $\chi=0$ and $\chi=\pi$ with a maximum deviation of the order of 0.1. Such oscillations are typical for integral transformations of piece-wise-joined functions.

3.4. Finiteness of the size of dislocation core

Thus, we have proved that in the limit of point dislocation ($\lambda=0$), the solution of the basic equation (48) exhibits a regular asymptotic behavior at large distances. However, the derivative $d\chi/d\kappa$ in this case has a logarithmic singularity at zero. In order to eliminate this singularity, we must take into account the finite width of the dislocation core. We return to the basic equation (48) with $\lambda\neq 0$, but will assume, as before, that this parameter is small (i.e., the size of the dislocation core is much smaller than the size of the disclination core which is of the order of unity in our dimensionless variables). Consequently, we now have two characteristic scales in dimensionless variables, i.e., $\kappa\propto\lambda$ and $\kappa\propto 1$, and it is necessary to analyze intermediate asymptotic forms for $\kappa\ll\lambda$, $\lambda\ll\kappa\ll 1$, and $\kappa\gg 1$.

We can write Eq. (48) in a more convenient form

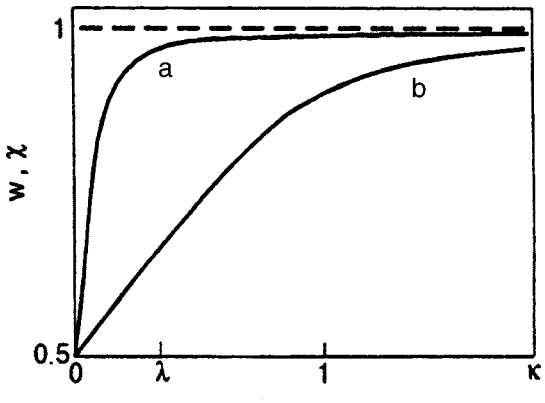

FIG. 2. Distribution of fields of displacements w(a) and spin rotations χ(b) at the core of a complex magnetostructural defect.

$$\frac{d\chi}{d\kappa}=\frac{1}{\pi}\int \kappa' d\kappa' \frac{\sin\chi(\kappa')}{(\kappa'-\kappa)(\kappa^2+\lambda^2)^{1/2}}. \tag{56}$$

Since the function χ decreases in proportion to $1/\kappa$ at large distances $\kappa\gg 1$, integral (56) converges at the upper limit. In the case of small values of κ we are interested in, the main contribution to the integral comes from the region of small κ'. Hence we can put $\sin\chi(\kappa)\approx 1$ in Eq. (56) and replace the integration between infinite limits by integration in the interval $[-1,1]$. This leads to the following expression for the derivative $d\chi/d\kappa$:

$$\pi\frac{d\chi}{d\kappa}\simeq -2\ln\lambda+\frac{1}{\eta}\ln\frac{(1/\kappa-1-\eta)(\lambda^2/\kappa-1+\eta)}{(1/\kappa-1+\eta)(\lambda^2/\kappa+1+\eta)}, \tag{57}$$

where $\eta=(\kappa^2+\lambda^2)^{1/2}/\kappa$.

It follows from (57) that there is no logarithmic singularity at zero if we take into account the finiteness of the dislocation core: $d\chi/d\kappa=-(2/\pi)\ln\lambda$ for $\kappa=0$. For small values of κ, the profile of the function $d\chi/d\kappa$ has the form

$$\pi\frac{d\chi}{d\kappa}\approx -2\ln\lambda-2\left(\frac{\kappa}{\lambda}\right)^2, \quad \kappa\ll\lambda, \tag{58}$$

$$\pi\frac{d\chi}{d\kappa}\simeq -2\ln\kappa, \quad \lambda\ll\kappa\ll 1. \tag{59}$$

The corresponding distribution of magnetization $\chi(\kappa)$ is shown in Fig. 2 (curve b). The figure also shows relative displacements $w(\kappa)$ (curve a). Relative displacements increase linearly at the dislocation core: $w/\pi\simeq 1/2+\lambda\kappa/\pi$ (for $\kappa>0$) for $\kappa\lesssim\lambda$, attaining the power asymptotic form $w\propto 1/\kappa$. The magnetization field in a magnetic disclination varies at a considerably lower rate: $\chi/\pi\simeq 1/2-(2/\pi^2)\kappa\ln\lambda(0<\kappa<\lambda)$ at the dislocation core, and the main rotation of spins takes place at distances $\kappa\gtrsim 1$. (Note that the numerical analysis of the fields around two-dimensional topological defects revealed that power asymptotic forms are attained in actual practice at distances much larger than analytic estimates. For example, the displacement field around a crowdion (zero-dimensional analog of a dislocation) attains a power asymptotic form at distances 30 times larger than the corresponding analytic estimates.[10])

3.5. Bulk distribution of fields of a magnetoelastic topological defect

Concluding the section, we consider the distribution of elastic displacement fields and fields of spin rotations in the entire two-dimensional volume around a complex topological defect. Since the exact solution of the elastic problem for the difference in the displacements of atoms along the dislocation line $w(x)$ for $2D$ dislocations is known, the two-dimensional distribution of elastic displacements can be found exactly.

Writing solution (21) in the initial variables, substituting the obtained expression for $\partial u_{\pm}/\partial x$ (considering that $u_{\pm} = \pm w/2$) in accordance with (14), and carrying out the $\hat{H}$ transformation of this relation, we obtain the explicit form of the derivatives $\partial u_{\pm}/\partial z$ at the interface between half-spaces. Differentiating formula (13) with respect to z and substituting the obtained expression for $\partial u_{\pm}/\partial z$ into the right-hand side, we obtain after simple calculations the following final expression for the strain distribution in the $2D$ volume:

$$\frac{\partial u}{\partial z}(z \gtrless 0) = \frac{a}{2\pi} \frac{x\zeta}{[x^2 + \zeta^2 (z \pm b/2)^2]}, \tag{60}$$

where $\zeta = (a/b)\sqrt{\alpha/\beta}$.

Thus, expression (60) for strain in the Peierls model differs from the corresponding expression (4) in the continual theory in the replacement of the coordinate z in the denominator by the quantity $z \pm b/2$ for half-spaces with $z > 0$ and $z < 0$. In other words, the corresponding solution for each half-space has a singularity outside this volume. Formula (60) readily gives the distribution of the displacement field in the volume around the dislocation:

$$u(x, z \gtrless 0) = \frac{a}{2\pi} \arctan\left[\left(z \pm \frac{b}{2}\right) \frac{\zeta}{x}\right]. \tag{61}$$

Comparing this result with formula (3) following from the continual theory of elasticity, we see that the solution for a dislocation in the Peierls model has no singularity at zero and coincides with solution (3) at large distances.

In order to find the distribution of the magnetization field in the entire two-dimensional volume around a magnetic disclination, we must use formula (23), differentiate it with respect to z, and substitute expression (37) for effective force into it. This gives

$$\frac{d\psi}{dz} = \frac{z\xi}{b\pi} \int \frac{p \sin \chi(p) dp}{[(p-x)^2 + (z\xi)^2][p^2 + (a/2\sqrt{J_1/J_2})^2]^{1/2}}, \tag{62}$$

where $\xi = (a/b)\sqrt{J_1/J_2}$.

In order to find the asymptotic form of expression (62) at distances larger than the ''magnetic length'' $x, z \gg a\sqrt{J_1/J_2}$, we replace the expression $p/[p^2 + (a\sqrt{J_1/J_2}/2)^2]^{1/2}$ by the signum function and approximate $\sin \chi(p)$ by the expression $1/(p^2 + L^2)^{1/2}$, where L is a quantity of the order of the magnetic length. Then the integral in (62) can be evaluated in elementary functions,[11] although it has a cumbersome form. However, at distances larger than the ''magnetic length'' $x, z \gg L$, this expression can be expanded into a power series in x/L and z/L. The first terms of this expansion have the form

$$\frac{\partial \psi}{\partial z}(z \gtrless 0) \approx \frac{Lx}{b(x^2 + z^2\xi^2)} \left[1 \mp \frac{4Lz\xi}{\pi(x^2 + z^2\xi^2)} + O\left(\frac{L^2}{x^2}, \frac{L^2}{z^2}\right)\right]. \tag{63}$$

Comparing this formula (63) with the asymptotic form (10) of the solution in the linear theory, we arrive at the relation $L = a\sqrt{J_1/J_2}$ (in other words, $L = 2\tilde{l}$ in the dimensionless variables and indeed has the same order of magnitude as the ''magnetic length'').

Formula (63) leads to the final approximate expression for the distribution of spin deviations field in a two-dimensional disclination:

$$\psi(z \gtrless 0) \simeq \arctan\left[\left(z \pm \frac{2b}{\pi}\right) \frac{\xi}{x}\right], \quad x,\ z \gg a\xi. \tag{64}$$

At large distances from the center of the defect, this expression naturally coincides with formula (9) given above, but now the singularity for each half-space is displaced by an atomic spacing outside this volume, and the general solution has no singularity.

CONCLUSION

We have proposed a new two-dimensional model for describing the structure of complex magnetoelastic topological singularities in $2D$ AFM. This model generalizes the Peierls model to the case of two coupled fields of elastic displacements and of spin deviations. For these fields, we have derived a closed system of nonlinear integro-differential equations. In the absence of dislocations, this system has an exact solution for a two-dimensional magnetic vortex, while in the presence of a dislocation it has a solution for a coupled state of the dislocation and a magnetic disclination. For a special case of relation between elastic and magnetic anisotropies, we obtained an exact solution for such a defect. In the case when the anisotropy of elastic interactions is much smaller than the spatial anisotropy of exchange interaction, we obtained an approximate solution for a complex magnetostructural defect having no singularity at its core and having regular asymptotic forms at large distances from the center.

*E-mail: odudko@ilt.kharkov.ua

[1] A. M. Kosevich, B. A. Ivanov, and A. S. Kovalev, *Nonlinear Magnetization Waves. Dynamic and Topological Solitons* [in Russian], Naukova Dumka, Kiev (1983).
[2] A. Hubert, *Theorie der Domanenwande in geordneten Medien*, Springer, Heidelberg (1974).
[3] A. S. Kovalev and A. M. Kosevich, Fiz. Nizk. Temp. **3**, 259 (1977) [Sov. J. Low Temp. Phys. **3**, 125 (1977)].
[4] I. E. Dzyaloshinskii, Pis'ma Zh. Eksp. Teor. Fiz. **25**, 110 (1977) [JETP Lett. **25**, 98 (1977)].
[5] A. S. Kovalev, Fiz. Nizk. Temp. **20**, 1034 (1994) [Low Temp. Phys. **20**, 815 (1994)].

[6] B. A. Ivanov, V. E. Kireev, and V. P. Voronov, Fiz. Nizk. Temp. **23**, 845 (1997) [Low Temp. Phys. **23**, 635 (1997)].
[7] A. M. Kosevich, *Theory of Crystal Lattice* [in Russian], Vishcha Shkola, Kharkov (1988).
[8] M. E. Gouvea, G. M. Wysin, A. R. Bishop, and F. G. Mertens, Phys. Rev. B **39**, 11840 (1989).
[9] M. D. Greenberg, *Application of Green's Functions in Science and Engineering*, Prentice-Hall, Inc. Englewood Cliffs, New Jersey (1971).
[10] A. S. Kovalev, A. D. Kondratyuk, A. M. Kosevich, and A. I. Landau, Phys. Status Solidi B **177**, 117 (1993).
[11] I. M. Ryzhik and I. S. Gradshtein, *Tables of Integrals, Sums, Series, and Products* [in Russian], Gos. Izd. Tekh. Lit., Moscow (1951).

Translated by R. S. Wadhwa

QUANTUM EFFECTS IN SEMICONDUCTORS AND DIELECTRICS

Low-temperature spectroscopy of nonequivalent Pr^{3+} optical centers in a Y_2SiO_5 crystal

Yu. V. Malyukin, B. I. Minkov, R. S. Borisov, and V. P. Seminozhenko

*Institute of Single Crystals, National Academy of Sciences of the Ukraine, 310001 Kharkov, Ukraine**

N. V. Znamenskii, E. A. Manykin, D. V. Marchenko, and E. A. Petrenko

Russian Science Center ''Kurchatov Institute,'' 123182 Moscow, Russia
(Submitted January 27, 1998)
Fiz. Nizk. Temp. **24**, 571–576 (June 1998)

An analysis of the absorption and luminescence spectra of a Y_2SiO_5:Pr^{3+} crystal has revealed the existence of two Pr^{3+} optical centers associated with the presence of impurity ions at nonequivalent cation sites. It is found that energy is transported nonradiatively between the nonequivalent Pr^{3+} optical centers. and a preliminary analysis of the transport mechanism is carried out. [S1063-777X(98)00806-8]

1. INTRODUCTION

Crystals of Y_2SiO_5 (YSO) belong to the class of rare-earth silicates which have aroused considerable interest in recent years due to their prospective application as scintillators.[1,2] The unit cell of YSO contains two nonequivalent positions of the Y^{3+} ion[3] which can be occupied by impurity rare-earth (RE) ions introduced specially into the cation sites of the YSO crystal. Such a situation is really observed in crystals of YSO:Nd^{3+} [Ref. 4] and YSO:Eu^{3+} [Ref. 5] in which two types of optical centers corresponding to the localization of impurity ions at different cation sites of the YSO crystal were identified. Investigations of the optical spectrum of the YSO:Pr^{3+} crystals[6] over a wide spectral range (0.19–3 μm) have failed to reveal such properties for Pr^{3+} ions. On the contrary, optical spectral investigations of YSO:Pr^{3+} crystals in limited spectral range have revealed[7,8] spectral lines which were attributed to various Pr^{3+} optical centers.

In view of the disparities in the results obtained in Refs. 6–8, we made low-temperature spectroscopic studies of Pr^{3+} impurity centers in a YSO crystal, used the results for interpreting the observed spectral lines and confirmed the presence of two Pr^{3+} optical centers associated with the replacement of nonequivalent Y^{3+} cation sites in a YSO crystal.

2. EXPERIMENTAL TECHNIQUE

Optical absorption and luminescence spectra of a YSO:Pr^{3+} crystal were studied on an automatic spectrofluorimeter based on a grating monochromator MDR-23. The spectra were recorded on FEU-100 working in the phonon count mode. The control of the step actuator of the monochromator and the counting of one-photon pulses were carried out by electron modules operating in the KAMAK mode. The KAMAK crate was connected through interface with a personal computer based on INTEL-286 processor.

The source of the continuous spectrum was a 100W incandescent lamp fed by a stabilized power supply. The luminescence was excited in the crystal under investigation by an argon laser LGN-402 and a tunable organic dye laser.

Low temperatures were produced in an optical helium cryostat P−118, containing the samples in helium vapor.

The YSO:Pr^{3+} crystals were grown by the Czochralski method. The charge concentration of Pr was 0.1 at%. Samples for investigation were in the form of plates of thickness 1–5 mm.

3. ANALYSIS OF EXPERIMENTAL RESULTS

The $4f^2$ electron configuration of a Pr^{3+} ion in the Russel–Saunders base[9,10] produces four singlet energy levels $^1S_0$, $^1D_2$, $^1G_4$, $^1I_6$ and nine triplet energy levels $^3P_0$; $^3P_1$; $^3P_2$; $^3H_4$; $^3H_5$; $^3H_6$; $^3F_2$; $^3F_3$; $^3F_4$. Their relative arrangement, and hence the energy level diagram for the Pr^{3+} ion, is primarily determined by the Coulomb electron–electron interaction and the spin–orbit interaction.[9,10] We shall not consider weaker interactions since they are not manifested in optical spectra.[9,10] In accordance with Hund's rule and Pauli's principle,[9,10] the ground state of the Pr^{3+} ion corresponds to the term $^3H_4$. This is also confirmed by the available experimental data.[6,7,11–15] As the energy increases, other energy levels $^3H_5$; $^3H_6$; $^3F_2$; $^3F_3$; $^3F_4$ and $^1G_4$ start appearing above $^3H_4$. The frequency of electron transitions involving these levels are confined only to the IR spectral region.[6,11–13] The next energy levels determining the optical spectrum of the Pr^{3+} ion are $^2D_1$; $^3P_0$; $^3P_1$; $^1I_6$ and $^3P_2$.[6,11–15] The average energy gap between the centers of gravity of the levels $^1G_4$ and $^2D_1$ is 7000 cm^{-1}.[13] The level $^1S_0$ is very high on the energy scale ($\sim$50000 cm^{-1}) and frequencies of electron transitions involving this level lie in the far ultraviolet region.[13] We shall confine ourselves to a detailed analysis of the energy levels $^3H_4$, $^2D_1$, and $^3P_0$ in this work since it is easy to identfy them reliably by investigating the optical spectra of the Pr^{3+} ion.[11–15]

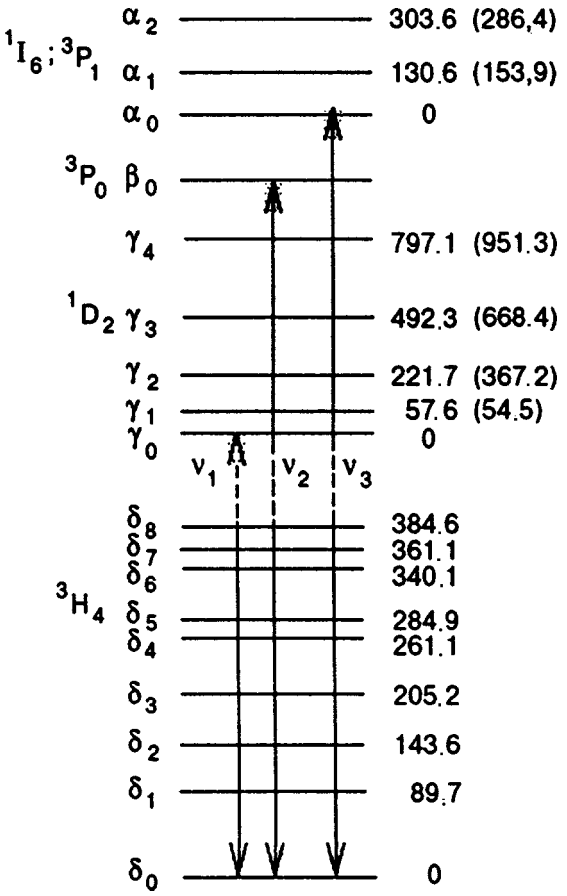

FIG. 1. Simplified energy level diagram of Pr^{3+} ions in a Y_2SiO_5 crystal: $\nu_1 = 16538.2(16483.7)$ cm^{-1}, $\nu_2 = 20540.2(20742.6)$ cm^{-1}, $\nu_3 = 20981.1 \times (20867.2)$ cm^{-1}. The numbers corresponding to the position of Stark components are given in cm^{-1}.

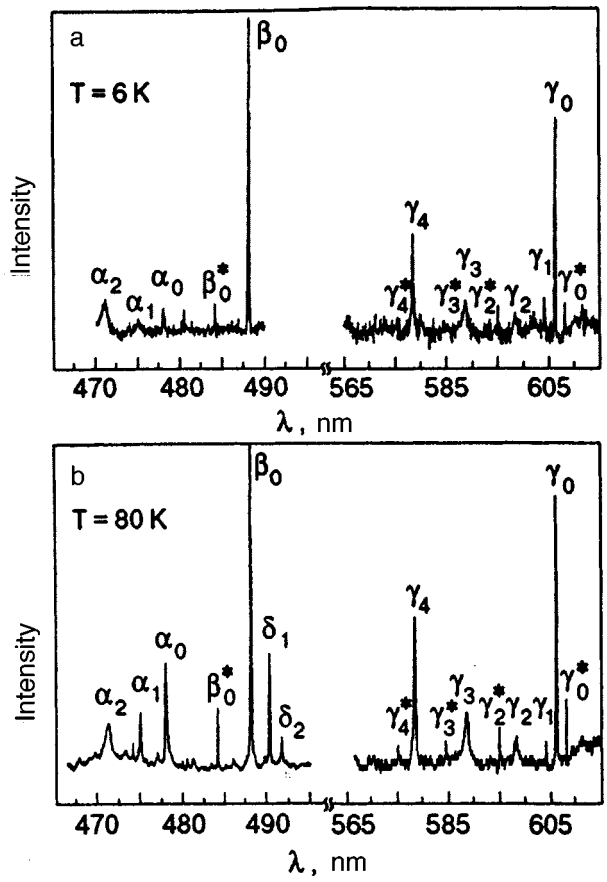

FIG. 2. Fragments of the absorption spectrum of a Y_2SiO_5:Pr^{3+} crystal at various temperatures T (in K): 6.0 (a) and 80 (b). Groups of lines belonging to different optical centers Pr^{3+} are marked with and without asterisks, respectively.

The crystal field weakly affects the $4f$ electrons of RE ions. Hence its effect boils down to a partial or complete removal of degeneracy of energy levels in their total magnetic moment.[9,10] In the first-order perturbation theory, the centers of gravity of the energy levels are not displaced by the crystal field.[9,10] The degeneracy of the energy levels of the Pr^{3+} ion is removed completely by the crystal field of YSO since the point symmetry group of both cation sites is C_1.[3] Under the action of the crystal field of YSO, the terms $^3H_4$ and $^1D_2$ are split into nine and five Stark components. The level $^3P_0$ is not split. According to the qualitative analysis presented here, we can construct a simplified energy-level diagram for the Pr^{3+} ion (Fig. 1). The Stark components of the terms $^3P_1$ and $^1I_6$ get mixed and cannot be separated reliably in the experimental spectra.[12–14] Hence the appurtenance of the three energy levels α_0, α_1, and α_2 shown above $^3P_0$ in Fig. 1 to particular terms is not possible. However, optical transitions involving these levels correspond to really observable spectral lines (see below). We shall use the energy level diagram shown in Fig. 1 to interpret the experimental spectra of the YSO:Pr^{3+} crystal and find the exact positions of Stark components of the terms $^3H_4$ and $^1D_2$, as well as the relative position of $^3H_4$, $^1P_2$ and $^3P_0$.

The absorption spectrum of the YSO:Pr^{3+} crystal consists of two groups of spectral lines which can be distinguished by their sharpness (Fig. 2). In each group, the ratio of the linewidth at half the height of the corresponding spectral lines is of the order of 3:1. At helium temperature, the interpretation of the absorption spectrum (Fig. 2) is quite simple since it can be expected that of the nine Stark components of the term $^3H_4$, only the lowest one will be populated (the Stark splitting is usually of the order of tens of cm^{-1}).[12] Using the results of investigation of the optical spectra of the Pr^{3+} ion in other crystal matrices,[11–15] one of the spectral line groups γ_0, γ_1, γ_2, γ_3, γ_4 and β_0 can be identified with the optical transitions from the lowest Stark component δ_0 of the term $^3H_4$ to five Stark components of the term $^1D_2$ and the term $^3P_0$ (Fig. 1). The correctness of such an interpretation is confirmed by the structure of the absorption spectrum of the YSO:Pr^{3+} crystal at $T = 80$ K (Fig. 2b) as well as its luminescence spectrum (Fig. 3). The low-frequency region of the absorption spectrum of the YSO:Pr^{3+} crystal at $T = 80$ K acquires reliably identifiable satellites δ_1 and δ_2 to the spectral lines γ_0, γ_2, γ_3, γ_4 and β_0. These satellites lie at equal frequency intervals from the spectral lines. For lines γ_0, γ_2, γ_3 and γ_4, the intensity of the spectral satellites δ_1 and δ_2 is low, hence they cannot be distinguished on the scale of Fig. 2b. Satellites of the spectral line γ_1 overlap with the high-intensity line γ_0. The highest intensity spectral satellites δ_1 and δ_2 have been observed only for the line β_0 (Fig. 2b). The constancy of the fre-

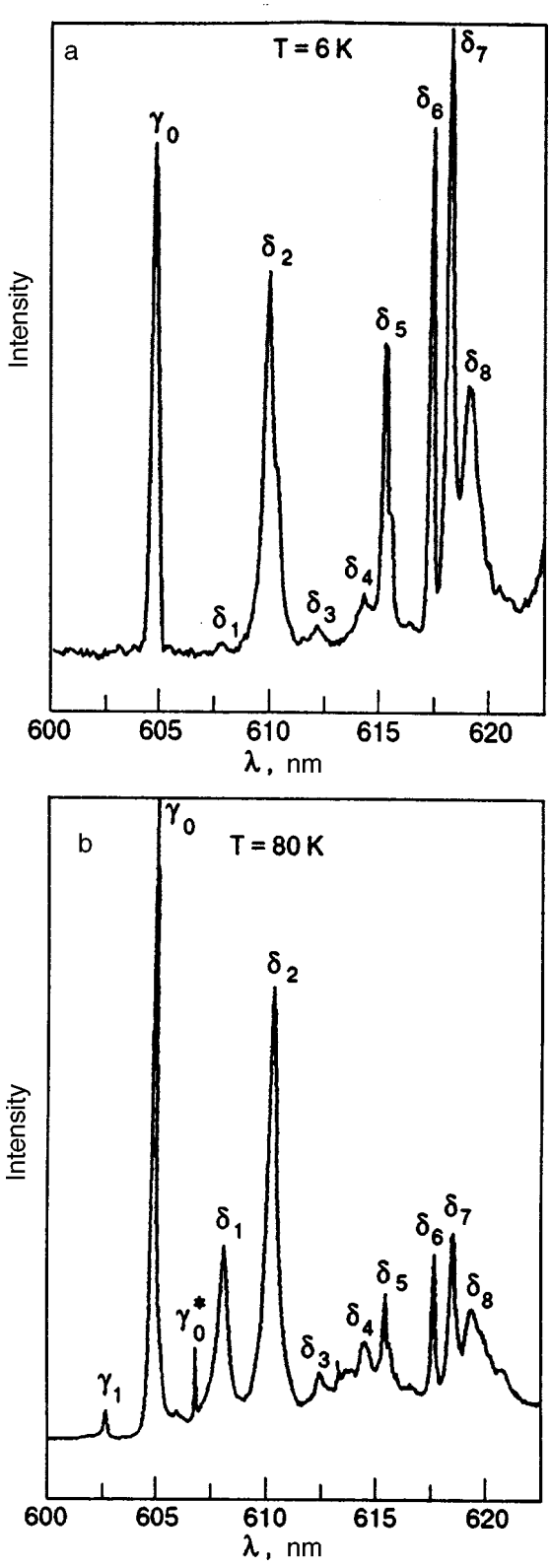

FIG. 3. Fragments of the luminescence spectrum of a Y_2SiO_5:Pr^{3+} crystal at different temperatures T (in K): 6.0 (a) and 80 (b).

quency intervals determining the position of the spectral satellites δ_1 and δ_2, as well as the temperature dependence of their intensity lead to the conclusion that they are associated with absorption from the thermally populated Stark components δ_1 and δ_2 of the term $^3H_4$ (Fig. 1).

Excitation of Pr^{3+} ions at the $\delta_0 \rightarrow \beta_0$ transition (as well as at the transitions $\delta_0 \rightarrow \alpha_0$, $\delta_0 \rightarrow \alpha_1$ and $\delta_0 \rightarrow \alpha_2$ leads to the emergence of identical luminescence spectral fragments (Fig. 3) originating from two spectral lines γ_0 and β_0 coinciding resonantly with identical lines in the absorption spectrum (Fig. 2). The frequency intervals determining the positions of the lines δ_1 and δ_2 in the luminescence spectrum (Fig. 3) coincide exactly with those determining the position of the temperature-dependent spectral satellites δ_1 and δ_2 in the absorption spectrum (Fig. 2b). Hence nine spectral lines $\delta_0, \delta_1, \delta_2, \delta_3, \delta_4, \delta_5, \delta_6, \delta_7, \delta_8$ (Fig. 3) can be identified with optical transitions from the metastable levels β_0 and γ_0 to nine Stark components of the term $^3H_4$ (Fig. 1). With increasing temperature, the luminescence spectrum (Fig. 3) shows a change in the intensity of certain spectral lines due to known mechanisms of phonon stimulation of parity-forbidden optical transitions.[9,10] At $T = 80$ K, the luminescence spectrum (Fig. 3b) acquires a line γ_1 that coincides resonantly with the identical line in the absorption spectrum (Fig. 2b) associated with emission from the thermally populated Stark component γ_1 (Fig. 1). An exact coincidence of the spectral lines coresponding to resonance transitions $\delta_0 \leftrightarrow \beta_0$ and $\delta_0 \leftrightarrow \beta_0$ (Fig. 1) in the absorption (Fig. 2) and luminescence (Fig. 3) spectra of the YSO:Pr^{3+} crystal is in conformity with the well-known fact that the luminescence of the Pr^{3+} ion takes place from two metastable levels β_0 and γ_0.[6,9–15] Consequently, one of the two spectral line groups conforms to the energy level diagram for the impurity ion Pr^{3+} (Fig. 1), which makes it possible to determine the Stark splitting of the terms $^3H_4$, $^1D_2$, and to determine the relative arrangement of the terms $^3H_4$, $^1D_2$ and $^3P_0$ of the same type of optical centers Pr^{3+} (Fig. 1).

The spectral position and number of weaker though sharper spectral lines (marked by letters with asterisks in Fig. 2) in the absorption spectrum of the YSO:Pr^{3+} crystal do not conform to the energy level diagram of the impurity ion Pr^{3+} with the above-mentioned Stark splitting of terms $^3H_4$ and $^1D_2$, as well as with the relative arrangement of terms $^3H_4$, $^1D_2$, and $^3P_0$ (Fig. 1). The spectral lines γ_0 and γ_0^* were attributed by Holliday *et al.*[7] to the absorption of impurity ions Pr^{3+} localized at various cation sites of the YSO crystal.[3] The half-width positions of the spectral lines γ_0 and γ_0^* were 30 and 10 Hz, respectively,[7] which correlates with the results of our measurements. The number of ''narrow'' spectral lines as well as their position in the spectrum (Fig. 2) lead to the assumption that they are indeed associated with the absorption of impurity ions Pr^{3+} localized at the other cation site in the YSO crystal.[3] All ''narrow'' spectral lines can be interpreted by using a simplified energy level diagram for Pr^{3+} ion (Fig. 1), but with different Stark splittings for terms $^3H_4$, $^1D_2$, and with different energy parameters determining the relative position of the terms being analyzed. The spectral lines β_0^*, γ_0^*, γ_2^*, γ_3^* and γ_4^* correspond to the absorption of impurity centers Pr^{3+} of the second type, associated with the optical transitions from the lowest Stark component of the term $^3H_4$ to Stark components of the term $^1D_2$ and to the term $^3P_0$ (Fig. 1). It can be assumed that the coincidence of the spectral line γ_1^* with the spectral line γ_0 of the first type of optical centers is accidental (Fig. 2). We

shall not analyze the ''narrow'' spectral lines in the region of optical transitions involving the terms $^3P_1$ and $^1I_6$ because of their ambiguous interpretation. At present, we have not been able to obtain luminescence spectrum for selective excitation of the crystal at the lines β_0^* or γ_0^*. Hence Stark splitting of the term $^3H_4$ for the Pr^{3+} optical centers of the second type remains undetermined. The parameters obtained from the experimental spectra and defining the structure of the energy levels of the Pr^{3+} impurity ions of the second type are shown in parentheses in Fig. 1.

Thus, an analysis and interpretation of the optical spectra of the YSO:Pr^{3+} crystal lead to the conclusion (in contrast to the results obtained in Ref. 6) that the Pr^{3+} impurity ions occupy two nonequivalent cation sites in the YSO crystal lattice.[3] However, the number of nonequivalent positions of the Pr^{3+} impurity ion in the YSO crystal is not confined to just two. Holliday *et al.*[7] used the burnt dip external Stark effect in the YSO:Pr^{3+} crystal to show that γ_0 consists of four spectral lines and γ_0^* contains two spectral lines corresponding to nonequivalent positions of the Pr^{3+} ion, but only within the given cation vacancy site. The crystal field of various cation vacancies of the YSO crystal affects the relative shift of the center of gravity of terms $^3H_4$, $^1D_2$, and $^3P_0$ and their Stark splitting in different ways (Fig. 2). Hence it can be assumed that the spectral satellite observed 8.1 cm^{-1} above the spectral line β_0 on the energy scale in Ref. 8 corresponds to the absorption of Pr^{3+} ions occupying one of four nonequivalent positions within one type of cation sites in the YSO crystal lattice. At helium temperatures, the impurity ion may move within a cation lattice site with a characteristic frequency determined by the energy difference between the corresponding nonequivalent positions and the magnitude of the potential barrier separating these positions.[16] The existence of such a movement of impurity ions in the YSO:Pr^{3+} crystal was confirmed in the results obtained in Refs. 8 and 17.

According to the data presented in Ref. 3, different cation positions of Y^{3+} differ on the microscopic scale in the mean separation between Y^{3+} and the nearest oxygen ions. Moreover, one of the Y^{3+} positions is coordinated by six and the other by seven oxygen ions.[3] Since the ionic radius of Pr^{3+}(1.06 Å) is larger than that of Y^{3+}(0.92 Å), the impurity ions predominantly replace the cation position with a larger ion–ligand mean separation during crystal growth. This is reflected in the line intensity of the absorption spectrum of the Pr^{3+} impurity ions at various cation sites of the YSO lattice (Fig. 2). In the case of selective excitation to the absorption lines β_0, α_0, α_1 and α_2 of the Pr^{3+} impurity ions of one type, the luminescence spectrum at $T=6.0$ K contains only their spectral lines (Fig. 3a) which is a well-known fact in low-temperature spectroscopy of isolated impurity centers in solid matrices.[16] However, if the excitation conditions do not change, the luminescence spectrum acquires at $T=80$ K a ''narrow'' spectral line γ_0^* (the remaining eight lines cannot be distinguished on account of their overlapping with higher-intensity lines $\delta_0, \delta_1, \delta_2, \delta_3, \delta_4, \delta_5, \delta_6, \delta_7, \delta_8$) belonging to the Pr^{3+} centers of the second type (Fig. 3b). The ratio of the intensities of the lines γ_0^* and γ_0 at the peak in the absorption (Fig. 2b) and luminescence (Fig. 3b) spectra was 1:4.5 and 1:9.5, respectively. While exciting luminescence in the lines α_0, α_1 and α_2 (Fig. 2), we did not observe the line β_0^* in the luminescence spectrum. Hence the process of excitation energy transfer involves Stark components of the terms $^1D_2$ belonging to praseodymium ions localized at different cation sites. This is logical since Stark components belonging to praseodymium ions localized at different cation sites have close energy values just for the term $^1D_2$, while the components γ_1^* and γ_0 have identical energy values. However, the mechanism of excitation transfer between two types of Pr^{3+} optical centers is not clear as yet. Within a single unit cell of YSO, the mean separation between nonequivalent Y^{3+} cation sites is of the order of 3 Å. For such separations, the Foerster–Dexler mechanism of nonradiative energy transfer can be operative.[18] However, it is unlikely that Pr^{3+} impurity ions would exist in pairs at nonequivalent cation sites of the same unit cell. Moreover, the Foerster–Dexler mechanism of energy transfer is determined by the overlapping of the donor emission spectrum with the acceptor absorption spectrum, and hence the transfer effect must also be observed at $T=6.0$ K (Fig. 3a). This conclusion can also be applied to the same extent to the conventional mechanism of reabsorption which may take place on account of overlapping of the Stark components γ_1^* and γ_0 of various optical centers. The absence of luminescence in the Pr^{3+} centers of the second type at $T=6.0$ K (Fig. 3a) and its emergence at $T=80$ K (Fig. 3b) indicate that the phonons in the crystal matrix participate in the nonradiative energy transport between Pr^{3+} ions localized at different cation vacancies in the YSO crystal. Such a mechanism is known to exist[2] and the transport probability is $\sim T^4$. In order to confirm the validity of such a mechanism of nonradiative transfer, we require more comprehensive investigations of the temperature and concentration dependences of the intensity of luminescence of the Pr^{3+} centers of the second type.

Thus, we have shown that like many other rare earth ions, the Pr^{3+} impurity ions may occupy nonequivalent cation sites in the YSO crystal. The observed transport of the excitation energy between nonequivalent Pr^{3+} optical centers in the YSO crystal cannot be explained by the Foerster–Dexler mechanism. In order to verify the phonon-induced nonradiative energy transport between impurity centers, we must study in detail the temperature and concentration dependences of the luminescence intensity of the γ_0^* and γ_0 spectral lines.

*E-mail: malyukin@isc.kharkov.ua

[1] P. Lecog, J. Lumin. **60–61**, 948 (1994).
[2] B. C. Grabmaier, J. Lumin. **60–61**, 967 (1994).
[3] B. A. Maksimov, Yu. A. Kharitonov, V. V. Ilyukhin, and N. V. Belov, Kristallogr. **15**, 926 (1970) [Sov. Phys. Crystallogr. **15**, 806 (1971) .
[4] A. M. Tkachuk, A. K. Przhevusskii, A. G. Morozova *et al.*, Optika i Spektroskopiya **60**, 288 (1986).
[5] M. Mitsunaga, T. Takagahara, R. Yano, and N. Uesugi, Phys. Rev. Lett. **68**, 3216 (1992).
[6] N. V. Kuleshov, V. P. Mikhailov, S. A. Radkevich *et al.*, Optika i Spektroskopiya **77**, 244 (1994) [Optics and Spectr. **77**, 226 (1994)].
[7] K. Holliday, M. Croci, E. Vauthey, and U. P. Wild, Phys. Rev. B **47**, 14741 (1993).

[8] Yu. V. Malyukin, E. A. Manykin, N. L. Pogrebnyak *et al.*, JETP **81**, 260 (1995).
[9] I. B. Bersuker, *Electronic Structure and Properties of Coordination Compounds* [in Russian], Khimiya, Leningrad (1986).
[10] N. A. Kulagin and D. T. Sviridov, *Introduction to the Physics of Activated Crystals* [in Russian], Vyssha Shkola, Kharkov (1990).
[11] W. N. Yen, W. C. Scot, and A. L. Schawlow, Phys. Rev. A **136**, 271 (1964).
[12] C. A. Morrison and R. P. Leavit, J. Chem. Phys. **71**, 2366 (1979).
[13] H. H. Caspers, H. E. Rast, and R. A. Buchanan, J. Chem. Phys. **43**, 2124 (1965).
[14] S. Matthies and D. Welsch, Phys. Status Solidi B **6S**, 125 (1975).
[15] B. R. Reddy and L. E. Erickson, Phys. Rev. B **27**, 5217 (1983).
[16] I. S. Osad'ko, Phys. Rep. **206**, 45 (1991).
[17] Yu. V. Malyukin, Fiz. Nizk. Temp. **23**, 993 (1997) [Low Temp. Phys. **23**, 746 (1997)].
[18] V. L. Ermolaev, E. N. Bodunov, E. B. Sveshnikova, and T. A. Shakhverdov, *Nonradiative Energy Transport of Electronic Excitation* [in Russian], Nauka, Leningrad (1977).

Translated by R. S. Wadhwa

Determination of characteristic parameters of n-$Cd_xHg_{1-x}Te$ from quantum oscillations

R. I. Bashirov, V. A. Elyzarov, A. Yu. Mollaev, and R. R. Bashirov

*Kh. I. Amirkhanov Institute of Physics, Dagestan Scientific Center of the Russian Academy of Sciences, 367003 Makhachkala, Dagestan**

(Submitted February 22, 1996; revised December 8, 1997)
Fiz. Nizk. Temp. **24**, 577–579 (June 1998)

The longitudinal and transverse magnetoresistances are studied in solid solutions of n-$Cd_xHg_{1-x}Te$ with $x=0.19$ and 0.226 at hydrogen and helium temperatures. Effective masses at the bottom of the conduction band are determined from an analysis of oscillation amplitudes at helium temperatures. The values of g-factors are determined from the splitting of the first magnetoresistance peak. © *1998 American Institute of Physics.*
[S1063-777X(98)00906-2]

The additional 0^+-peak and the splitting of 1,2,3,... peaks of quantum oscillations of magnetoresistance observed in Ref. 1, into two peaks[2] is widely used for determining some characteristic parameters of semiconductors, such as the spectroscopic splitting factor and the electron effective mass. The effective mass and the g- factor of $Cd_xHg_{1-x}Te$ solid solution were determined for a number of compositions.[3–7] Transport processes in $Cd_xHg_{1-x}Te$ in quantizing magnetic fields remain the objects of considerable interest,[8–11] although the use of experimental data for obtaining band characteristics of the material involves considerable difficulties. The problems are generated by the heterogeneity of the composition of solid solutions of $Cd_xHg_{1-x}Te$ arising due to the difference between the liquidus and solidus curves on the state diagrams as well as heterogeneity in the impurity distribution. Further investigations of the system are required to improve the reliability of the characteristics of solutions with preset compositions.

In this communication, we describe the results of low-temperature investigation of solid solutions of n-$Cd_xHg_{1-x}Te$ with $x=0.19$ and electron concentration $n=8\cdot10^{15}$ cm^{-3} (sample 1) and $x=0.226$ for $n=1.08\times10^{15}$ cm^{-3} (sample 2) at $T=4.2$ K. Such a choice of the sample parameters makes it possible to compare experimental data with the results calculated over a wide range of nonparabolicity of the conduction band.

The samples having the size $7\times1.7\times0.7$ mm were cut from two ingots obtained by recrystallization from the two-phase mixture and annealed in mercury vapor, were etched in a mixture of butanol and bromine in the ratio 95:5. Indium probes were soldered to them. The composition of the samples were determined from Hall measurements in the intrinsic conductivity range by using Schmit's formula[12]

$$E_g=1.59x-0.25+5.233\cdot10^{-4}T(1-2.08x)+0.327x^3, \quad (1)$$

where T is the sample temperature.

The transverse (ρ_{xx}) and longitudinal (ρ_{zz}) magnetoresistance were measured in stationary magnetic fields at liquid helium and nitrogen temperatures. The field dependences of these effects and their second derivatives were recorded by an $x-y$ recorder (Fig. 1). In order to determine the position of oscillation peaks on the magnetic field scale and their maximum number, we used differentiating RC-circuits. The accuracy of the method in the stationary field was $\pm2\%$. Table I contains some characteristics of n-$Cd_xHg_{1-x}Te$ (n and μ are the electron concentration and mobility) and the results of investigations at 4.2 and 20 K.

Let us now consider the results of measurements presented in Fig. 1 and in Table 1. In the liquid helium temperature range, the splitting of the first three peaks of ρ_{xx} and ρ_{zz} and the emergence of an additional 0^+-peak on the $\partial^2\rho_{xx}/\partial H^2$ curves are observed. It should be noted that the additional 0^+ peak in sample 1 is observed at 4.2 K nor only in the transverse, but also in the longitudinal magnetoresistance. The positions of peaks H_N^- and H_N^+ on the magnetic field scale are determined by the formulas[13,14]

$$H_N^+=n^{2/3}\frac{\hbar c}{e}(\sqrt{2}\pi^2)^{2/3}\left[\sum_{M=0}^{N}(\sqrt{M}+\sqrt{M+\beta})\right]^{2/3}, \quad (2)$$

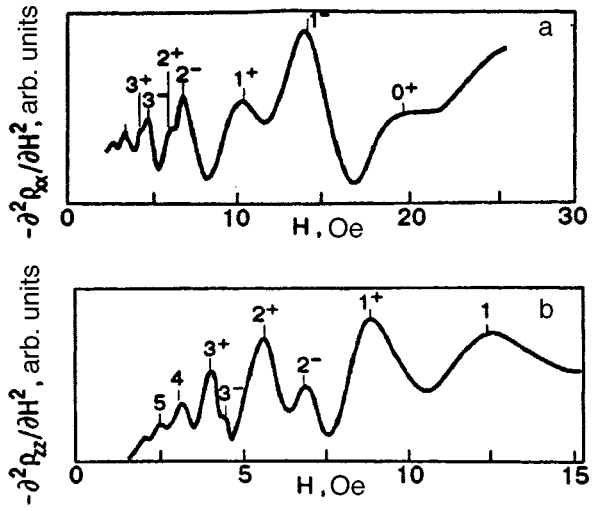

FIG. 1. Dependences of the second derivative of the transverse magnetoresistance of sample 1 (a) and of the longitudinal magnetoresistance of sample 2 (b) on the magnetic field strength at $T=4.2$ K.

TABLE I. Physical characteristics of n-$Cd_xHg_{1-x}Te$ samples at 4.2 and 20 K.

Sample	x, mole	T, K	E_g, meV	n, 10^{15} cm^{-3}	μ, 10^3 cm^2/V·s	m^*/m_0, 10^{-2}		m_0^*/m_0, 10^{-2}		$\|g\|$		γ
						Exp.	Theor	Exp.	Theor	Exp.	Theor	
1	0.19	20	61	14	184	-	-	-	-	-	-	-
		4.2	55	8	265	0.81	0.88	0.44	0.49	112	104	0.95
2	0.226	20	119	3.12	45	-	-	-	-	-	-	-
		4.2	115	1.08	70	1.38	1.32	1.08	1.03	58	74	0.28

$$H_N^- = n^{2/3}\frac{\hbar c}{e}(\sqrt{2}\pi^2)^{2/3}\left[\sum_{M=1}^{N}(\sqrt{M}+\sqrt{M-\beta})\right]^{2/3}, \quad (3)$$

where $\beta = gm^*/2m_0$, m^* being the effective mass of an electron at the Fermi level and m_0 the mass of a free electron.

The value of β was determined by us from the ratio H_I^-/H_I^+ for split peaks of the first maximum and amounts to 0.454 for the first sample and 0.4 for the second sample.

The value of the electron effective mass at the Fermi level was determined from the ratio of experimentally measured amplitudes of the peaks for sample 1 for 7.8 kOe at $T = 4.2$ and 2.19 K and was found to be $m^* = 8.1\cdot 10^{-3} m_0$.

The determination of the Fermi level energy E_F^N for small quantum numbers N should be refined. The resonance condition

$$E_F^N = \left(N+\frac{1}{2}\right)\hbar\omega_c \pm \frac{1}{2}\beta\hbar\omega_c, \quad \text{where} \quad \omega_c = \frac{eH}{m^*c},$$

and formulas (2) and (3) lead to

$$E_F^{N+} = 1.21E_F\frac{(N+1/2+\beta/2)}{[\Sigma_{M=0}^{N}\sqrt{M}+\sqrt{M+\beta}]^{2/3}},$$

$$E_F^{N-} = 1.21E_F\frac{(N+1/2-\beta/2)}{[\Sigma_{M=1}^{N}\sqrt{M}+\sqrt{M-\beta}]^{2/3}},$$

where $E_F = (\hbar^2/2m^*)(3\pi^2 n)^{2/3}$ is the Fermi level in zero magnetic field. For small N, the oscillations of the Fermi level in a magnetic field can noticeably affect the values being measured. For example, for $\beta = 0.454$ we have $E_F^{0+} = 1.15E_F$, $E_F^{1-} = 1.08E_F$, $E_F^{1+} = 1.06E_F$, and so on. Since the value of the effective mass m^* at the Fermi level was determined from the ratio of oscillation amplitudes for H_1^+, we have $m_0^* = m^*\alpha^{-1/2}$ for the effective mass at the bottom of the conduction band, where $\alpha^{1/2} = [1.06(2E_F/E_g)+1]$, which gives $m_0^* = 4.38\cdot 10^{-2} m_0$. Calculations based on Kane's two-band model give the values $m^* = 0.88\cdot 10^{-2} m_0$ and $m_0^* = 0.49\cdot 10^{-2} m_0$.

Here $E_g = 0.055$ eV at 4.2 K and $E_F = eh/m^*\Delta(1/H) = 0.022$ eV, where $\Delta(1/H) = (2e/\hbar c)\times(1/(3\pi^2 n))^{2/3}$ is the period of oscillations. Using the values of β and the effective mass m^* obtained at 4.2 K, we obtain the value of the g-factor at the Fermi level: $|g| = 112$.

Carrying out a similar procedure for sample 2, we obtain the effective mass and the spectroscopic splitting factor given in the table.

According to Tsidil'kovskii,[14] the spectroscopic splitting factor determining the scale of the splitting of Landau levels can be represented in the form

$$|g| = 2\frac{m_0}{m_0^*}\frac{\Delta}{3E_g+2\Delta}, \quad (4)$$

where Δ is the energy of spin–orbit splitting of the valence band. The obtained values of β for the two samples make it possible to estimate the energy of spin–orbit splitting $\Delta \approx 0.8$ eV.

In the case of narrow-band materials, $\Delta \gg E_g$, and hence the spin–orbit interaction weakly affects the value of the g-factor. At the same time, the g-factor strongly depends on small variations of concentration in the vicinity of the junction between a gapless semiconductor to an ordinary superconductor, which is associated with the corresponding variation of the effective mass at the Fermi level.

The departure from parabolicity of the conduction band in the Kane model is characterized by the parameter $\gamma = k_F P/E_g$,[15] where $k_F = (3\pi^2 n)^{1/3}$ is the wave vector for electrons at the Fermi level, and the matrix element of the momentum operator for $Cd_xHg_{1-x}Te$ alloys is $P = 8\times 10^{-8}$ eV·cm^{-1}.[10] The spectrum of charge carriers is parabolic ($E \sim k^2$) when the condition $\gamma \ll 1$ is satisfied, this is observed near the bottom of the conduction band. As the band gets filled, the energy–momentum relation starts deviating from the quadratic law. The parameters γ for samples 1 and 2 given in Table I give an idea about the extent of nonparabolicity of the conduction band at the Fermi level in both cases.

Table I shows that the values of the effective mass at the Fermi level and at the bottom of the conduction band as well as the value of the g-factor at the Fermi level are in good agreement with the theoretical values both for a sample with a strong deviation from parabolicity in the conduction band and for one with a weak nonparabolicity.

This research was carried out under financial support of the Russian Foundation of Fundamental Studies (project No. 97-02-16545).

*E-mail: kamilov@physics.sinol.ru

[1] Kh. I. Amirkhanov, R. I. Bashirov, Yu. E. Zakiev, and A. Yu. Mollaev, in *Abstracts of Papers to the IX All-Union Conference on Low-Temperature Physics*, Leningrad (1962); Kh. I. Amirkhanov, R. I. Bashirov, and Yu. E. Zakiev, Dokl. Akad. Nauk SSSR **148**, 1279 (1963) [Sov. Phys. Dokl. **8**, 182 (1963)]; Fiz. Tverd. Tela (Leningrad) **5**, 469 (1963) [Sov. Phys. Solid State **5**, 340 (1963)].

[2] M. S. Bresler, R. V. Parfen'ev, and S. S. Shalyt, Fiz. Tverd. Tela (Leningrad) **7**, 1266 (1965) [Sov. Phys. Solid State **7**, 1025 (1965)].
[3] G. A. Antcliffe, Phys. Rev. B **2**, 345 (1970).
[4] K. Suizu and S. Narita, Solid State Commun. **10**, 627 (1972); Phys. Lett. **43A**, 353 (1973).
[5] H. Kahlert and G. Bauer, Phys. Rev. Lett. **30**, 1211 (1973).
[6] N. N. Berchenko, V. E. Krevs, and M. V. Pashkovskii, Sov. Phys. Solid State **14**, 2815 (1972) [Sov. Phys. Solid State **14**, 2447 (1973)].
[7] S. A. Aliev, Fiz. Tekhn. Poluprovodn. **9**, 2212 (1975) [Sov. Phys. Semicond. **9**, 1438 (1975)].
[8] Yu. G. Arapov, B. B. Ponikarov, I. M. Tsidil'kovskii, and N. G. Shelushinina, Fiz. Tekhn. Poluprovodn. **13**, 684 (1979) [Sov. Phys. Semicond. **13**, 402 (1979)].
[9] K. Takita, T. Ipposhi, and K. Masuda, Appl. Phys. Lett. **50**, 833 (1987).
[10] S. B. Rafol, I. K. Sou, and J. P. Fanrie, J. Appl. Phys. **70**, 4326 (1991).
[11] S. B. Rafol, P. S. Wijewanasurya, I. K. Sou *et al.*, J. Appl. Phys. **73**, 216 (1993).
[12] J. L. Schmit and E. L. Stelzer, J. Appl. Phys. **40**, 4865 (1969).
[13] L. E. Gurevich and A. L. Efros, Zh. Eksp. Teor. Fiz. **43**, 561 (1962) [Sov. Phys. JETP **16**, 402 (1962)].
[14] I. M. Tsidil'kovskii, *Electrons and Holes in Semiconductors* [in Russian], Nauka, Moscow (1972).
[15] N. N. Berchenko and M. V. Pashkovskii, Usp. Fiz. Nauk **119**, 323 (1976) [Sov. Phys. Usp. **19**, 872 (1976)].

Translated by R. S. Wadhwa

PHYSICAL PROPERTIES OF CRYOCRYSTALS

Continuous radiation of excimer complexes in argon and neon crystals

A. G. Belov,*) I. Ya. Fugol', and E. M. Yurtaeva

B. Verkin Institute for Low Temperature Physics and Engineering, National Academy of Sciences of the Ukraine, 310164 Kharkov, Ukraine

(Submitted January 14, 1998; revised February 10, 1998)
Fiz. Nizk. Temp. **24**, 580–594 (June 1998)

This research is devoted to an analysis of continuous luminescence spectra of argon and neon crystals in the ranges 4–7 and 9–17 eV, respectively. The experimental results of this research are compared comprehensively with the data on the gaseous phase and with the luminescence of exciplexes of inert-gas halogenides. It is proposed on the basis of the detailed comparison of different experimental data that the continuum with a peak at 6.2 eV can be identified with radiation decay of the excimer complex $Ar_2^+O^-$. The formation of a similar exciplex $Ne_2^+O^-$ with charge transfer is observed in the neon matrix doped strongly with oxygen. © *1998 American Institute of Physics.* [S1063-777X(98)01006-8]

1. INTRODUCTION

Broad continuous radiation in the VUV spectral region is typical of complex processes of energy relaxation in excited inert gases R* and their compounds with other elements (RX)*. This radiation can be due to the following three factors: (1) the presence of a broad energy gap between the excited (R*) and the ground (R) state of a rare gas; (2) the formation of strongly coupled molecular excimers R_2^* and RX* in the excited state, and (3) the steep repulsive term of the ground state R_2 and RX, which determines the broad continuous spectrum of the observed radiation. The coupling in excimer molecules can be of various natures. We can single out the three basic types of interaction: resonant interaction, covalent bond, and interaction with charge transfer. The resonant interaction is observed in compounds of the R_2^* type. The dissociation energy D_e for such molecules is usually low ($\leqslant 0.7$ eV).[1] The covalent bond is manifested during the interaction of noble gas atoms with the lowermost valence excitations of other elements, e.g., oxygen: RO*($^1S,^1D$).[2] The binding energy varies from 0.1 to 0.7 eV and attains its maximum value in heavy inert gases. Complexes R^+X^- with charge transfer are characterized by the strongest coupling and are typical of halogenides of inert gases with $D_e \approx 5$ eV.[1] Such complexes are also inherent in compounds of inert gases with other elements with positive affinity to electron: H, OH, O, and S.[2–5] In real molecules, several types of interaction can operate simultaneously. Owing to a large depth of the potential well for R^+X^- complexes, the radiant energy of such molecules is much lower than for R_2^*. Thus, excimer continuums of inert gases and their compounds can be observed in a wide spectral range from 9.7 eV(Ar_2^*) to 1.7 eV(XeO*), which makes them attractive objects for laser generation.[2,6,7]

Recently, the attention of researchers was attracted by the ''third continuum'' (III) observed in luminescence of inert gases both in the gaseous state,[8–13] and in crystals.[14–23] In contrast to the second continuum ($R_2^* \rightarrow R+R$) and first continuum ($R_2^{**} \rightarrow R+R$), the nature of the third continuum is not completely clear. It lies approximately 3 eV below the radiant energy of R_2^* and hence cannot be attributed to neutral excitations of noble gases R_2^*. Its origin can be associated either with a system of higher-lying ionic states of pure inert gases (R_2^+, R_2^{2+}), or with a system of lower-lying states of compounds of inert gases with impurities. At present two basic versions of the origin of the III continuum in the gaseous phase exist: (*A*) $R_2^{+*} \rightarrow R^+ + R$[8,24] and (*B*) $(R_2^{2+})^* \rightarrow R^+ + R^+$.[25] It is assumed that radiative transitions occur to repulsive terms of ionic states. At the same time, transitions to bound lower-lying molecular terms R_2^+ and R_2^{2+} were not observed in the spectra of the gaseous phase. In the solid phase, the continuous radiation in this spectral range was assumed to be of impurity origin since its intensity increased upon addition of oxygen and nitrogen[16,18] and decreased after purification of the initial gas.[19,26] In some publications,[15,18,20] this radiation was attributed to excimers (RO*). Subsequently,[22,23] another version was put forth. An analysis of photoexcitation spectra for the III continuum in solid argon proved that for the excitation energy above the bottom E_g of the conduction band, the probability of populating the states responsible for this radiation is approximately twice as high as for the energy of exciton excitation. This observation formed the basis of the assumption concerning the ionic origin of the observed continuum, namely, its affiliation to $(Ar_2^+)^*$ in analogy to version (*A*) for the gaseous phase. The aggregate of data on the temperature dependence and thermoluminescence obtained in Refs. 22 and 23 can be described under the assumption that positive and negative charges generated during excitation are accumulated in the crystal. Thus, the main problem at the present stage lies in the establishing the fact that the origin of III continuums in the gaseous and solid phases is the same. It is

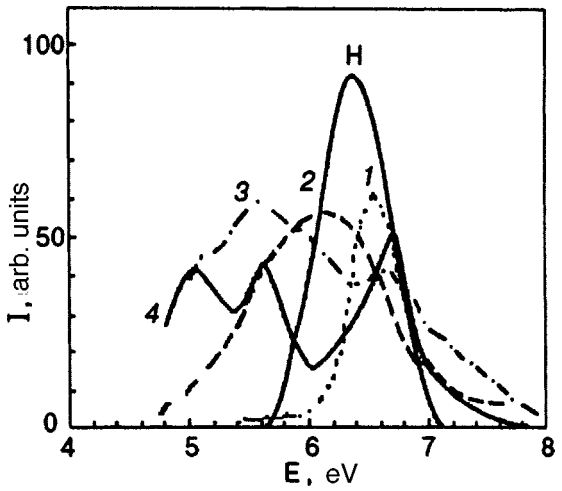

FIG. 1. Spectra of the III continuum in the gaseous phase of Ar for various gas densities ρ, cm^{-1}:10^{17} (curve *1*),[28] 1.3×10^{19} (curve *2*),[27] 2.7×10^{19} (curve *3*),[27] 4.6×10^{20} (curve *4*),[11] $\rho=2.2\times10^{22}$ cm^{-1}(*H*).

also important to determine radiant states in each phase taking into account peculiarities of energy relaxation.

For this purpose, we consider in greater detail the results of experiments with argon. The spectral parameters of the III continuum in the gaseous phase of Ar turned out to be very unstable, and the results were contradictory in some cases. The position on the energy scale, half-width, and intensity depend considerably on the gas pressure and other experimental conditions (Fig. 1).[8,11,27,28]

An increase in the gas density ρ from 10^{16} to 10^{19} cm^{-3} leads to a decrease in the ratio of intensities of the III and II continuums by a factor of 25, and the ratio $I_{III}/I_{II}=0.2$ for $P=1$ bar($\rho=2.7\times10^{19}$ cm^{-3}).[27,28] A further increase in the Ar density (upon a transition to solid argon) to $\rho=10^{22}$ cm^{-3} can lead to further decrease in this ratio.[24] Klein and Carvalho[24] noted that the intensity of luminescence of the III continuum in the gaseous phase was quite high, but it was not observed in the liquid and solid phases. However, other authors (see, for example, Refs. 15–18) reported on continuous luminescence in crystalline argon with a peak at 6.25 eV, whose position was virtually independent of experimental conditions. The intensity ratio I_{III}/I_{II} for continuums in the crystal was determined by the purity of the initial gas and increased after the addition of oxygen.[16,18] A similar continuum with a peak at 6.3 eV along with two other bands at 7.6 and 7.1 eV was also observed in the solid mixture Ne–Ar–O_2.[29] It should be noted that, conversely, the addition of oxygen in the gaseous phase led to the suppression of the III continuum.[30] Recent experiments with gaseous mixtures of argon with oxygen-containing molecules revealed the presence of three narrow excimer luminescence bands with peaks at 8.3, 6.8, and 6.0 eV.[10,31] The two latter bands lie against the background of a broad continuum with $E_{max}=6.52$ eV (Fig. 2). The observed bands were attributed to transitions from the lowermost state of the complex $Ar^+O^-(^3\Pi)$ with charge transfer to the ground energy level and two lowermost valence terms $ArO(X\,^3\Pi)$ and $ArO^*(1\,^1\Sigma$ and $^1\Pi)$ respectively (Fig. 2b).

Close spacing but different behavior of continuous luminescence in the gaseous and solid phases of argon necessitate a more detailed analysis of its origin. The search and analysis of the III continuum in the luminescence of solid Ne are also of considerable interest. Recent studies revealed its presence in the gaseous phase.[12,28] The observation of a similar continuum in the crystal for which the existence of positive Ne_2^+ ions was proved in Ref. 32 could clarify the ionic origin of luminescence of the III continuum in inert gas crystals.

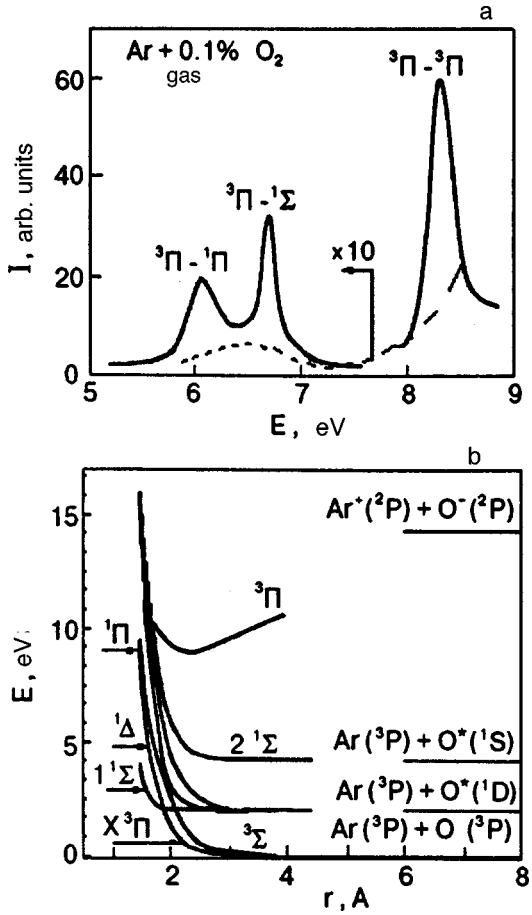

FIG. 2. (a) Luminescence spectrum for ArO in the gaseous phase,[5,10,31] the dashed curve corresponds to pure Ar radiation. (b) Schematic diagram of ArO potentials.

In this paper, we describe the results of analysis of pure and impurity Ar and Ne crystals with a high oxygen concentration. The experimental technique is described in Sec. 2, and the main experimental results obtained from an analysis of concentration and temperature dependences of continuous luminescence in Ar and Ne are presented in Sec. 3. Sections 4.1 and 4.2 are devoted to an analysis of spectroscopic properties of the observed radiation in Ar and Ne crystals as well as the III continuum in the gaseous phase. A comparative analysis is carried out for luminescence of the molecular continuum II of Ar_2^*. In Sec. 4.3, it is proposed that the crystalline continuum in argon should be identified as an excimer compound with oxygen. A comparison is made with fluorides of rare gases. Peculiarities of excitation spectra and temperature dependence are discussed in Secs. 4.4 and 4.5 proceeding from two points of view on the origin of the III continuum. Finally, in Sec. 4.6 estimates are made and as-

sumptions concerning the identification of luminescence observed in concentrated Ne–O mixtures are formulated.

2. EXPERIMENTAL TECHNIQUE

Spectroscopic experiments with pure crystals of the inert gases Ar and Ne as well as their mixtures with oxygen were carried out by the method of luminescent analysis with the excitation of samples by monochromatic electrons with the energy $E_e \cong 2$ keV. The crystals were grown by evaporation from the gaseous phase at the condensation temperature $T_c = 8$ K for Ne and $T_c = 30$ K for Ar and then cooled slowly. The obtained polycrystals were optically transparent. The initial gases were preliminarily purified from impurities in a special setup by using liquid lithium. Optical experiments were made in a helium flow cryostat with controlled temperature of a copper substrate in the range from 2.5 to 78 K. Radiation was recorded simultaneously in the visible and VUV spectral ranges by using spectral devices DFS-24 and VMR-2 in the individual quantum counting mode. The spectral resolution was 0.015 and 0.05 nm for the visible and VU ranges, respectively. The working vacuum in the cryostat was sustained at 10^{-10} bar. The experimental technique is described in greater detail in Ref. 20.

3. RESULTS

3.1. Argon

Figure 3 shows luminescence spectra of Ar crystals grown from the initial gas of various purity and molar concentration c of oxygen varying from 10^{-4} to 1%. The spectra contain the well-known molecular continuum (II) $Ar_2^*(^{1,3}\Sigma_u^+ \rightarrow X\ ^1\Sigma_g^-)$ with $E_{max} = 9.8$ eV and the continuous radiation (III?) under investigation observed in the interval from 5.6 to 7.1 eV. The peak of this continuum lies near 6.25 eV and has a half-width $\Delta = 0.8$ eV. In addition, one more weak continuous band with $E_{max} = 4.92$ eV and $\Delta = 0.335$ eV was detected in the range of near UV radiation. We denote these continuums as H and G, respectively. The band G is approximately two orders of magnitude weaker than the H band. The intensity ratio for these bands is virtually independent of oxygen concentration. In the visible range of the spectrum, we also observed[20] the well-known luminescence of the excimer complex $ArO^*(2\ ^1\Sigma \rightarrow 1\ ^1\Sigma)$ with $E_{max} = 2.2$ eV, whose intensity increases after the addition of oxygen. For a high concentration of O_2 in the Ar matrix ($c \approx 1\%$), the spectrum also acquires a series of molecular bands corresponding to radiation of $O_2^*(C\ ^3\Delta_u^+ \rightarrow X\ ^3\Sigma_g^-)$, and lying in the range 1.8–3 eV.[33]

An increase in oxygen concentration intensifies the luminescence of continuum H due to quenching of intrinsic luminescence of the matrix. Figure 3 demonstrates the redistribution of intensities between the bands of Ar_2^* and H in favor of the latter band upon an increase in the O_2 content in the matrix. Figure 4 shows the dependence of the intensity ratio I_H/I_{Ar} on oxygen concentration on the logarithmic scale. In the O_2 concentration range from 10^{-4} to 1%, the ratio I_H/I_{Ar} varies approximately by a factor of 250. The absolute intensity peak of the H band is attained for the intermediate concentration $c = 10^{-1}$%.[18] It should also be noted that a similar continuous radiation with a peak at 7.6 eV was observed in the spectra of argon containing nitrogen, the peak intensity being also attained for $c \cong 10^{-1}$% N_2.[18]

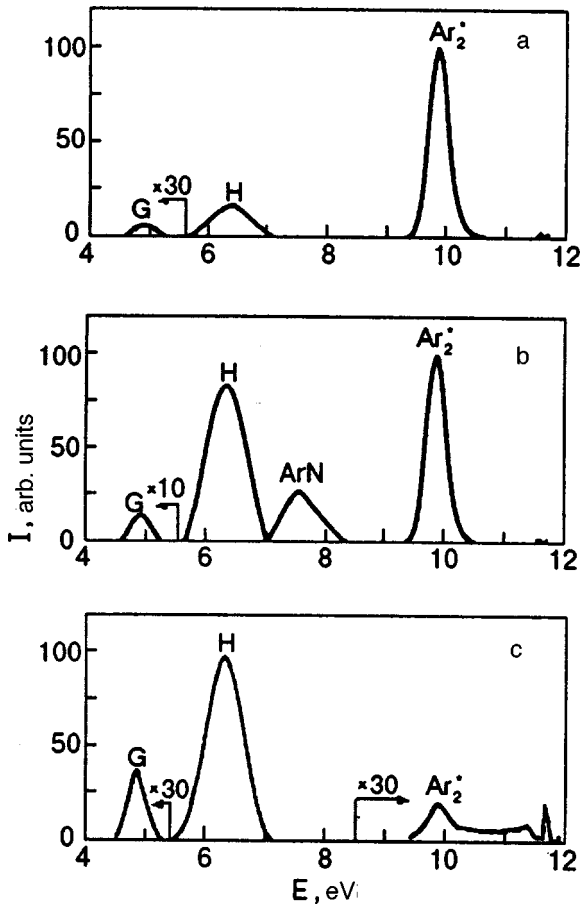

FIG. 3. Luminescence spectra for $Ar–O_2$ crystal with various oxygen concentrations c,%: 10^{-4} (a), 10^{-3} (b), and 1 (c).

Figure 5 shows the variation of the shape and position of the G and H bands in Ar crystals for oxygen concentrations varying from 10^{-3} to 1%. In spite of considerable variation of impurity content, and hence the radiation intensity, the

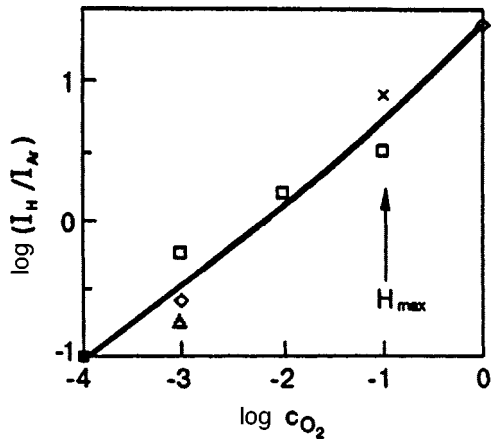

FIG. 4. Dependence of the relative intensity of the H band on the oxygen concentration in the argon matrix. The arrow shows the position of the absolute intensity peak of the H band.[18]

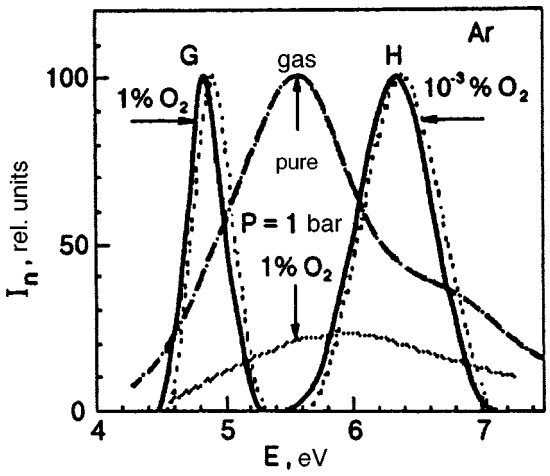

FIG. 5. Dependence of the shape and position of the *G* and *H* bands on oxygen concentration: solid curve corresponds to 1% O_2 and dashed curve to 10^{-4}% O_2 (normalized intensity). The spectrum of gaseous Ar (pure and with 1% O_2 impurity) is also shown.[30]

shape of both bands virtually remains unchanged. Only a small shift of the peak towards lower energies is observed from a high concentration of O_2. This shift amounts to 0.07 eV for the *H* band and 0.08 eV for the *G* band. A weak dependence of the shape of luminescence bands on oxygen concentration differs basically from the changes occurring in the gaseous phase, in which the addition of oxygen lads to the emergence of two narrower bands corresponding to the compound $Ar^+O^-(^3\Pi)$ against the background of the initially observed continuum.[31] The difference between the spectra of strongly and weakly concentrated solutions of crystalline Ar is insignificant, indicating the invariability of the corresponding emitting centers in nominally pure Ar and in the crystal containing an appreciable amount of oxygen.

The addition of xenon to Ar crystals containing oxygen leads to effective quenching of the *G* and *H* bands (Fig. 6). The luminescence spectrum acquires in this case the characteristic bands $XeO^*(2\,^1\Sigma \rightarrow 1\,^1\Sigma)$, described by Goodman *et al.*[34] The intensity of these bands increases with Xe concentration and attains its peak value approximately at 1% Xe. The dependences of intensities of the *G* and *H* bands on Xe concentration are absolutely identical. These dependences resemble the corresponding dependence for $ArO^*(2\,^1\Sigma \rightarrow 1\,^1\Sigma)$. Although the addition of Xe also leads to quenching of intrinsic luminescence of Ar_2^*, the shape of the $I_H(c)$ curve differs considerably from that of $I_{Ar}(c)$. The latter virtually remains unchanged in the region of low Xe concentrations, i.e., is less sensitive to the inert gas impurities than the *H* band. This is probably due to the fact that the decrease in the intensities of the *G* and *H* bands is mainly due to the interception of excitation by lower-lying terms (XeO^*).

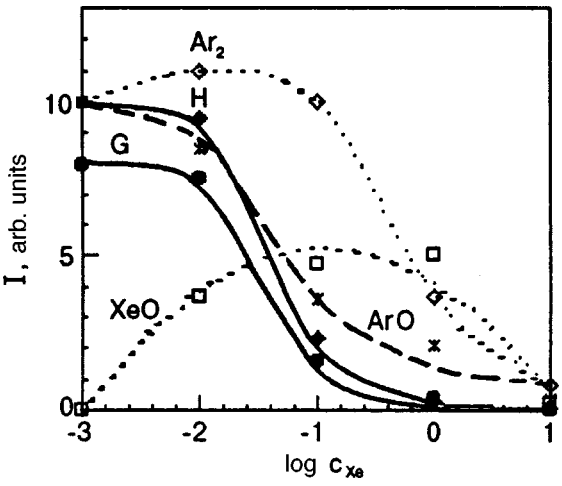

FIG. 6. Suppression of *G* and *H* bands by Xe impurity in Ar crystals. The obtained curves are compared with intensities I_{Ar}, I_{ArO}, and I_{XeO}.

Concluding the section, let us consider the temperature dependences for the *H*, ArO^*, and Ar_2^* bands. In this case, a correlation in the behavior of luminescence of the *H* and ArO^* bands under various experimental conditions is also observed. Figure 7 shows the temperature dependences for samples grown from preliminarily purified and nonpurified gaseous Ar. The ratio of the intensities of the *H* and Ar_2^* bands at $T=5$ K was 0.16 and 1.2, respectively. The shape of the $I_H(T)$ curve clearly depends on the sign of temperature gradient. Sample heating leads to a step-wise change in the intensity with a kink near $T=13$ K. This segment of the temperature dependence is similar to that observed in Refs. 18, 23 and 35. Sample cooling down to very low temperatures leads to a monotonic increase in the intensities of the *H* and ArO^* bands. The behavior of such bands obviously differs from the behavior of $Ar_2^*(T)$ whose intensity, on the contrary, increases with temperature. This increase is of a step nature. The intensity of $Ar_2^*(T)$ starts increasing approximately at 15 K, and the shape of this curve is similar to that of defective component of radiation of $Kr_2^*(T)$.[36] It was found that the total decrease in the intensity of the *H* band: $\Delta I_H = I_H(T_{min}) - I_H(T_{max})$ is not connected quantitatively with an increase in the intensity of the Ar_2^* band: $\Delta I_{Ar} = I_{Ar}(T_{min}) - I_{Ar}(T_{max})$. In a pure sample, $\Delta I_H / \Delta I_{Ar} = 0.23$, while the value of this ratio in a sample containing impurities is an order of magnitude larger and amounts to 3.4. The general form of the $\Delta I(T)$ curves is shown in Fig. 8. The changes in the intensities of the *H* band upon heating of the sample Ar-10^{-3}% O_2 are more pronounced, while for the Ar_2^* band they are less significant.

It should also be noted that Ar crystals with a high oxygen impurity concentration display clearly manifested thermoluminescence in the molecular transitions of oxygen $C^3\Delta_u^+ \rightarrow X^3\Sigma_g^-$. In the absence of an additional excitation, the heating of preliminarily irradiated samples led to the emergence of bluish glow at $T \geqslant 15$ K (see Fig. 7). The thermoluminescence intensity peak was attained at 23 K, while its complete quenching was observed at 28 K. However, we never observed thermoluminescence of the *H* or ArO^* bands even for a high intensity of their luminescence in the cathode luminescence spectrum.

3.2. Neon

Figure 9 shows the luminescence spectra an impure of Ne crystal and the III continuum observed in the gaseous phase.[28] The crystal obviously emits no radiation which

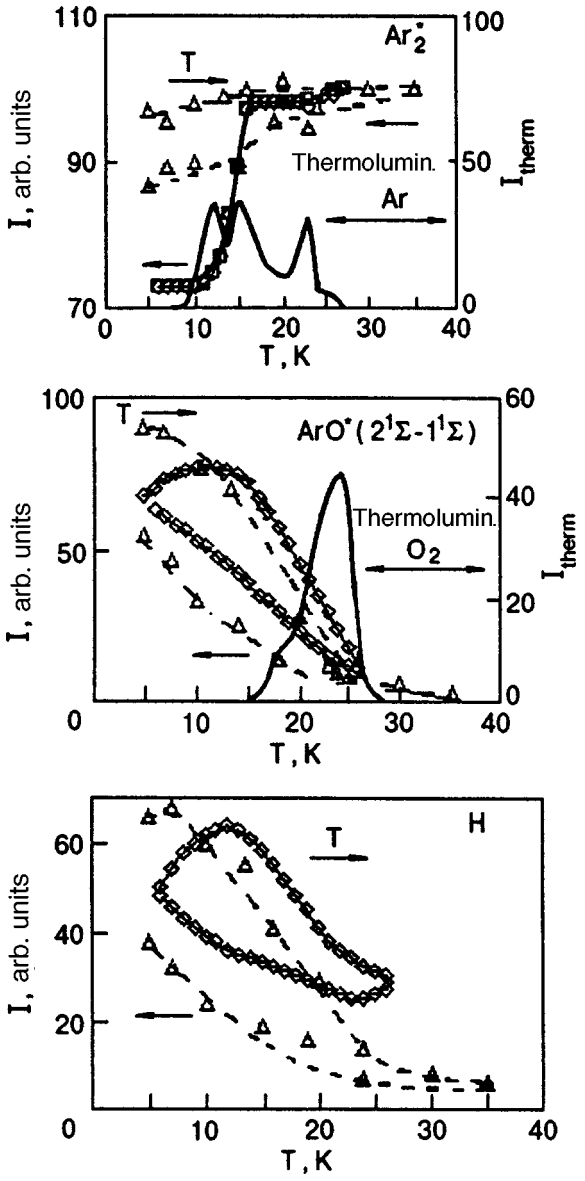

FIG. 7. Dependence of intensities of the Ar_2^*, ArO, and *H* bands on the crystal temperature for various oxygen concentrations *c*,%:10^{-3}(△) and 10^{-4}(□). The arrows indicate the direction of the temperature cycle. The solid curve shows the thermoluminescence spectra for argon[55] and molecular oxygen (our results).

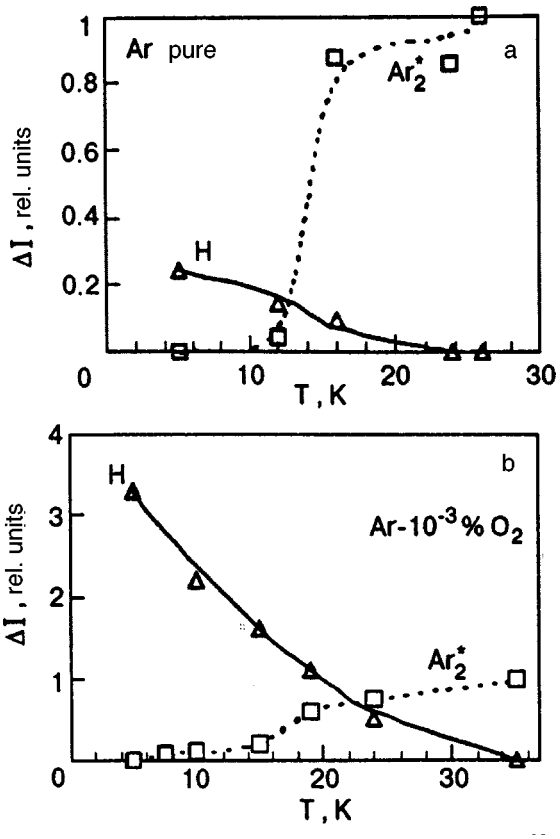

FIG. 8. Relative variation of the intensities of the *H* and Ar_2^* band as functions of the crystal temperature: purified argon (a) impure argon (b). $\Delta I_{Ar}=(I_{Ar}^{max}-I_{Ar}^{min})/I_{Ar}^{max}$, $\Delta I_H=(I_H^{max}-I_H^{min})/I_{Ar}^{max}$.

could be identified with this continuum. The luminescence intensity is mainly concentrated in the quasi-atomic transition Ne*($^3P_1\rightarrow{}^1S_0$). The intensity of molecular luminescence of Ne_2^* lying near 16.6 eV approximately 1/4 of the intensity of radiation associated with Ne*($^3P_1\rightarrow{}^1S_0$). Besides, one more weak band with $E_{max}=11.65$ eV and halfwidth $\Delta=0.23$ eV is observed. We are not aware of any information of this band in the gaseous phase. The addition of 1% of oxygen to the Ne matrix increases the intensity of this band significantly as compared to the molecular luminescence of Ne_2^* (Fig. 9b), but its value is at least an order of magnitude smaller than the intensity of quasi-atomic luminescence of O* in the Ne matrix for any concentration of O_2.[37] In the VUV spectral range, the transitions from the lowermost Rydberg states of O*(^5S and ^3S) to the ground energy level ^3P are characterized by the highest intensity, while in the visible range the most intense transition takes place between the valence states of O*($^1S\rightarrow{}^1D$). It should be noted that the luminescence associated with O*($^1S\rightarrow{}^1D$) is an analog of the transition of ArO*($2\,^1\Sigma\rightarrow 1\,^1\Sigma$) in the argon matrix.[20,37]

The addition of Xe to the solid solution Ne–O_2 leads to suppression of oxygen atomic centers O* and to an increase in the excimer bands of XeO*. As in the case of the Ar matrix, the dependence of the intensities I[O*(^5S)] and I[O*(^1S)] on the Xe concentration mutually correlate, but differ significantly from the quenching of intrinsic luminescence of Ne*($^3P_1\rightarrow{}^1S_0$) (Fig. 10).

4. DISCUSSION OF RESULTS

4.1. Argon

Let us analyze the available data in three aspects. For this purpose, we compare the results of investigations in the gaseous and solid phases, compare the Rg–O_2 system with the Rg–F_2 systems for which numerous results on the structure of excimer complexes in the gas and in the matrix have been obtained, and also compare the main features of radiation of bands *G* and *H* in the Ar matrix with the behavior of the excimer ArO*($2\,^1\Sigma$) with a valence bond.

First of all, let us carry out a detailed analysis of spectroscopic parameters obtained for the III continuum in the gaseous and solid phases in order to determine the effect of

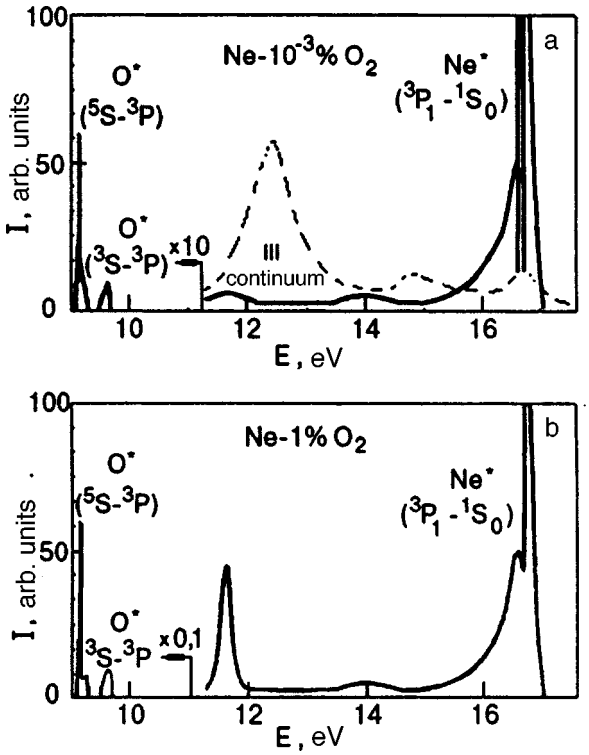

FIG. 9. (a) Luminescence spectra of a nominally pure Ne crystal and III continuum in the gaseous phase (dashed curve). (b) Luminescence spectra of a Ne crystal with 1% oxygen impurity.

matrix environment on the luminescence under investigation. The shape, position, and width of the III continuum radiation in gaseous Ar are close to the parameters of the *H* band in the crystalline phase only in narrow limits of experimental conditions, i.e., under low gas pressures $P<0.2$ bar and short time of radiation registering ($t_{\text{reg}}<10$ ns).[27,28] Figure 1 (curve *1*) shows the shape of the gaseous III continuum obtained apparently in the most pure form owing to the pulsed excitation technique and low gas pressure. This made it possible to eliminate the contribution from luminescence of three-atom molecules of Ar_3^*.[28] Under these conditions, the position of the peak of the III continuum in the gas is $E_{\max}=6.525$ eV, while the half-width is $\Delta=0.52$ eV. Accordingly, the energy shift relative to the *H* band in the crystal towards higher energies amounts approximately to 0.3 eV. An increase in pressure and registering time leads to a considerable broadening and shift of the peak towards lower energies (see Fig. 1). An increase in t_{reg} from 3.5 to 100 ns increases this shift to 0.6 eV,[27] so that the displacement relative to the *H* band towards lower energies now amounts to 0.3 eV. Similarly, an increase in pressure shifts the peak of the III continuum successively from 6.52 eV at $P=0.2$ bar to 5.64 eV at $P=2$ bar. The overall contour of the band becomes much broader, and the III continuum at $P=17$ bar has three peaks (at 6.7, 5.64, and 5.0 eV) of approximately the same width and intensity, embracing the range from 8.3 to 4 eV. A transition to the solid phase is associated with a further increase in pressure, and hence in the atomic density from 4.6×10^{20} to 2.2×10^{22} cm^{-3}. The inverse process of convolution of the multistructural wide-band luminescence into a single band *H* with $E_{\max}=6.25$ eV and the half-width $\Delta=0.52$ eV appears as hardly possible in view of the following considerations. During a transition from the gas to the solid, the II continuum of Ar_2^* is transformed only slightly.[38] The shift of the luminescence peak of Ar_2^* towards lower energies amounts to only 0.04 eV, which is an order of magnitude smaller than the shift of the *H* band relative to the III continuum in the gas. In this case, the width of Ar_2^* band decreases by 0.13 eV, while the *H* bands, on the contrary, is broadened by 0.3 eV as compared to the gas (see Fig. 5). Thus, the luminescence parameters of the II continuum of Ar_2^*, which is obviously of the same origin in the gaseous and in solid phases, change insignificantly under the effect of the matrix environment, which differs basically from the behavior of the III continuum under similar conditions.

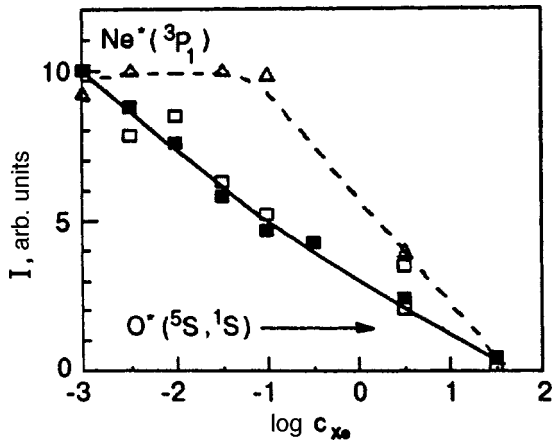

FIG. 10. Suppression of quasi-atomic oxygen centers in solid Ne by introducing Xe impurity: O*(^5S)(■), O*(^1S)(□), and intrinsic luminescence of Ne*(△).

This conclusion is also confirmed by the measurements of lifetime of the II and III continuums. For the II continuum, the lifetime of the short (t_1) and long (t_2) components do not undergo significant changes in the crystalline environment: $t_1=5$, 5.5, and 3.2 ns in the gas, Ne matrix, and solid Ar, respectively. The III continuum displays a completely different behavior. The lifetime of luminescence in the gaseous phase with $E_{\max}=6.5$ eV amounts to 5 ns,[27] while in the solid phase it apparently increases to several hundreds nanoseconds according to the measurements for the band with $E_{\max}=6.3$ eV in solid neon with an Ar impurity.[29] Such a considerable increase in the lifetime of the same state upon a transition from the gaseous phase to the crystalline matrix is hardly probable.

In the light of this comparison, the identification of the *H* band in solid Ar with the III continuum in the gaseous phase, which is associated with the luminescence of $(Ar_2^+)^*$ or $(Ar_2^{2+})^*$ appears as problematic. In this connection, we consider the results characterizing the probability of luminescence of ionic and neutral states depending on gas pressure in the case of electron excitation.[39] The initial probability of populating the ionic states R^+ is approximately equal to 80%. As a result of recombination and relaxation processes which are accelerated considerably upon an increase in pressure, the ratio of densities *N* of emitting ionic and neutral molecules becomes much smaller. For the luminescence

TABLE I. Luminescence energy peaks E_{RF} and E_{RO} for fluorides and oxides of inert gases and half-widths $\Delta_{1/2}$ of corresponding spectral bands. The energy values are in eV.

	Fluorides			Oxides			
			Gas				
Molecule	Transition	E_{RF}	$\Delta_{1/2}$	Molecule	Transition	E_{RO}	$\Delta_{1/2}$
					$^3\Pi-{}^3\Pi$	8.27	0.34
Ar^+F^-	$^2\Sigma-{}^2\Sigma$	6.42	0.31	Ar^+O^-	$^3\Pi-{}^1\Sigma$	6.7	0.14
					$^3\Pi-{}^1\Pi$	6.05	0.23
$Ar_2^+F^-$	$^2B_2-{}^2B_2$	4.35	0.60	$Ar_2^+O^-$	-	6.6*	0.7*
			Crystal				
$Ar_2^+F^-$	$^2B_2-{}^2B_2$	3.94	0.60	$Ar_2^+O^-$	–	6.25** 4.84**	0.67 0.34

Remark: Our estimates are marked by an asterisk. Double asterisks show our results.

recording time $t_{reg}=10$ ns and pressures $P=1.4$, 8.5, and 42.5 bar, the ratio $N(R_2^+)^*/N(R_2)^*=5\times10^{-2}$, 2×10^{-2} and $<10^{-3}$, respectively. Extrapolating this sequence to the limiting case of a solid, we can assume that the ratio of luminescence intensities of ionic and neutral states should not exceed 10^{-3}. However, the observed bands H and Ar_2^* have comparable intensities. The probability of excitation of doubly ionized states R_2^{2+} under electron excitation of the gas amounts to only 7% as compared to R_2^+.[40] On the other hand, the probability of R_2^{2+} quenching as a result of dissociative recombination with electrons is four times higher than for R_2^+,[40] which additionally decreases the probability of luminescence from these states. It should be borne in mind that the rate of dissociative recombination in solid Ar is two orders of magnitude higher than in the gaseous phase due to an increase in the electron mobility.[41] Thus, nonradiative perishing of ionic states with a high density of the substance apparently becomes predominant. At any rate, the quantum radiation yield for the III continuum amounts to only 5% even in a gas with the density $\rho=6\times10^{19}$ cm^{-3} and continues to decrease upon an increase in pressure.[40]

Comparing the spectra of the gaseous and solid phases of argon, we can also observe that the crystals containing a nitrogen impurity in addition to oxygen impurity display another continuum lying on the high-energy side of the H band ($E_{max}=7.6$ eV). This continuum has the width and shape similar to those for H and exhibits the same dependence on the N_2 concentration as the dependence of the H band on the O_2 concentration. In the gaseous phase, no analog of this radiation was observed. At the same time, similar continuous bands were detected for Kr and Xe crystals containing the N_2 impurity in the regions of 6.35 and 5.7 eV respectively. In our opinion, the existence of another analogous continuum associated with the presence of another impurity makes the identification of the H band with the luminescence of $(Ar_2^+)^*$ dubious. Indeed, the enhancement of the H band due to the stabilization of Ar_2^+ near O_2 impurity centers proposed by Grigorashchenko *et al.*[23] does not agree with the too large energy shift of the second band (1.2 eV) associated with the N_2 impurity.

4.2. Neon

A comparison of the continuous luminescence of Ar with the neon spectra does not confirm the identification of the III continuum in a gas with the continuum observed in the solid either. In contrast to argon, crystalline neon does not exhibit a luminescence similar the III continuum, although the experimental conditions for the two gases are quite identical.[28] The energies of stabilization of molecular ions R_2^+ calculated in a solid Ne and Ar[42] have comparable values: -1.1 and -0.7 eV respectively. Hence it follows that the R_2^+ centers, which are stable in solid Ar, must be equally stable in solid Ne. The potential curves of ionic states of neon and argon are also similar. Consequently, it would be natural to expect the emergence of the III continuum luminescence in the solid state also if it exists in the gas. And conversely, the absence of continuum must reflect the principal difference between neon and other inert gases including argon. This difference can be associated with the absence of excimer compounds of neon with oxygen, as proved earlier.[2,20] For this reason, we shall consider as the second stage of discussion the version of the impurity origin of the H band proceeding from the results of analysis of binary mixtures Ar–O_2 and Ne–O_2.

4.3. Oxides of rare gases

Experiments demonstrate considerable enhancement of the H and G bands with increasing oxygen concentration, which suggests their relation with the formation of excimers ArO*. This assumption is confirmed by the well-pronounced correlation in the behavior of the H and ArO* bands depending on the concentration of the Xe impurity and the temperature of the crystal. We also observed similar dependences for quasi-atomic centers $O^*(^5S)$ and $O^*(^1S)$ in solid Ne, which also confirms the effect of oxygen on the H band. Nevertheless, the spectral characteristics of luminescence of gaseous and solid mixtures of argon with oxygen seem to be quite different at first glance, which hampers their direct comparison.

The main results of experiments are presented in Table I.

At low pressures in the Ar–0.1% O_2 gas mixture, excimer luminescence with a peak at 8.3 eV with a strong asymmetry in the high energy range prevails. The same spectrum is typical of all halogenides of rare gases R^+X^-, including $Ar^+F^-(^2\Sigma\rightarrow{}^2\Sigma)$. Luminescence near 8.3 eV was attributed to a similar transition $Ar^+O^-(^3\Pi\rightarrow{}^3\Pi)$.[4,5] Subsequently, two other peaks at 6.7 and 6.05 eV were detected.[10,31] These peaks are associated with transitions from the state $Ar^+O^-(^3\Pi)$ to the lowermost energy levels of the valence compound $ArO^*(1\,^1\Sigma$ and $2\,^1\Pi)$. The intensity of these bands is at least an order of magnitude lower than the intensity of the main peak at 8.3 eV.[5] The luminescence lifetime $\tau\cong 150$ ns of the bands 6.7 and 6.05 eV, but for the band 8.3 eV it was not measured. However, its order of magnitude can be estimated at approximately 5 ns since $\tau=10$ ns for a similar luminescence of $Xe^+O^-(^3\Pi\rightarrow{}^3\Pi)$,[4] $\tau=4$ ns for $Ar^+F^-(^2\Sigma\rightarrow{}^2\Sigma)$,[43] and $\tau=12$ ns for $Xe^+F^-(^2\Sigma\rightarrow{}^2\Sigma)$.[43]

None of the observed luminescence bands of Ar^+O^- in the gaseous phase can be directly transformed into the *H* continuum observed in the solid phase. The widths of these bands in the gas are too small as compared to the *H* band. As we go over to the solid state, the widths of excimer bands usually become smaller due to acceleration of vibrational relaxation in the excited state. This can be clearly seen for the luminescence band of Xe^+F^- in solid argon.[44] On the other hand, a comparison with the spectra of Ar–F_2 gas mixtures shows that a comparatively narrow band of Ar^+F^- ($E_{max}=6.42$ eV, $\Delta=0.31$ eV) is observed at low pressures as in Ar–O_2 mixtures, while another continuum having much larger width and corresponding to a lower energy ($E_{max}=4.35$ eV, $\Delta=0.60$ eV) which can be identified as the luminescence of $Ar_2^+F^-$ appears at $P=2$ bar. In the solid phase, the band Ar^+F^- disappears completely, while the $Ar_2^+F^-$ luminescence is shifted by 0.4 eV towards lower energies, which corresponds to the matrix shift of excimer luminescence in inert matrices.[45] One more weaker and broader band with $E_{max}=3.49$ eV was attributed to $Ar_6^+F^-$ luminescence. Thus, it would be natural to attribute tentatively the *H* band to $Ar_2^+O^-$ luminescence. If the matrix shift for $Ar_2^+O^-$ is the same as for $Ar_2^+F^-$, the $Ar_2^+O^-$ band in the gaseous phase should be observed near 6.6 eV. This means that the band virtually overlaps with the III continuum in the gas, which naturally hampers its direct observation. This assumption is confirmed by a small but noticeable increase in the luminescence intensity of the continuum in the region of 6.5 eV in Ar–0.1% O_2 mixtures at $P=2$ bar, when the formation of $Ar_2^+O^-$ is quite probable. At the same time, Strickler and Arakava[30] proved that the III continuum observed by them at $P=1$ bar is clearly quenched by oxygen admixture. This suggests the presence of an additional band in the region of 6.5 eV, whose intensity increases with the O_2 concentration.

According to the identification proposed for the *H* band, the luminescence of the *G* band can be associated with the transition from the state $Ar_2^+O^-$ to the energy level Ar_2O^* connected genetically with the state $ArO^*(1\,^1\Sigma)$. Indeed, the difference between the radiant energies of the *H* and *G* bands is $E_{max}(H)-E_{max}(G)=1.48$ eV. This value coincides to within 0.1 eV with the energy difference for the transitions from the state $Ar^+O^-(^3\Pi)$ to the energy level $X\,^3\Pi$ and $1\,^1\Sigma$ in the gaseous phase [$E(X\,^3\Pi)-E(1\,^1\Sigma)=8.3-6.7=1.6$ eV]. The ratio of the intensities of the *H* and *G* bands is also of the same order of magnitude as the ratio of the intensities of the peaks at 8.3 and 6.7 eV in the gaseous phase.[5] The lifetime of the *H* band ($\tau=270$ ns)[29] is quite comparable with the luminescence lifetime of $Ar_2^+F^-$ ($\tau=200$ ns). Finally, the energy shift and broadening of the *H* and *G* bands relative to the luminescence of Ar^+O^- matches with the same parameters for $Ar_2^+F^-$ relative to Ar^+F^-. It should be noted that the decrease in the energy of transition of $Ar_2^+O^-$ as compared to Ar^+O^- ($\Delta E=1.55$ eV) turned out to be slightly smaller than for similar compound of argon with fluorine (2.07 eV), but lies within the limits obtained for $Xe_2^+F^-$(1.5 eV)[46] and $Xe_2^+D^-$(1.46 eV).[47] This discrepancy can be due to a decrease in the binding energy in the $Ar_2^+O^-$ molecule in view of a weaker affinity to electron in the oxygen atom as compared to the fluorine, which amounts to 1.465 and 3.4 eV, respectively. On the other hand, the repulsive term of the ground state of Ar_2O is in all probability steeper than for Ar_2F, which can also lead to a relative shift in the transition energy towards lower values.

Since the exact calculations of the potentials of $Ar_2^+O^-$ and Ar^+O^- which would confirm the validity of this assumption have not been made, we can estimate the luminescence energy of $Ar_2^+O^-$ in the gaseous phase only approximately by using the method proposed by Wadt and Hay.[48] The decrease in the transition energy of $Ar_2^+O^-$ relative to Ar^+O^- associated with the formation of the additional bond in Ar_2^+ will be assumed to be equal to the energy of dissociation of $D(Ar_2^+)=1.23$ eV.[49] Subtracting the additional repulsive energy of Ar_2 in the ground state for the equilibrium distance $r_e(Ar_2^+)=2.46$ Å, i.e., $\Delta E(Ar_2)=0.74$ eV,[50] we obtain the luminescence energy for $Ar_2^+O^-$:

$$E(Ar_2^+O^-)=E(Ar^+O^-)-D(Ar_2^+)-\Delta E(Ar_2)=6.3\ \text{eV}. \quad (1)$$

Taking into account the roughness of the estimate, we can say that this value virtually coincides with the energy of continuous luminescence observed in the gas mixture of argon with oxygen at $P=2$ bar.[31]

4.4. Excitation spectra

In the light of the above assumptions, let us consider in greater detail the excitation spectrum of the *H* band, which was obtained by Ogurtsov *et al.*[22] and served as the basic version of the ionic origin of the continuum observed in solid Ar. The spectrum contains several peaks in the range below the bottom of the conduction band E_g, which correspond to exciton absorption $n=1,1'$ and $n=2,3$ ($E_{ex}=12.2$, 13.7, and 13.9 eV) as well as an additional peak identified as the surface state near 13 eV. A smooth ascent of the effectiveness of excitation, which also continues above E_g, starts at approximately the same energy, i.e., 1.3 eV below the conduction band. The second stage of the ascent, which attains peaks near 33 eV, starts at the energy 23 eV, i.e., slightly below $2E_{ex}$. In our opinion, this spectrum does not contradict the identification of the *H* band with the luminescence of

$Ar_2^+O^-$, but may cause certain complications in its interpretation if we presume its ionic origin. Above all, the presence of peaks in the energy range below the bottom of the conduction band indicates possible population of the corresponding states without ionization of atoms. Otherwise, we must assume a two-stage excitation of luminescence centers responsible for the continuum under investigation. Let us first consider the most probable one-stage process.

The excitation spectrum indicates that the surface state near 13 eV makes a contribution to the formation of luminescence centers along with excitons $\Gamma(3/2,1/2)$ $n=1,1',2$. This peak is close to the energy of dissociation limit for Ar^+O^-: $E(Ar^+)-E(O^-)=14.16-1.465=12.7$ eV. A further ascent of the efficiency of excitation, which starts from this energy, is in good agreement with the above assumption. The excitation spectrum of the *H* band in this region has the form typical of excitation of impurity centers in the Ar matrix,[51] and at the same time differs slightly from the spectra typical of the ionization of matrix atoms.[52] For example, the spectra of photoemission of electrons from crystalline Ar[52] have a sharper edge near the bottom of the conduction band, which lies only 0.2 eV below E_g rather than a smooth protracted ascent as in the case of the *H* band. The photoemission spectrum also has small peaks in the region of exciton energy, but their contribution to the total intensity is an order of magnitude lower than for the *H* band. The origin of these peaks is associated with the ionization of residual impurity in the sample. It should also be noted that the excitation spectrum of the *H* band considered above resembles the photoexcitation spectrum of the excimer Ar^+O^- in the Ne matrix.[29] The shift of the peaks towards higher energies by 0.45 eV corresponds to the shift of $E_{ex}(n=1)Ar^*$ in the Ne matrix relative to the intrinsic matrix, which amounts to 0.5 eV.[52] Ogurtsov *et al.*[22] observed considerable difference between the excitation spectra of the *H* band and the defective component of the molecular band $Ar_2^*(M_1)$. This difference could be associated with a large contribution of the surface states to the luminescence of M_1, which was detected by the same authors later.[53] Consequently, the strong effect of reflection at the surface could be responsible for the difference in the two spectra. On the contrary, a comparison with the excitation of the defect-free component $Ar_2^*(M_2)$ reveals striking similarity of the two spectra with a shift of only 0.1 eV towards the low-energy region for the *H* band. It should also be noted that this spectrum strongly resembles the absorption spectrum of solid Ar in the energy range below E_g.[54]

The main distinction of the excitation spectrum of the continuum under investigation is the large contribution of hole states as compared to excitons. This can reflect a high probability of populating $Ar_2^+O^-$ through the bound ionic states $(Ar_2O)^+$ and $(ArO)^+$:

$$Ar^+ + Ar \rightarrow Ar_2^+ + O \rightarrow (Ar_2O)^+ + e^- \rightarrow Ar_2^+O^- \qquad (2)$$

or

$$Ar^+ + O \rightarrow (ArO)^+ + Ar \rightarrow (Ar_2O)^+ + e^- \rightarrow Ar_2^+O^-. \qquad (3)$$

The trapping of electrons at oxygen impurity centers can increase additionally the efficiency of formation of Ar_2O^- through the ionic states of the matrix

$$Ar_2^+ + O^- \rightarrow Ar_2^+O^-. \qquad (4)$$

At the same time, the population of $Ar_2^+O^-$ during the excitation of neutral states should occur through the intersection of the energy levels Ar_2^*O and $Ar_2^+O^-$, which can be a less effective process:

$$Ar^* + Ar \rightarrow Ar_2^* + O \rightarrow (Ar_2^*O) \rightarrow Ar_2^+O^-. \qquad (5)$$

Let us now consider the possibility of two-step excitation of the *H* band, which must be presumed for its attributing to the luminescence of $(Ar_2^+)^*$ or $(Ar_2^{2+})^*$. In this case, exciton peaks in the excitation spectrum must correspond to the probability of repeated excitation of (Ar_2^+) or (Ar_2^{2+}) ions frozen in the matrix. It was proved by Ogurtsov *et al.*[55] that a fraction of ions is indeed conserved in the lattice. This is manifested in thermoluminescence of the Ar_2^* band upon heating of preliminarily irradiated samples. However, the intensity of this luminescence is several orders of magnitude lower than for the Ar_2^*, and hence cannot be registered as a band whose intensity is comparable with that of the band emerging as a result of direct excitation of $(Ar_2^+)^*$ above E_g as follows from the spectrum presented above. It was proved in the previous section that the concentration of ionic centers amount to a few percent even in the gaseous phase. Naturally, this value in the crystal cannot be higher in view of acceleration of recombination processes. Fajardo and Apkarian[56] proved, for example, that the density of accumulated charged pairs in an inert crystal with 1% of electronegative impurity amounts to only 10^{17} cm^{-3}, i.e., does not exceed 10^{-3} %. Temperature dependences of the *H* band obtained under different experimental conditions can serve as an indirect proof of the lack of correlation between the intensity of the *H* band and the concentration of frozen radicals (Ar_2^+) in the matrix. We shall consider this question in greater detail below.

4.5. Temperature dependence

The temperature dependence of the *H* band has the form typical not only of the luminescence of $ArO^*(2\,^1\Sigma \rightarrow 1\,^1\Sigma)$, but also of other excimers in inert matrices: $(ArN)^*$ in Ar,[18] $(KrO)^*$ in Kr,[57] and $(XeO)^*$ in Xe.[35] The temperature dependence of the intensity of these bands also exhibit a kink at temperatures 12, 28, and 50 K, respectively. More detailed experiments with argon revealed that the shape of the temperature curve can change significantly depending on the experimental conditions. Excitation density, impurity concentration, and the rate of thermocycling may determine these changes to a considerable extent. The recombination of oxygen atoms frozen in the matrix at low temperatures obviously make their own contribution to the observed process. This follows from a comparison of the building-up of thermal luminescence of the O_2 molecule and attenuation of the *H* band illustrated in Fig. 7. A similar thermal quenching of $(XeO)^*$ bands in the Xe matrix, which is associated with recombination, is described by Danilichev

TABLE II. Luminescence energy E_R of atoms of inert gases and their compounds with fluorine and oxygen in the gaseous phase E_{RF} and E_{RO} as well as the luminescence energy difference ΔE_R for sequence of elements. The energy values are in eV.

Atom	E_R	ΔE_R	Molecule	E_{RF}	ΔE_{RF}	Molecule	E_{RO}	ΔE_{RO}
Ne*	16.62	5.07	Ne^+F^-	11.48	5.06	Ne^+O^-	–	–
Ar*	11.55	1.65	Ar^+F^-	6.42	1.42	Ar^+O^-	8.3	1.41
Kr*	9.9	1.59	Kr^+F^-	5.0	1.48	Kr^+O^-	6.89	1.61
Xe*	8.31	–	Xe^+F^-	3.52	–	Xe^+O^-	5.28	–

and Apkarian.[58] An increase in temperature also leads to thermal luminescence of Ar_2^*, which is attributed to the recombination of the frozen Ar_2^+ centers and electrons released from traps: $Ar_2^+ + e^- \rightarrow Ar_2^*$.[23,55] If we proceed from the version of the ionic origin of the *H* band, and hence two-stage channel of its excitation, the luminescence of Ar_2^* proves to be associated directly with the luminescence of the *H* band since the excitation of the same frozen Ar_2^+* centers is one of the channel of populating (Ar_2^+).[23,55] Thus, temperature dependences of both bands should display a certain quantitative interrelation under any experimental conditions. However, we observe the opposite pattern: stronger variations of the intensity of the *H* band are accompanied by weaker variations of the luminescence of Ar_2^* (see Fig. 8). As a result, the relative variation of the intensities $\Delta I_H/\Delta I_{Ar}$ differs by an order of magnitude for samples with different extent of purification of the initial gas. Such a behavior can be explained only by presuming the impurity origin of the luminescence continuum under investigation. Finally, the thermoluminescence spectrum for Ar_2^* has three clearly manifested peaks at 12, 17, and 23 K, which are not manifested in any way on the temperature dependence of quenching of the *H* band. Summarizing what has been said above, we conclude that the contribution of two main processes to the temperature dependence of I_H, i.e., the recombination of oxygen atoms frozen in the matrix and the trapping of intrinsic excitons of argon at these centers, is apparently most probable. The influence of defects and impurity concentration should be analyzed in greater detail.

4.6. Neon

Comparing the fluorides and oxides of inert gases, we note that the complexes Ne^+F^- with charge transfer possess a strong coupling and are observed in luminescence spectra along with other fluorides of inert gases. At the same time, luminescence of such compounds with oxygen has not been detected to out knowledge. In this connection, we paid special attention to the weak emission band in crystalline neon with $E_{max}=11.65$ eV. According to our results obtained in this research, the intensity of this band increases upon the addition of oxygen, but it cannot be attributed to atomic transitions primarily in view of the absence of any energy correspondence with atomic energy levels of O*. Besides, a considerable width of this band and the absence of fine structure, which is typical of luminescence of atomic centers in the Ne matrix, confirm this conclusion. The identification of the band with $E_{max}=11.65$ eV with a molecular transition of O_2^* was complicated above all by its position on the energy scale, which is close to the ionization energy of $O_2(E_i = 12.1$ eV). This energy range contains a large number of high-energy Rydberg states of O_2^*, which are separated by an energy interval of only 0.1 eV. These states partially overlap with one another or are intersected by dissociation branches of lower-lying weakly coupled energy levels.[1] This apparently leads to rapid nonradiative relaxation of high-energy excitations of O_2^* since no emission of oxygen was observed in this spectral range in the gaseous or solid phases according to the available data. The absence of a vibrational structure does not agree with the possibility of a molecular transition either. Thus, the observed band should be attributed with maximum probability to the luminescence of an excimer compound of oxygen with nitrogen. The data contained in Tables II and III suggest[1,6,48,52] that it can correspond to the $Ne_2^+O^-$ state. The luminescence energy $E^G(Ne_2^+O^-)$ in the gaseous state can be estimated on the basis of the regularity manifested in the sequence of luminescence energies in the Ne–Xe series (see Table II):

$$E^G(Ne^+O^-) = E^G(Ar^+O^-) + E^G(Ne^+F^-) - E^G(Ar^+F^-)$$
$$= 8.3 + 11.48 - 6.42 \cong 13.3 \text{ eV}. \quad (6)$$

Considering that the matrix shift in Ne is negative $[\Delta E^{G-S}(Ne^+F^-) = E^C(Ne^+F^-) - E^S(Ne^+F^-) = -1.38]$,[59] we can obtain the following estimate for the luminescence energy of Ne^+O^- it its own matrix:

$$E^S(Ne^+O^-) = E^G(Ne^+O^-) - \Delta E^{G-S}(Ne^+F^-)$$
$$\cong 13.3 + 1.3 = 14.6 \text{ eV}. \quad (7)$$

Since this spectral region does not contain any radiation associated with oxygen, we can estimate the energy of transition from the lower-lying state of $Ne_2^+O^-$. Assuming that the energy gain in the formation of this molecule is approximately the same as for $Ne_2^+F^-$, we obtain, in accordance with Table III,

TABLE III. Energies E_{R_2F} corresponding to luminescence peaks for triatomic molecules in gaseous phase and their shift relative to the energy E_{RF} of the corresponding diatomic molecules as well as half-widths $\Delta_{1/2}$ of luminescence bands.

Molecule	E_{R_2F}, eV	$E_{RF}-E_{R_2F}$, eV	$\Delta_{1/2}$, eV
$Ne_2^+F^-$	10.37; 10.16; 8.55	1.11; 1.42; 2.93	0.16
$Ar_2^+F^-$	4.35	2.07	0.60
$Kr_2^+F^-$	3.1	1.9	–
$Xe_2^+F^-$	2.03	1.5	–

$$E^S(\mathrm{Ne}_2^+\mathrm{O}^-)=E^S(\mathrm{Ne}^+\mathrm{O}^-)-E^S(\mathrm{Ne}^+\mathrm{F}^-)+E^S(\mathrm{Ne}_2^+\mathrm{F}^-)$$
$$\cong\begin{cases}14.6-2.9=11.7 & (A)\\ 14.6-1.4=13.2 & (B).\end{cases} \quad (8)$$

The energy of transition (A) coincides to within 0.1 eV with the position of the energy band with $E_{\max}=11{,}65$ eV. Transition (B) can be associated with upper-lying states $\mathrm{Ne}_2^+(^2P_{1/2})1/2u$ occurring 1.4 eV above the lowermost energy level $\mathrm{Ne}_2^+(^2P_{3/2})1/2u$.[60] The state $\mathrm{Ne}_2^+(^2P_{1/2})$ possesses a much lower binding energy, and hence does not form a stable compound with oxygen. The half-widths of the emission bands $\mathrm{Ne}_2^+\mathrm{O}^-$ and $\mathrm{Ar}_2^+\mathrm{O}^-$ amounting to 0.20 and 0.67 eV are in good agreement with the luminescence parameters of fluorides of inert gases. The corresponding values of $\mathrm{Ne}_2^+\mathrm{F}^-$ and $\mathrm{Ar}_2^+\mathrm{F}^-$ amount to 0.16 and 0.6 eV, respectively.

The formation of $\mathrm{Ne}_2^+\mathrm{O}^-$ molecules is most probable for high oxygen concentrations ($c\sim1\%$). The rate of recombination of Ne_2^+ with an electron can apparently compete with the rate of formation of a stable compound with an oxygen impurity atom at the neighboring lattice site. However, the efficiency of formation of $\mathrm{Ne}_2^+\mathrm{O}^-$ remains an order of magnitude lower than the efficiency of formation of an isolated center $\mathrm{O}^*(^5S)$ according to the ratio of intensities of the corresponding emission bands.

5. CONCLUSION

This research is devoted to an analysis of luminescence of Ar and Ne cryocrystals in the spectral range below the intrinsic molecular luminescence of R_2^*. Two basic versions of the origin of the continuous H band at the peak of 6.25 eV, which is most typical of solid argon, are considered. One version is associated with the identification of this band with the emission of excited ionic states $(\mathrm{R}_2^+)^*$ or $(\mathrm{R}_2^{2+})^*$, while the other version associates this band with the luminescence of the exciplex oxygen complex with inert gas atoms. We analyzed the intensity of the H band as a function of the oxygen impurity concentration and temperature of the crystal as well as its suppression by a more reactive Xe impurity. A comparison with the corresponding parameters of intrinsic luminescence of Ar_2^* and luminescence of the exciplex $\mathrm{ArO}^*(2\,^1\Sigma)$ indicates the most probable connection of the H band with the high-energy state of argon oxide. A comparative analysis of analogous compounds of fluorides of rare gases in the gaseous and solid matrices makes it possible to identify the observed luminescence as the complex $\mathrm{Ar}_2^+\mathrm{O}^-$ with charge transfer. We also observed an additional luminescence band G (4.9 eV) corresponding to a transition from the same state of $\mathrm{Ar}_2^+\mathrm{O}^-$ to the lowermost excited energy level associated with $\mathrm{ArO}^*(1\,^1\Sigma)$. Theoretical estimates proposed for the luminescence energy of $\mathrm{Ar}_2^+\mathrm{O}^-$ in a high-density gas and in the crystal are in good agreement with the experimentally observed luminescence energies.

The photoexcitation spectrum of the H band obtained by Ogurtsov *et al.*[22] does not contradict the proposed identification and makes it possible to single out two mechanisms of populating a luminescence center, viz., through the formation of local hole states of Ar_2^+ and through the exciton excitations with $n=1\,\Gamma(3/2,1/2)$. An analysis of the temperature dependence of the luminescence of the H band indicates the absence of its one-to-one correspondence with the population of the hole centers. The intensity of the H band is apparently determined by the accumulation of free O radicals in the matrix and by the probability of trapping of intrinsic excitation of argon by these radicals. An emission band corresponding to a similar exciplex complex $\mathrm{Ne}_2^+\mathrm{O}^-$ with charge transfer was observed in the neon matrix.

One of the authors (I. Ya. Fugol') is grateful to the International Foundation (ISSEP) for partial financing of this research by the International Soros Program Supporting Education in Science (ISSEP), grant No. Spu072067.

*)E-mail: belov@ilt.kharkov.ua

[1] K.-P. Huber and G. Herzberg, *Molecular Spectra and Molecular Structure*, Van Nostrand, New York (1979).
[2] T. H. Dunning, Jr. and J. Hay, J. Chem. Phys. **66**, 3767 (1977).
[3] J. L. Lemair, W. U. L. Tchang-Brillet, N. Shafiraden *et al.*, J. Chem. Phys. **91**, 6657 (1989).
[4] J. Xu, D. W. Setser, and J. K. Ku, Chem. Phys. Lett. **132**, 427 (1986).
[5] A. Kvaran, A. Ludvikson, W. S. Hartree, and J. P. Simons, Chem. Phys. Lett. **137**, 209 (1989).
[6] *Excimer Lasers* (ed. by Ch. Rhodes), Springer, Heidelberg (1979).
[7] N. Schwentner and V. A. Apkarian, Chem. Phys. Lett. **154**, 413 (1989); G. Zerza, G. Sliwinski, and N. Schwentner, Appl. Phys. **55**, 331 (1992).
[8] A. Kh. Amirov, O. V. Korshunov, and V. F. Chinov, J. Phys. B **27**, 1753 (1994) and references cited therein.
[9] H. Langhoff, J. Phys. B **27**, L709 (1994).
[10] D. E. Jonson, Chem. Phys. Lett. **238**, 71 (1995).
[11] E. Robert, A. Khacef, C. Cachoncinlle, and J. M. Pouvesle, Opt. Commun. **117**, 179 (1995).
[12] W. Krotz, A. Ulrich, B. Bush *et al.*, Laser Part. Beams **11**, 521 (1993).
[13] C. Cachoncinlle and J. M. Pouvesle, J. Chem. Phys. **96**, 6085 (1992).
[14] J. Jortner, L. Meyer, S. A. Rice, and E. G. Wilson, J. Chem. Phys. **42**, 4250 (1965).
[15] M. Creusburg, Solid State Commun. **9**, 665 (1971).
[16] E. E. Huber, Jr., D. A. Emmons, and R. M. Lerner, Opt. Commun. **11**, 155 (1974).
[17] I. Ya. Fugol', E. V. Savchenko, A. G. Belov, and Yu. B. Poltoratskii, Pis'ma Zh. Eksp. Teor. Fiz. **19**, 378 (1974) [JETP Lett. **19**, 209 (1974)].
[18] Y. B. Poltoratskii and I. Ya. Fugol', Fiz. Nizk. Temp. **4**, 783 (1978) [Sov. J. Low Temp. Phys. **4**, 373 (1978)].
[19] T. Reimann, W. L. Brawn, and R. E. Johnson, Phys. Rev. B **37**, 1455 (1988).
[20] E. M. Yurtaeva, I. Ya. Fugol', and A. G. Belov, Fiz. Nizk. Temp. **16**, 101 (1990) [Sov. J. Low Temp. Phys. **16**, 54 (1990)].
[21] U. Schriever, T. Hebert, and D. M. Kolb, Ber. Bunsenges. Phys. Chem. **96**, 1032 (1992).
[22] A. Ogurtsov, M. Runne, A. Karl *et al.*, *Jahresbericht Annuel Report II*, Hasylab, DESY, Hamburg (1995); J. Becker, S. Koording, A. N. Ogurtsov *et al.*, *Jahresbericht Annuel Report II*, Hasylab, DESY, Hamburg (1996) (to be published in J. Luminescence (1998)).
[23] O. N. Grigorashchenko, S. A. Gubin, A. N. Ogurtsov, and E. V. Savchenko, J. Electron Spectrosc. Relat. Phenom. **79**, 107 (1996).
[24] G. Klein and M. J. Carvalho, J. Phys. B **14**, 1283 (1981).
[25] H. Langhoff, Opt. Commun. **68**, 31 (1988).
[26] H. A. Koehler, L. J. Ferderber, D. L. Redhead, and P. J. Ebert, Phys. Rev. A **9**, 768 (1974).
[27] W. Krotz, A. Ulrich, B. Busch *et al.*, Phys. Rev. B **43**, 6089 (1991).
[28] T. Griegel, H. W. Drotleff, J. W. Hammer, and K. Petkau, J. Chem. Phys. **93**, 4581 (1990).
[29] M. Fritsch, *Spektroskopische Untersuchungen an Edelgasoxiden in Edelgasmatrizen*, Hamburg University (1991).
[30] T. D. Strickler and E. T. Arakava, J. Chem. Phys. **41**, 1783 (1964).
[31] S. Neeser, M. Voitik, and H. Langhoff, J. Chem. Phys. **102**, 1639 (1995).
[32] A. G. Belov, E. M. Yurtaeva, and V. N. Svishchev, Fiz. Nizk. Temp. **7**, 350 (1981) [Sov. J. Low Temp. Phys. **7**, 172 (1981)].

[33] J. Goodman and L. E. Brus, J. Chem. Phys. **67**, 1482 (1977).
[34] J. Goodman, J. C. Tully, V. E. Bondybey, and L. E. Brus, J. Chem. Phys. **66**, 4802 (1977).
[35] I. Ya. Fugol', A. G. Belov, and E. I. Tarasova, Pis'ma Zh. Éksp. Teor. Fiz. **43**, 530 (1986) [JETP Lett. **43**, 687 (1986)].
[36] I. Ya. Fugol', E. V. Savchenko, A. N. Ogurtsov, and O. N. Grigorashchenko, Physica B **190**, 347 (1993).
[37] A. G. Belov, I. Ya. Fugol', and E. M. Yurtaeva, Fiz. Nizk. Temp. **18**, 177 (1992) [Sov. J. Low Temp. Phys. **18**, 123 (1992)].
[38] E. Morikava, R. Reininger, P. Gurtler *et al.*, J. Chem. Phys. **19**, 1469 (1989).
[39] D. C. Lorets, Physica C **82**, 19 (1976).
[40] M. Schuman and H. Langhoff, J. Chem. Phys. **101**, 4763 (1994).
[41] K. Shinsaka, M. Codama, T. Srithanzatana, *et al.*, J. Chem. Phys. **88**, 7529 (1988).
[42] M. Umehara, Phys. Rev. B **33**, 4237 (1986).
[43] T. H. Dunning and P. J. Hay, J. Chem. Phys. **69**, 134 (1978).
[44] C. J. Hoffman, D. C. Imre, R. Zadoyan *et al.*, J. Chem. Phys. **98**, 9233 (1993).
[45] H. Kunttu, J. Feld, R. Alimi *et al.*, J. Chem. Phys. **92**, 4856 (1990).
[46] L. Wiedemas, M. E. Fajardo, and V. A. Apkarian, J. Chem. Phys. **92**, 342 (1988).
[47] P. Gurtler, M. Kraas, and T. Tschetscher, Europhys. Lett. **11**, 115 (1990).
[48] W. R. Wald and P. J. Hay, J. Chem. Phys. **68**, 3850 (1978).
[49] H. H. Michels, R. H. Holbs, and L. A. Wright, J. Chem. Phys. **69**, 5151 (1978).
[50] R. A. Aziz, J. Chem. Phys. **99**, 4518 (1993).
[51] S. S. Hansnain, I. H. Munro, and T. D. S. Hamilton, J. Phys. C **10**, 1097 (1977).
[52] N. Schwentner, E. E. Koch, and J. Jortner, *Electronic Excitations in Condensed Rare Gases*, Springer-Verlag, Berlin (1985).
[53] E. V. Savchenko, A. N. Ogurtsov, S. A. Gubin, and O. N. Grigorashchenko, in *Proceedings of the Int. Conf. Luminescence-96*, P8-191, Prague (1996).
[54] V. Saile, M. Skibowski, W. Steinmann *et al.*, Phys. Rev. Lett. **37**, 305 (1976).
[55] A. N. Ogurtsov, E. V. Savchenko, O. N. Grigorashchenko *et al.*, Fiz. Nizk. Temp. **22**, 1205 (1996) [Low Temp. Phys. **22**, 922 (1996)].
[56] M. F. Fajardo and V. A. Apkarian, J. Chem. Phys. **89**, 4102 (1988).
[57] A. G. Belov, I. Ya. Fugol, and E. M. Yurtaeva, Phys. Status Solidi B **175**, 123 (1993).
[58] A. V. Danilychev and V. A. Aprakian, J. Chem. Phys. **99**, 8617 (1993).
[59] C. Bressler, W. C. Lawrence, and N. Schwentner, J. Chem. Phys. **102**, 48 (1995).
[60] D. J. Trevor, J. E. Pollard, W. D. Brewer *et al.*, J. Chem. Phys. **80**, 6083 (1984).

Translated by R. S. Wadhwa

LOW-TEMPERATURE PHYSICS OF PLASTICITY AND STRENGTH

Effect of impurity barriers on low-temperature anomalies in plasticity parameters of β-Sn

A. N. Diulin, G. I. Kirichenko, V. D. Natsik,* and V. P. Soldatov

B. Verkin Institute for Low Temperature Physics and Engineering, National Academy of Sciences of the Ukraine, 310164 Kharkov, Ukraine

(Submitted January 8, 1998; revised February 10, 1998)
Fiz. Nizk. Temp. **24**, 595–604 (June 1998)

Plastic deformation determined by the slip of $(100)\langle 010\rangle$ screw dislocations in single crystals of β-Sn solid solutions with different concentrations of Cd, In, and Zn impurities is studied in the temperature range 1.6–150 K. Low-temperature anomalies of the yield stress τ_0 and activation volume γ (kinks in the temperature dependence of $\tau_0(T)$ and peaks on the stress dependence of the activation volume $\gamma(\tau)$) are observed. The parameters of anomalies are found to be determined to a considerable extent by the concentration of impurity atoms in the alloy and by the height of the barriers formed by impurity atoms for dislocations. The observed effects are compared with the predictions of the theory describing the influence of impurities on the motion of dislocations through Peierls barriers of complex shape. The results of analysis of experimental data are in agreement with the assumption concerning the two-hump shape of the lattice potential relief in the $(100)\langle 010\rangle$ slip system. © *1998 American Institute of Physics.* [S1063-777X(98)01106-2]

INTRODUCTION

Mechanical properties of body-centered and some hexagonal metals as well as semiconductor and alkali-halide crystals display several peculiarities that distinguish them as a special group of Peierls crystals. This term emphasizes the decisive role of lattice barriers for dislocations (Peierls barriers) in the plasticity of such crystals. The main peculiarities of Peierls crystals include high values of yield stress (critical shear stresses) and their strong temperature dependence in the low-temperature region as well as typical low- temperature brittleness and limited plasticity associated with it. An analysis of the low-temperature plasticity of body-centered metals revealed one more type of singularity, viz., more or less clearly manifested kinks on the temperature dependences $\tau_0(T)$ of the yield stress (Fig. 1a) and peaks on the dependence $\gamma(\tau)$ of the activation volume on the deforming stress, which correspond to these kinks (Fig. 1b). Finally, some of weakly doped Peierls crystal display a specific effect of impurity softening. These peculiarities (anomalies) were first discovered in bcc metals,[1–10] but are manifested most clearly for β-Sn single crystals with a body-centered tetragonal lattice.[11,12]

A qualitative explanation of the above anomalies can be obtained at present from an analysis of the kink mechanism of thermally activated motion of dislocations through Peierls barriers.[13–22] However, the details of this mechanism and their relation with the fine structure of specific anomalies have not been determined unambiguously. For example, the anomalies illustrated in Fig. 1 were explained by different authors on the basis of several hypotheses clarifying the kink mechanism of the dislocation flow.

It should be noted above all that anomalies of this type were predicted theoretically[13,14] even before their experimental observation as a consequence of the complex shape of Peierls barriers and should be expected for crystals with two-hump lattice barriers (Fig. 2a). The model of a two-hump barrier and its various corollaries have been discussed recently in a series of publications.[18,19,21,22]

However, the experimentally observed anomalies in some bcc metals (such as single crystals of very pure Fe,[2,20] Nb,[6,7] or Ta[6,9]) were manifested quite weakly and do not require the assumption about a two-hump barrier for their description. The analysis carried out by Seeger[16,17] revealed that fine singularities of the yield stress and activation volume in such cases can be described by accurately taking into account the short- and long-range forces in the calculation of the energy of formation of kink pairs.

On the other hand, the anomalies in pure β-Sn proved to be so strong[11] that they could hardly be explained only by the complexity of the shape of the Peierls relief. For this reason, in Ref. 11 we used the following two assumptions for explaining the anomalies, viz., the joint effect of Peierls barriers and internal stresses on the mobility of dislocations in β-Sn, and a nonmonotonic temperature dependence of internal stresses in the region of the anomalies. The nonmonotonic temperature dependence of the strain-hardening factor at the easy slip stage, which was observed in this temperature region, served as an additional argument in favor of the second assumption.

The influence of impurity atoms on the anomalies under

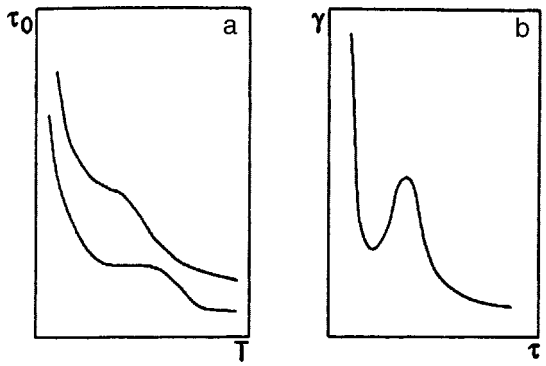

FIG. 1. Schematic diagram of experimentally observed types of temperature dependence of yield stress (a) and stress dependence of activation volume (b) in a Peierls crystal.

consideration is of special interest. Local distortion of the lattice potential relief associated with impurities can strongly affect the conditions of formation and motion of dislocation kinks, which must be reflected in the behavior of macroscopic characteristics of the plasticity of Peierls crystals. The effect of doping on the low-temperature anomaly of the activation volume of bcc metals was detected in experiments described in Refs. 1, 3–5, while a significant change in the yield stress anomaly in β-Sn up to its vanishing under the action of impurities was observed in Ref. 12. A theoretical description of the effect of impurity atoms on the kink mechanism of dislocation motion through two-hump Peierls barriers was proposed by Petukhov and Polyakov.[19] This theory predicts a specific dependence of the height of the activation volume peak (see Fig. 1b) on the height (intensity) of impurity barriers as well as on their concentration. According to these authors,[19] the main criterion controlling the effect of doping on the anomaly of the plasticity parameters of the crystal with two-hump Peierls barriers is the magnitude of the maximum force of interaction of a dislocation with a solitary impurity atom. Such a force has a critical value above which the anomaly should vanish, while for impurities of lower intensity it is preserved. The theory also predicts an interesting peculiarity in the effect of impurity on the form of the $\gamma(\tau)$ dependence, i.e., a logarithmic decrease in the peak height with increasing intensity and concentration of impurity barriers. These theoretical results make it possible to carry out a more unambiguous experimental verification of the hypothesis concerning possible relation between the plasticity anomalies in question with the two-hump shape of Peierls barriers.

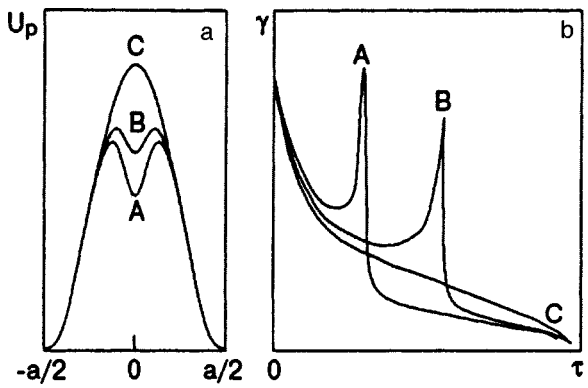

FIG. 2. (a) Schematic representation of a two-hump Peierls potential and its possible variation upon an increase in the impurity concentration in a crystal: pure crystal (A) and alloys with impurity concentration $C_B < C_C$ (curves B and C). (b) Stress dependence of activation volume for potentials A, B, and C.[5]

In this research, such a verification is carried out for weakly concentrated alloys of β-Sn with Cd, In, and Zn. It was proved by us earlier[11] that low- temperature plasticity of high-purity Sn single crystals (99.9995%) oriented for predominant slip in the $(100)\langle 010\rangle$ system is controlled by the motion of screw dislocations through Peierls barriers and displays typical anomalies in the temperature range 60–70 K, which are manifested more clearly than in other Peierls crystals. The single crystals of β-Sn preserve a noticeable plasticity and the smooth nature of the flow upon their cooling down to helium temperatures as well as under doping with small amounts of impurities. These properties distinguish these materials as unique objects for studying the Peierls mechanism of slip.

This research mainly aims at an analysis of the effect of intensity and concentration of impurity barriers on the behavior of anomalies in the yield stress and activation volume of β-Sn single crystals. For this purpose, we chose Cd, Zn, and In impurities which have noticeably different values of the size and module mismatching relative to Sn and studied samples with identical atomic concentrations of impurities of each species.

1. EXPERIMENTAL TECHNIQUE

1.1. Sample preparation and deforming

Single crystals of Sn alloys with Cd, Zn, and In impurities were grown from melt in batches 10 samples from one seed by the modified Bridgman technique.[23] The initial components used for preparing alloys contained foreign impurities whose concentration did not exceed 10^{-5} at. %. According to Hansen and Anderko,[24] the solubility of Cd and Zn in solid Sn is approximately 1 at. %, and the solubility of In varies (according to different authors) from 3 to 7 at. %. The concentration spectrum was studied by us in greatest detail for the Sn–Cd system containing four alloys with 0.01, 0.04, 0.21, and 0.53 at. % Cd. The Sn–Zn system was represented by three alloys with 0.005, 0.01, and 0.53 at. % Zn, while the Sn–In systems included alloys with 0.01, 0.1, and 0.53 at. % In.

The samples under investigation had a working part of size $25\times5\times1.5$ mm with heads in the form of blades for clamping. The samples were deformed by uniaxial tension under the creep conditions at a given constant temperature T by weight loading. The longitudinal axis of the grown crystal coincided with the $\langle 110\rangle$ direction, ensuring maximum shear stresses in the $(100)\langle 010\rangle$ slip system. A schematic diagram of sample loading is presented in Fig. 3a. The load on the sample was changed step-wise, which corresponds to the increment $\Delta\tau$ of the shear stress of the order of 0.2–0.4 MPa. The strain increments $\Delta\varepsilon(t)$ corresponding to each increment of load were recorded automatically by an electronic

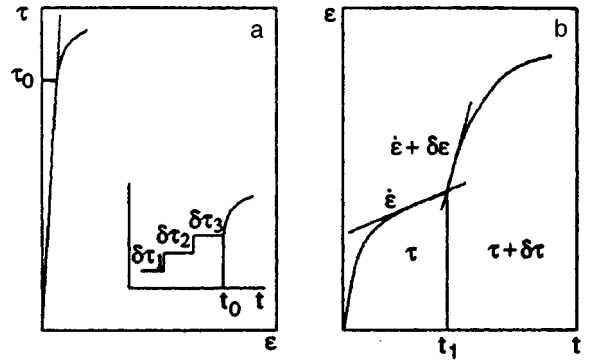

FIG. 3. (a) Schematic diagram of a segment of the stress–strain curve $\tau(\varepsilon)$, τ_0 is the yield stress. The inset shows the diagram of sample deformation under step loading of the crystal by additional loads $\Delta\tau$, t_0 is the instant of time corresponding to the attainment of yield stress. (b) Variation of the creep rate due to the increment $\delta\tau \ll \Delta\tau$ of stress acting on the sample.

recorder to within 5×10^{-5}. Such a loading mode ensured an average strain rate of the crystal of the order of 5×10^{-5} s^{-1}. The strain-hardening curves $\tau(\varepsilon)$ corresponding to the above average strain rate were plotted from the known increments of stress $\Delta\tau$ and corresponding increment of strain max $\Delta\varepsilon$. A detailed analysis of such curves obtained for Sn alloys with Cd and Zn impurities over a wide range of low temperatures is presented in Refs. 12 and 25. Here, we shall be interested only in the behavior of two points on the stress–strain curve, viz., the yield stress τ_0 and the deforming stress τ_5 corresponding to 5% strain.

We also recorded the differential parameter of plasticity $(\partial \ln\dot{\varepsilon}/\partial\tau)_{T,\varepsilon}$, viz., the strain rate sensitivity to deforming stress at a constant temperature T. The value of this quantity was measured along the entire stress–strain curve. The schematic diagram of the experiment is presented in Fig. 3b: after attaining the chosen value of the total strain ε, the loading $\Delta\tau$ generated the next creep curve. At the instant t_1 corresponding to the attainment of the creep rate $\dot{\varepsilon}\simeq10^{-5}$ s^{-1}, a small additional load $\delta\tau$ of the order of 0.1–0.2 MPa was applied, and the increment $\delta\dot{\varepsilon}$ of the strain rate was measured. Using the obtained dependence $(\partial \ln\dot{\varepsilon}/\partial\tau)_{T,\varepsilon}$ on strain ε, we determined the value of rate sensitivity corresponding to $\varepsilon=5\%$. The derivative $(\partial \ln\dot{\varepsilon}/\partial\tau)_{T,\varepsilon}$ we are interested in was calculated as the ratio of finite increments $[\ln(\dot{\varepsilon}+\delta\dot{\varepsilon})-\ln\dot{\varepsilon}]/\delta\tau$.

The experiments described above were made in the temperature range 1.6–150 K. Intermediate temperatures were obtained by using the technique described in Ref. 26. Temperatures below 4.2 K were obtained by evacuation of helium vapor. At temperatures below the superconducting transition temperature for tin ($T_c=3.7$ K), the sample was deformed in a solenoid whose magnetic field exceeded the critical value $H_c=30.5$ mT.

1.2. Yield stress

The yield stress τ_0 was defined as the stress under which the deviation from the linear initial segment of the curves $\tau(\varepsilon)$ corresponding to elastic deformation of the sample was

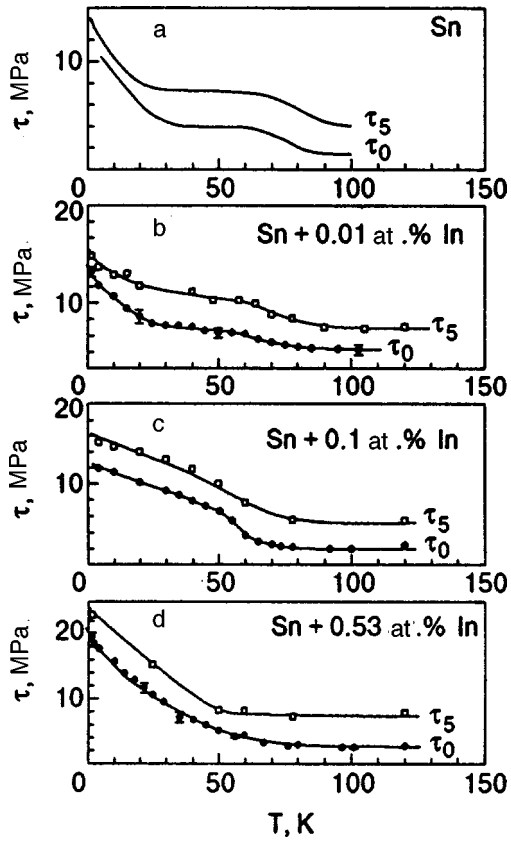

FIG. 4. Temperature dependences of the deforming stress τ_5 and the yield stress τ_0 for pure β-Sn (a) and its alloys with In impurities (b–d).

observed (see Fig. 3a). The value of this quantity is close to the stress corresponding to the onset of irreversible creep, which can easily be determined from the change in the shape of $\Delta\varepsilon(t)$ curves under loading of the crystal (see the inset to Fig. 3a): before the yield stress is reached, the increment of elastic strain corresponds to specific (Γ-shaped) creep curves, while at the yield stress and immediately after it these curve acquire a well-manifested transient stage (the instant t_0 in the inset) corresponding to the developed plastic flow. These methods supplementing one another make it possible to correct the obtained values of τ_0, minimizing the error of their calculation.

Another important circumstance in the estimation of the behavior of the yield stress is the minimization of the spread in the values of τ_0 due to structural and crystallographic difference of the samples under investigation. Special construction of the graphite ampules used by us allowed us to grow large batches of crystals with a preset shape and orientation from the same seed, which could be used as working samples without any additional mechanical treatment (cutting, grinding, or polishing). This method of sample preparation minimizes the influence of random unfavorable factors. In order to reduce their role even further and to control the reproducibility of the results, we measured τ_0 in the same sample at various temperatures. The first measurement was made at the upper limit of the temperature interval; then the sample was unloaded, cooled to a slightly lower temperature, and reloaded to τ_0. Such a procedure was repeated 5–6

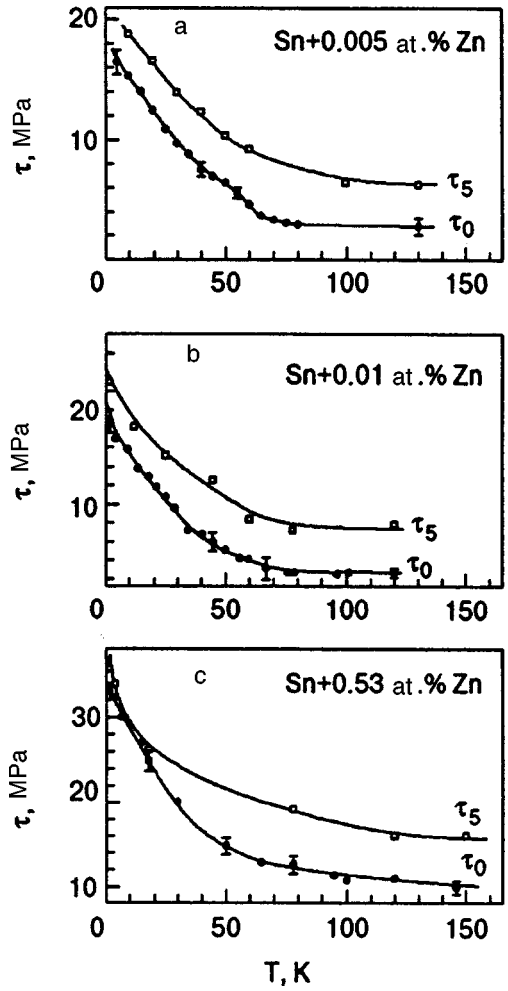

FIG. 5. Temperature dependences of the deforming stress τ_5 and the yield stress τ_0 for alloys of β-Sn with Zn impurities.

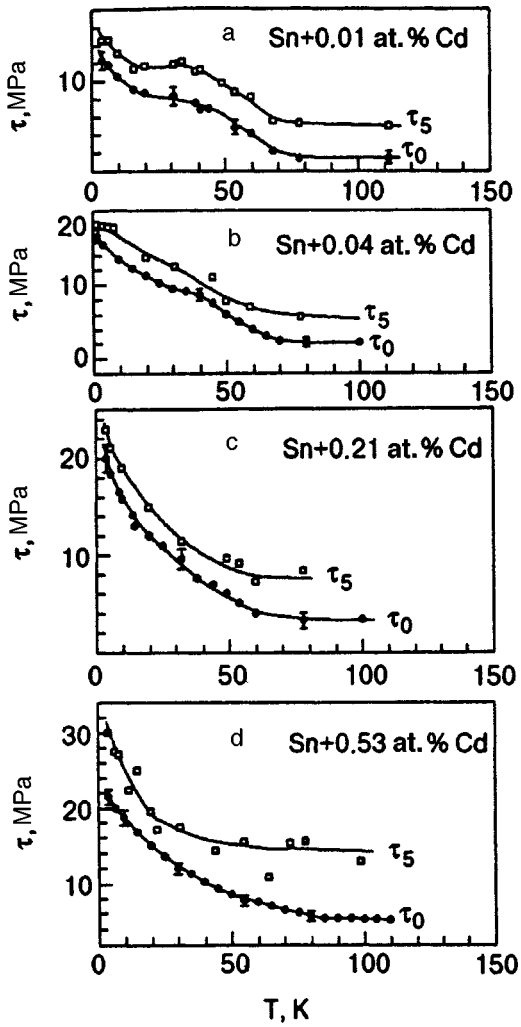

FIG. 6. Temperature dependences of the deforming stress τ_5 and the yield stress τ_0 for alloys of β-Sn with Cd impurities.

times for the same sample, which allowed us to cover quite large temperature intervals. This method allowed us to obtain the $\tau_0(T)$ dependences for several sample from the same batch with a step 1 K in the temperature range below 4.2 K and with a step 5–10 K above 4.2 K.

1.3. Activation volume

In order to determine the temperature dependence $\gamma_\varepsilon(T)$ of activation volume for a fixed value of strain, we used the relation

$$\gamma_\varepsilon(T)=kT\left(\frac{\partial \ln \dot{\varepsilon}}{\partial \tau}\right)_{T,\varepsilon}=kT\,\frac{\ln(\dot{\varepsilon}+\delta\dot{\varepsilon})-\ln \dot{\varepsilon}}{\delta\tau}, \qquad (1)$$

where k is the Boltzmann constant. Using the experimental curves $\tau_\varepsilon(T)$ (τ_ε is the deforming stress corresponding to strain ε, we carry out the transition $\gamma_\varepsilon(T)\rightarrow\gamma(\tau)$. The values of γ measured by us correspond to the strain $\varepsilon=5\%$ in the sample at each temperature. For this reason, the curves $\gamma_5(T)$ for each sample were correlated with the experimental curves $\tau_5(T)$. The $\gamma(\tau)$ dependences obtained as a results of such a recalculation formed the subject of our analysis. The correlation with the 5% strain was required since the derivative $(\partial \ln \dot{\varepsilon}/\partial\tau)_{T,\varepsilon}$ near the yield stress exhibits a considerable dependence on strain and a large statistical spread, while in the strain range $\varepsilon\sim 4-5\%$ its value stabilizes. The same peculiarity is also typical of pure tin,[11] and hence the $\gamma(\tau)$ dependence obtained by us earlier for pure Sn corresponded to approximately the same strain of the samples.

2. EXPERIMENTAL RESULTS AND THEIR DISCUSSION

2.1. Experimental results

Keeping in mind the problem formulated above, we shall confine our analysis to the discussion of only those results that illustrate directly the effect of impurities on the anomalous behavior of yield stress and activation volume. Other aspects of impurity effects will be analyzed in subsequent publications.

Figures 4, 5, and 6 show series of $\tau_0(T)$ and $\tau_5(T)$ curves characterizing the influence of type and concentration of impurities on the temperature dependence of yield stress and deforming stress. Each point on the $\tau_0(T)$ curves is the result of averaging of 3–4 measurements made on the same sample as well as on different samples. The spread in data typical of various temperature intervals is denoted by ''whiskers.'' The $\tau_5(T)$ dependence is represented by the results of

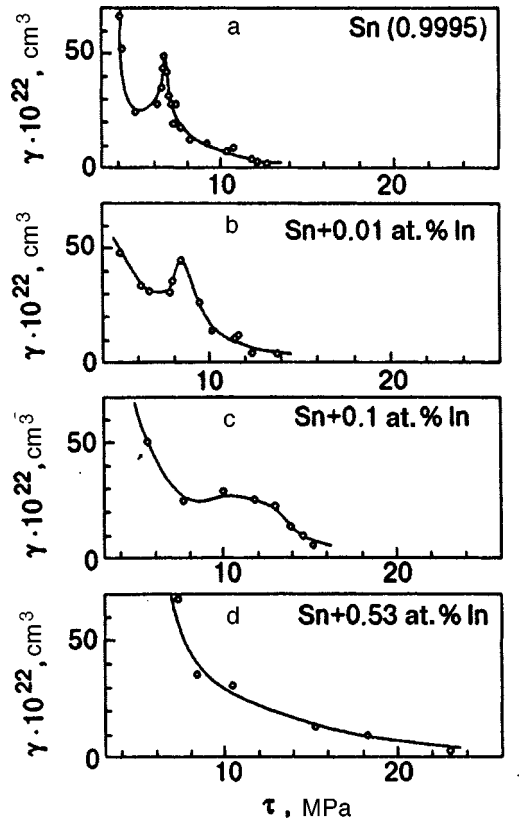

FIG. 7. Stress dependences of activation volume for pure β-Sn (a) and its alloys with In impurities (b–d).

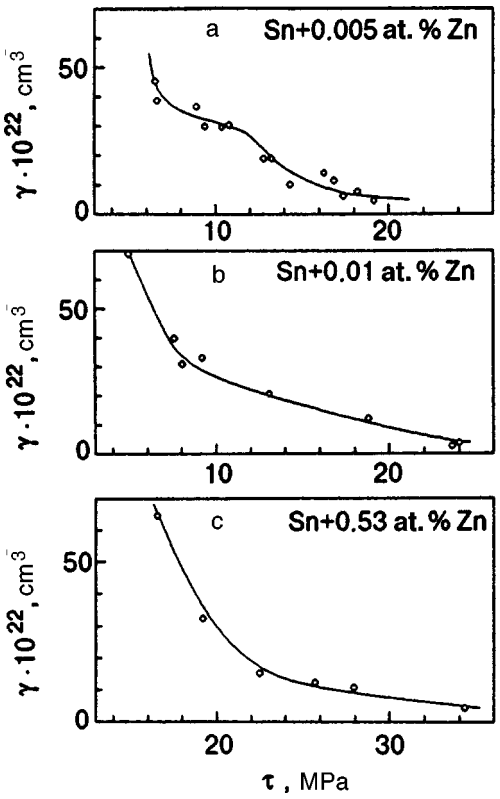

FIG. 8. Stress dependences of activation volume for alloys of β-Sn with different concentrations of Zn impurities.

individual measurements at a fixed temperature. The main conclusions that can be drawn from an analysis of these curves can be formulated as follows.

(1) All three alloys with low impurity concentrations display more of less clearly manifested kinks on the $\tau_0(T)$ and $\tau_5(T)$ curves, similar to the kinks detected for pure β-Sn.
(2) The intensity of the anomaly is determined by the type of the impurity and its concentration in the alloy.
(3) Each alloy has a threshold concentration above which the anomaly disappears.
(4) The magnitude of the threshold concentration depends on the type of the impurity introduced into tin.
(5) The position of the anomaly region on the temperature scale is shifted towards lower temperature relative to the position in pure Sn for all the alloys.

Figure 4 (Sn–In alloy) and Fig. 5 (Sn–Zn alloy) show two extreme tendencies in the effect of impurities on the $\tau_\varepsilon(T)$ anomaly: the low impurity concentration (0.01 at. %) in the case of indium which readily dissolves in tin preserves the clearly manifested anomaly, while the same concentration in the case of poorly soluble zinc leads to the disappearance of the anomaly. All the stages of the influence of impurities on the anomaly can be traced in detail in Fig. 6 (Sn–Cd alloy). In this case, the anomaly disappears for the doping impurity concentration 0.53 at. %, i.e., the values of the threshold concentration for Cd and Zn impurities differ approximately by a factor of 50.

The anomaly and the nature of its variation are manifested even more strongly on the dependences $\gamma(\tau)$ of the activation volume on the deforming stress (Figs. 7, 8, and 9). The presence of clearly manifested peaks on these curves for low impurity concentrations confirms the tendency of nonmonotonic variation of activation volume with stress, which is typical of Peierls crystals (see Figs. 1b and 2b). There exists a clearly manifested correlation between the peaks and kinks on the $\gamma(\tau)$ and $\tau_0(T)$ curves. These anomalies appear and disappear at approximately identical concentrations of the doping impurity, which can be seen most clearly for the Sn–Cd alloy (see Figs. 6 and 9). Such a correlation reflects the fact that both anomalies have the same origin.

The series of $\gamma(\tau)$ curves shown in Fig. 9 and belonging to a Sn–Cd alloy makes it possible to trace in detail the behavior of the peak upon an increase in the Cd concentration. It can be seen that an increase in the concentration leads to a gradual decrease in the peak height, accompanied by blurring and displacement of the peak (relative to its position in pure tin) towards higher stresses. The peak disappears and the $\gamma(\tau)$ curve becomes completely smooth for the Cd concentration 0.53 at. % at which the kink of the $\tau_0(T)$ curve also disappears. A comparison of Fig. 4 with Fig. 7 and of Fig. 6 with Fig. 9 shows that the anomalies on the $\gamma(\tau)$ dependences are manifested most clearly. For this reason, the parameter γ can be used for a more correct estimation of the threshold concentration C_{th} above which the anomaly disappears. The value of C_{th} can be determined most reliably for the Sn–Cd alloy ($C_{\text{th}}^{\text{Cd}} \approx 0.53$ at. %). The value of the threshold concentration $C_{\text{th}}^{\text{In}}$, apparently lies between 0.1 and 0.5

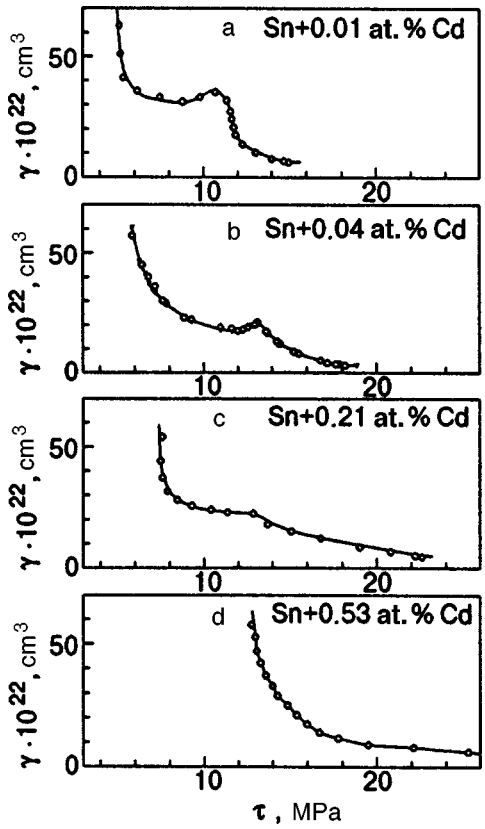

FIG. 9. Stress dependences of activation volume for alloys of β-Sn with different concentrations of Cd impurities.

at. % In for the Sn–In alloy and between 0.005 and 0.01 at. % Zn for the Sn–Zn alloy.

2.2. Discussion of results

It was mentioned above that one of the reasons behind the anomalous behavior of the parameters under investigation in a Peierls crystal is the specific structure of its potential relief, viz., the two-hump shape of the barriers forming this relief. According to the conclusions of the theory developed by Petukhov and Polyakov,[19] point defects in such a crystal must be responsible for some peculiarities in the behavior of anomalies, such as:

(1) perservation of anomalies for low values of defect concentrations;
(2) vanishing of anomalies for a certain critical value of impurity barrier intensity (the force of interaction between a point defect and a dislocation moving in the Peierls relief);
(3) smoothing of the $\tau_0(T)$ curves and decrease in the height of the activation volume peak with increasing concentration and barrier intensity.

Moreover, according to Aono *et al.*,[5] an increase in the concentration of point (impurity) barriers can lead to a shift of activation volume peaks on the $\gamma(\tau)$ curve (see Fig. 2b). Such a displacement was attributed by Aono *et al.*[5] to a change in the depth of the intermediate valley in the two-hump Peierls potential under the effect of impurities (see Fig. 2a).

Let us analyze our results from the point of view of their correlation with the results of theoretical analysis listed above. The first of these results is of qualitative nature and is in good agreement with the data obtained for all the alloys studied by us. For example, anomalous effect are clearly manifested for the Sn–Cd alloy in the concentration range from 0.01 to 0.21 at. %.

In order to verify the second conclusion of the theory, we must choose a quantitative characteristic for the intensity of impurity barriers. We used the dimensionless quantity q introduced by Fleischer:[27,28]

$$q=|\delta_G-\alpha\delta_R|; \qquad (2)$$

$$\delta_G=\frac{2(G_{\mathrm{Sn}}-G_i)}{2G_{\mathrm{Sn}}+|G_{\mathrm{Sn}}-G_i|}; \quad \delta_R=\frac{R_{\mathrm{Sn}}-R_i}{R_{\mathrm{Sn}}}.$$

The symbol q denotes a combined mismatching parameter (barrier intensity) taking into account the contribution of dimensional and module discrepancies to the intensity of interaction between a dislocation and impurity atoms, G_{Sn} and G_i are the shear moduli for tin and the material playing the role of the impurity, R_{Sn} and R_i atomic radii of tin and an atom of the doping element, and the coefficient $\alpha=16$ for screw dislocations and $\alpha=3$ for edge dislocations.

In our analysis of the low-temperature plastic flow of pure β-Sn in the slip system $(100)\langle 010\rangle$, we assumed[11] that it is due to the motion of screw dislocations through Peierls barriers. Retaining this assumption for the case of doped Sn crystals, we can calculate the intensity of impurity barriers decelerating the motion of dislocations (see Table I). Table I also contains information on atomic radii and shear moduli (at helium temperature or close to it) for the components of alloys.

It can be seen from the table that In, Cd, and Zn impurities introduced into tin create barriers of different intensity for dislocations: the highest barriers are formed by Zn atoms and the lowest barriers are created by In atoms.

TABLE I. Dimensional and modular noncorrespondence and the intensity of impurity barriers of In, Cd, and Zn in a tin matrix.

Element	R, Å[29,30]	δ_R	$G=G_{44}$, GPa	δ_G	q
Sn (matrix)	1.62	0	28.2 [Ref. 30 and 32]	0	0
In	1.66	0.024	8 [Ref. 30]	0.53	0.146
Cd	1.57	0.031	24.5 [Ref. 30 and 33]	0.122	0.38
Zn	1.37	0.154	46 [Ref. 30]	−0.48	2.94

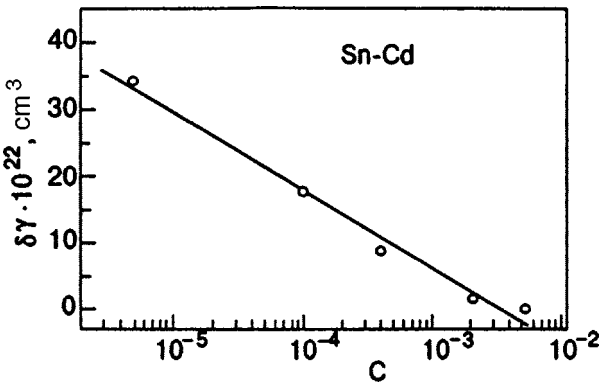

FIG. 10. Dependence of the height of activation volume peak in the Sn–Cd alloy on the Cd impurity concentration.

According to the criterion proposed by Petukhov and Polyakov,[19] the concentration region of existence of anomalies for the Sn–Zn alloy must be much narrower than the corresponding regions for Sn–In and Sn–Cd alloys. A comparison of Figs. 5 and 8 shows that such a tendency is observed indeed: the threshold concentration for the Sn–Zn alloy is lower than that for the Sn–Cd alloy by approximately a factor of 50.

The theory[19] predicts a logarithmic dependence of the heights of the activation volume peak $\delta\gamma$ on the impurity concentration C and the intensity q of the impurity barrier:

$$\delta\gamma \simeq A_0 \ln\left[\left(\frac{\tau_P}{G}\right)^{5/4}\left(\frac{1}{qC^{3/2}}\right)\right], \tag{3}$$

where A_0 is a constant and τ_P the Peierls stress. Using the data presented in Fig. 9 and Table I, we plot the dependences $\delta\gamma(q)$ and $\delta\gamma(C)$ for the Sn–Cd alloy, which are presented in Figs. 10 and 11. It can be seen that the logarithmic dependence of the activation volume peak height on the concentration and intensity of the barriers, which follows from expression (3), is observed satisfactorily for this alloy. The results of our experiments are also in accord with the assumption formulated by Aono *et al.*,[5] according to which the lattices barriers are gradually smoothed upon the introduction of impurity atoms, and the intermediate dip disappears at a certain impurity concentration (see Fig. 2a). This effect must be manifested on the macroscopic level in a displacement of the activation volume peaks along the stress axis, which was detected by us for the Sn–Cd alloy (see Fig. 9).

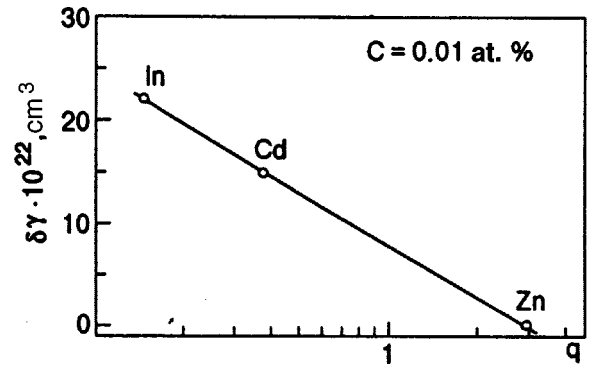

FIG. 11. Dependence of the height of activation volume peak on the intensity of impurity barriers for the alloys Sn–0.01 at. % In, Sn–0.01 at. % Cd, and Sn–0.01 at. % Zn.

Thus, the obtained experimental data and their analysis suggest a two-hump shape of Peierls barriers for screw dislocations of the (100)⟨010⟩ in β-Sn. It should be emphasized that this conclusion is of a purely qualitative nature. Unfortunately, the potentialities of a quantitative analysis for obtaining empirical values of the parameters of the two-hump potential relief are limited even for the Sn–Cd alloy having the broadest spectrum of impurity concentrations. These limitations are due to the following two important circumstances: (1) the asymptotic nature of formula (3) which does not permit a rigorous theoretical determination of the peak height $\delta\gamma$ on the $\gamma(\tau)$ curve, and (2) the small number of points on the curves presented in Figs. 10 and 11 and the lack of a criterion for an accurate quantitative determination of the peak height in Figs. 7–9.

It should be noted that we are still not in a position to explain an extended plateau on the $\tau_0(T)$ curve for pure and slightly doped β-Sn in the temperature range 40–60 K only by the two-hump shape of Peierls barriers.

CONCLUSIONS

(1) The low-temperature creep of single crystals of β-Sn based alloys, which is determined by the slip system (100)⟨010⟩, is studied in detail. It is found that a series of alloys of β-Sn with various concentrations of Cd, In, and Zn exhibit anomalous behavior of the yield stress τ_0 and activation volume γ, which is manifested in noticeable kinks on the temperature dependence $\tau_0(T)$ and in the emergence of peaks on the stress dependences of activation volume $\gamma(\tau)$. Similar anomalies were observed earlier for pure β-Sn.[11]

(2) It is found that the observed anomalies are determined by the impurity concentration in alloys and the intensity of impurity-induced barriers for dislocations. It is shown that the height of the activation volume peak depends logarithmically on these quantities.

(3) The regularities observed in experiments are compared with the conclusions of the theory[19] describing the motion of a dislocation through two-hump barriers of the crystal relief; it is found that the experimental results are in good qualitative agreement with the predictions of the theory. This suggests that the lattice (Peierls) barriers for screw dislocations of the slip system (100)⟨010⟩ in β-Sn have a two-hump shape described for the first time in Refs. 13 and 14.

This research was carried out under the financial support of the Ukrainian State Foundation of Fundamental Studies, project No. 2.4/156 ''Bion.''

*)E-mail: natsik@ilt.kharkov.ua

[1] D. J. Quesnel, A. Sato, and M. Meshii, Mater. Sci. Eng. **5**, 199 (1975).
[2] J. Diehl, M. Schreenev, S. Steiger, and Zwiesele, Scr. Metall. **10**, 949 (1976).
[3] D. K. Bowen and G. Taylor, Acta Metall. **25**, 417 (1977).
[4] E. Kuramoto, Y. Aono, and K. Kitajima, Scr. Metall. **13**, 1039 (1979).

[5] Y. Aono, K. Kitajima, and E. Kuramoto, Scr. Metall. **15**, 275 (1981).
[6] S. Takeuchi, T. Hashimoto, and K. Maeda, Trans. Jpn. Inst. Met. **23**, 60 (1982).
[7] F. Ackerman, H. Mugrabi, and A. Seeger, Acta Metall. **31**, 1353 (1983).
[8] H.-J. Kaufman, A. Luft, and D. Schulze, Cryst. Res. Technol. **19**, 357 (1984).
[9] H. Werner, Phys. Status Solidi A **104**, 63 (1987).
[10] D. Brunner and J. Diehl, Phys. Status Solidi A **104**, 145 (1991).
[11] G. I. Kirichenko, V. D. Natsik, and V. P. Soldatov, Fiz. Met. Metalloved. **65**, 386 (1987).
[12] G. I. Kirichenko, V. D. Natsik, and V. P. Soldatov, Fiz. Nizk. Temp. **18**, 1270 (1992) [Sov. J. Low Temp. Phys. **18**, 887 (1992)].
[13] J. E. Dorn and S. Raynak, Trans. Metall. Soc. AIME **230**, 1052 (1964).
[14] P. Guyot and J. E. Dorn, Can. J. Phys. **45**, 983 (1967).
[15] S. Takeuchi, Philos. Mag. A **39**, 661 (1979).
[16] A. Seeger, Z. Metallkd. **72**, 369 (1981).
[17] A. Seeger, J. Phys. Colloq. **42**, C5-20 (1981).
[18] E. Kuramoto, Y. Aono, and T. Tsutsumi, Kristallogr. **32**, 1324 (1987) [Sov. Phys. Crystallogr. **32**, 778 (1987)].
[19] B. V. Petukhov and Yu. I. Polyakov, Kristallografiya **32**, 1324 (1987).
[20] D. Brunner and J. Diehl, Z. Metallkd. **83**, 828 (1992).
[21] H. Koiziumi, H. O. K. Kirchner, and T. Suzuki, Acta Metall. Mater. **41**, 3483 (1993).
[22] T. Suzuki, H. Koiziumi, and H. O. K. Kirchner, Acta Metall. Mater. **43**, 2177 (1995).
[23] Yu. G. Kazarov, in *Physics of Condensed State* [in Russian], Vol. 11, Kharkov (1973).
[24] M. Hansen and K. Anderko, *Constitution of Binary Alloys*, McGraw-Hill, NY (1958).
[25] A. N. Diulin, G. I. Kirichenko, V. D. Natsik, and V. P. Soldatov, Fiz. Nizk. Temp. **23**, 1122 (1997) [Low Temp. Phys. **23**, 843 (1997)].
[26] G. I. Kirichenko and V. P. Soldatov, Fiz. Met. Metalloved. **54**, 560 (1982).
[27] R. L. Fleischer, Acta Metall. **9**, 996 (1961).
[28] R. L. Fleischer, Acta Metall. **11**, 203 (1963).
[29] W. Pearson, *The Crystal Chemistry and Physics of Metals and Alloys*, Wiley, New York (1972).
[30] G. V. Samsonov (Ed.), *Properties of Elements* [in Russian], Metallurgiya, Moscow (1976).
[31] I. N. Frantsevich, F. F. Voronov, and S. A. Bakuta, *Elastic Constants and Moduli of Metals and Nonmetals* [in Russian], Naukova Dumka, Kiev (1982).
[32] A. A. Hendrickson and E. Fine, AIME **221**, 103 (1970).
[33] W. Mason and R. Thurston (Eds.), *Physical Acoustics. Principles and Methods*, Academic Press, New York (1968–1970).

Translated by R. S. Wadhwa

BRIEF COMMUNICATIONS

On transfer of motion between superfluid liquid and superconducting condensate

S. I. Shevchenko and S. V. Terent'ev

*B. Verkin Institute for Low Temperature Physics and Engineering, National Academy of Sciences of the Ukraine, 310164 Kharkov, Ukraine**

(Submitted January 21, 1998)
Fiz. Nizk. Temp. **24**, 605–608 (June 1998)

The problem of transfer of motion from a superfluid ^{4}He film to electrons in a superconducting film is considered. The conditions under which atoms of ^{4}He film drag superconducting electrons are determined. An experiment is proposed for detecting the predicted effect. © *1998 American Institute of Physics.* [S1063-777X(98)01206-7]

The problem of transfer of motion from one superfluid liquid to another emerged in connection with the possibility of transition of ^{3}He atoms dissolved in superfluid ^{4}He to the superfluid state. It was assumed initially[1–3] that one superfluid liquid does not drag another during its motion. However, it was shown by Andreev and Bashkin[4] that each of the two superfluid movements is accompanied by a transport of both components of the solution. Since the superfluidity of ^{3}He atoms dissolved in ^{4}He has not been detected experimentally so far, the validity of the predictions made by Andreev and Bashkin for the ^{3}He–^{4}He solution cannot be verified for the time being.

In the present communication, we shall indicate another possibility of detecting transfer of motion between two superfluid liquids.

Suppose that the surface of a superconducting film of thickness smaller than the coherence length is covered by a thin film of superfluid ^{4}He. Under the action of the Van der Waals forces, a layer of ^{4}He atoms adjoining the surface of the superconductor passes to the crystalline state. However, the thickness of this layer usually does not exceed the atomic spacing. As a result, the interaction of ^{4}He atoms with electrons in the superconductor will not be negligible and may lead to transfer of motion from one superfluid liquid to the other. For definiteness, we shall consider transfer of motion from ^{4}He to electrons in the superconductor.

The drag of electrons by moving ^{4}He atoms occurs owing to density fluctuations in a superconducting and a superfluid films violating the translational invariance of the system. The density fluctuations in a superconductor are of quite different types at low temperatures and at temperatures close to T_c. At low temperatures, it is sufficient to take into consideration just the collective (plasma) oscillations whose frequency ω tends to zero in the limit of small values of the wave vector $k(\omega \sim k^{1/2})$ in the case of a thin superconducting film (which can be treated as a two-dimensional film). At temperatures close to T_c, we must take into account not only the collective modes but also the one-particle excitations arising due to breaking of Cooper pairs. We shall confine our analysis to the case of low temperatures when depairing can be disregarded and Cooper pairs can be treated as bosons with mass $M=2m$ and charge $Q=2e$, where m and e are the electron mass and charge, respectively. Consequently, the problem of transfer of motion from the atoms of a superfluid ^{4}He film to the electrons in the superconductor may be replaced by the problem of entrainment between neutral and charged Bose gases for a qualitative description.

The energy of electron interaction with helium atoms can be written in the form

$$\int \rho_{\mathrm{He}}(\mathbf{r}_1) V(\mathbf{r}_1-\mathbf{r}_2) \rho_{2e}(\mathbf{r}_2) d\mathbf{r}_1 d\mathbf{r}_2 . \tag{1}$$

Here, $\rho_{\mathrm{He}}(\mathbf{r})$ is the density of helium atoms and $\rho_{2e}(\mathbf{r})$ is the density of Cooper pairs. The potential $V(\mathbf{r})$ associated with the polarization of helium atoms by the electrons in the superconductor is defined as

$$V(\mathbf{r}) = -\frac{\alpha Q^2}{(d^2+r^2)^2}, \tag{2}$$

where α is the polarizability of the ^{4}He atom and d is the thickness of the solid layer between the superfluid film and the superconductor. In view of a sharp decrease in the potential $V(\mathbf{r})$ with increasing r, we can replace (2) by the expression

$$V(\mathbf{r}) = -\frac{\alpha Q^2}{d^4}\, a^2 \delta(\mathbf{r}) \equiv -U a^2 \delta(\mathbf{r}), \tag{3}$$

where a is a length of the order of atomic spacing, and $\delta(\mathbf{r})$ is the δ- function.

In the second-order perturbation theory, the energy correction associated with the interaction (1) can be defined as (S is the area of the system)

$$\Delta \mathscr{E} = -U^2 a^4 S^2 \times \sum_{n,m} \sum_{\mathbf{k}} \langle 0|\hat{\rho}_{\mathrm{He}}(\mathbf{k})|n\rangle\langle n|\hat{\rho}_{\mathrm{He}} \times(-\mathbf{k})|0\rangle \frac{\langle 0|\hat{\rho}_{2e}(-\mathbf{k})|m\rangle\langle m|\hat{\rho}_{2e}(\mathbf{k})|0\rangle}{E^n_{\mathrm{He}}+E^m_{2e}-E^0_{\mathrm{He}}-E^0_{2e}}. \tag{4}$$

For a Bose gas, the density operator $\hat{\rho}(\mathbf{k})$ is connected with the creation and annihilation operators $\hat{b}^+(\mathbf{k})$ and $\hat{b}(\mathbf{k})$ of an elementary excitation through the relation

$$\hat{\rho}(\mathbf{k})=\left(\frac{\varepsilon(k)n}{E(k)S}\right)^{1/2}[\hat{b}(\mathbf{k})+\hat{b}^+(-\mathbf{k})]. \tag{5}$$

Here, $\varepsilon(k)=\hbar^2k^2/2M$, and $E(k)$ is the energy of an elementary excitation. For a neutral Bose gas, $E(k)$ coincides with the Bogoliubov spectrum. For a charged Bose gas, we have

$$E(k)=\left[\left(\frac{\hbar^2k^2}{2M}\right)^2+\frac{2\pi Q^2n_s\hbar^2k}{M}\right]^{1/2}, \tag{6}$$

where $n_s\equiv\langle\rho_{2e}\rangle$ is the equilibrium density of electrons in the superconductor. Equation (6) is written under the condition that the Bose gas is at rest. If the Bose gas moves with a velocity $\mathbf{v}_s$, Eq. (6) must be supplemented with the term $\hbar\mathbf{k}\cdot\mathbf{v}_s$.

In the following, we shall be interested only in the increment to energy $\mathscr{E}$ from (4) associated with the motion of atoms in a ^{4}He film and electrons in a superconducting film. Using formulas (4) and (5), we can easily show that this correction is equal to

$$\delta\mathscr{E}=-U^2a^4\sum_{\mathbf{k}}\frac{\varepsilon_1(k)n_{\mathrm{He}}}{E_1(k)}\frac{\varepsilon_2(k)n_s}{E_2(k)}\frac{[\mathbf{k}\cdot(\mathbf{v}_{s1}-\mathbf{v}_{s2})]^2}{[E_1(k)+E_2(k)]^3}. \tag{7}$$

Here $n_{\mathrm{He}}\equiv\langle\rho_{\mathrm{He}}\rangle$ is the equilibrium density of atoms in a superfluid film, subscripts 1 and 2 mark the quantities corresponding to a ^{4}He film and a superconducting film, respectively. It can be seen that the increment $\delta\mathscr{E}$ depends on the velocity $\mathbf{v}_s\equiv\mathbf{v}_{s1}-\mathbf{v}_{s2}$ of ^{4}He atoms moving relative to electrons and vanishes together with $\mathbf{v}_s$.

Calculations[7] can be simplified considerably if we take into account the fact that the mass M_{He} of a helium atom is about three orders of magnitude larger than the mass $M=2m$ of a pair. As a result, the inequality $E_1(k)\ll E_2(k)$ is satisfied for all significant values of k for $n_{\mathrm{He}}\approx n_s$. Taking this fact into consideration, we obtain from Eq. (7)

$$\delta\mathscr{E}=-\frac{2U^2a^4n_{\mathrm{He}}n_sM^3}{\pi\hbar^4}\left(\frac{\hbar^2}{8\pi Q^2Mn_s}\right)^{2/3}\times\frac{2\pi\sqrt{3}}{9}(\mathbf{v}_{s1}-\mathbf{v}_{s2})^2. \tag{8}$$

Here and below, the area of the system is assumed to be equal to unity.

Formula (8) does not give the entire correction to the energy of the system associated with nonzero velocities $\mathbf{v}_{s1}$ and $\mathbf{v}_{s2}$, but only its part associated with the electron interaction with helium atoms. Formula (8) must be supplemented with the kinetic energy of helium atoms and electrons

$$\frac{n_{\mathrm{He}}M_{\mathrm{He}}v_{s1}^2}{2}+\frac{n_sMv_{s2}^2}{2}. \tag{9}$$

Differentiating the sum of expressions (8) and (9) with respect to $\mathbf{v}_{s2}$ and equating the result to zero, we obtain an equation defining the velocity $\mathbf{v}_{s2}$ for a given velocity $\mathbf{v}_{s1}$.

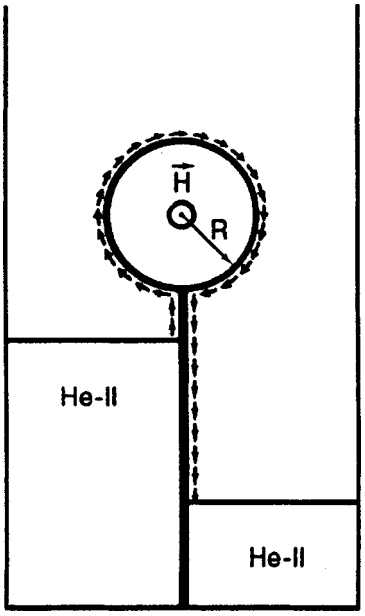

FIG. 1. Schematic diagram of the experiment for detecting the drag of superconducting electrons by superfluid helium. The arrows show the flow of the He II film over the surface of a superconducting cylinder and the wall separating the vessels with helium.

However, the expression obtained after differentiation and multiplied by Q/M coincides exactly with the expression for the electric current induced in the superconducting film by the flow of helium atoms in the superfluid film. Thus, it seems that we have arrived at a conclusion according to which the motion of particles of a superfluid liquid is not transferred to particles of another superfluid liquid. However, this conclusion is erroneous.

In order to find the source of this error, we take into account the fact that the current in a superconducting film is given in the general case by the expression

$$\mathbf{J}_{s2}=\frac{Q}{M}\left[n_s\left(\hbar\nabla\varphi-\frac{Q}{c}\mathbf{A}\right)+\frac{\partial\delta\mathscr{E}}{\partial\mathbf{v}_{s2}}\right], \tag{10}$$

where φ is the phase of the order parameter and $\mathbf{A}$ is the vector potential of the magnetic field generated by the current $\mathbf{J}_{s2}$. The following two cases must be distinguished: (1) the ends of the superconducting film are disconnected, and (2) the superconducting film forms a closed loop.

In the first case, $\nabla\varphi$ can assume arbitrary values, and the phase difference established between the ends of the film is such that the current $\mathbf{J}_{s2}$ is zero. In this case, the atoms of the superfluid ^{4}He film do not drag electrons in the superconducting film indeed.

In the second case, we must take into account the fact that the phase φ satisfies the condition $\oint\nabla\varphi d\mathbf{l}=2\pi n$, where n is an integer. As a result, the current $\mathbf{J}_{s2}$ is zero only for discrete values of the velocity $\mathbf{v}_{s1}$. For example, for low velocities $\mathbf{v}_{s1}$ it is advantageous from the energy point of view that the phase φ be zero. The current $\mathbf{J}_{s2}$ in this case differs from zero. In order to find the current $\mathbf{J}_{s2}$, say, for the case when the superconducting film is a hollow cylinder of radius R (see Fig. 1), we must solve Maxwell's equation

curl$\mathbf{H}=4\pi\mathbf{J}/c$, assuming that $\mathbf{J}=-(Q^2n_s/Mc)\mathbf{A}+(Q/M)\times(\partial\delta\mathscr{E}/\partial\mathbf{v}_{s2})$. As a result, it can be easily shown that

$$\mathbf{J}_{s2}=\frac{Q}{M}\,\frac{1}{1+\gamma}\,\frac{\partial\delta\mathscr{E}}{\partial\mathbf{v}_{s2}}, \tag{11}$$

where $\gamma=2\pi n_sQ^2R/Mc^2$.

Perhaps, the simplest way in which the emergence of current in a superconducting film can be detected is to measure the magnetic flux produced by the current. This magnetic flux is given by

$$\Phi\equiv H\pi R^2=\frac{4\pi}{c}\,\frac{\pi R^2}{1+\gamma}\,\frac{Q}{M}\left|\frac{\partial\delta\mathscr{E}}{\delta\mathbf{v}_{s2}}\right|. \tag{12}$$

For $\gamma\gg1$, we obtain

$$\Phi=\frac{4\sqrt{3}}{27\pi}\left(\frac{U}{\hbar^2/Ma^2}\right)^2\frac{2\pi R}{\hbar}\,Mv_{s1}n_{\mathrm{He}}\left(\frac{\hbar^2}{8\pi Q^2Mn_s}\right)^{2/3}\Phi_0, \tag{13}$$

where $\Phi_0=hc/2e$ is the magnetic flux quantum.

In order to estimate the quantity Φ, we must consider the fact that the polarizability of a helium atom is $\alpha=2\times10^{-25}$ cm^3. In this case, putting $a=d=5\times10^{-8}$ cm, $R=1$ cm, $n_{\mathrm{He}}=10^{15}$ cm^{-2} and $M=2\times10^{-27}$ g, it can be shown easily that for $v_{s1}=10$ cm/s, the magnetic flux $\Phi\simeq2\pi\cdot10^{-4}\Phi_0$. This quantity is within the sensitivity range of modern SQUIDs (see, for example, Ref. 5).

Thus, we have shown that one superfluid liquid may drag another during its motion. The flow of the superfluid component in a ^{4}He film leads to the emergence of current in a superconducting film only if the superconducting film forms a closed loop. Among other things, the existence of current in a superconducting film may be detected by measuring the magnetic flux produced by the current.

*E-mail: shevchenko@ilt.kharkov.ua

[1] I. M. Khalatnikov, Zh. Éksp. Teor. Fiz. **32**, 653 (1957) [Sov. Phys. JETP **5**, 542 (1957)]; Pis'ma Zh. Eksp. Teor. Fiz. **17**, 534 (1973) [JETP Lett. **17**, (1973)].
[2] Z. M. Galasiewicz, Phys. Lett. **43A**, 149 (1973); Phys. Cond. Mat. **18**, 141, 155 (1974).
[3] V. P. Mineev, Zh. Éksp. Teor. Fiz. **67**, 683 (1974) [Sov. Phys. JETP **40**, 338 (1974)].
[4] A. F. Andreev and E. P. Bashkin, Zh. Éksp. Teor. Fiz. **69**, 319 (1975) [Sov. Phys. JETP **42**, 164 (1975)].
[5] R. C. Black, F. C. Wellstood, E. Dantsker *et al.*, Appl. Phys. Lett. **66**, 99 (1995).

Translated by R. S. Wadhwa